Model and algorithm development for the retrieval of atmospheric aerosol properties from nadir mode measurements by the DOAS instrument SCIAMACHY onboard Envisat

Suniti Vinod Sanghavi

INAUGURAL - DISSERTATION
zur
Erlangung der Doktorwürde
der
Naturwissenschaftlich-Mathematischen
Gesamtfakultät
der
Ruprecht-Karls-Universität
Heidelberg

vorgelegt von
Diplom-Physikerin Suniti Vinod Sanghavi
geboren in Mumbai, Indien

Tag der mündlichen Prüfung: 10. Dezember, 2008

Model and algorithm development for the retrieval of atmospheric aerosol properties from nadir mode measurements by the DOAS instrument SCIAMACHY onboard Envisat

Gutachter: Prof. Dr. Ulrich Platt
Dr. Jochen Landgraf

Kurzzusammenfassung

Der Einfluss von Aerosolen auf den Strahlungshaushalt der Atmospäre ist mit grossen Unsicherheiten verbunden und bedarf intensiver Forschung. In dieser Arbeit wurde ein Inversionsalgorithmus entwickelt, um aus Daten des SCIAMACHY-Spektrometers an Bord von ENVISAT Informationen über Aerosole abzuleiten. Der Algorithmus verwendet Spektren im Bereich der O_2 A- und B-Banden zur Bestimmung der optischen Dichte von Aerosolen (AOT), des Ångström Exponenten sowie der vertikalen Höhenverteilung. Modellieren gemessener Reflektanzen ist sowohl für die Bestimmung der Bodenalbedo als auch für die Bestimmung der Aerosoleigenschaften essentiell. In dieser Arbeit wurde 'AeroRad', ein 10-Strahl 1D planparalleles Strahlungstransportmodell mit Verwendung von Gauss-Seidel Iterationen, entwickelt, um die vom Satelliten gemessene Strahlung zu simulieren. Ein neues Merkmal von 'AeroRad' ist die symmetrische Ausrichung der 10-Strahl Geometrie längs der Achse der einfallenden Sonnenstrahlung. Dies erlaubt eine bessere Simulation der für Aerosole typischen preferentiellen Vorwärtsstreuung. Sensitivitätsstudien wurden mit synthetischen Messungen durchgeführt, wobei sich die Inversion als sehr robust erwies. Zur Behandlung instrumenteller Probleme wie fehlerhafter radiometrischer oder Wellenlängen Kalibration wurden Korrekturfaktoren in den Zustandsvektor der Inversion eingebaut, um diese Parameter simultan mit den Aerosoleigenschaften für das jeweilige Bodenpixel zu invertieren. Die Inversionsmethode wurde mit realen SCIAMACHY Daten über Kanpur (Indien) im Jahre 2003 getestet. Ein Vergleich monatlicher Mittelwerte der invertierten AOT zeigt eine gute Übereinstimmung mit bodengebundenen Messungen des AERONET Netzwerkes. Ein für die Region typischer Anstieg der AOT von April bis Juni wurde beobachtet und kann mit vermehrtem Auftreten von Wüstenstaub erklärt werden. Obwohl die Bestimmung globaler Verteilungen von Aerosoleigenschaften mit der hier entwickelten Inversionsmethode zumindest fü SCIAMACHY aufgrund mehrerer Faktoren noch unrealistisch scheint, so wurde gezeigt, dass eine Inversion mehrerer Aerosolparameter prinzipiell möglich ist wenn Informationen aus mehreren Spektralbereichen kombiniert werden.

Short summary

The impact of aerosols on the earth's radiation budget is subject to large uncertainties and warrants further investigation. In this work, an inversion procedure has been developed for the full retrieval of aerosol optical thickness (AOT), Ångström exponent and the vertical profile of the aerosol concentration over a ground pixel from multispectral measurements made by the DOAS instrument SCIAMACHY onboard Envisat. The algorithm makes use of moderate resolution spectra of the strong O_2 A and B bands. Forward modeling of the measured reflectances is essential for both albedo determination and aerosol retrieval. 'AeroRad', a 10-stream 1D plane parallel radiative transfer model using Gauss-Seidel iterations has been developed for the simulation of reflectances observed by a nadir pointing satellite instrument. A novel feature of AeroRad is the symmetric alignment of its streams around the direction of incident direct solar radiation, allowing for better simulation of strong forward peaks typical of aerosols. Sensitivity studies have been carried out using synthetic measurements, wherein the retrieval method has proved to be fairly robust. Instrumental issues such as wavelength and radiometric calibration errors are dealt with by incorporating respective correction factors into our state vector, retrieving them simultaneously with the aerosol properties. The inver-

sion is tested with real SCIAMACHY data for measurements over Kanpur, India during the year 2003. Comparing mean monthly AOT's, a good agreement between our retrievals and AERONET measurements is obtained. A typical increase in AOT from April to June could be observed and can be associated with desert dust. Even though a smoothly functioning global coverage of aerosols using the full retrieval procedure may not yet be realistic, it is shown that an inversion of multiple aerosol parameters is, in principle, possible by combining information from different spectral regions.

Contents

1 Aerosols **2**

1.1 What are aerosols? 2

1.2 Mechanisms for the formation of aerosols 4

1.2.1 Dispersion 4

1.2.2 Nucleation, condensation and coagulation 5

1.3 Size distribution of aerosols 7

1.4 Removal mechanisms and atmospheric lifetimes of aerosols 8

1.5 Vertical distribution of aerosols 10

1.6 Impact of aerosols on the climate 12

1.7 Types of aerosols and their sources 13

1.7.1 Soil dust 13

1.7.2 Sea salt 14

1.7.3 Industrial dust, primary anthropogenic aerosols 14

1.7.4 Carbonaceous aerosols (organic, black carbon, and biogenic SOAs) . . . 14

1.7.5 Primary biogenic aerosols 15

1.7.6 Sulphates 15

1.7.7 Nitrates 16

1.7.8 Volcanoes 16

1.8 Global monitoring of aerosols 21

1.9 Satellite based remote sensing of aerosols 21

1.9.1 Moderate Resolution Imaging Spectroradiometer (MODIS) 21

1.9.2 Multi-angle Imaging SpectroRadiometer (MISR) 22

1.9.3 POLarization and Directionality of the Earth's Reflectances (POLDER) 22

1.10 The SCanning Imaging Absorption SpectroMeter for Atmospheric CHartography (SCIAMACHY) . . . 23
1.10.1 Operational aerosol products hitherto available from SCIAMACHY/GOME data . . . 23
1.11 Retrieval of aerosols from SCIAMACHY data: advantages and disadvantages . 26
1.11.1 Advantages . . . 26
1.11.2 Disadvantages . . . 26

2 Modeling 28

2.1 Basic principle . . . 28
2.2 Equation of radiative transfer . . . 29
2.3 Single-scattering radiation . . . 32
2.4 Multiple-scattering radiation . . . 34
2.5 Model comparisons . . . 40
2.5.1 I/I_0 vs. SZA . . . 42
2.5.2 I/I_0 vs. LZA . . . 43
2.5.3 I/I_0 vs. albedo . . . 44
2.5.4 I/I_0 spectra in regions of strong absorption . . . 46
2.6 Representation of aerosols in AeroRad . . . 48
2.6.1 Aerosol phase function . . . 50
2.7 Influence of aerosols on radiative transfer . . . 55
2.7.1 Dependence of single and multiple-scattering reflectivity on aerosol type 55
2.7.2 Dependence of single and multiple-scattering reflectivity on aerosol loading 56

3 Determination of the lambertian albedo 67

3.1 Reflectances above a given ground pixel . . . 68
3.2 Uncertainties of clear-sky identification . . . 74
3.3 Bidirectional reflectance . . . 80
3.4 Calculation of ground albedo . . . 83
3.5 Accuracy of albedo determination . . . 84
3.6 Error in albedo determination . . . 85
3.7 Albedo measurements from SCIAMACHY . . . 98
3.7.1 Multispectral method for the identification of a clear-sky scenario 98

3.7.2 Determination of surface albedo using SCIAMACHY measurements . . 100

4 Aerosol retrieval from space 106

4.1 Parametrization of aerosols: the state vector 106

4.2 Choice of measurement vector 107

4.3 Basic principle: Optimal estimation 108

4.3.1 The forward model, $\mathbf{F}(\vec{x})$ 108

4.3.2 The Jacobi matrix, $\mathbf{K}$ 109

4.3.3 Bayes' Theorem 110

4.3.4 Uncertainties associated with the measurement and the a priori state vector: the covariance matrices $\mathbf{S}_\epsilon$ and $\mathbf{S_a}$ 110

4.3.5 Degrees of freedom 111

4.3.6 Information content of a measurement 112

4.3.7 The retrieval method 112

4.4 Sensitivity studies 114

4.4.1 Sensitivity to aerosol optical thickness, τ_{700} 114

4.4.2 Sensitivity to Ångström exponent, α_{700} 117

4.4.3 Sensitivity to the peak height of the vertical distribution of aerosol, z_p . 119

4.4.4 Sensitivity to peak width of the vertical distribution of aerosol, σ_p . . . 122

4.5 Summary 124

5 Application to SCIAMACHY spectra 125

5.1 Forward model adaption for SCIAMACHY 126

5.1.1 Shifting of the measured solar irradiance spectrum with respect to the measured earthshine spectrum 127

5.1.2 Spectral shift and squeeze 128

5.1.3 Uncertainties in the radiometric calibration of the instrument 129

5.2 Synthetic test examples 131

5.3 Sensitivity of the retrieval to model parameter error 133

5.3.1 Surface albedo 133

5.3.2 A priori aerosol type 134

5.4 Aerosol retrievals from SCIAMACHY measurements over Kanpur in 2003 . . . 135

5.4.1 Comparison of SCIAMACHY aerosol retrievals with AERONET 137

5.5 A brief analysis of aerosol retrievals from SCIAMACHY measurements over Kanpur in 2003 140
5.6 Conclusion 144

6 Conclusion and outlook **146**
6.1 Outlook 148

List of Figures **162**

List of Tables **163**

References **164**

Acknowledgements **172**

Chapter 1

Aerosols

In this chapter, we classify atmospheric aerosols into different types based on source, size and abundance, study their direct and indirect effects and discuss the role they play in the radiative forcing of the atmosphere. We then discuss some of the methods and instruments employed for the measurement of aerosols and the advantages of satellite measurement for their global monitoring. We analyze and compare different satellites instruments based on their retrieval strategies. Finally, we examine the suitability of the instrument SCIAMACHY onboard Envisat for aerosol monitoring and lay out its advantages and shortcomings in this respect.

1.1 What are aerosols?

'Aerosol' refers to solid or liquid particles (or particulate matter (PM)) suspended in the atmosphere. Examples are smoke, oceanic haze, air pollution, and smog. The word aerosol derives from the fact that matter 'floating' in air is a suspension (a mixture in which solid or liquid or combined solid-liquid particles are suspended in a fluid). To differentiate suspensions from true solutions, the term sol evolved - originally meant to cover dispersions of tiny (sub-microscopic) particles in a liquid. With studies of dispersions in air, the term aerosol has evolved to embrace both liquid droplets, solid particles, and combinations of these.

Atmospheric aerosols range from natural aerosols like desert dust, sea spray, soot and ash from forest and grassland fires and volcanic ash, to anthropogenic aerosols like secondary organic aerosols due to biomass burning and automobile exhaust, sulphate particles formed from industrial emissions, airplane contrails and wind blown dust from land areas where water and vegetation have been removed. Averaged over the globe, aerosols made by human activities currently account for about 10% of the total amount of aerosols in our atmosphere. Most of that 10% is concentrated in the Northern Hemisphere, especially downwind of industrial sites, slash-and-burn agricultural regions, and overgrazed grasslands.

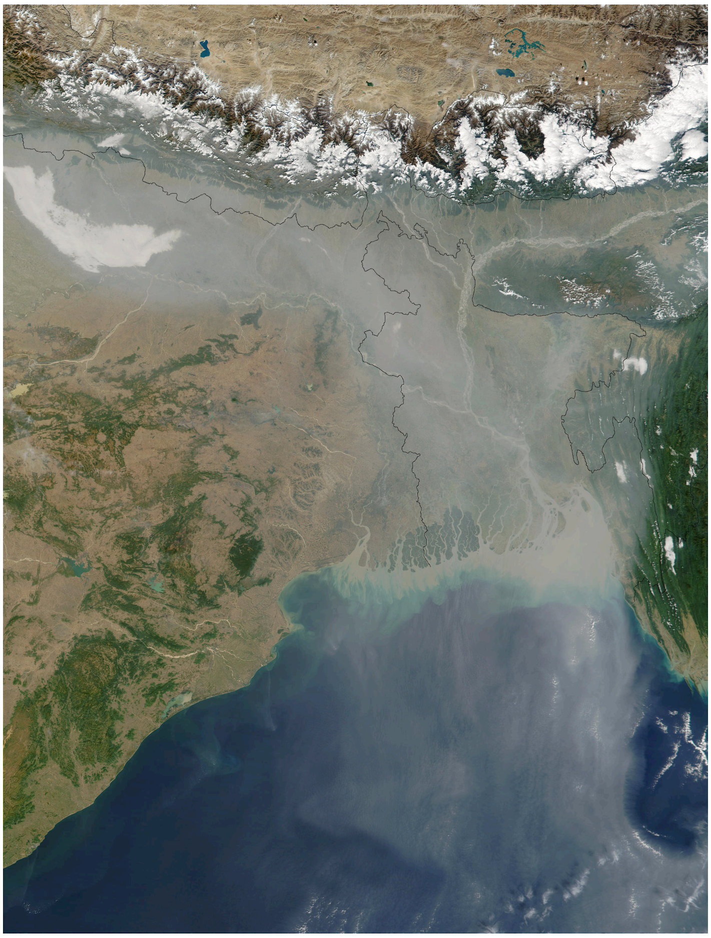

Figure 1.1: Aerosol pollution over Northern India and Bangladesh (http://visibleearth.nasa.gov/).

All this particulate matter ranges in size from about a few nanometers to a few hundred microns. Some of these particles are emitted directly into the atmosphere (primary emissions) and some are emitted as gases and form particles in the atmosphere (secondary emissions). The formation mechanisms of aerosols are covered in Section 1.2.

Under normal circumstances, the majority of aerosols form a thin haze in the lower atmosphere (troposphere), where they are washed out of the air by rain within about a week. Aerosols are also found in the lower part of the stratosphere. A severe volcanic eruption, such as Mount Pinatubo in the Philippines in 1991, can eject large amounts of aerosol into the stratosphere as shown in Fig.1.6. Since there are no convective cycles producing rain in the stratosphere, these aerosols can remain there for many months, producing beautiful sunsets around the globe, and possibly causing summer temperatures to be cooler than normal. It is estimated that Mount Pinatubo injected about 20 million tons of sulfur dioxide into the atmosphere, reducing average global temperatures over the following year by about half a degree.

Aerosols, in general, impact air quality, impairing visibility and causing respiratory health problems. They can also transport fungal and viral or microbial pathogens, which can lead to disease outbreaks in different parts of the world. They affect the climate by changing the way radiation is transmitted through the atmosphere. Changes in the atmospheric concentrations of aerosols, besides greenhouse gases, land cover and solar radiation, alter the energy balance of the climate system, thus driving climate change. They affect the absorption, scattering and emission of radiation within the atmosphere and at the Earth's surface. The resulting positive or negative changes in energy balance due to these factors, expressed as radiative forcing, determine their warming or cooling influences on global climate. Over last 30 years, several major aerosol types have been identified leading to general ideas about the amount of aerosol to be found in different seasons and locations. Still, key details about the amount and properties of aerosols are needed to calculate effect on surface and atmospheric temperatures; so far, it has not been possible to make these measurements on a global scale with a high degree of certainty. According to the latest IPCC report, anthropogenic aerosols (primarily sulphate, organic carbon, black carbon, nitrate and dust) produce a cooling effect, with a total direct radiative forcing of -0.5 [-0.9 to -0.1] $\mathsf{W/m^2}$ and an indirect cloud albedo forcing of -0.7 [-1.8 to -0.3] $\mathsf{W/m^2}$. In addition, aerosols also influence other atmospheric phenomena such as precipitation (*Forster et al.*, 2007). Section 1.6 deals with the various direct and indirect effects of aerosols on the radiative forcing properties of the atmosphere.

1.2 Mechanisms for the formation of aerosols: dispersion and nucleation

New aerosol particles are brought into existence in the atmosphere by two main channels (*Roedel*, 2000), viz.

- By dispersion and lofting of substances from the earth surface that occur in a condensed form, e.g. mineral dust and sea salt. Such aerosols are primary aerosols as their formation does not involve any phase transformations.
- From the gas phase by condensation of supersaturated vapor (homogeneous nucleation). Such vapors may be produced by chemical reaction between originally gaseous components of the atmosphere (eg. $\mathsf{H_2SO_4}$ vapor from $\mathsf{SO_2}$). Aerosols formed thus are secondary by definition.

In the following, we expand briefly on each of the above mechanisms.

1.2.1 Dispersion

Mineral dust and sea-spray are the two largest global sources of aerosols. This is because they mainly arise from arid or semi-arid continental regions and oceans respectively. Arid regions of the world cover about one-third of the global land area, while oceans cover about 71% of the earth's surface. Both aerosol types are produced by dispersion processes.

Mineral dust aerosols are produced by the lofting of particles from the earth's surface into the air by the wind. Lofting of solid particles bound to the surface is set off by motion of the particles tangential to the ground surface due to the drag exerted on them by the wind

(*Roedel*, 2000). This results in a reduced surface of contact between the underlying surface and the particle, which in turn reduces the adhesion between them. The aerodynamic buoyant forces thus become more effective, lofting particles into the air. For particles smaller than $\approx 0.1\,\mu\mathrm{m}$ the adhesion to the surface outweighs the buoyant force of the wind, as a result of which mineral dust aerosol is composed primarily of coarse particles.

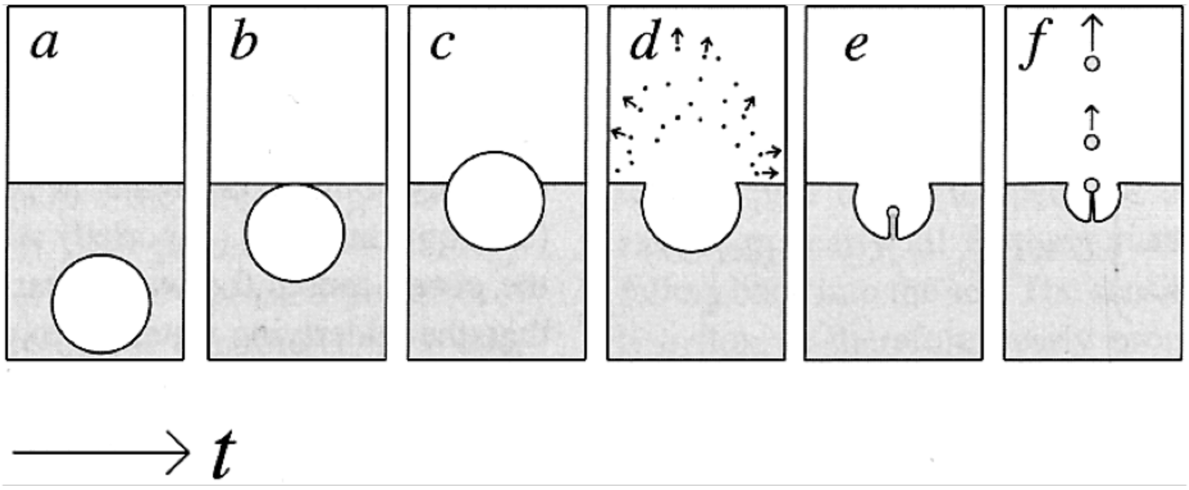

Figure 1.2: Sea spray droplet formation due to the bursting of entrained bubbles.

Sea salt aerosols are produced by the bursting of bubbles at the ocean surface. The bubbles are produced due to strong winds which causes entrainment of air into the ocean water leading to white cap formation. The bubbles have a diameter of about $100\,\mu\mathrm{m}$ or less. As the bubbles burst, sea spray is by two mechanisms (*Roedel*, 2000) as shown in Fig. 1.2:

1. The film forming the surface of the bubble first disintegrates into a large number of tiny droplets, with diameters less than if the order of a few micrometers.
2. This is followed by the propulsion due to the surface tension of the bubble of a central jet consisting of 3-8 droplets, sized about 10% of the bubble diameter.

Sea spray droplets evaporate in the air to about 50%-30% of their original diameter. Complete evaporation remains unlikely due to the hygroscopicity of sea salt. The presence of sea salt in the marine atmosphere is restricted to the lower layers ($< 3\,\mathrm{km}$) with a number density of $\approx 100\,\mathrm{cm}^{-3}$.

1.2.2 Nucleation, condensation and coagulation

Nucleation plays a fundamental role in the formation from the gas phase (air) of trace substances and water in the liquid or solid phase. A transformation from, for example, a vapor phase to a liquid phase does not occur spontaneously. Rather, small nuclei must form initially in the gaseous phase. This first step in the phase transformation can be very slow. Once the initial nucleation step has occurred, the nuclei of the new phase grow rapidly.

Nucleation can occur in the absence or presence of foreign material. Homogeneous nucleation is the nucleation of vapor on embryos comprised of vapor molecules only in the absence of foreign substances. Heterogeneous nucleation is the nucleation on a foreign substance or surface, such as an ion or a solid particle. In addition, nucleation processes can be homomolecular (involving a single species) or heteromolecular (involving two or more species). Consequently, four types of nucleation processes can be identified (*Seinfeld and Pandis*, 2006):

1. Homogeneous-homomolecular: self-nucleation of a single species. No Foreign nuclei or surfaces involved.

2. Homogeneous-heteromolecular: self-nucleation of two or more species. No Foreign nuclei or surfaces involved.

3. Heterogeneous-homomolecular: nucleation of a single species on a foreign substance.

4. Heterogeneous-heteromolecular: nucleation of two or more species on a foreign substance.

Homogeneous nucleation takes place in a supersaturated vapor phase. The degree of supersaturation of a molecular species A in air at temperature T is defined by the saturation ratio $S = p_A/p_A^S(T)$, where p_A is the partial pressure of A and $P_A^S(T)$ is the saturation vapor pressure of A in equilibrium with its liquid phase at temperature T. If A is water (H_2O), the same quantity expressed as a percentage is called the Relative Humidity (RH). $S < 1$ for subsaturated vapor, $S = 1$ for saturated vapor and $S > 1$ for supersaturated vapor.

The phase change of molecules from gas to liquid as the vapor pressure exceeds the saturation vapor pressure over a flat liquid surface of effectively infinite extent is driven by the corresponding decrease in the Gibbs free energy of the system. This does not hold for the condensation of vapor into small droplets, however, as the energy needed to provide the surface tension to hold a small droplet exceeds the energy released due to condensation for partial vapor pressures far exceeding the saturation vapor pressure. Since, in the absence of foreign bodies, small droplets need to be formed before they can grow into larger stable droplets, the onset of homogeneous-homonuclear nucleation is very slow and may occur only when the vapor may become supersaturated by undergoing various thermodynamic processes such as isothermal compression, isobaric cooling or adiabatic expansion.

For homogeneous-heteromolecular nucleation, i.e. when two or three vapor species are present, neither of which is supersaturated, nucleation can still take place as long as the participating vapor species are supersaturated with respect to their liquid solution. In this case, the formation of a liquid droplet is aided by the release of the heat of solution in the exothermic case. The most important such system naturally occurring in the atmosphere is that of sulphuric acid (H_2SO_4) and water (H_2O) undergoing binary nucleation(*Kulmala and Laaksonen*, 1990), followed by ternary nucleation of sulphuric acid (H_2SO_4), ammonia (NH_3) and water (H_2O)(*Kulmala et al.*, 2000) and the nucleation of organic vapors(*Hoffmann et al.*, 1997b).

Heterogeneous nucleation can occur on ions, insoluble particles or soluble particles. The most important heterogeneous nucleation processes in the atmosphere involve nucleation of vapor molecules on aerosol particles, both insoluble and soluble. Nucleation of water vapor on soluble particles is the process by which cloud and fog droplets form in the atmosphere.

Nucleation deals with the formation of a single particle. A population of particles in the atmosphere leads to interactions between individual particles. Changes occur in the population when a vapor compound condenses on the particles (condensation) or when the particles collide and adhere (coagulation).

The processes of nucleation, condensation as well as coagulation govern the size distribution of the aerosol population. The general form of the size distribution is dealt with in the next section.

1.3 Size distribution of aerosols

As a result of particle emission, in situ formation and the variety of subsequent processes, the atmospheric aerosol size distribution is characterized by a number of modes. The volume or mass distribution is dominated in most cases by the accumulation mode ($\approx 0.1\,\mu\mathrm{m} - 2\,\mu\mathrm{m}$) and the coarse mode ($\approx 2\,\mu\mathrm{m} - 50\,\mu\mathrm{m}$) as shown in the lower panel of Fig. 1.3.

Accumulation mode particles are the result of primary emissions, condensation of secondary sulphates, nitrates and organics from the gas phase, and coagulation of smaller particles. In a number of cases, the accumulation mode consists of two overlapping submodes: the condensation mode and the droplet mode (*John et al.*, 1990) as is shown in the lower panel of Fig. 1.3. The condensation submode results from primary particle emissions, and growth of smaller particles by coagulation and vapor condensation. The droplet submode is created during cloud processing of some of the accumulation mode particles. Particles in the coarse mode are usually produced by mechanical dispersion processes due to wind or erosion (dust, sea salt, pollens, etc.). Most of the material in the coarse mode is primary, but there may be some secondary sulphates and nitrates.

A different picture of the aerosol size distribution emerges by plotting the number of particles instead of their mass (Fig. 1.3, upper panel). It is found that particles with diameters larger than $0.1\,\mu\mathrm{m}$, which contribute practically all the aerosol mass, are negligible in number compared to smaller particles. Two modes usually dominate the aerosol number distribution in urban and rural areas: the nucleation mode (particles smaller than $\approx 10\,\mathrm{nm}$) and the Aitken nuclei (particles with diameters between $\approx 10\,\mathrm{nm} - 100\,\mathrm{nm}$). Nucleation mode particles are usually fresh aerosols created in situ from the gas phase by nucleation. The nucleation mode may or may not be present depending on the atmospheric conditions. Most of the Aitken nuclei start as primary particles, and secondary material condenses on them as they are transported though the atmosphere. Nucleation mode particles have negligible mass while larger Aitken nuclei form the accumulation mode in the mass distribution.

Particles with diameters larger than $2.5\,\mu\mathrm{m}$ are identified as coarse particles, while those with diameters less than $2.5\,\mu\mathrm{m}$ are called fine particles. The fine particles include most of the total number of particles and a small fraction of the mass. Fine particles with diameters less than $0.1\,\mu\mathrm{m}$ are often called ultrafine particles.

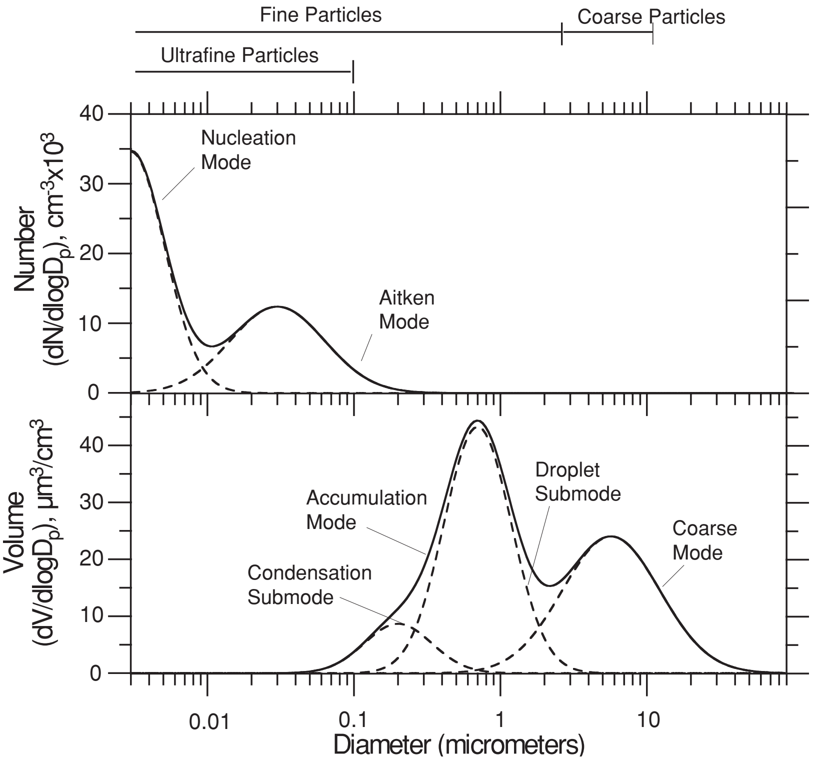

Figure 1.3: Typical number and volume distributions of atmospheric particles with the different modes (*Seinfeld and Pandis*, 2006).

Atmospheric aerosol size distributions are generally described as the sum of n lognormal distributions

$$n_N^o(\log D_p) = \sum_{i=1}^{n} \frac{N_i}{(2\pi)^{1/2}\log\sigma_i} \exp\left[-\frac{(\log D_p - \log \bar{D}_{pi})^2}{2\log^2\sigma_i}\right] \tag{1.1}$$

where N_i is the number concentration, $\bar{D}_{pi}$ is the median diameter, and σ_i is the standard deviation of the ith lognormal mode. Thus, $3n$ parameters are required for the description of the full aerosol size distribution.

1.4 Removal mechanisms and atmospheric lifetimes of aerosols

Once an aerosol particle is suspended in the atmosphere, it may get altered, removed or destroyed, giving it an average residence time of the order of a few days to about a week. Removal processes can be grouped into two broad categories: dry deposition and wet deposition.

Dry deposition denotes the direct transfer of particles to the earth's surface and proceeds without the aid of precipitation. Dry deposition includes two mechanisms:

1. Gravitational settling, which simply means a particle falling under gravity. Very large particles fall, reaching a terminal velocity, which can be found by equating the force due

to gravity with the viscous drag (from StokesÕ law) of the ambient medium. Aerosols fall through the boundary layer at this rate until they strike the surface.

2. Turbulent deposition is the most effective dry vertical transport mechanism in the boundary layer. Particlulate matter possesses sufficient inertia to allow particles to be projected over large distances as in desert storms, depending on the size of the particle.

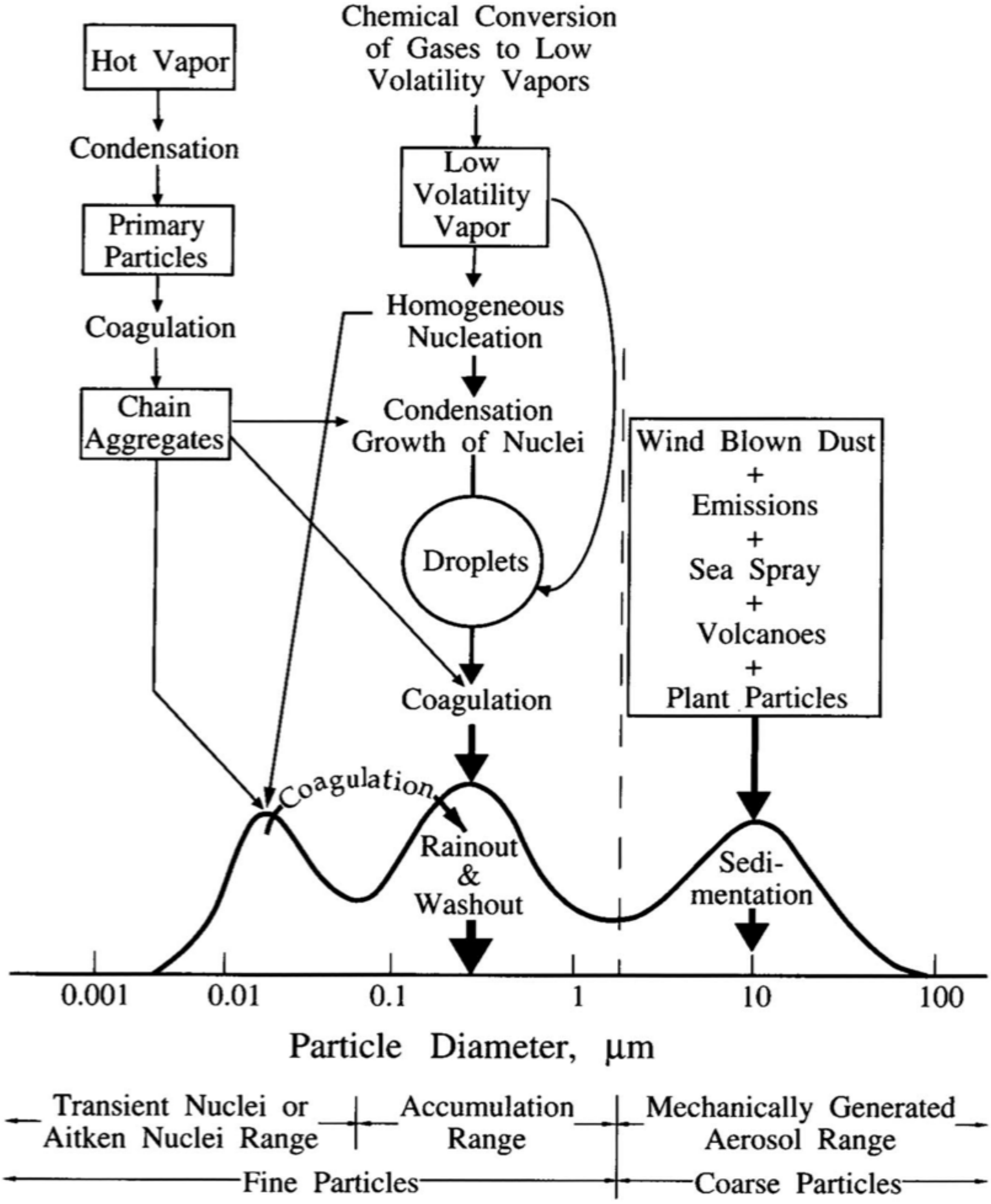
Hot Vapor
Condensation
Primary Particles
Coagulation
Chain Aggregates
Chemical Conversion of Gases to Low Volatility Vapors
Low Volatility Vapor
Homogeneous Nucleation
Condensation Growth of Nuclei
Droplets
Coagulation
Coagulation
Rainout & Washout
Wind Blown Dust + Emissions + Sea Spray + Volcanoes + Plant Particles
Sedi-mentation
0.001
0.01
0.1
1
10
100
Particle Diameter, µm
Transient Nuclei or Aitken Nuclei Range
Accumulation Range
Mechanically Generated Aerosol Range
Fine Particles
Coarse Particles

Figure 1.4: Idealized schematic of the distribution of particle surface area of an atmospheric aerosol (*Whitby and Cantrell*, 1976). Principal modes, sources, and particle formation and removal mechanisms are indicated. (Adapted from *Seinfeld and Pandis* (2006))

Wet deposition, on the other hand, encompasses all processes by which airborne species are transferred to the earth's surface in aqueous form (rain, snow or fog). Wet deposition mechanisms include:

1. Rainout, which describes the removal of a cloud condensation nucleus. Aerosol particles act as the nuclei for the condensation of cloud droplets. In clouds with sufficiently high liquid water content, some of these drops grow large enough to gravitationally settle to the surface as rain drops.
2. Washout, describing the removal of aerosol by cloud droplets. If an aerosol is incorporated into an already existing cloud drop, and that drop grows large enough to fall as rain, the particle is said to have been washed out. The difference between washout and rainout is the required pre-existence of a collecting drop for washout.
3. Sweepout, relating to the aerosol below the cloudbase of a raining cloud, which can impact into falling raindrops. If the impact leads to incorporation of the aerosol into the drop, the aerosol is deposited with the raindrop and is swept out by it.
4. Occult deposition, which is a slightly more complicated concept than the other three wet processes mentioned above. Impaction efficiency is the likelihood that a particle will strike a surface feature encountered in a flow, rather than be deflected around the object. It is a strong function of size, with larger aerosol being more likely to impact on a surface feature than smaller particles. Aerosol can be incorporated into droplets in clouds making contact with the surface of the ground (e.g. fog, orographic clouds). The impaction efficiency of these droplets is higher than that of the aerosol they nucleate on. This produces an enhanced probability of impaction for such aerosol incorporated into drops. Sticking efficiency is the probability that an impacted object will not bounce off and be instantly resuspended. Providing the sticking efficiency of cloud drops is not significantly lower than that of the nucleating aerosol, clouds contacting the ground can give rise to an enhanced deposition rate for small aerosol.

It can be seen from Fig. 1.4 that ultrafine and Aitken mode particles generally undergo further condensation and coagulation until they gain enough size to belong to the accumulation mode. The lifetime of ultra fine particles ranges from a few minutes to a few hours, while fine particles reside in the atmosphere for a few hours or days before they are altered into larger particles by coagulation or are removed by various deposition processes. Particles in the coarse mode stay in the atmosphere for a few hours or days until they are removed, mainly by gravitational settling. Accumulation mode particles are so-named because particle removal mechanisms are least efficient in this regime, causing the accumulation of particles, which can remain suspended in the atmosphere for weeks before being removed predominantly due to wet deposition.

1.5 Vertical distribution of aerosols

The vertical distribution of aerosol mass concentration typically shows an exponential decrease with altitude upto a height H_p and a more or less constant profile above H_p (*Gras*, 1991). The aerosol mass concentration as a function of height z can be expressed as

$$M(z) = M_0 \exp\left(-\frac{z}{H_p}\right), \tag{1.2}$$

where M_0 is the surface concentration and H_p is the scale height. *Jaenicke* (1993) proposed values of H_p equal to 900 m for marine, 730 m for remote continental, 2000 m for desert and 30,000 m for polar aerosol types.

The aerosol number concentration may increase or decrease exponentially with altitude. A suggestion for the form of the profile (*Jaenicke*, 1993) is

$$N(z) = N_0 \left[\exp\left(-\frac{z}{\|H_p'\|}\right) + \left(\frac{N_B}{N_0}\right)^n\right]^n, \tag{1.3}$$

where

$$n = \frac{H_p'}{\|H_p'\|}$$

and N_B is the number concentration of the background aerosol. For marine aerosol H_p' varies from -290 to 440 m.

These vertical profiles are rough representations of long-term averages. Aerosol concentrations in anthropogenic plumes, areas affected by local sources, and nucleation events in the free troposphere display significant variability in their vertical profiles.

The greatest variability in profiles occurs on a diurnal scale within the earth's boundary layer, where primary emissions (dust, carbonaceous, sea-spray, etc.) constitute most of the particulate mass.

Low aerosol mass concentrations observed in the remote free troposphere (background aerosol) are found to be correlated with high number concentrations of ultrafine, volatile aerosol (*Clarke*, 1992). These observations suggest that clean regions of the middle and upper troposphere act as significant source regions for new atmospheric nuclei. As reactive gases are pumped to higher levels of the atmosphere by convective clouds, the atmosphere is simultaneously cleansed of preexisting aerosol, creating optimal conditions for this type of new particle production (*Clarke*, 1993). The nuclei have a long enough lifetime to allow them to be mixed throughout the troposphere (including into the boundary layer), where they may serve as the source of aerosol and CCN.

Stratospheric aerosols originate in a large part from transport of long-lived sulfur (mainly COS) gases from the troposphere to the stratosphere, where they are oxidized to sulfate, and from periodic injection of volcanic emissions. Polar stratospheric cloud particles comprise the other types of stratospheric aerosol. Type II PSCs are thought to be composed primarily of water ice. Type I PSCs are composed primarily of nitric acid (HNO_3) and water.

1.6 Impact of aerosols on the climate

Aerosol effects on the climate are generally classified as direct, semi-direct, first indirect and second indirect.

Table 1.1: Overview of the different aerosol indirect effects and range of the radiative budget perturbation [$\mathrm{W\,m^{-2}}$] at the top-of-the atmosphere (F_{TOA}), at the surface (F_{SFC}) and the likely sign of the change in global mean surface precipitation (P) (*Lohmann and Feichter*, 2001)

Effect	Cloud type	Description	F_{TOA}	F_{SFC}	P
Indirect aerosol effect for clouds with fixed water contents (cloud albedo or Twomey effect)	All clouds	The more numerous smaller cloud particles reflect more solar radiation	-0.5 to -1.9	similar to F_{TOA}	n/a
Semi-direct effect	All clouds	Absorption of solar radiation by soot may cause evaporation of cloud particles	+0.1 to -0.5	larger than F_{TOA}	decrease
Thermodynamic effect	Mixed-phase clouds	Smaller cloud droplets delay the onset of freezing	?	?	increase or decrease
Glaciation indirect effect	Mixed-phase clouds	More ice nuclei increase the precipitation efciency	?	?	increase
Riming indirect effect	Mixed-phase clouds	Smaller cloud droplets decrease the riming efciency	?	?	decrease
Surface energy budget effect	All clouds	Increased aerosol and cloud optical thickness decrease the net surface solar radiation	n/a	-1.8 to -4	decrease

The direct aerosol effect occurs due to the highly scattering nature of aerosols. Non absorbing aerosols backscatter incident sunlight, leading to cooling of the earth's surface and atmosphere. This negative radiative forcing due to aerosols is believed to be partly offsetting the heating due to greenhouse gases (*Reader and Boer* (1998);*Kiehl and Briegleb* (1993);*Hegerl et al.* (1997)). The direct effect of aerosol can also include the positive forcing due to a strongly absorbing aerosol, e.g. soot.

Black carbon (BC) that may be present in aerosols can lead to a reduction in cloud cover, and thereby, in liquid water path. This is labeled the "semi-direct effect". It is caused by absorption of radiation by the BC which leads to evaporation of cloud droplets. Model studies using the

ECHAM4 GCM concluded that the reduction in cloud cover and liquid water path could respectively amount to 4% and 10 $\mathsf{g/m^2}$ in highly polluted areas of the northern hemisphere. This heating can also partially offset the cooling due to the indirect effect (*Lohmann and Feichter*, 2001).

The first indirect effect describes the increase in cloud albedo with increasing aerosol loading. Aerosols act as cloud condensation nuclei (CCN), thereby determining the initial cloud droplet number concentration, albedo, precipitation and lifetime of warm clouds. For a given liquid water path, more aerosols means distribution over more CCN, and thus, smaller droplets. Smaller droplets are better scatterers, as a result of which the cloud albedo increases. This is the first indirect, or Twomey or cloud albedo effect (*Twomey*, 1991), accounting for a cooling between -0.5 and -1.9 $\mathsf{W/m^2}$.

Furthermore, the smaller cloud droplets resulting from a larger number of aerosols available as CCN leads also to a decrease in precipitation efficiency, thereby prolonging cloud lifetimes. This is the second indirect or cloud lifetime effect (*Albrecht*, 1989), causing cooling between -0.3 and -1.4 $\mathsf{W/m^2}$.

Table 1.6 summarizes the various radiative effects of aerosols.

1.7 Types of aerosols and their sources

Aerosols occur in several types, depending upon whether they are natural or manmade, whether their production mechanism is secondary or primary, depending on whether they are coarse or fine, depending on their radiative warming or cooling effect, etc. In the following, aerosols are primarily classified on the basis of their source. The source strengths, size distributions, and radiative forcing of each type is discussed. Fig. 1.5 shows production rates of the most dominant aerosol types and the resultant global optical depth as simulated by the CHAM/GRANTOUR model.

1.7.1 Soil dust

The greatest source of aerosols are arid land areas such as deserts and dry water beds, releasing dust and sand into the atmosphere. The global source strength of soil dust is estimated to be 1000-5000 Tg/yr. The atmospheric lifetime of dust particles depends on their size. Large particles are quickly removed by gravitational settling while sub-micron sized particles remain suspended in the atmosphere for several weeks. To estimate the radiative effects of dust aerosol, information is needed on the size and refractive index of the particles and on whether the minerals are mixed externally or exist as internal aggregates. Typical volume-median diameters of dust particles are of the order of 2 to 4 mm. Refractive indices measured on Saharan dust are often used to estimate the global dust radiative forcing (*Tegen et al.*, 1996). This dust has a single scattering albedo significantly below one, resulting in weak forcing due to partial cancellation of solar and thermal forcing, as well as cancellation of positive and negative forcing over different geographic regions (*Tegen and Lacis*, 1996). However, different refractive indices of dust from different regions as well as regional differences in surface albedo lead to a large uncertainty in the resulting top-of-atmosphere dust forcing (*Sokolik and Toon* (1996); *Claquin et al.* (1998); *Claquin et al.* (1999)).

1.7.2 Sea salt

Sea salt aerosols are mainly released due to the bursting of entrained air bubbles during white-cap formation, which depends strongly on wind speed. Owing to its high single scattering albedo and hygroscopicity, this aerosol is a dominant contributor to light scattering and cloud formation, especially in those regions of the marine atmosphere where wind speeds are high and/or other aerosol sources are weak (*O'Dowd et al.* (1997); *Murphy et al.* (1998); *Quinn et al.* (1998)). Sea salt particles cover a wide size range (about 0.05 to 10 mm diameter), and have a correspondingly wide range of atmospheric lifetimes. For the present-day climate, the total sea salt flux from ocean to atmosphere is estimated to be 3,300 Tg/yr, within the range of previous estimates (1,000 to 3,000 Tg/yr, *Erickson and Duce* (1988); 5,900 Tg/yr, *Tegen et al.* (1997)).

1.7.3 Industrial dust, primary anthropogenic aerosols

Transportation, coal combustion, cement manufacturing, metallurgy, and waste incineration are among the industrial and technical activities that produce primary aerosol particles. Recent estimates for the current emission of these aerosols range from about 100 Tg/yr (*Andreae and Henderson-Sellers*, 1995) to about 200 Tg/yr (*Wolf and Hidy*, 1997). These aerosol sources are responsible for the most conspicuous impact of anthropogenic aerosols on environmental quality, and have been widely monitored and regulated. As a result, the emission of industrial dust aerosols has been reduced significantly, particularly in developed countries. Considering their source strength and the fact that much of the industrial dust is present in a size fraction that is not optically very active (> 1 mm diameter), it is probably not of climatic importance at present. On the other hand, growing industrialisation without stringent emission controls, especially in Asia, may lead to increases in this source to values above 300 Tg/yr by 2040 (*Wolf and Hidy*, 1997).

1.7.4 Carbonaceous aerosols (organic, black carbon, and biogenic SOAs)

Carbonaceous aerosols account for a large but highly variable fraction of atmospheric aerosols. The main sources for carbonaceous aerosols are biomass and fossil fuel burning, and the atmospheric oxidation of biogenic and anthropogenic volatile organic compounds (VOC). Organic aerosols form the single largest component of biomass burning aerosols. These aerosols are known to scatter light at least as strongly as sulphate aerosols. Organics are the predominant constituents of upper-troposphere aerosols. Due to the presence of polar functional groups such as carboxylic and dicarboxylic acids, these aerosols are hydrophilic and can actively participate in cloud formation, thus playing an important role in the indirect climate effect of aerosols as well. The global emission of sub-micron sized organic aerosol from biomass and fossil fuel burning has been estimated at 45 to 80 and 10 to 30 Tg/yr, respectively (*Penner et al.* (1996); *Cooke et al.* (1999); *Scholes et al.* (1996)). The volatile nature of organics have so far hindered their precise quantification. Black carbon, present in the form of soot or tarry substances, plays an important role in the direct aerosol effect due to its light-absorbing character. Combustion processes are the dominant source for black carbon. Recent estimates place the global emissions from biomass burning at 6 to 9 Tg/yr and from fossil fuel burning at 6 to 8 Tg/yr (*Penner et al.* (1991); *Cooke and Wilson* (1996); *Penner et al.* (1996); *Cooke et al.* (1999); *Scholes et al.* (1996)). However, as with organics, considerable uncertainties persist regarding the source strengths of light-absorbing aerosols. Biogenic hydrocarbons get oxidized in the atmosphere to produce low volatility compounds that readily form aerosols. Due to their gas-particle conversion, these secondary organic aerosols (SOA) are sub-micron sized. Producion of aerosols from biogenic compounds is governed by oxidation processes. While oxidation by O_3 and NO_3 is more efficient than by the OH radical, it is limited only to polluted areas where concentrations of O_3 and NO_3 become substantial. Global production of biogenic SOA's thus depends largely on oxidation by OH. The subsequent condensation of organic compounds onto aerosols depends not only on the partial pressure of the biogenic compounds and the ambient temperature but also on the presence of other aerosol organics that can absorb products from gas-phase hydrocarbon oxidization (*Odum et al.* (1996); *Hoffmann et al.* (1997a); *Griffin et al.* (1999a)). When combined with appropriate transport and reaction mechanisms in global chemistry transport models, these hydrocarbon emissions yield estimated ranges of global biogenically derived SOA of 13 to 24 Tg/yr (*Griffin et al.*, 1999b) and 8 to 40 Tg/yr (*Penner et al.*, 1998). Anthropogenic VOC can also be oxidised to organic particulate matter, but account for a very small source strength for this aerosol type, about $0.6 \pm 0.3\,\mathsf{Tg/yr}$ (*Picott et al.*, 1992; *Odum et al.*, 1996).

1.7.5 Primary biogenic aerosols

Primary biogenic aerosol consists of plant debris (cuticular waxes, leaf fragments, etc.), humic matter, and microbial particles (bacteria, fungi, viruses, algae, pollen, spores, etc.). Presently, little information is available to allow for a reliable estimation of the contribution of primary biogenic particles to the total aerosol loading of atmosphere. In an urban, temperate setting, concentrations of 10 to 30% of the total aerosol volume in both the sub-micron and super-micron size fractions have been found (*Matthias-Maser and Jaenicke*, 1995). Their contribution in densely vegetated regions, particularly the moist tropics, could be even more significant. The presence of humic-like substances makes this aerosol light-absorbing, especially in the UV-B region (*Havers et al.*, 1998), and there is evidence that primary biogenic particles may be able to act both as cloud droplets and ice nuclei (*Schnell and Vali*, 1976). They may, therefore, be of importance for both direct and indirect climatic effects.

1.7.6 Sulphates

With the exception of sea-salt DMS and gypsum dust, sulphate is produced by chemical reactions in the atmosphere from gaseous precursors. The main precursors of sulphate aerosols are SO_2 from anthropogenic sources and volcanoes, and DMS from biogenic sources, mainly marine phytoplankton. The source distribution for SO_2 is fairly well-known and its magnitude is known to vary between 67-130 TgS/yr (*Lelieveld et al.*, 1997). Estimating the emission of marine biogenic DMS requires a gridded database of its concentration in surface sea water and a parametrization of the sea/air gas transfer process. A mean estimate obtained by this method is 24 TgS/yr (*Kettle and Andreae*, 2000). Global sulphate burdens vary strongly as a result of not only precursor variations, but also differences in deposition rates. Sulphate in aerosol particles is present as sulphuric acid, ammonium sulphate, and intermediate compounds, depending on the availability of gaseous ammonia to neutralise the sulphuric acid formed from SO_2. However, the hydration behaviour and refractive indices or all these aerosols remain fairly uniform in comparison to the differences in their respective source strengths and lifetimes.

1.7.7 Nitrates

Nitrate aerosol production is closely linked to the relative abundances of sulphate and ammonium in the atmosphere. If ammonium abundances exceed that of sulphate, it may be available for reaction with nitrates to form aerosols which are efficient scatterers of radiation. If this is not the case, the nitric acid deposits on other alkaline minerals or sea-salt in the atmosphere (*Bassett and Seinfeld* (1984);*Murphy and Thomson* (1997);*Gard et al.* (1998)), which generally exist in the coarse mode, reducing the single scattering albedo and radiative efficiency of the resultant aerosol (*Li-Jones and Prospero*, 1998). Until recently, nitrates were not considered noteworthy because of their low atmospheric burdens and negligible contribution to direct radiative forcing. However, their relevance is expected to increase over the coming century. For example, the SRES A2 emissions scenario projects that NO_x emissions will more than triple in that time period while SO_2 emissions decline slightly. Assuming increasing agricultural emissions of ammonia, it is conceivable that direct forcing by ammonium nitrate could become comparable in magnitude to that due to sulphate (*Adams et al.*, 2001). Nitrate forcing is already quite important at the regional scale in parts of Europe, India and North America with elevated NO_x and NH_3 emissions, where NH_4NO_3 aerosol concentrations may be high enough to exceed those of sulphate.

1.7.8 Volcanoes

Primary dust and gaseous sulphur are the two most important components of volcanic emisions for the formation of aerosols. The dust flux is estimated to range from 4-10000 Tg/yr (*Jones et al.*, 1994) with a best estimate of 33 Tg/yr (*Andreae*, 1995). Estimates of the emission of sulphur containing species from quiescent degassing and eruptions range from 7.2 TgS/yr to 14 ± 6 TgS/yr (*Stoiber et al.* (1987); *Spiro et al.* (1992); *Graf et al.* (1997); *Andres and Kasgnoc* (1998)). These estimates are highly uncertain because only very few of the potential sources have ever been measured and the variability between sources and between different stages of activity of the sources is considerable. Volcanic sulphate aerosols lead to the formation of ice nuclei in the upper troposphere, producing a strong indirect radiative effect. Volcanic SO_2 also has a longer lifetime than anthropogenic SO_2 due to lack of deposition mechanisms at the altitudes at which they are emitted, causing the production of sulphate aerosols to be 4.5 times more effective, albeit the anthropogenic source strength is 5 times greater (*Graf et al.*, 1997). In the stratosphere, most sulphate aerosol is produced by the UV photolysis of carbonyl sulphide(COS) to sulphate. In the lower stratosphere, though, about a third of the sulphate is injected directly from the tropical troposphere, accounting for a third of the total sulphate mass (*Weisenstein et al.*, 1997). During volcanically inactive periods, the global stratospheric sulphate load is about 0.15 TgS (*Kent and McCormick*, 1984), which accounts for 15% of the total sulphate load (in the stratosphere and the troposphere together). Volcanic eruptions violent enough tp penetrate the stratosphere are relatively rare. Nevertheless, their transient climatic effects are large and longlasting. Historical records of such eruptions have shown that over 100 Tg of SO_2 can be injected during a single event, having led to strong transient cooling effects of −0.14 to −0.3°C for eruptions in the 19th and 20th centuries (*Robertson et al.*, 2001).

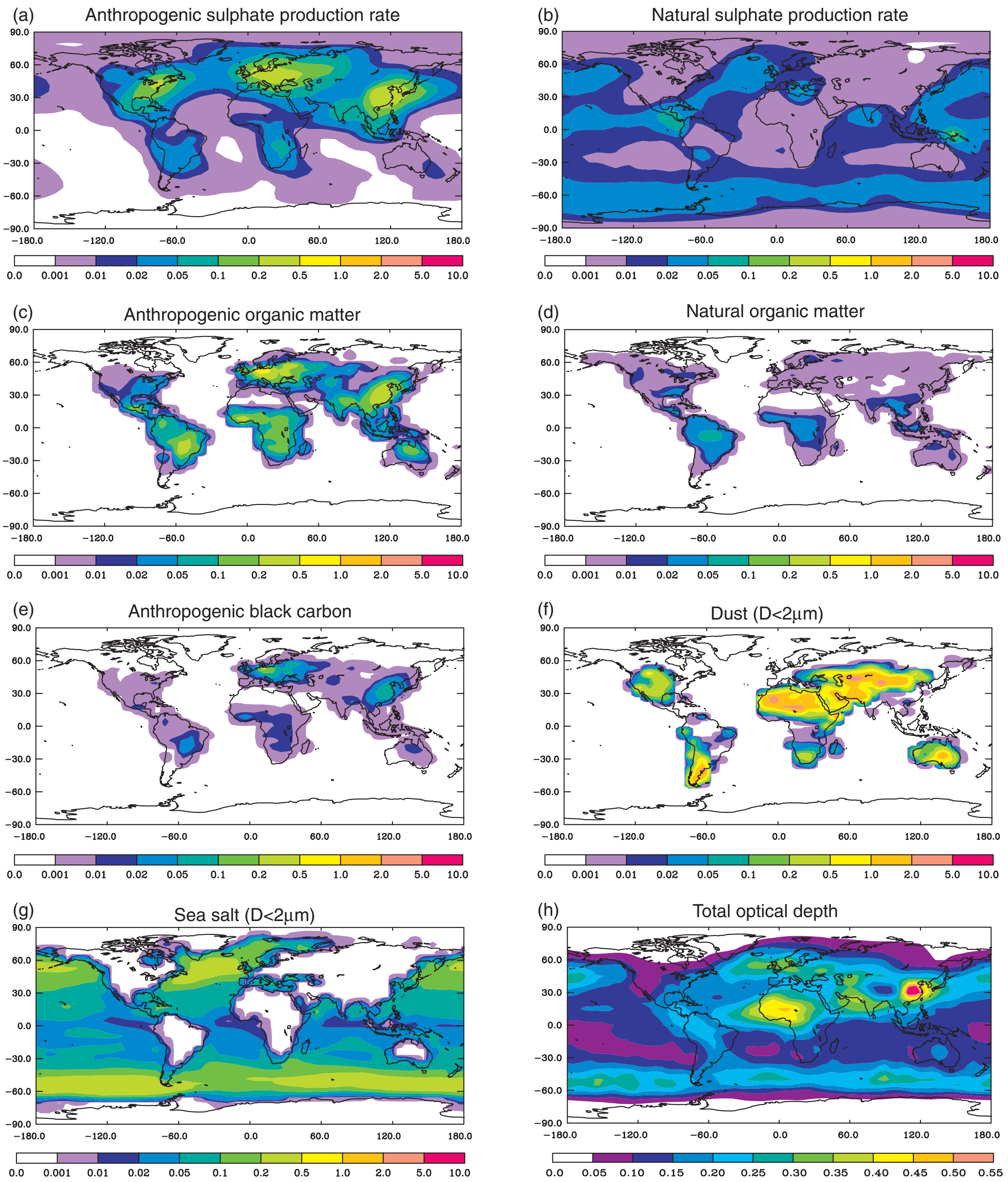

(a) Anthropogenic sulphate production rate

(b) Natural sulphate production rate

(c) Anthropogenic organic matter

(d) Natural organic matter

(e) Anthropogenic black carbon

(f) Dust (D<2µm)

(g) Sea salt (D<2µm)

(h) Total optical depth

90.0
60.0
30.0
0.0
−30.0
−60.0
−90.0
−180.0
−120.0
−60.0
0.0
60.0
120.0
180.0
0.0 0.001 0.01 0.02 0.05 0.1 0.2 0.5 1.0 2.0 5.0 10.0
0.0 0.05 0.10 0.15 0.20 0.25 0.30 0.35 0.40 0.45 0.50 0.55

Figure 1.5: Annual average source strength in $\mathsf{kgkm^{-2}hr^{-1}}$ for each of the aerosol types considered here (a to g) with total aerosol optical depth (h). Shown are (a) the column average H_2SO_4 production rate from anthropogenic sources, (b) the column average H_2SO_4 production rate from natural sources (DMS and SO_2 from volcanoes), (c) anthropogenic sources of organic matter, (d) natural sources of organic matter, (e) anthropogenic sources of black carbon, (f) dust sources for dust with diameters less than 2 µm, (g) sea salt sources for sea salt with diameters less than 2 µm, and (h) total optical depth simulated by the CHAM/GRANTOUR model. Source: IPCC 2001, Ch. 5, Fig. 5.2

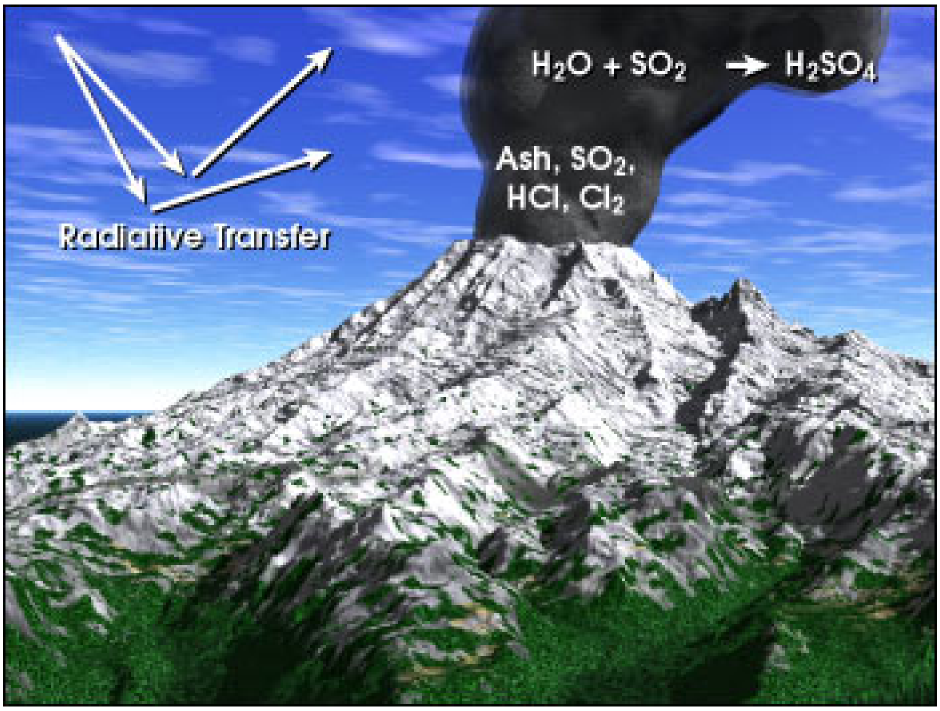

Figure 1.6: As volcanoes erupt, they blast huge clouds into the atmosphere. These clouds are made up of particles and gases, including sulfur dioxide SO_2. Several megatons of sulfur dioxide gas from a major volcanic eruption can reach the stratosphere. There, the sulfur dioxide is converted to tiny persistent sulfuric acid (H_2SO_4) aerosols by reaction with the ambient water vapor H_2O. These aerosols reflect energy coming from the sun, thereby preventing the sun's rays from heating Earth's surface. Volcanic eruptions are thought to be responsible for the global cooling that has been observed for a few years after a major eruption. The amount and global extent of the cooling depend on the force of the eruption and, possibly, on its location relative to prevailing wind patterns. (Graphic by Robert Simmon, Goddard DAAC)

Table 1.2: Annual source strength for present day emissions of aerosol precursors (Tg N, S or C /year)

	N. Hemisphere	S. Hemisphere	Global	Range
NO_2 (as TgN/yr)	32	9	41	
Fossil fuel	20	1.1	21	
Aircraft	0.54	0.04	0.58	0.4-0.9
Biomass burning	3.3	3.1	6.4	2-12
Soils	3.5	2.0	5.5	3-12
Agricultural soils			2.2	0-4
Natural soils			3.2	3-8
Lightning	4.4	2.6	7.0	2-12
NH_3 (as TgN/yr)	41	13	54	40-70
Domestic animals	18	4.1	21.6	10-30
Agriculture	12	1.1	12.6	6-18
Human	2.3	0.3	2.6	1.3-3.9
Biomass burning	3.5	2.2	5.7	3-8
Fossil fuel and industry	0.29	0.01	0.3	0.1-0.5
Natural soils	1.4	1.1	2.4	1-10
Wild aminals	0.10	0.02	0.1	0-1
Oceans	3.6	4.5	8.2	3-16
SO_2 (as TgS/yr)	76	12	88	67-130
Fossil fuel and industry	68	8	76	60-100
Aircraft	0.06	0.004	0.06	0.03-1.0
Biomass burning	1.2	1.0	2.2	1-6
Volcanoes	6.3	3.0	9.3	6-20
DMS or H_2S (as TgS/yr)	11.6	13.4	25	12-42
Oceans	11	13	24	13-36
Land biota and soils	0.6	0.4	1.0	0.4-5.6
Volatile organic emissions (as TgC/yr)	171	65	236	100-560
Anthropogenic	104	5	109	60-160
Terpenes	67	60	127	40-400

1.8 Global monitoring of aerosols

As seen in the previous section, aerosols and their precursors have largely regional sources. Also, their atmospheric lifetimes range from a few hours to a few weeks (with the exception of stratospheric aerosol), allowing no time for large-scale mixing. As a result, aerosol distributions display very high spatial and temporal variations. Unlike for well-mixed gases like tropospheric CO_2, O_2 or stratospheric O_3, local measurements would not suffice to characterize aerosols and determine their effect on global climate. Hence, monitoring aerosols globally necessitates a wide network of coordinated ground based measurements or satellite measurements. AERONET (AErosol RObotic NETwork) is a federation of ground based remote sensing aerosol networks established by NASA and LOA-PHOTONS (CNRS), greatly expanded by international collaborators. It provides a longterm, continuous and readily accessible public domain database of aerosol optical, mircrophysical and radiative properties. The network imposes standardization of instruments, calibration, processing and distribution, providing globally distributed observations of spectral aerosol optical depth (AOD), inversion products, and precipitable water in diverse aerosol regimes. Other examples of ground based aerosol networks are AeroCAN (The canadian aerosol network), GLOBE (Global Learning and Observations to Benefit the Environment), MPLNET (The Micro-pulse Lidar Network) and SKYNET (with obeservation sites located mainly in Eastern Asia from Mongolia to Thailand as well as in Japan). Satellites currently dedicated to monitoring aerosol are AVHRR (on NOAA, Metop), POLDER (on ADEOS, ADEOS II), MISR (on Terra), MODIS (on Terra, Aqua), AATSR (on Envisat 1), MERIS (on Envisat 1), GLI (on ADEOS II) and OMI (on EOS CHEM). Some instuments employing unique retrieval strategies will be discussed more in detail in the next section.

1.9 Satellite based remote sensing of aerosols

There are several satellite instruments dedicated to monitoring aerosols, most importantly retrieving the aerosol optical thickness[1] (AOT). Here we shall briefly describe the key specifications, available aerosol data products and retrieval strategies of the following satellite instruments:

1.9.1 Moderate Resolution Imaging Spectroradiometer (MODIS)

MODIS is a key instrument onboard the Terra (EOS AM) and Aqua (EOS PM) satellites. Terra and Aqua orbit the Earth in sun-synchronous, nearly polar circular orbits, with equator crossing times of 10:30 am and 1.30 pm, respectively. Terra MODIS and Aqua MODIS acquire data in 36 spectral bands, achieving global coverage in 1-2 days.

---

[1] "Aerosol Optical Thickness" is the degree to which aerosols prevent the transmission of light. The aerosol optical depth or optical thickness (τ) is defined as the integrated extinction coefficient over a vertical column of unit cross section. Extinction coefficient is the fractional depletion of radiance per unit path length. The optical thickness along the vertical direction is also called normal optical thickness (compared to optical thickness along slant path length).

The MODIS Aerosol Product monitors the ambient aerosol optical thickness over the oceans globally and over a portion of the continents. Further, aerosol size distribution is derived over the oceans, and aerosol type is derived over the continents. Daily Level 2 data are produced at the spatial resolution of a $10 \times 101\mathsf{km}$ (at nadir)-pixel array.

The MODIS retrieval algorithm is founded on a multi-spectral reflectance based principle to enable retrievals over ocean and land types not limited to dark vegetation. The algorithm uses MODIS bands 1 through 7 (ranging from 0.46 to 2.2 µm) and 20 (3.66 - 3.84 µm) after prior cloud screening using MODIS data. Over land, dynamic aerosol models are derived from ground-based sky measurements to be used in the net retrieval process.

1.9.2 Multi-angle Imaging SpectroRadiometer (MISR)

MISR onboard Terra employs nine discrete cameras pointed at fixed angles, one viewing the nadir (vertically downward) direction and four each viewing the forward and aftward directions along the spacecraft ground track, in order to have multiangle views of each point along the track. MISR collects data only on the daylit side of the Earth. During each orbit, MISR obtains a swath of imagery that is 360 km wide and about 20,000 km long. The selected swath width of 360 km allows for global coverage in a period of 9 days, the time scale over which changes in the reflectance due to seasonally changing vegetation are observable. The instrument records images in 4 spectral bands centered around $0.45, 0.56, 0.67$ and $0.87\,\mu\mathsf{m}$ respectively.

The aerosol products delivered by MISR include parameters such as tropospheric aerosol optical depth, aerosol composition and size.

The retrieval algorithm over land follows two distinct pathways: over dense vegetation, it uses the low reflectance of the surface along with multiangle measurements to determine aerosol optical thickness and the best fitting aerosol model. In the absence of dense vegetation, the algorithm uses the angular dependence of spectral contrasts in the reflection function to determine aerosol optical thickness and aerosol model.

1.9.3 POLarization and Directionality of the Earth's Reflectances (POLDER)

The French space agency, CNES, developed the POLDER instrument, hitherto carried onboard ADEOS I and now ADEOS II (ADvanced Earth Observation Satellite), developed by the Japanese space agency, JAXA. ADEOS has a sun-synchronous, nearly polar orbit with an acending node at 10:30 am. With a field of view of ±43° along track and ±51° cross track, POLDER as a 2400km swath which allows a daily coverage of almost the whole Earth. The spatial resolution of the instrument is $6\,\mathsf{km} \times 7\,\mathsf{km}$ at nadir, increasing at higher incidence angles due to the earth's curvature. POLDER has 15 spectral bands which range from 443nm to 910 nm. Two of these spectral bands are centered on molecular absorption bands: 0.763 µm (O_2) and 0.910 µm (H_2O).

The instrument retrieves Aerosol Optical Thickness and Ångström exponent over land and ocean based on contrasting the polarization due to the earth's surface/ocean surface, molecular scattering and aerosol scattering. The retrieval avails of a very dense sampling of the bidirectional reflectance of a given site, since the satellite passes over the same site every day with a new angular range. Furthermore, the combination of polarization and directionality adds another dimension to the conventional analysis of spectral signatures of aerosols and clouds, allowing for better cloud filtering.

1.10 The SCanning Imaging Absorption SpectroMeter for Atmospheric CHartographY (SCIAMACHY)

SCIAMACHY is an imaging spectrometer onboard ENVISAT observing the Earth from a nearly polar, sun-synchronous orbit with a descending node time of 10:00 am. SCIAMACHY measures in three viewing geometries:Nadir, Limb, and Occultation.

In the Nadir mode the atmospheric column directly under the spacecraft is observed. Each scan covers an area on the ground of up to 960km across track with a standard resolution of 60km×30km and a maximum resolution of 26km×15km. In the Limb mode the instrument scans at different tangent altitudes over a range of up to 100km in vertical direction with a geometrical vertical resolution of approximately 2.6km.

Global coverage at the equator is achieved within 6 days when using the standard alternating Limb/Nadir scan option. The primary mission objective of SCIAMACHY is to perform global measurements of trace gases in the troposphere and in the stratosphere. The solar radiation transmitted, backscattered and reflected from the atmosphere is recorded at relatively high resolution (0.2 nm to 0.5 nm) over the range 240 nm - 1700 nm, and in selected regions between 2000 nm and 2400 nm. The high resolution and the wide spectral range make it possible to detect many different trace gases despite low concentrations (the mixing ratios of many constituents are of the order of 10^{-6}) using predominantly the differential optical absorption spectroscopy (DOAS) method. The large wavelength range is also ideally suited for the detection of clouds and aerosols, though actual retrievals are disadvantaged by the low spatial resolution.

1.10.1 Operational aerosol products hitherto available from SCIAMACHY/GOME data

Global aerosol data are retrieved from GOME[2] and SCIAMACHY measurements. The retrieval is carried out using top of Atmosphere (TOA) reflectances in nadir-viewing conditions, using channels selected in the most transparent atmospheric windows.

---

[2] GOME, a nadir-scanning ultraviolet and visible spectrometer for global monitoring of atmospheric Ozone, launched on-board ERS-2 in April 1995, was a precursor to SCIAMACHY active until 2003. It had a smaller spectral range of $0.24 - 0.79\,\mu\text{m}$ and a larger ground pixel size of $40 \times 320\,\text{km}$.

Absorbing Optical Thickness

Algorithms for the retrieval of the aerosol optical thickness over land and over water from GOME data have been developed (*Kusmierczyk-Michulec and de Leeuw*, 2005) showing good correlation with AERONET data. Maps of global aerosol optical thickness produced operationally until mid-2003 from GOME data (*Guzzi*, 2001) can be found at http://www.temis.nl/airpollution/aerosol.html. These maps, however, only present retrievals over the ocean.

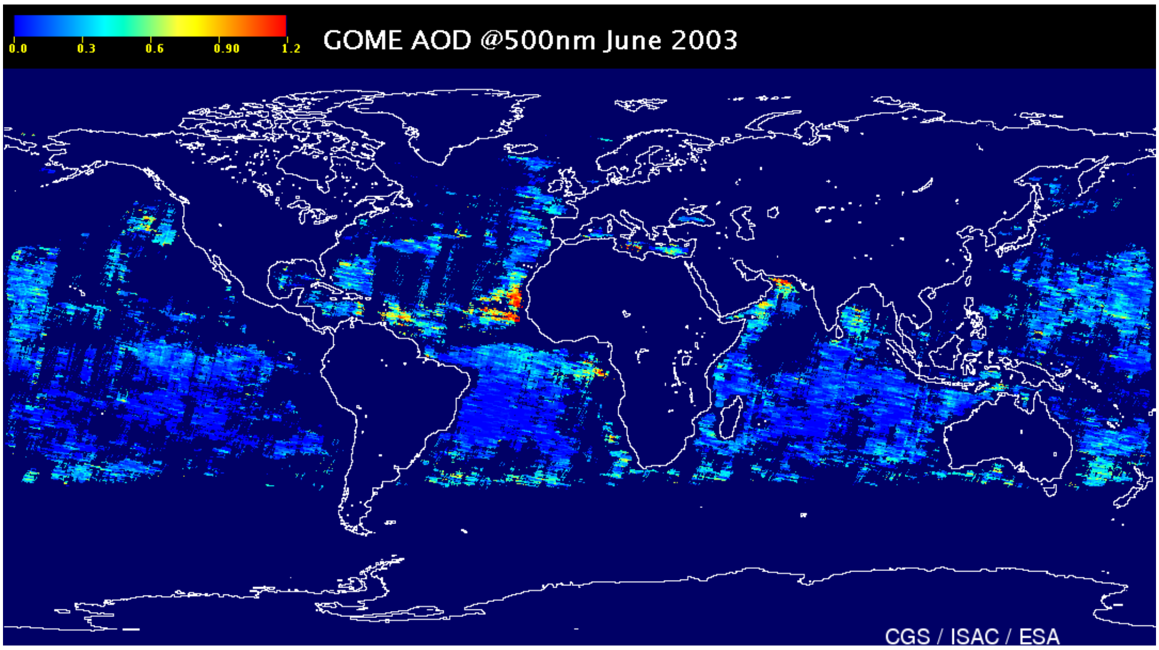

Figure 1.7: Retrieval of global AOT over ocean surfaces from GOME data (http://www.temis.nl/airpollution/aerosol.html)

In principle, SCIAMACHY is better suited than GOME for the retrieval of aerosols due to its smaller ground pixel and wider wavelength range. *Di Nicolantonio et al.* (2006) devised a pseudo-inversion using Levenberg-Marquardt least squares fitting of global atmospheric aerosol optical thickness from SCIAMACHY data. The retrieval makes use of reflectances obtained by a processor named ASP dedicated to "Aerosol retrieval from SCIAMACHY data Processing".

Absorbing Aerosol Index

The Absorbing Aerosol Index (AAI) indicates the presence of elevated absorbing aerosols in the Earth's atmosphere. Since the AAI is able to distinguish between scattering and absorbing effects, it does not suffer much from cloud contamination. The aerosol types that are mostly seen in the AAI are desert dust and biomass burning aerosols. The AAIs are derived from the reflectances measured by GOME at 335 and 380 nm and reflectances measured by SCIAMACHY at 340 and 380 nm. The figure below shows the most recent AAI measurements obtained by SCIAMACHY.

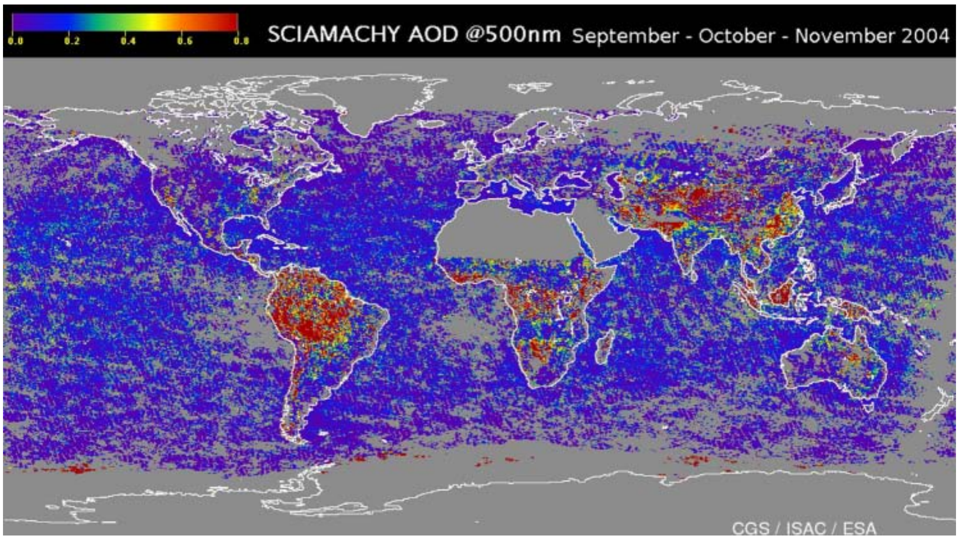
0.0
0.2
0.4
0.6
0.8
SCIAMACHY AOD @500nm September - October - November 2004
CGS / ISAC / ESA

Figure 1.8: Mean AOT at 500 nm for September, October and November 2004 as retrieved by ASP from SCIAMACHY nadir measurements.

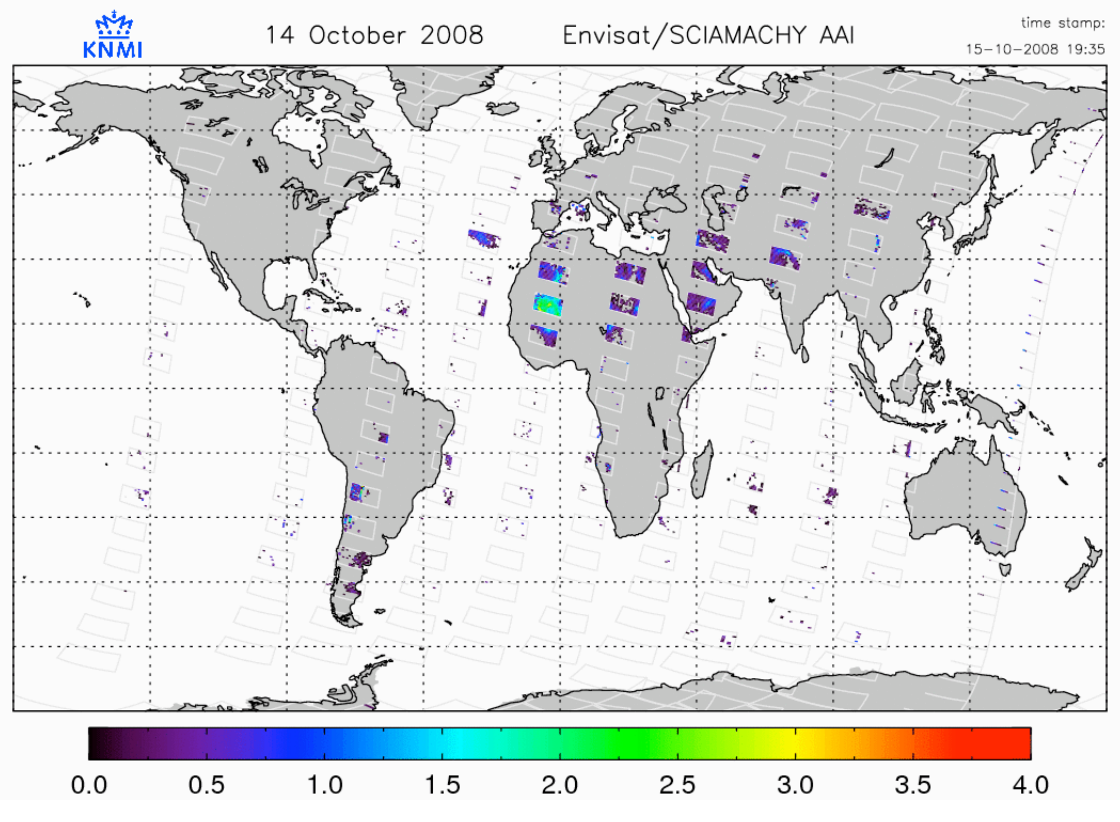
KNMI
14 October 2008
Envisat/SCIAMACHY AAI
time stamp:
15-10-2008 19:35
0.0
0.5
1.0
1.5
2.0
2.5
3.0
3.5
4.0

Figure 1.9: Latest Absorbing Aerosol Index (AAI) results obtained by SCIAMACHY

The SCIAMACHY Absorbing Aerosol Index (AAI) is derived daily since July 2002. Sunglint situations and observations with high solar zenith angles are filtered out. The algorithm corrects for the radiometric calibration problem of SCIAMACHY. Due to radiometric degradation of the SCIAMACHY UV channels, the AAI values used to be anomalously high for data measured since about the end of 2004. This problem has been solved and current data can be used without restrictions.

1.11 Retrieval of aerosols from SCIAMACHY data: advantages and disadvantages

To judge the feasibility of aerosol retrieval from SCIAMACHY data, we weigh the advantages offered by those data against the challenges posed by them. In the following, we look in detail at each of these.

1.11.1 Advantages

The main advantages of SCIAMACHY for the retrieval of aerosols are:

1. Wide spectral range: Aerosols display varied behaviour over different parts of the spectrum - their extinction cross-sections, single scattering albedoes and phase functions are all functions of wavelength, carrying information on the size distribution of the aerosol particles. Aerosols also interfere with the extent to which sunlight can penetrate the atmosphere, leaving a strong signature of the vertical distribution of the aerosol in the presence of an absorbing species whose vertical profile is known, eg. O_2, O_4, CO_2.
2. High spectral resolution: The relatively high spectral resolution of SCIAMACHY preserves most of the spectral structure of reflected light, which carries signatures of the relative abundances of aerosols and trace gases and of the vertical extent of aerosols.
3. Polarization data from PMD's: The six polarization measurement devices (PMD's) built into SCIAMACHY are not only conceived to measure broadband polarization of light, but also have a fine spatial resolution that makes them invaluable for the detection of clouds. The polarization measurements may be used to contrast aerosols against land/water - in addition to providing valuable information about the aerosol, this would also enable the accurate detection of aerosol-free scenarios, essential for the determination of ground albedo/BRDF.
4. Limb data: Limb data may be used for detection of stratospheric aerosols. This would be of great interest in the event of a strong volcanic eruption.

1.11.2 Disadvantages

Given even a perfect instrument, the retrieval of aerosols is made difficult by the large number of variables describing a given aerosol distribution and because the retrieval of aerosols is closely intertwined with the simultaneous retrieval of the surface reflectance, which in turn may vary strongly with time and viewing geometry. The following shortcomings pose further difficulties for the retrieval of aerosols from SCIAMACHY measurements:

1. Low spatial resolution: A ground pixel of size 60km×30km generally features a high probability of cloud contamination, all but eliminating the prospect of continuous retrievals in the mid-latitudes. Furthermore, the ground pixel of this size may contain strong relief, showing sharp variations of albedo, elevation and aerosol loading.

2. Different ground pixel sizes for some spectral channels: In order to be able to make full use of the wide spectral range of SCIAMACHY, it is necessary to be viewing the same ground pixel at all wavelengths at the same time. This, however, does not hold true for several spectral channels having different ground pixel sizes due to their different integration times. This is true of channel 4 covering the spectral range $604 - 805\,\mathrm{nm}$ which features lines of O_4 absorption.

3. Single viewing geometry: Inspite of the limb geometry, the only effective viewing mode in the lower troposphere is the Nadir mode. This leads to loss of information about the phase function of the aerosol that could have been afforded by additional viewing modes. The phase function is a good indicator of the aerosol type, which otherwise has to be assumed from a priori data.

4. Bad radiometric calibration rendering certain channels useless: Unlike DOAS measurements for which SCIAMACHY is mainly conceived, aerosol retrievals are highly sensitive to the radiometric calibration of the measured spectra. This disqualifies several channels, especially those in the UV and the NIR, for aerosol retrieval.

The methods listed in Section 1.10.1 have been largely successful in providing a global image of aerosols observed by SCIAMACHY. SCIAMACHY, however, offers a wealth of information about the observed aerosol scenario, thanks to its wide medium resolution spectral range. In this thesis, we attempt to develop a rigorous inversion scheme that retrieves not only the aerosol optical thickness, but also the Ångstöm exponent and the vertical distribution of the aerosol, taking advantage of capabilities unique to medium resolution spectrometers like SCIAMACHY.

Vertical information about aerosols coupled with AOT and the Ångstöm exponent may be invaluable for studying the transport of aerosols on a global level and for observing the formation of secondary aerosol nuclei and their height resolved evolution as will be demonstrated in Chapter 5. While the absence of information regarding surface reflection and the complications caused by errors in the radiometric calibration of SCIAMACHY currently make it very difficult to apply our rigorous inversion on a global scale, our method provides a prototype for future generations of instruments like SCIAMACHY.

In the following chapter, we develop a model, AeroRad, for the simulation of atmospheric aerosols for use in our retrieval algorithm. This model is also used for the determination of ground albedo using time series analysis, expanded upon in Chaper 3. Chapter 4 deals with the development of the retrieval strategy, the formulation of a solution to the retrieval problem using optimal estimation and the sensitivity analysis of the retrieval algorithm. Chapter 5 presents actual retrievals made using SCIAMACHY measurements. We conclude with Chapter 6, with a discussion of future possibilities for the retrieval of aerosols from space.

Chapter 2

Modeling

To estimate the influence of aerosols on the reflectance spectrum detected by satellite in the UV/Vis/NIR, we have developed the semi-analytical radiative transfer model AeroRad. The model has been rigorously tested against other well-established models such as SCIATRAN (*Rozanov et al.*, 2005) and LINTRAN (*Hasekamp and Landgraf*, 2002) and the Monte Carlo based model McArtim (*Deutschmann*, 2009), with good agreement in each case. In the following, the basic principles and structure of the model are discussed, accompanied by comparisons with LINTRAN, SCIATRAN and McArtim. This is followed by case studies of different atmospheric scenarios, in spectral regions around both the O_2 A and B bands and under various nadir viewing geometries.

2.1 Basic principle

We assume a 1-D plane-parallel model atmosphere divided into horizontal layers of sufficiently small optical thickness. Collimated light is incident at the top of this atmosphere from the sun, which propagates through the atmosphere towards the earth's surface, undergoing extinction due to absorption or scattering by atmospheric species at each horizontal layer before undergoing absorption or scattering at the earth's surface. Atmospheric refraction is found to be negligible in nadir geometries and is hence switched off for our retrieval application. In the absence of aerosols, atmospheric scattering can be attributed to molecular (Rayleigh) scattering processes, whereas absorption occurs in different spectral regions due to O_2, O_3, or trace gas species such as SO_2, NO_2, NO_3, BrO, ClO, $OClO$, $HCHO$, CO_2, etc. Aerosols and clouds contribute both to scattering and (to a lesser extent) absorption of light. Surface reflectance at the bottom of the model atmosphere (BOA) may be lambertian (as is generally assumed over land), specular (eg. over oceans) or specified by a given bidirectional reflectance distribution function (BRDF). In the UV/Vis/NIR, atmospheric or ground emission of light is negligible and hence will not be considered.

Immediately as a collimated beam of sunlight enters the atmosphere, a *diffuse* component of light emerges as light gets scattered into all possible directions, while the incident beam suffers extinction in accordance with the Beer-Lambert law along its original direction (neglecting bending due to variations in the refractive index of ambient air). Light scattered from the direct beam into the detector is scattered only once whereas light arriving from the diffuse component has already been scattered at least once before. We refer, henceforth, to these two components as the single scattering and the multiple scattering components respectively of the signal registered by the detector.

We need to simulate both the *direct* and the *diffuse* components of radiation traversing the atmosphere to be able to determine the total reflectance signal registered by the detector. While the calculation of the direct component is straightforward, the diffuse component calls for partition of space into so-called *streams* along which scattered light can propagate. AeroRad allows for partition into 10, 34 or 74 streams, with progressively more accurate results. For geometries not involving very high ($\approx 90^\circ$) solar or line-of-sight zenith angles, the variance of the modeled result from the desired limit is small. Due to its relative speed, the 10-stream version is used in this work. We apply the Gauss-Seidel iterative scheme(*Herman et al.*, 1980) to simulate multiple scattering. A salient feature of AeroRad in this respect is that the streams are oriented symmetrically around the direction of incident radiation with two narrow central cones pointing in and against the direction of the incident beam respectively. Consequently, the phase function for scattering of light from the incident solar beam into the streams becomes azimuthally independent[1], saving a great amount of computing time by avoiding the need to calculate an effective phase function individually for each stream. Also, in the case of strongly forward and/or backward peaked phase functions characteristic of most aerosols, this scheme provides a spatial resolution that allows for a more accurate representation of the actual scattering behaviour. In the following, the basic equation of radiative transfer and the calculation of the single and multiple-scattered components of incident radiation are discussed.

2.2 Equation of radiative transfer

Adopting a plane parallel set-up, we consider the atmosphere to be sliced into N horizontal layers, giving rise to $N + 1$ boundaries, with the top of atmosphere bounded by $i = 0$ and the ground being at $i = N$ (see Fig. 2.1). Each of these N layers is characterized by n molecular species including trace gases in addition to other air molecules (mainly N_2, O_2 and CO_2) and aerosol particles, each assumed to be distributed homogeneously within the layer. The gaseous species have concentrations c_{ij} and absorption cross sections σ_{ij}, where $i = 1, 2, \ldots N$ and $j = 1, 2, \ldots n$. The total molecular concentration within each layer is denoted by c_i and the corresponding Rayleigh cross section is σ_{rayl}. Aerosol concentration and extinction cross section are denoted by c_i^{aer} and κ_i^{aer} respevtively[2].

---

[1] This does not hold true in case of irregularly shaped particles that may exhibit an azimuthally varying phase function. In this work, however, all particles are assumed to be spherical so that their single scattering properties can be obtained from the Mie theory (*Sanghavi*, 2003), resulting in an azimuthal independence of the phase function.

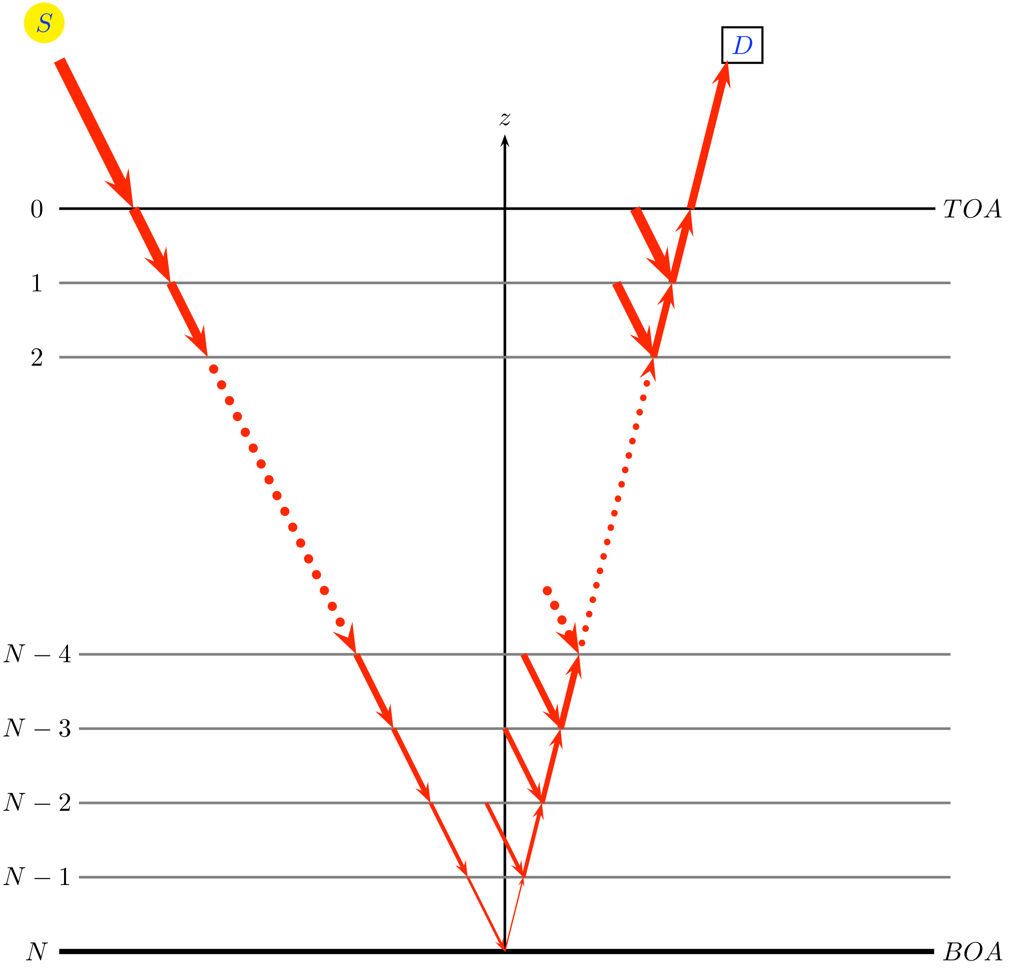

Figure 2.1: Vertical structure of the model atmosphere. S represents the sun as the source of incoming radiation and D represents the detector pointing at a point on the earths surface whose zenith is is directed along $\vec{z}$.

The geometrical thickness Δz_i of each layer is given by the difference in altitude between the upper and lower boundaries of the layer. The corresponding change in optical thickness $\Delta\,\tau$ as we go from the lower bound to the upper bound of the layer is given as

$$\Delta\,\tau_i = -(c_i\,\sigma_{rayl} + c_i^{aer}\,\kappa_i^{aer} + \Sigma_{j=1}^{n}\,c_{ij}\,\sigma_{ij})\cdot\Delta\,z_i. \tag{2.1}$$

Since the primary source of light (the sun) is located beyond the top of the model atmosphere

---

[2] For the purpose of retrieval from SCIAMACHY measurements we assume the aerosol composition as remaining uniform at all heights during the retrieval, resulting in the simplification $\kappa_i^{aer} = \kappa^{aer}$.

(TOA), the optical depth τ along the incident solar beam increases from $\tau = 0$ at TOA to $\Sigma_{i=1}^{N} \Delta\tau_i$ at BOA/ground. Thus its increase is directed opposite to that of increasing altitude, giving rise to the negative sign in the above equation.

Consider a light beam of intensity I at an optical depth τ propagating in a direction (μ, ϕ), where $\mu = \cos\theta$, θ being the angle made by the beam with the local zenith (for light propagating downward, $\mu < 0$, since $\theta > \frac{\pi}{2}$) and ϕ is the azimuthal angle of the beam. The basic equation governing the transfer of solar intensity (*Liou*, 1992) may be written in its scalar approximation as

$$\mu \frac{dI(\tau, \mu, \phi)}{d\tau} = I(\tau, \mu, \phi) \; - \; J(\tau, \mu, \phi), \tag{2.2}$$

where J is the source function. Three factors contribute to the source function: thermal emission by the medium constituting the atmosphere, multiple scattering of diffuse radiation, and single scattering of the attenuated direct solar irradiance arriving at at the level corresponding to an optical depth τ from TOA. Thermal energy emitted by the earth and the atmosphere system is negligible in the UV/VIS/NIR compared to that incident from the sun. Consequently, only scattering of diffuse and direct radiation contribute to J.

If we consider only the propagation of the direct unscattered beam of sunlight having intensity I_{direct}, the source function J vanishes, leaving out only terms involving I_{direct} in equation 2.2

$$\mu \frac{dI_{direct}(\tau, \mu, \phi)}{d\tau} = I_{direct}(\tau, \mu, \phi). \tag{2.3}$$

This represents the attenuation of direct sunlight as it propagates through the atmosphere.

For diffuse radiation, the source function is given by

$$J(\tau, \mu, \phi) = \frac{\omega \bar{\sigma}_{extn}}{4\pi} \int_0^{2\pi} \int_{-1}^{1} I(\tau, \mu', \phi')\, P(\mu, \phi; \mu', \phi')\, d\mu\, d\phi + \frac{\omega \bar{\sigma}_{extn}}{4\pi}\, I_0\, P(\mu, \phi; \mu_0, \phi_0) e^{-\tau/\mu_0}, \tag{2.4}$$

where ω is the mean single scattering albedo, $\bar{\sigma}_{extn}$ is the mean extinction cross-section and P is the mean scattering phase function, which represents the angular distribution of scattered energy as a function of the direction of propagation $(\mu.\phi)$ before and (μ', ϕ') after scattering. $P(\mu, \phi; \mu', \phi')$ is the mean of the individual phase functions of all atmospheric species weighted by their respective concentrations and scattering cross-sections. The single scattering albedo, ω, is defined as the ratio of the scattering cross-section, σ_s to the extinction (scattering plus absorption) cross-section, σ_e, i.e.

$$\omega = \frac{\sigma_s}{\sigma_e} \tag{2.5}$$

Thus, for a given atmospheric layer i,

$$\omega_i = \frac{c_i \sigma_{rayl} \; + \; c_i^{aer} \sigma^{aer}}{c_i \sigma_{rayl} \; + \; c_i^{aer} \kappa^{aer} \; + \; \Sigma_{j=1}^{n} c_{ij} \sigma_{ij}}, \tag{2.6}$$

$$\bar{\sigma}_{extn}^{i} = c_i \sigma_{rayl} \; + \; c_i^{aer} \kappa^{aer} \; + \; \Sigma_{j=1}^{n} c_{ij} \sigma_{ij}, \tag{2.7}$$

and

$$P_i(\mu, \phi; \mu', \phi') = \frac{c_i \sigma_{rayl} p_{rayl}(\mu, \phi; \mu', \phi') \; + \; c_i^{aer} \sigma^{aer} p_{aer}(\mu, \phi; \mu', \phi')}{c_i \sigma_{rayl} \; + \; c_i^{aer} \kappa^{aer} \; + \; \Sigma_{j=1}^{n} c_{ij} \sigma_{ij}}, \tag{2.8}$$

where σ^{aer} is the effective scattering cross section of an aerosol particle and p_{rayl} and p_{aer} are the Rayleigh and aerosol phase functions respectively. All phase functions $p(\mu, \phi; \mu', \phi')$ are normalized, so that

$$\frac{1}{4\pi} \int_{\phi'=0}^{2\pi} \int_{\mu'=-1}^{1} p(\mu, \phi; \mu', \phi')\, d\mu'\, d\phi' = 1. \tag{2.9}$$

Consequently, $P_i(\mu, \phi; \mu', \phi')$ is also a phase function normalized to unity.

Solving Equations 2.2, 2.3 and 2.4 for each layer of the model atmosphere provides the direct beam and the diffuse component of radiation propagating along each stream at every optical depth in the atmosphere. The boundary conditions at the interfaces between adjoining layers are coupled, i.e. light emerging from one layer is the light entering the next layer at the interface between them. Light scattered from both, the direct component (single scattering) and the diffuse component along each stream (multiple scattering) into the receiving cone of the detector accounts for the signal registered by it.

2.3 Single-scattering radiation

The direct radiation at an optical depth τ is obtained by solving Eq.2.3 as

$$I_{direct}(\tau, \mu_0, \phi_0) = I_0 \ \exp(-\frac{\tau}{\mu_0}), \tag{2.10}$$

where (μ_0, ϕ_0) is the direction of the incident solar radiation and I_0 is the solar intensity at the TOA.

Now consider the rth layer of the model atmosphere. The optical depth of the atmosphere at the $(r-1)^{th}$ boundary is given by

$$\tau_{r-1} = \Sigma_{i=1}^{r-1} \Delta\tau_i. \tag{2.11}$$

Thus, the intensity of direct light incident at the plane of the boundary $r-1$ is given by

$$I_{direct}(\tau_{r-1}, \mu_0, \phi_0) = I_0 \ \exp(-\frac{\tau_{r-1}}{\mu_0}), \tag{2.12}$$

and the intensity of direct sunlight incident at an optical depth $\Delta\tau'$ below the upper boundary $r-1$ can be written as

$$I_{direct}(\tau_{r-1} + \Delta\tau', \mu_0, \phi_0) = I_0 \ \exp(-\frac{\tau_{r-1}}{\mu_0}) \ \exp(-\frac{\Delta\tau'}{\mu_0}), \tag{2.13}$$

This constitutes the source function for single scattering of direct sunlight at the optical depth $\tau_{r-1} + \Delta\tau'$. To obtain the amount of direct light scattered into the direction (μ, ϕ) by an infinitesimal element $d\tau'$ at an optical depth $\Delta\tau'$ below the upper boundary of the layer r, we set $I(\tau_{r-1} + \Delta\tau', \mu, \phi) = 0$ since there is no direct light propagating along (μ, ϕ). Using Eq. 2.4 to express the source function and substituting it into Eq. 2.2, we get

$$\mu \frac{dI(\tau_{r-1} + \Delta\tau', \mu, \phi)}{d\tau'} = \frac{\omega_r}{4\pi} \bar{\sigma}^r_{extn} \, P_r(\mu, \phi; \mu_0, \phi_0)\, I_0 \ \exp(-\frac{\tau_{r-1}}{\mu_0}) \ \exp(-\frac{\Delta\tau'}{\mu_0}) \tag{2.14}$$

or, equivalently,

$$dI(\tau_{r-1}+\Delta\tau',\mu,\phi) = \frac{\omega_r}{4\pi}\frac{1}{\mu}\bar{\sigma}^r_{extn}\,P_r(\mu,\phi;\mu_0,\phi_0)\,I_0\,\exp(-\frac{\tau_{r-1}}{\mu_0})\,\exp(-\frac{\Delta\tau'}{\mu_0})\,d\tau'. \qquad (2.15)$$

Analogous to Eq. 2.13, this light suffers an extinction $\exp(-\frac{\tau_{r-1}}{\mu})\,\exp(-\frac{\Delta\tau'}{\mu})$ before it reaches the top of atmosphere, assuming $\mu > 0$, i.e. the scattered light travels upward through the atmosphere. Thus, the total intensity of light arriving at the TOA due to scattering of direct sunlight by an infinitesimal layer $d\tau'$ at an optical depth $\tau_{r-1}+\Delta\tau'$ in the direction (μ,ϕ) is given by

$$\begin{aligned} dI'^{ss}_{\tau_{r-1}+\Delta\tau'}(\mu,\phi) &= \frac{\omega_r}{4\pi}\frac{1}{\mu}\bar{\sigma}^r_{extn}\,P_r(\mu,\phi;\mu_0,\phi_0)\,I_0\,\exp(-\frac{\tau_{r-1}}{\mu_0})\,\exp(-\frac{\Delta\tau'}{\mu_0})\,d\tau' \\ &\quad\cdot\exp(-\frac{\tau_{r-1}}{\mu})\,\exp(-\frac{\Delta\tau'}{\mu}) \\ &= \frac{\omega_r}{4\pi}\frac{1}{\mu}\bar{\sigma}^r_{extn}\,P_r(\mu,\phi;\mu_0,\phi_0)\,I_0\,\exp(-\frac{\tau_{r-1}}{\bar{\mu}})\,\exp(-\frac{\Delta\tau'}{\bar{\mu}})\,d\tau', \qquad (2.16)\end{aligned}$$

where

$$\frac{1}{\bar{\mu}} = \frac{1}{\mu}+\frac{1}{\mu_0}. \qquad (2.17)$$

Thus the total intensity of direct light scattered once by the entire layer r in the direction (μ,ϕ) and reaching the TOA is obtained by integrating the above equation between the limits $\Delta\tau' = 0$ and $\Delta\tau' = \Delta\tau_r$. Writing $d\tau' = d\Delta\tau'$ in the above equation we get

$$\begin{aligned}\Delta\,I'^{scatt}_r(\mu,\phi) &= \int_0^{\Delta\tau_r}\frac{\omega_r}{4\pi}\frac{1}{\mu}\bar{\sigma}^r_{extn}\,P_r(\mu,\phi;\mu_0,\phi_0)\,I_0\,\exp(-\frac{\tau_{r-1}}{\bar{\mu}})\,\exp(-\frac{\Delta\tau'}{\bar{\mu}})\,d\Delta\tau', \\ &= \frac{\omega_r}{4\pi}\frac{\mu_0}{\mu_0+\mu}\,\bar{\sigma}^r_{extn}\,P_r(\mu,\phi;\mu_0,\phi_0)I_0\left[\exp\left(\frac{-\tau_{r-1}}{\bar{\mu}}\right)-\exp\left(\frac{-\tau_r}{\bar{\mu}}\right)\right]. \qquad (2.18)\end{aligned}$$

Summing over all layers $i = 1, 2, ...N$, we get the total single scattering radiation arriving at the TOA in the direction (μ,ϕ). If the viewing geometry of the satellite is such that it registers light arriving in the direction (μ_d,ϕ_d), the total single scattering radiation recorded by the detector is

$$\begin{aligned} I_{ss}(\mu_d,\phi_d) &= \Sigma^N_{i=1}\,\Delta\,I^{scatt}_r(\mu_d,\phi_d) \\ &= I_0\frac{1}{4\pi}\frac{\mu_0}{\mu_0+\mu_d}\,\Sigma^N_{i=1}\,\omega_i\bar{\sigma}^i_{extn}\,P_i(\mu_d,\phi_d;\mu_0,\phi_0) \\ &\quad\cdot\left[\exp\left(\frac{-\tau_{i-1}}{\bar{\mu}}\right)-\exp\left(\frac{-\tau_i}{\bar{\mu}}\right)\right] \qquad (2.19)\end{aligned}$$

The single scattering signal becomes more dominant at larger wavelengths, constituting most of the signal around 700 nm in the absence of aerosols. In the presence of aerosols though, multiple scattering becomes large enough to exceed the single scattering signal even at large wavelengths.

2.4 Multiple-scattering radiation

The simulation of multiple scattering involves:

1. **The division of space into sections, called *streams* representing different spatial directions.** Ideally, this would imply an infinite number of streams, each representing an infinitesimal cone around a given direction. This, however, is neither practicable nor necessary in most cases. A good approximation can be made by (more or less) evenly dividing a sphere representing space into a finite number of sections, each representing light propagating around a central direction (see Fig.2.2).

   In AeroRad, this sphere is assigned a coordinate system whose z-axis is aligned along the direction of incident solar radiation. We refer, henceforth, to the earth-bound local coordinate system as S_E and the coordinate system around the incident solar radiation as S_S. Thus, S_S is chosen such that, its z-axis $\bar{z}_S$ makes an angle θ_0 with respect to the zenith, i.e. $\bar{z}_E$. Further, we choose $\bar{x}_S$ to be aligned in the same direction as $\bar{x}_E$. Streams in AeroRad are thus directed symmetrically along and around the direction of incident solar radiation ($\mu_0 = \cos\theta_0, \phi_0$). Relative to this beam, now represented for uniformity in S_E as (θ_0, ϕ_0), the 10-stream mode employs a central cone of half-width $\Delta\theta_{1/2} = 20°$ around $\bar{z}_S \equiv (0°, 0°)$ and 4 surrounding sections, each of polar angular width $\Delta\theta = 70°$ and azimuthal width $\Delta\phi = 90°$ around $(55°, s\%4 \cdot 90°), s \in [1, 4]$, in the forward hemisphere. The backward hemisphere is merely a mirror-reflection of the forward hemisphere with a central cone around the relative direction $-\bar{z}_S \equiv (180°, 0°)$ and 4 surrounding sections each around (125°,s%4·90°), $s \in [1, 4]$. The other modes are analogously structured, with the central directions in S_S in the forward hemisphere of the 34-stream mode being $(0, 0°)$ with $\Delta\theta_{1/2} = 10°$ for the central cone surrounded by $(30°, s\%8 \cdot 45°)$ and $(70°, s\%8 \cdot 45°)$, where $s \in [1, 16]$ and $\Delta\theta = 40°$, $\Delta\phi = 45°$. Similarly, the directions for the forward hemisphere of the 74-stream mode are $(0°, 0°)$, with $\Delta\theta_{1/2} = 9°$ and $(22.5°, s\%12 \cdot 30°), (49.5°, s\%12 \cdot 30°)$ and $(76.5°, s\%12 \cdot 30°)$, where $s \in [1, 36]$ and $\Delta\theta = 27°, \Delta\phi = 30°$.

   Given S streams, we shall denote the angles made by the central directions (θ_{0s}, ϕ_{0s}) (which are measured relative to (θ_0, ϕ_0)) with respect to the local zenith and their local azimuths as θ_{zs} and ϕ_{zs}, where $s \in [1, S]$. These angles (given $\phi_0 = 0°$) are given by

$$\theta_{zs} = \arccos\left(\cos\theta_0 \cos\theta_{0s} - \sin\theta_0 \sin\theta_{0s} \cos\phi_{0s}\right) \tag{2.20}$$

and

$$\phi_{zs} = \begin{cases} 360° - \phi'_s & \text{if } \psi < 0 \\ \phi_{0s} & \text{if } \psi = 0 \\ \phi'_s & \text{if } \psi > 0 \end{cases}$$

where

$$\psi = \sin\theta_{0s}(\cos\phi_{0s} \cos\theta_0 \sin\phi_0 - \sin\phi_{0s} \cos\phi_0) + \cos\theta_{0s} \sin\theta_0 \sin\phi_0 \tag{2.21}$$

and

$$\phi'_s = \arccos\left[\frac{\sin\theta_{0s}(\cos\phi_{0s}\cos\theta_0\cos\phi_0 - \sin\phi_{0s}\sin\phi_0) + \cos\theta_{0s}\sin\theta_0\cos\phi_0}{\sin\left(\arccos\left(\cos\theta_0\cos\theta_{0s} - \sin\theta_0\sin\theta_{0s}\cos\phi_{0s}\right)\right)}\right] \tag{2.22}$$

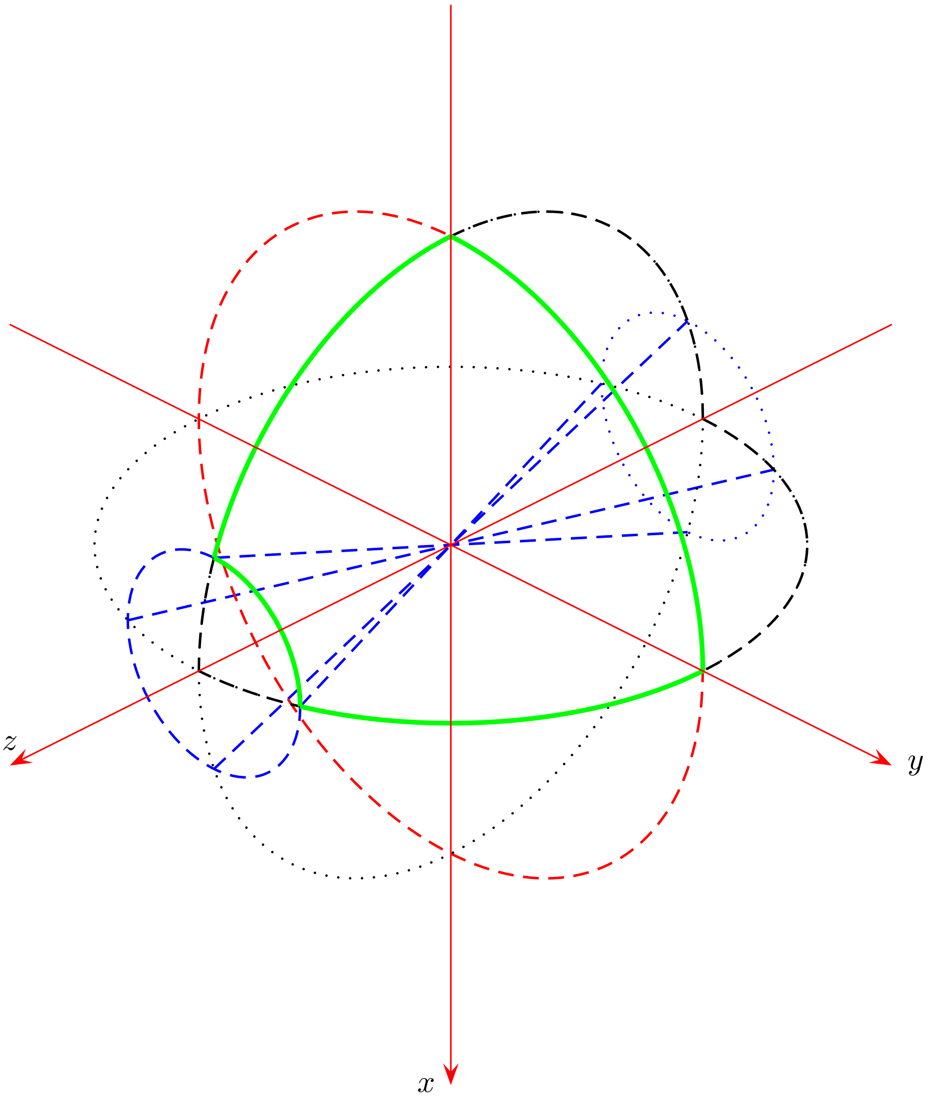

Figure 2.2: Division of space into streams in the 10-stream version of AeroRad. The z-axis is aligned with the direction of incident solar radiation. The cone (outlined in blue) around the direction of propagation of the incident solar beam is made narrow in order to be able to better account for strongly forward and backward peaked scattering, common in case of aerosols. The green line outlines on of the the four forward azimuthal streams.

The angles (θ_{zs}, ϕ_{zs}) are of utmost importance for tracking scattered light emerging from the incident solar beam. Also important for the calculation of scattering of diffuse light from one direction into another are the mutual angles θ_{pq} between two streams p and q, where $p, q \in [1, S]$. These mutual angles are given by

$$\theta_{pq} = \arccos\left(\cos\theta_{0p}\cos\theta_{0q} - \sin\theta_{0p}\sin\theta_{0q}\cos\left(\phi_{0p} - \phi_{0q}\right)\right) \tag{2.23}$$

Finally, we need the angles (θ_{sd}, ϕ_{sd}) made by the streams with respect to the line of sight of the detector (θ_d, ϕ_d), which, analogous to Eq.2.23 can be calculated as:

$$\theta_{sd} = \arccos\left(\cos\theta_{zs}\cos\theta_d - \sin\theta_{zs}\sin\theta_d\cos\left(\phi_{zs} - \phi_d\right)\right) \tag{2.24}$$

2. **The calculation of effective phase functions $P^{eff}(\theta_0, \phi_0; \theta_{zs}, \phi_{zs}), P^{eff}(\theta_{zp}, \phi_{zp}; \theta_{zq}, \phi_{zq})$ and $P^{eff}(\theta_{zs}, \phi_{zs}; \theta_d, \phi_d)$.**

   $P_i^{eff}(\theta_0, \phi_0; \theta_{zs}, \phi_{zs})$ describes the scattering of radiation from the incident solar beam into each of the streams for a given atmospheric layer i. It is defined as

   $$P_i^{eff}(\theta_0, \phi_0; \theta_{zs}, \phi_{zs}) = \int_{\Delta\Omega} p(\theta_0, \phi_0; \Omega')\, d\Omega', \tag{2.25}$$

   where p_i represents the combined phase function for Rayleigh and aerosol scattering as in Eq.2.4. Here Ω' does not correspond to any uniform progression of θ' or ϕ', as a result of which they are difficult to separate and the limits of the above definite integral are cumbersome to define. This can be greatly simplified by shifting from the local frame of reference to the incident beam frame of reference (as elaborated above), so that

   $$\begin{aligned} (\theta_0, \phi_0) &\rightarrow (0, 0), \\ \Delta\Omega &\rightarrow \int_{\phi'=\phi_1}^{\phi_2} \int_{\theta'=\theta_1}^{\theta_2} \sin\theta' d\theta' d\phi', \end{aligned} \tag{2.26}$$

   where the subscripts 1 and 2 indicate the lower and upper bounds respectively of the polar and azimuthal angles defining the stream. Thus, we can write

   $$P_i^{eff}(\theta_0, \phi_0; \theta_{zs}, \phi_{zs}) = \int_{\phi'=\phi_1}^{\phi_2} \int_{\theta'=\theta_1}^{\theta_2} p_i(0, 0; \theta', \phi')\, \sin\theta' d\theta' d\phi', \tag{2.27}$$

   which, using the azimuthal independence of the phase function p_i, can be further simplified to yield

   $$P_i^{eff}(\theta_0, \phi_0; \theta_{zs}, \phi_{zs}) = \Delta\phi \int_{\theta'=\theta_1}^{\theta_2} p_i(\theta')\, \sin\theta' d\theta', \tag{2.28}$$

   where $\Delta\phi$ represents the azimuthal width of the stream. The integration over $p_i(\theta')$ involves integration over the Rayleigh phase function p_{rayl} given by

   $$p_{rayl}(\theta') = \frac{3}{4}(1 + \cos^2\theta') \tag{2.29}$$

   in addition to the computationally expensive numerical summation of the Mie phase function for aerosols, p_{aer}, thus making the above simplifications very valuable.

   For the estimation of $P^{eff}(\theta_{zp}, \phi_{zp}; \theta_{zq}, \phi_{zq})$ representing scattering of diffuse radiation from stream p to stream q, we assume the entire radiation contained within a stream to be directed along the central axis of the stream. This reduces, without too large a loss of accuracy, the relation

   $$\begin{aligned} &P_i^{eff}(\theta_{zp}, \phi_{zp}; \theta_{zq}, \phi_{zq}) \\ &= \int_{\theta'=\theta_1}^{\theta_2} \sin\theta' d\theta' \int_{\phi'=\phi_1}^{\phi_2} d\phi' \int_{\theta''=\theta_3}^{\theta_4} \sin\theta'' d\theta'' \int_{\phi''=\phi_3}^{\phi_4} d\phi'' p_i(\theta', \phi'; \theta'', \phi'') \end{aligned} \tag{2.30}$$

to

$$P_i^{eff}(\theta_{zp}, \phi_{zp}; \theta_{zq}, \phi_{zq}) = p_i(\theta_{zp}, \phi_{zp}; \theta_{zq}, \phi_{zq}) \int_{\theta''=\theta_3}^{\theta_4} \int_{\phi''=\phi_3}^{\phi_4} \sin\theta'' d\theta'' d\phi'', \qquad (2.31)$$

where the subscripts 1 and 2 denote the lower and upper bounds of the polar and azimuthal angles defining stream p and the subscripts 3 and 4 denote the corresponding lower and upper bounds of stream q. Here again, we have considered the incident solar beam frame of reference. The angles θ_{pq} calculated in the previous section are used for the calculation of the combined phase function p_i.

$P^{eff}(\theta_{zs}, \phi_{zs}; \theta_d, \phi_d)$ represents the scattering of diffuse radiation from stream s into the line of sight (θ_d, ϕ_d) of the detector. Here again the assumption that the entire radiation within a stream propagates along its central axis results in the following simplification:

$$P_i^{eff}(\theta_{zs}, \phi_{zs}; \theta_{zs}, \phi_{zs}) = p_i(\theta_{zs}, \phi_{zs}; \theta_d, \phi_d). \qquad (2.32)$$

Here we adhere to the local frame of reference, using the angles θ_{sd} for the calculation of p_i.

3. **The tracing of diffuse radiation from the sun to the detector.** Now that we can calculate the distribution of scattered light amongst streams $s, s \in [1, S]$ in each layer $i, i \in [1, N]$, we can trace diffuse light on its path throughout the atmosphere. This involves the calculation of different scattering orders of downwelling and upwelling fluxes through the atmosphere down to the earth's surface, accounting for their extinction as they traverse it. As soon as the solar incident beam enters the atmosphere, scattering takes place into each of the streams. If a stream s points upward, i.e. has a solar zenith angle $\theta_{zs} < 90°$, it carries upwelling radiation, while streams pointing downward, i.e. having solar zenith angle $\theta_{zs} > 90°$ carry downwelling radiation. First order diffuse radiation is generated by scattering from the incident light beam. It is called 'first order' because it has undergone scattering only once. Downwelling first order diffuse radiation suffers extinction through all intermediate layers of the atmosphere before being scattered, either by an atmospheric scatterer (aerosol/air molecule) or by the ground, thereby generating 2^{nd} order diffuse radiation. Upwelling first order radiation similarly undergoes extinction in all intermediate layers until it either escapes the atmosphere or gets scattered in the atmosphere, thus generating 2^{nd} order diffuse radiation. Each order of diffuse radiation thus undergoes scattering to generate diffuse light of a higher order. As the order of diffuse radiation increases, its intensity falls (sometimes after reaching a peak) due to the intermediate extinction by the medium forming the atmosphere. Thus the intensities of the different orders of diffuse radiation form a convergent series, whose sum we find using the Gauss-Seidel iterative method. Gauss-Seidel iteration can be roughly compared to the method of successive orders of scattering (*Lenoble et al.*, 2007), both having similar difficulties with large optical thickness, but the Gauss-Seidel method has the advantage with respect to the latter that its computational time is independent of the value of the single scattering albedo, which in the case of the method of successive orders of scattering causes very slow convergence as the single scattering

albedo approaches unity (*Lenoble*, 1985) - a scenario not unexpected when dealing with aerosols.

The Gauss-Seidel procedure calls for first tracing the propagation of (downwelling) diffuse radiation from TOA through the earth's surface, followed by the same procedure for (upwelling) backscattered radiation from the surface through TOA. This procedure is repeated to simulate further orders of scattering until the desired accuracy is reached. First of all, we classify our streams based on whether $\theta_{zs} < 90°$ or $\theta_{zs} > 90°$ into upwelling and downwelling streams respectively. Thus, we have $\frac{S}{2}$ upwelling and $\frac{S}{2}$ downwelling streams, which we shall denote by s_u and s_d respectively. Let $I^k_{is_u}$ and $I^k_{is_d}$ denote the intensities of radiation contained in the upwelling stream s_u and downwelling stream s_d respectively, in the i^{th} vertical atmospheric layer during the k^{th} iteration. The total upwelling and downwelling intensities at the end of the k^{th} iteration are given by $I_{is_u} = \Sigma_k I^k_{is_u}$ and $I_{is_d} = \Sigma_k I^k_{is_d}$, respectively.

During the first iteration, we follow the incident solar beam and the 1^{st} and, in turn, 2^{nd} and higher order downwelling fluxes created downward, i.e. from $i = 1$ through $i = N$, through the atmosphere. The incident solar beam generates $1st$ order upwelling and downwelling radiation along its path, while the downwelling 1^{st} order radiation generates higher orders (limited by one scattering event per vertical layer) of up- and downwelling radiation as it continues on its path down the atmosphere. Thus, during the downwelling trace of the first iteration, we have

$$\begin{aligned} I^k_{is_u} &= I_0 e^{-\tau_{i-1}/\mu_0} P^{eff}_i(\theta_0, \phi_0; \theta_{zs_u}, \phi_{zs_u}) \mu_0 \overline{\mathcal{R}}(i, 0, s_u) \\ &\quad + I^k_{(i-1)s'_d} P^{eff}(\theta_{zs'_d}, \phi_{zs'_d}; \theta_{zs_u}, \phi_{zs_u}) \overline{\mu}_{s'_d} \overline{\mathcal{R}}(i, s'_d, s_u) \\ &\quad \Big[+ \rho\mu_0 I_0 e^{-\tau_i/\mu_0} + \rho\overline{\mu}_{s'_d} I^k_{is'_d} \overline{\mathcal{E}}(i, s'_d) \;\; (\text{if } i = N) \Big] \end{aligned} \tag{2.33}$$

and

$$\begin{aligned} I^k_{is_d} &= I_0 e^{-\tau_{i-1}/\mu_0} P^{eff}_i(\theta_0, \phi_0; \theta_{zs_d}, \phi_{zs_d}) \mu_0 \overline{\mathcal{T}}(i, 0, s_d) \\ &\quad + I^k_{(i-1)s'_d} P^{eff}(\theta_{zs'_d}, \phi_{zs'_d}; \theta_{zs_d}, \phi_{zs_d}) \overline{\mu}_{s'_d} \overline{\mathcal{T}}(i, s'_d, s_d) + I^k_{(i-1)s_d} \overline{\mathcal{E}}(i, s_d), \end{aligned} \tag{2.34}$$

where $\overline{\mathcal{R}}(i, s'_d, s_u)$ represents the reflection function of the vertical layer i between the directions represented by the streams s'_d and s_u, $\overline{\mathcal{T}}(i, s'_d, s_d)$ represents the effective transmission function of the vertical layer i across the directions represented by the streams s'_d and s_d and $\overline{\mathcal{E}}(i, s)$ represents the effective extinction due to layer i of the radiation carried by stream s. These quantities will be elaborated upon later in this section.

On reaching $i = N$, we add the downwelling flux intensities $I^k_{is_d}$ to the respective I_{is_d} and reset $I^k_{is_d} = 0$. Now, we trace $I^k_{is_u}$ upward through the atmosphere, i.e. from $i = N$ through $i = 1$. The upwelling trace yields

$$I^k_{is_u} = I^k_{(i+1)s'_u} P^{eff}(\theta_{zs'_u}, \phi_{zs'_u}; \theta_{zs_u}, \phi_{zs_u}) \overline{\mu}_{s'_u} \overline{\mathcal{T}}(i, s'_u, s_u) + I^k_{(i+1)s_u} \overline{\mathcal{E}}(i, s_u), \tag{2.35}$$

and

$$I^k_{is_d} = I^k_{(i+1)s'_u} P^{eff}(\theta_{zs'_u}, \phi_{zs'_u}; \theta_{zs_d}, \phi_{zs_d}) \overline{\mu}_{s'_u} \overline{\mathcal{R}}(i, s'_u, s_d). \tag{2.36}$$

On reaching TOA, i.e. $i = 0$, we add the upwelling flux intensities $I^k_{is_u}$ to the respective I_{is_u} and reset $I^k_{is_u} = 0$. Now, we start the 2^{nd} iteration, which, like all the following iterations, is identical to the 1^{st} iteration with the exception of all terms in Eq. 2.33 and 2.34 involving I_0, which are now set to 0.

Assuming, for the moment, that all the radiation in a stream s propagates along its central direction (μ_s, ϕ_s), we can obtain simple expressions for $\mathcal{E}, \mathcal{R}$ and $\mathcal{T}$.

$\mathcal{E}(i, s)$ takes on the simple form of extinction in accordance with the Beer-Lambert law as

$$\mathcal{E}(i, s) = \exp -\frac{\Delta\tau_i}{\mu_s}. \tag{2.37}$$

For $\mathcal{R}$, we consider one of s and s' to be upwelling and the other to be a downwelling stream. Then the reflection function of layer i from stream s' into stream s or vice versa is given by

$$\mathcal{R}(i, s', s) = \mathcal{R}(i, s, s') = \frac{\omega}{4\pi}\,\frac{1}{\mu_{s'} + \mu_s}\left\{1 - \exp\left[-\Delta\tau_i\left(\frac{1}{\mu_{s'}} + \frac{1}{\mu_s}\right)\right]\right\}, \tag{2.38}$$

For $\mathcal{T}$, we assume s and s' to be either both upwelling or both downwelling streams. Then the transmission function of layer i from stream s' into stream s or vice versa is given by

$$\mathcal{T}(i, s', s) = \frac{\omega}{4\pi}\,\frac{1}{\mu_{s'} - \mu_s}\left\{\exp\left[-\frac{\Delta\tau_i}{\mu_{s'}}\right] - \exp\left[-\frac{\Delta\tau_i}{\mu_s}\right]\right\}. \tag{2.39}$$

Keeping in mind, however, that each stream represents a finite section of space and not merely individual directions, we need to find equivalent terms for all spatial values involved in the above equations. For example, $\overline{\mu_s}$ in Eq.2.33 represents the mean value of μ' included in stream s, i.e.

$$\overline{\mu_s} = \int_{\mu'_z} d\mu'_z = \int_{\phi'=\phi_1}^{\phi_2}\int_{\theta=\theta_1}^{\theta_2} \mu_0\mu' - \sqrt{(1-\mu_0^2)(1-\mu'^2)}\,\cos\phi'\,d\mu' d\phi', \tag{2.40}$$

where $\mu' = \cos\theta'$. Here, μ_z is measured in the local frame of reference and then expressed in terms of μ as measured in the solar beam frame of reference. Similarly,

$$\begin{aligned}\overline{\left(\frac{1}{\mu_s}\right)} &= \int_{\mu'_z} \frac{1}{\mu'_z} d\mu'_z \\ &= \int_{\phi'=\phi_1}^{\phi_2}\int_{\theta=\theta_1}^{\theta_2} \frac{1}{\mu_0\mu' - \sqrt{(1-\mu_0^2)(1-\mu'^2)}\,\cos\phi'}\,d\mu' d\phi', \end{aligned} \tag{2.41}$$

and

$$\begin{aligned}\overline{\exp -\frac{1}{\mu_s}} &= \int_{\mu'_z} \exp\left(-\frac{1}{\mu'_z}\right) d\mu'_z \\ &= \int_{\phi'=\phi_1}^{\phi_2}\int_{\theta=\theta_1}^{\theta_2} \exp\left(-\frac{1}{\mu_0\mu' - \sqrt{(1-\mu_0^2)(1-\mu'^2)}\,\cos\phi'}\right) d\mu' d\phi', \end{aligned} \tag{2.42}$$

Since

$$\overline{\exp - \frac{\Delta\tau_i}{\mu_s}} = \left(\overline{\exp - \frac{1}{\mu_s}}\right)^{\Delta\tau_i}, \tag{2.43}$$

and

$$\overline{\exp - \Delta\tau_i \left[\frac{1}{\mu_s} + \frac{1}{\mu'_s}\right]} = \left(\overline{\exp - \frac{1}{\mu_s}} \cdot \overline{\exp - \frac{1}{\mu'_s}}\right)^{\Delta\tau_i}, \tag{2.44}$$

we can calculate the effective extinction, the reflection function and the transmission function of each layer i using $\overline{\mu_s}$ and $\overline{\exp - \frac{1}{\mu_s}}$ as follows

$$\overline{\mathcal{E}}(i, s'_d, s_u) = \left(\overline{\exp - \frac{1}{\mu_s}}\right)^{\Delta\tau_i}, \tag{2.45}$$

$$\overline{\mathcal{R}}(i, s', s) = \frac{\omega}{4\pi} \frac{1}{\overline{\mu}_{s'} + \overline{\mu}_s} \left\{ 1 - \left(\overline{\exp - \frac{1}{\mu_s}} \cdot \overline{\exp - \frac{1}{\mu'_s}}\right)^{\Delta\tau_i}, \right\}, \tag{2.46}$$

and

$$\overline{\mathcal{T}}(i, s', s) = \frac{\omega}{4\pi} \frac{1}{\overline{\mu}_{s'} - \overline{\mu}_s} \left\{ \left(\overline{\exp - \frac{1}{\mu'_s}}\right)^{\Delta\tau_i} - \left(\overline{\exp - \frac{1}{\mu_s}}\right)^{\Delta\tau_i} \right\}. \tag{2.47}$$

4. **The iteration of multiple scattering until a stable value of reflectance is obtained.** When the above iterations converge, resulting in stable values of I_{is_u} and I_{is_d}, each stream in each layer contains our simulation of the diffuse radiation at height z_i propagating around the central direction of that stream. This light can now undergo a final scattering event that sends it into the receiving cone of the detector, producing the multiple scattering component of the total signal registered by it.

   The intensity of light arriving at the detector per unit solid angle from the upwelling diffuse radiation contained in stream s_u of layer i is given by

   $$\Delta I_{is_u} = I_{is_u} e^{-\tau_{i-1}/\mu_d} P(\mu_{s_u}, \phi_{s_u}; \mu_d, \phi_d) \overline{\mu}_{s_u} \overline{\mathcal{T}}(i, s_u, d), \tag{2.48}$$

   and that of light arriving at the detector per unit solid angle from the downwelling diffuse radiation contained in stream s_d of layer i is given by

   $$\Delta I_{is_d} = I_{is_d} e^{-\tau_{i-1}/\mu_d} P(\mu_{s_d}, \phi_{s_d}; \mu_d, \phi_d) \overline{\mu}_{s_d} \overline{\mathcal{T}}(i, s_d, d), \tag{2.49}$$

   so that the total multiple scattering signal arriving at the detector is given by

   $$I_{ms} = \Sigma_{i=1}^{N} \left(\Delta\, I_{is_u} + \Delta\, I_{is_d}\right). \tag{2.50}$$

2.5 Model comparisons

In the following we compare reflectances (I_d/I_0) measured at the detector simulated using AeroRad with 3 other models (LINTRAN, SCIATRAN and McArtim) in the O_2 A- and B-band wavelength ranges.

LINTRAN is the vector radiative transfer model developed at the Netherlands Institute of Space Research (SRON). It solves the vector radiative transfer equation in a plane parallel atmosphere providing the Stokes parameters of the light reflected by the Earth atmosphere. The model is verified against other existing vector radiative transfer models. Since we deal with total reflectances irrespective of polarization in our study, we use reflectances generated by LINTRAN in its scalar mode for our comparison.

The SCIATRAN radiative transfer models (RTMs) are next generation RTMs based on the well-known GOMETRAN model which was originally developed to simulate solar radiation backscattered from the atmosphere and reflected from the Earth's surface in the spectral range 240–800 nm as measured by the Global Ozone Monitoring Experiment (GOME) in nadir viewing geometry. A successor RTM called SCIATRAN was extended to cover the spectral range 240–2380 nm comprising the 8 spectral channels of the Scanning Imaging Absorption Spectrometer for Atmospheric Chartography (SCIAMACHY) instrument. SCIATRAN versions up to 1.2 utilize the pseudo-spherical approach, including refraction, appropriate for solar zenith angles up to about 92¡ and near-nadir viewing angles. The new generation of the SCIATRAN radiative transfer model (version 2.0) comprises all features of the latest SCIATRAN 1.2 RTM supporting additionally radiative transfer calculations in a spherical atmosphere. We use reflectances generated by SCIATRAN 2.0 in the plane-parallel mode for our comparison study.

McArtim is an acronym for

- Monte Carlo
- Atmospheric Radiative Transfer
- Inversion Model.

McArtim has been developed at the Institute of Environmental Physics, Heidelberg, and has also undergone ongoing comparison with other models.

Uniformity among the different models regarding the scenario being simulated is warranted by the use of the same vertical profiles by all models.

In order to reproduce high values of optical thickness due to scattering at these wavelengths without the use of aerosols (which is complicated due different implementations of aerosol scattering by different models), we simply scale the respective Rayleigh cross sections to a higher value. Furthermore, the phase function for Rayleigh scattering is simpler than most aerosol phase functions, allowing for easier interpretation. We use scaling factors of 1x, 5x and 20x for each comparison.

We compare the behaviour of reflectance I/I_0 with respect to changes in solar zenith angle θ_0, line-of-sight zenith angle θ_d and the surface albedo ρ which is assumed to be lambertian. For this, we consider wavelengths 682 nm and 756 nm, both largely free of trace gas absorption, so that atmospheric scattering and ground reflectance contribute the most to the signal at the detector. Fig.2.3 shows the vertical profiles of the optical thickness, $\Delta\tau_i$, and single scattering albedo, $\Delta\omega_i$, of each layer i of the atmosphere as represented in AeroRad.

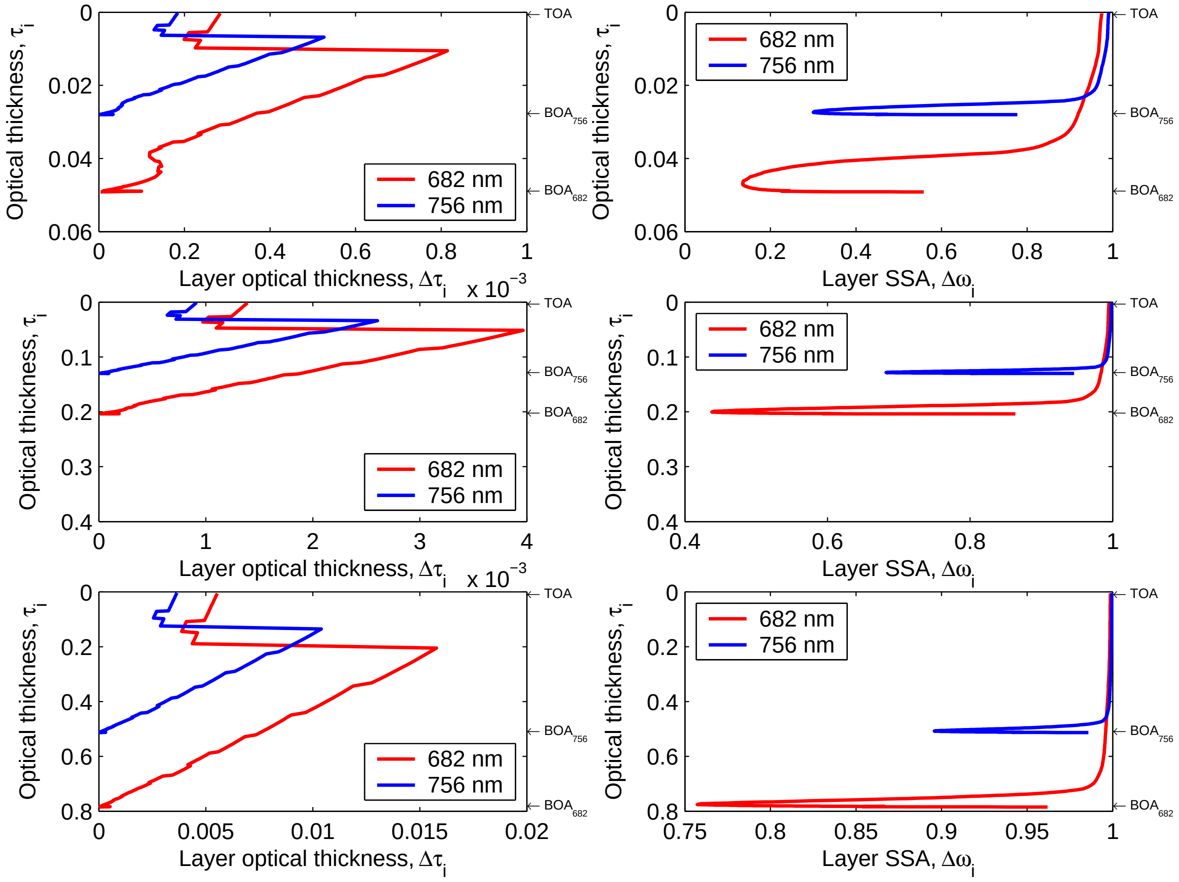

Figure 2.3: The left panels show the optical thickness $\Delta\tau_i$ of layer i with respect to the optical thickness of the atmosphere at the layer ($\tau_i = 0$ at TOA). The panels on the right hand side show the effective single scattering albedo $\Delta\omega_i$ of layer i with respect to the optical thickness of the atmosphere at the layer. The red curves represent 682 nm and the blue curve represents 756 nm. On each side, the panels represent a Rayleigh scaling factor of 1x in the top row, 5x in the middle and 20x at the bottom.

2.5.1 I/I_0 vs. SZA

To study the variation in atmospheric reflectance I/I_0 with respect to solar zenith angle, θ_0, we set the line-of-sight zenith angle, $\theta_d = 0°$, and switch off surface reflectance by setting the albedo, $\rho = 0$. The SZA is varied from 0° through 20° and 40° to a maximum of 60°.

Fig.2.4 shows the total reflectances simulated by LINTRAN (solid blue line), SCIATRAN (solid green line), McArtim (solid magenta line) and AeroRad (solid red line) in addition to the single scattering component of the total reflectance available from LINTRAN (dashed blue line) and AeroRad (dashed red line).

For the single scattering component we see near parity between the LINTRAN and AeroRad reflectances with a maximum difference of 2.32% with respect to the lower value seen at SZA= 0° and a scaling factor of unity at 682 nm. This reflects the relatively straightforward calculation of the direct component of incident solar radiation.

The complexity associated with the calculation of the diffuse component of solar radiation is evident from the much larger divergence of total reflectances simulated by the different models as the models show a maximum divergence of $\approx 3.12\%$ for a scaling factor of 1, $\approx 12\%$ for a scaling factor of 5, and $\approx 6\%$ for a scaling factor of 20 for SZA$= 0°$ (chosen as reference due to the general absence of individual outliers). At higher scaling factors, AeroRad exhibits markedly higher reflectances at small SZA's and rather low reflectances at large SZA, which, while reflecting the general ability of AeroRad to simulate forward-peaked scattering, also indicates relatively crude averaging over the angular extent of a stream. While not presenting a serious handicap for our purposes, it points out an area requiring further refinement.

The general trend demonstrated by all models is that the atmospheric reflectance (since there is no surface reflection) is maximum at small SZA, gradually tapering off for increasing SZA. This may be seen as a direct consequence of the smaller light path covered and thus the lower extinction suffered by the light entering the detector when the sun stands closer to the zenith.

2.5.2 I/I_0 vs. LZA

To study the variation in atmospheric reflectance I/I_0 with respect to line-of-sight zenith angle, θ_d, we set the solar zenith angle, $\theta_0 = 0$, and remove surface reflectance by setting the albedo, $\rho = 0$. Since we are mainly interested in nadir scanning scenarios, the LZA is varied from 0° through 5° and 10° to 15°.

As can be seen from Fig. 2.5, we again see near parity between the single scattering components of the reflectances simulated by LINTRAN and AeroRad.

At LZA$= 0°$, total reflectances simulated by the different models as the models show maximum divergences of $\approx 3.12\%$, 12% and 6% for scaling factors of 1, 5 and 20, respectively. Higher values of reflectance are registered by both McArtim and AeroRad. The elevated AeroRad reflectances may be explained by the greater forward scattering experienced at lines of sight varying between $0° - 15°$ with respect to zenith, given SZA$= 0°$. However, as mentioned before, this may also be caused by distortions due to crude averaging within the streams, calling for further improvement of the model.

While LINTRAN and SCIATRAN suggest near-independence of the observed reflectances with respect to the line-of-sight (in the range $0° - 15°$), AeroRad consistently shows a mild increase in reflectance with respect to LZA. McArtim also indicates an increase with respect to LZA, though not as markedly as AeroRad. There may be two competing effects at play in this regard: the light path from the scatterer towards the detector becomes longer as the LZA increases, causing more extinction and a resultant decrease in reflectance on one hand, but at the same time allowing for the occurrence of more scattering into the direction of the detector since there are more scattering points contained by this path. While LINTRAN and SCIATRAN suggest that these effects balance each other, AeroRad leads to the conclusion that the presence of more scattering points outweighs the greater extinction taking place along the light path. The less monotonously increasing trend shown by McArtim suggests both possibilities, dependent on the particular geometry.

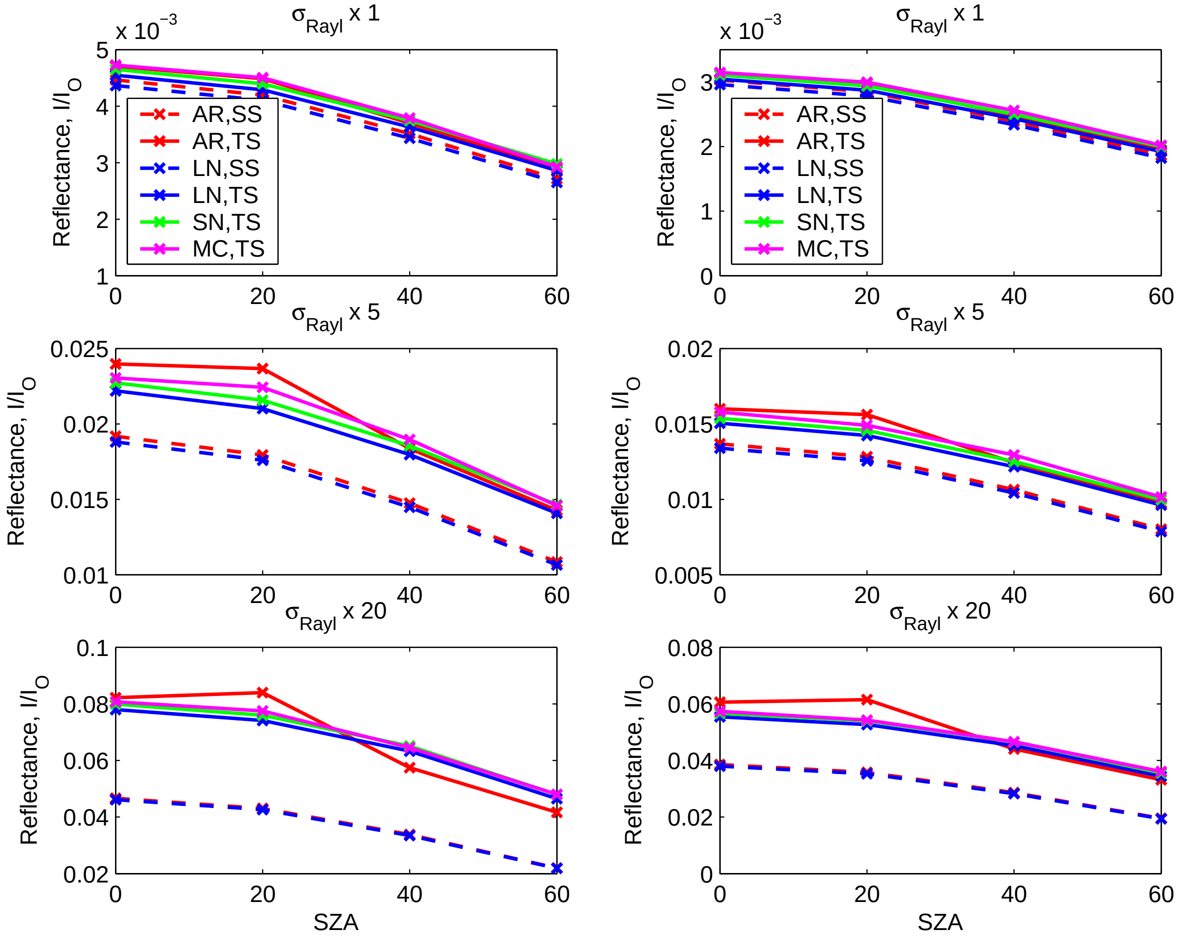

Figure 2.4: Variation in reflectance with respect to solar zenith angle. Line-of-sight is assumed to be aligned with nadir and the earth's surface is assumed to be completely black. The left panels show reflectances at 682 nm for a Rayleigh scaling factor of 1x at the top, 5x in the middle and 20x at the bottom panel. The right hand side panels represent reflectances at 756 nm in the same order of scaling factors. In each case, the red curve indicates single scattering reflectance and the blue curve shows total (single+multiple scattering) reflectance as simulated by AeroRad. The green line indicates the total reflectance simulated by SCIATRAN.

2.5.3 I/I_0 vs. albedo

To study the variation in atmospheric reflectance I/I_0 with respect to (lambertian) surface albedo, ρ, we set the solar and line-of-sight zenith angles, $\theta_0 = \theta_d = 0$ and vary the lambertian surface albedo from 0 through 0.03 to 0.06 (corresponding to a reflection of nearly 20% of the light incident on the surface).

The single-scattering reflectances generated by LINTRAN and AeroRad again show near parity as can be seen from Fig. 2.6.

Although the total reflectance curves fan out at larger albedo values, their percentage divergence is maximum at $\rho = 0$, corresponding to $\approx 3.12\%$, 12% and 6% for scaling factors of 1, 5

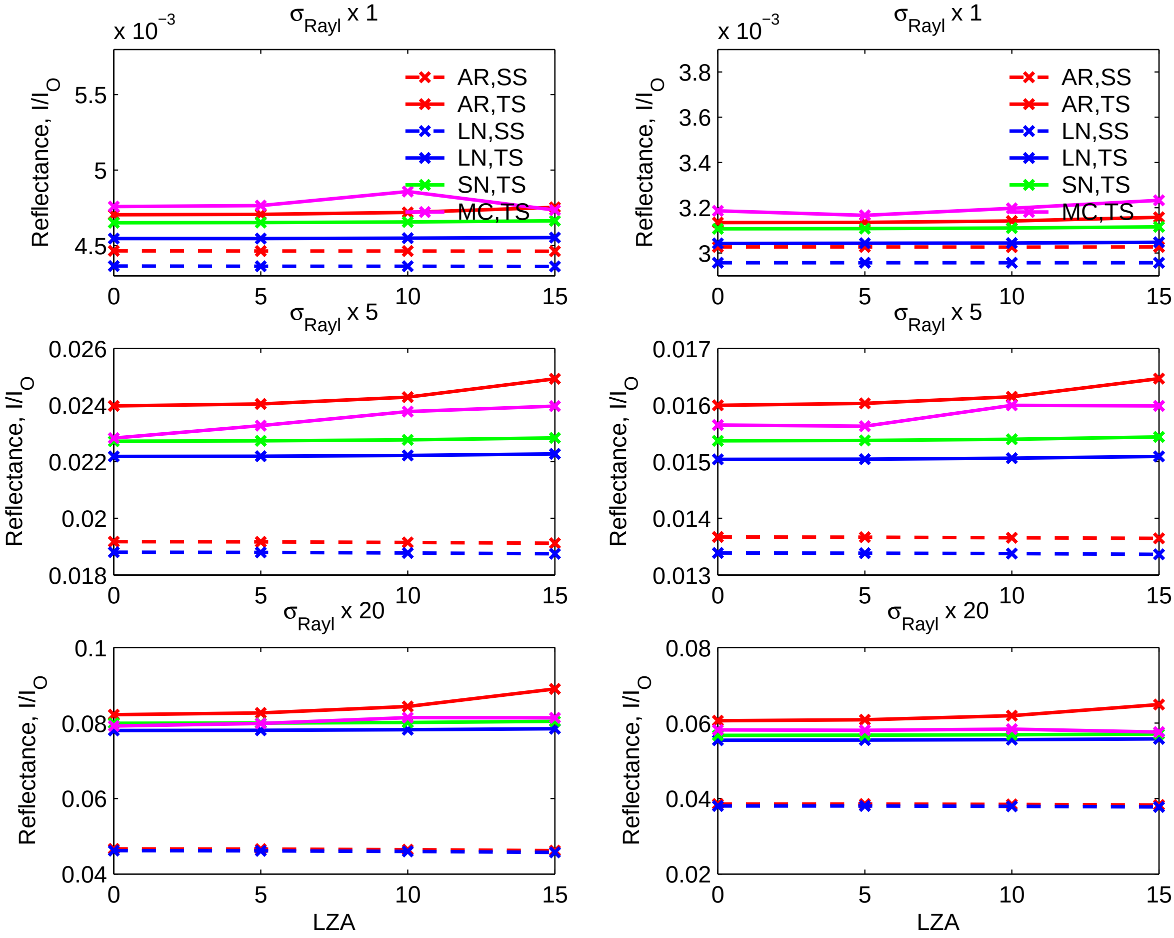

Figure 2.5: Variation in reflectance with respect to line-of-sight zenith angle. The sun is assumed to be at zenith and the earth's surface is assumed to be completely black. The left panels show reflectances at 682 nm for a Rayleigh scaling factor of 1x at the top, 5x in the middle and 20x at the bottom panel. The right hand side panels represent reflectances at 756 nm in the same order of scaling factors. In each case, the red curve indicates single scattering reflectance and the blue curve shows total (single+multiple scattering) reflectance as simulated by AeroRad. The green line indicates the total reflectance simulated by SCIATRAN.

and 20, respectively. The reflectance simulated by AeroRad can be seen to be distinctly elevated for scaling factors of 5 and 20, again reflecting the forward peaking at $SZA = LZA = 0°$.

The single scattering component of the reflectance is linearly proportional to the surface albedo. At the albedo values considered here, it is evident that multiple scattering increases with albedo for a purely Rayleigh atmosphere. The slope of the total reflectance curve, however, may rise or fall with albedo depending on the presence of absorbers or different types of aerosol present in the atmosphere above the surface, as will be seen in the next chapter.

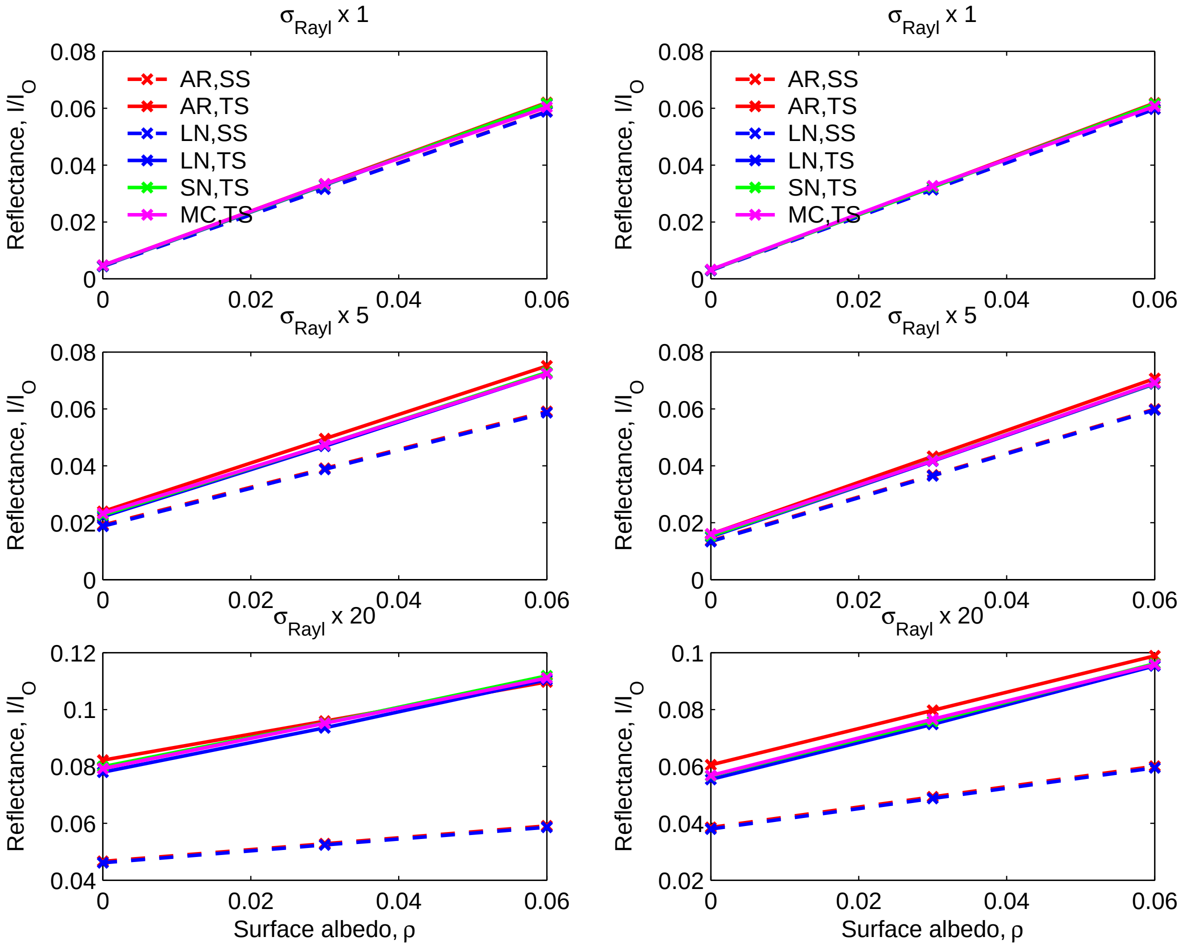

Figure 2.6: Variation in reflectance with respect to albedo. The sun is assumed to be at zenith and the line-of-sight is assumed to be aligned with nadir. The reflection at the earth's surface is assumed to be lambertian. The left panels show reflectances at 682 nm for a Rayleigh scaling factor of 1x at the top, 5x in the middle and 20x at the bottom panel. The right hand side panels represent reflectances at 756 nm in the same order of scaling factors. In each case, the red curve indicates single scattering reflectance and the blue curve shows total (single+multiple scattering) reflectance as simulated by AeroRad. The green line indicates the total reflectance simulated by SCIATRAN.

2.5.4 I/I_0 spectra in regions of strong absorption

We further compare the simulation of lines of strong absorption in the A- and B-bands respectively. For this, we choose the spectral regions 687 − 688 nm and 762 − 765 nm respectively, each with a spectral resolution of 0.005 nm. Fig. 2.7 shows LINTRAN, SCIATRAN and AeroRad simulations of the corresponding reflectance spectra for the three Rayleigh cross-section scaling factors of $1\times, 5\times$ and $20\times$ at SZA=LZA= 0 over a black surface.

Fig. 2.7 shows closer details of these reflectances, which show a general agreement between all models, AeroRad producing higher reflectances at wavelengths featuring low or no absorption due to increased detection of the scattering peak given the position of the sun at zenith and the nadir pointing detector. SCIATRAN produces slightly narrower lines than LINTRAN and AeroRad which show a near overlap at wavelengths of strong absorption.

It is also apparent that multiple scattering gets rapidly diminished with increasing absorption, so that reflectances at wavelengths of high absorption consist of only the single scattering component.

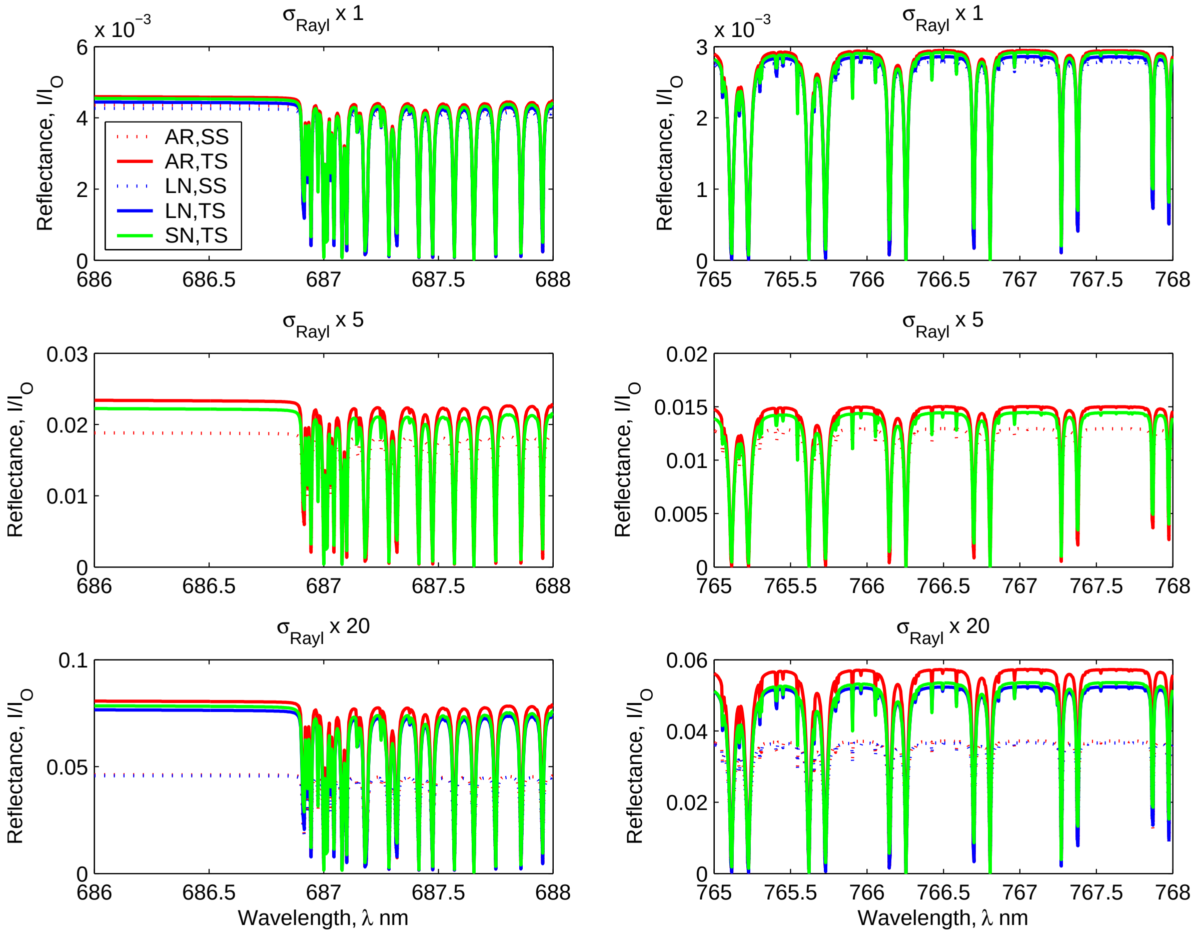

Figure 2.7: Reflectance spectra simulated in the O_2 A- and B-bands. The sun is assumed to be at zenith and the line-of-sight is assumed to be aligned with nadir. The earth's surface is assumed to be completely black. The left panels show reflectances in the B-band for a Rayleigh scaling factor of 1x at the top, 5x in the middle and 20x at the bottom panel. The right hand side panels represent reflectances in the A-band in the same order of scaling factors. In each case, the red curve indicates single scattering reflectance and the blue curve shows total (single+multiple scattering) reflectance as simulated by AeroRad. The green line indicates the total reflectance simulated by SCIATRAN.

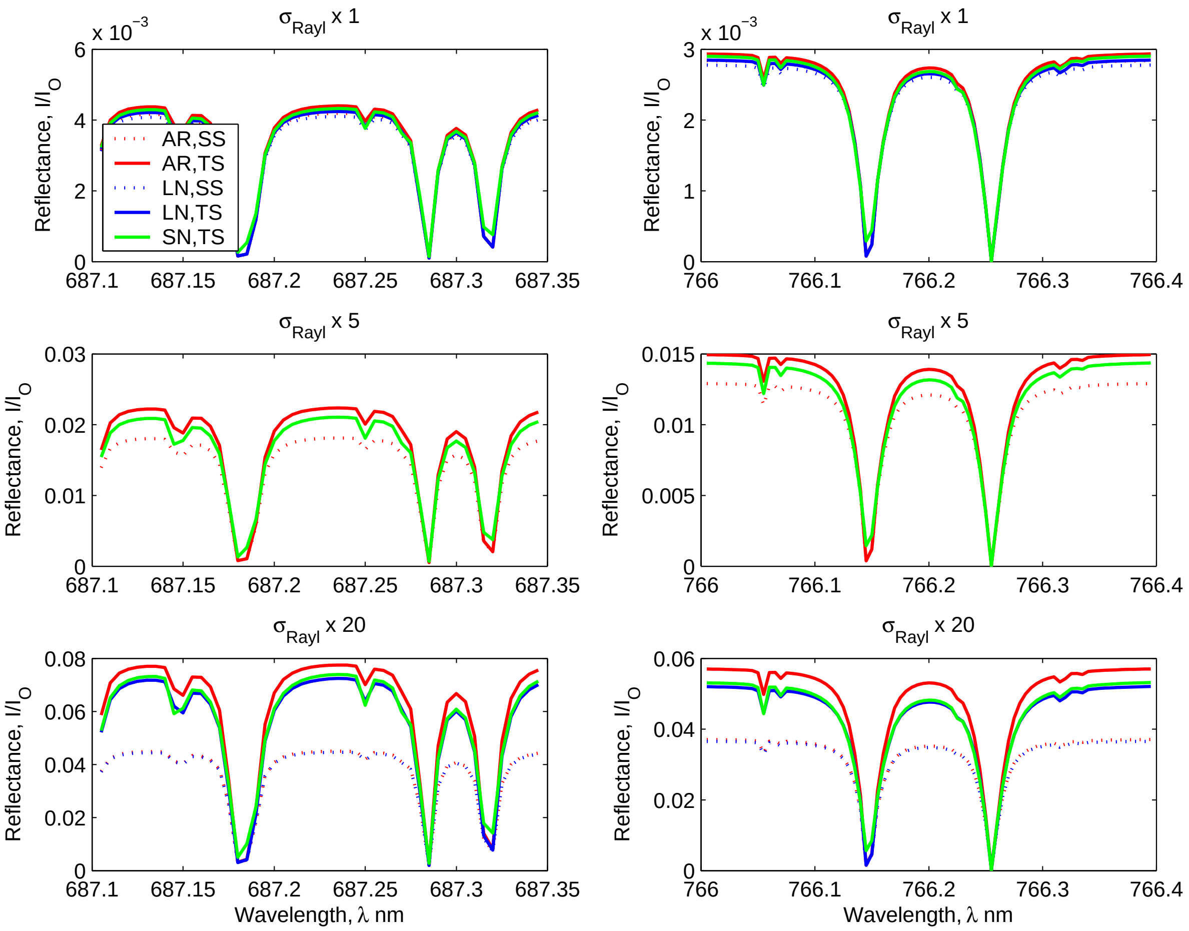

Figure 2.8: Reflectance spectra simulated in the O_2 A- and B-bands. The sun is assumed to be at zenith and the line-of-sight is assumed to be aligned with nadir. The earth's surface is assumed to be completely black. The left panels show reflectances in the B-band for a Rayleigh scaling factor of 1x at the top, 5x in the middle and 20x at the bottom panel. The right hand side panels represent reflectances in the A-band in the same order of scaling factors. In each case, the red curve indicates single scattering reflectance and the blue curve shows total (single+multiple scattering) reflectance as simulated by AeroRad. The green line indicates the total reflectance simulated by SCIATRAN.

2.6 Representation of aerosols in AeroRad

As seen in the previous chapter, it takes a large set of parameters to fully describe an aerosol scenario. Most aerosols occurring in the atmosphere do not yield to a simple description because:

1. The particles may be of irregular shape,
2. A single particle may be composed of different substances in mixed phase, eg. a dust particle embedded in a liquid droplet.
3. The size distributions are usually multimodal distributions of unknown form, and may vary with altitude,

4. The vertical and lateral distribution of the aerosol may be irregular and aerosol composition may show local variations,
5. The real and imaginary parts of the complex refractive index typically vary nonlinearly with wavelength,
6. The total aerosol loading (aerosol column density) usually shows strong spatiotemporal variation.

This problem is eased by approximating a given aerosol scenario by a homogeneous aerosol type of spherical shape which can be completely described by its size distribution, vertical profile and complex refractive index. The following assumptions reduce the number of variables required to characterize aerosol scenarios:

1. Aerosol particles are homogeneous and spherical in shape,
2. Their complex refractive index remains more or less constant at all wavelengths involved,
3. Their size distribution is independent of altitude and can be represented by a bimodal lognormal distribution,
4. The vertical extent of any aerosol scenario can be approximated by a lognormal profile.

Thus, the variables required to characterize an aerosol scenario in AeroRad are:

1. real component of the refractive index, m_r,
2. imaginary component of the refractive index, m_i,
3. mean radius of the fine mode, r_f,
4. standard deviation of the fine mode, σ_f,
5. mean radius of the coarse mode, r_c,
6. standard deviation of the coarse mode, σ_c,
7. mode fraction of the coarse mode, μ,
8. total aerosol column, $Nparticles/cm^2$,
9. peak height of lognormal vertical profile, z_p,
10. peak width of lognormal vertical profile, σ_p.

The first 7 of the above parameters will be referred to throughout this thesis as the 'microphysical parameters' of the aerosol. 24 model scenarios, adapted from (...), have been constructed using these parameters to describe 5 different types of aerosols. The Mie Theory can be used to calculate the extinction cross-section $\kappa_p(x)$, single scattering albedo $\omega_p(x)$ and phase function $p_p(x, \theta)$ of an aerosol particle of any size r at any wavelength λ, given its refractive index

(m_r, m_i). Here, the subscript p represents a single aerosol particle and x stands for the 'size parameter' of the particle. The size parameter is defined by the following relationship

$$x = \frac{2\pi\, r}{\lambda/m_r} \tag{2.51}$$

These quantities, also referred to as the single scattering parameters of the particle, can be averaged over its entire size distribution $(r_f, \sigma_f, r_c, \sigma_c, \mu)$ to obtain the effective single scattering parameters of the aerosol (κ, ω, $p(\theta)$), where κ denotes the extinction cross section, ω denotes the single scattering albedo and $p(\theta)$ is the phase function of the aerosol. Thus, we have the following relationships between the single scattering parameters of an aerosol distribution and those of its individual particles

$$\kappa(\lambda) = \Sigma_r\, \kappa_p(x)\rho(r)\Delta\, r, \tag{2.52}$$

$$\omega(\lambda) = \frac{\Sigma_r\, \omega_p(x)\kappa_p(x)\rho(r)}{\Sigma_r\, \kappa_p(x)\rho(r)}\Delta\, r \tag{2.53}$$

and

$$p(\lambda, \theta) = \frac{\Sigma_r\, p_p(x, \theta)\omega_p(x)\kappa_p(x)\rho(r)}{\Sigma_r\, \omega_p(x)\kappa_p(x)\rho(r)}\Delta\, r, \tag{2.54}$$

where $\rho(r)$ is the size distribution function of the aerosol. These quantities, together with the total aerosol column C_{aer} can be encapsulated into the effective AOT, τ, and the Ångström exponent, α_λ, of the aerosol distribution as follows

$$\tau(\lambda) = C_{aer}\kappa(\lambda), \tag{2.55}$$

and

$$\alpha_\lambda = -\frac{d(\log\tau)}{d(\log\lambda)}, \tag{2.56}$$

which along with the vertical profile paramters will be referred to henceforth as the 'macro-physical parameters' of the aerosol.

2.6.1 Aerosol phase function

The aerosol phase function $p(\vec{\Omega};\vec{\Omega'})$ is a measure of the probability density of scattering of light incident in the direction $\vec{\Omega}$ by the aerosol into a cone of angle $d\Omega'$ around the direction $\vec{\Omega'}$. Thus,

$$\frac{1}{4\pi}\oint p(\vec{\Omega};\vec{\Omega'})\, d\Omega' = 1. \tag{2.57}$$

The phase function of the aerosol is independent of total aerosol loading and of its vertical profile, making it a fundamental characteristic of the aerosol. To understand the scattering behaviour of atmospheric aerosols, it is thus helpful to know their phase functions, which

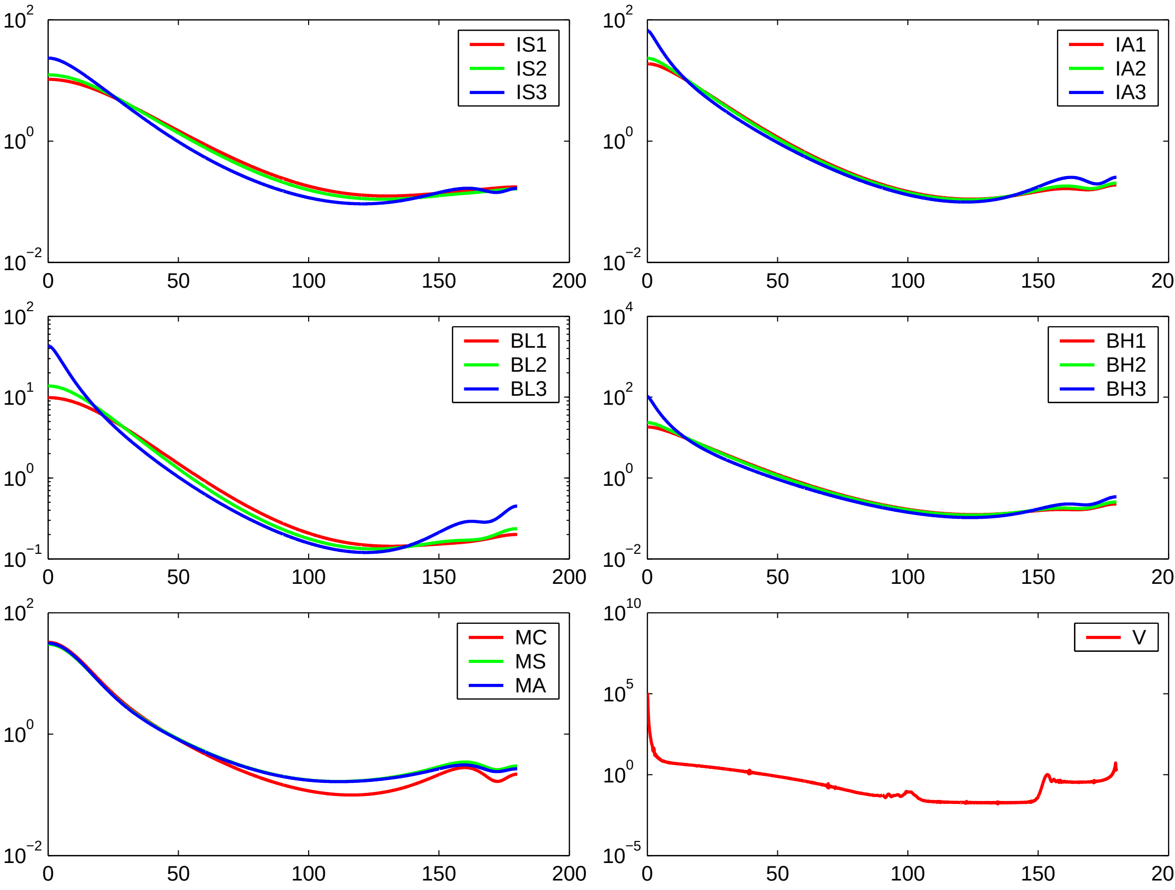

Figure 2.9: Phase functions of all spherical model aerosol types plotted against angle of scattering at 685 nm.

depend upon the complex refractive index and size distribution of the aerosol and vary with wavelength.

Fig. 2.9 and Fig. 2.10 show the effective phase functions of all the spherical aerosol models included in AeroRad at wavelengths in the O_2 B and A-bands, respectively. The top two panels show scattering and absorbing industrial aerosols respectively. Each panel has three aerosol sub-types, the red curve repFresting the finest and the blue curve representing the coarsest size distribution of the three. The same applies to the second row of panels, representing low altitude ($\approx 3\,\text{km}$) biogenic aerosol on the left and high altitude ($\approx 5\,\text{km}$) biogenic aerosol on the right. The bottom panel represents maritime aerosols (the red curve represents clean maritime aerosol usually found in remote oceans, while the green and the blue curves represent scattering and absorbing maritime aerosols, found closer to continental coastlines) on the left and a volcanic aerosol on the right. All aerosol types are strongly forward peaked, with a minimum around 120°, before attaining a small backward peak. In each case, we notice that the coarser the aerosol gets (see blue curves), the sharper is its forward peak. This is a result of larger sized particles in the distribution, causing the aerosol to have a larger effective size parameter. The greater the size parameter, the sharper is the forward peak. An extreme case of strong forward peaking is the volcanic aerosol, having a mono-modal peak radius at

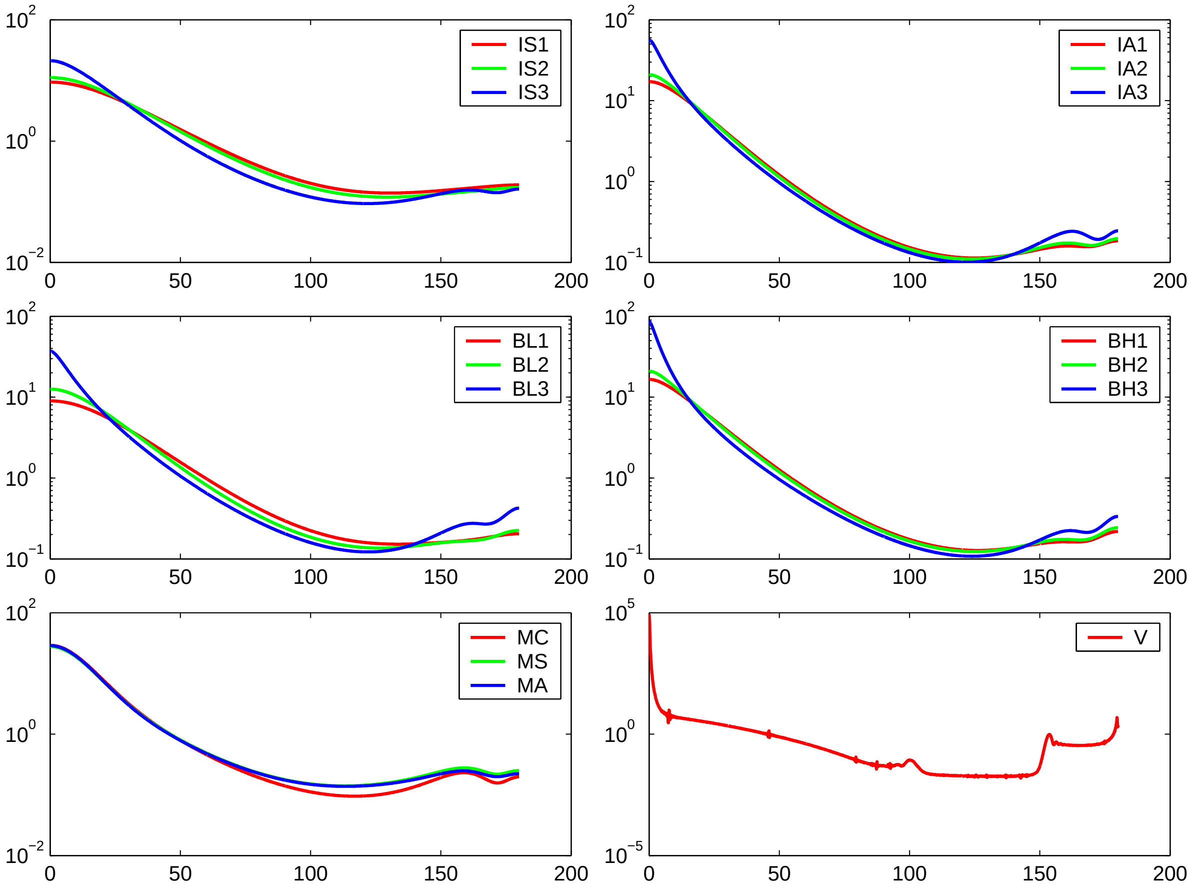

Figure 2.10: Phase functions of all spherical model aerosol types plotted against angle of scattering at 760 nm.

$0.23\,\mu$m. Although there is not a marked difference between the phase functions at 685 and 760 nm, it can be seen that the phase functions become flatter with increasing wavelength. In other words, the peaks are sharper at smaller wavelengths, which again is explained by the fact that the effective size parameter is greater at shorter wavelengths.

Table 2.1: Aerosol size distribution and refractive index for the selected aerosol models. Several of the five major types are divided into sub-types according to the amount of absorption or the vertical, log-normal distribution. These sub-types can contain a number of aerosol models that differ in particle size distribution and/or refractive index. The industrial and biogenic types have a bimodal distribution. The mean particle radius and its standard deviation are given separately for both modes. The number concentration of the coarse mode relative to the total number concentration is represented by the fraction μ.

			Mean (μm)	Radius	Standard (μm)	Deviation	Coarse mode fraction	Refractive	Index
Type	Subtype	Model	r_f	r_c	σ_f	σ_c	μ	m_r	m_i
Industrial	IS	IS1	0.078	0.497	1.499	2.160	$4.36\ 10^{-4}$	1.4	0.004
		IS2	0.088	0.509	1.499	2.160	$4.04\ 10^{-4}$	1.4	0.004
		IS3	0.137	0.567	1.499	2.160	$8.10\ 10^{-4}$	1.4	0.004
	IA	IA1	0.085	0.641	1.560	2.004	$7.00\ 10^{-4}$	1.45	0.012
		IA2	0.090	0.676	1.560	2.004	$6.84\ 10^{-4}$	1.45	0.012
		IA3	0.109	0.804	1.560	2.004	$6.95\ 10^{-4}$	1.45	0.012
Biomass	BL	BL1	0.074	0.511	1.537	2.203	$1.70\ 10^{-4}$	1.5	0.010
		BL2	0.087	0.567	1.537	2.203	$2.06\ 10^{-4}$	1.5	0.010
		BL3	0.124	0.719	1.537	2.203	$2.94\ 10^{-4}$	1.5	0.010
	BH	BH1	0.076	0.665	1.492	2.075	$2.07\ 10^{-4}$	1.5	0.020
		BH2	0.080	0.705	1.492	2.075	$2.05\ 10^{-4}$	1.5	0.020
		BH3	0.097	0.866	1.492	2.075	$1.99\ 10^{-4}$	1.5	0.020
Volcanic[b]	V	V	0.230	-	0.800	-	-	1.45	$7.5\ \ 10^{-7}$

---

[a] Wavelength dependent with (H)igh or (L)ow absorbance and (S)pherical or (N)on spherical particles.

[b] Only used in case of eruptions.

Table 2.2: Aerosol size distribution and refractive index for the selected aerosol models, continued.

			Mean (μm)	Radius	Standard (μm)	Deviation	Coarse mode fraction	Refractive	Index
Type	Subtype	Model	r_f	r_c	σ_f	σ_c	μ	m_r	m_i
Desert Dust	DL	DL3KS	0.052	0.67	1.697	1.806	$4.35\ 10^{-3}$	1.53	[a] LS
		DL5KS	0.052	0.67	1.697	1.806	$4.35\ 10^{-3}$	1.53	[a] LS
		DL3KN	0.052	0.67	1.697	1.806	$4.35\ 10^{-3}$	1.53	[a] LN
		DL5KN	0.052	0.67	1.697	1.806	$4.35\ 10^{-3}$	1.53	[a] LN
	DH	DH3KS	0.052	0.67	1.697	1.806	$4.35\ 10^{-3}$	1.53	[a] HS
		DH5KS	0.052	0.67	1.697	1.806	$4.35\ 10^{-3}$	1.53	[a] HS
		DH3KN	0.052	0.67	1.697	1.806	$4.35\ 10^{-3}$	1.53	[a] HN
		DH5KN	0.052	0.67	1.697	1.806	$4.35\ 10^{-3}$	1.53	[a] HN
Oceanic	MS	MS	0.030	0.240	2.030	2.030	$1.55\ 10^{-4}$	1.4	0.004
	MA	MA	0.030	0.240	2.030	2.030	$1.55\ 10^{-4}$	1.4	0.012
	MC	MC	0.030	0.240	2.030	2.030	1.5310^{-2}	1.4	$5\quad 10^{-8}$
Volcanic[b]	V	V	0.230	-	0.800	-	-	1.45	$7.5\quad 10^{-7}$

[a] Wavelength dependent with (H)igh or (L)ow absorbance and (S)pherical or (N)on spherical particles.

[b] Only used in case of eruptions.

2.7 Influence of aerosols on the radiative properties of the atmosphere: model studies using AeroRad

Every section of the atmosphere, characterized by its distinct composition in terms of molecular density, trace gas absorptivity and aerosol loading, contributes by way of absorption and scattering to the reflectivity measured by satellite. Assuming the atmosphere above a given location to be laterally homogeneous, we investigate this contribution at different wavelengths under different aerosol loadings and aerosol types in the following. Setting the surface albedo, $\rho = 0$, we consider the total reflectance, I/I_0 measured by satellite to be the sum of the contributions $\Delta_i(I/I_0)$, originating due to reflection from layer i of the atmosphere and having undergone extinction through all intermediate layers above it. For a better understanding of the involved processes, we separate $\Delta_i(I/I_0)$ into its respective single and multiple-scattering components, $\Delta_i^{ss}(I/I_0)$ and $\Delta_i^{ms}(I/I_0)$. In all the scenarios listed below, we have considered both the sun and the satellite to be aligned with the local zenith. In each case, we consider the wavelengths 682 nm and 687 nm, lying just outside and deep within the $\mathsf{O_2}$ B-band respectively, and 757 nm, 761 nm and 763 nm, lying just outside, in the middle of the R-branch and within the P-branch of the $\mathsf{O_2}$ A-band respectively.

2.7.1 Dependence of single and multiple-scattering reflectivity on aerosol type

In this section, we study the vertical profiles of single and multiple scattering reflectances corresponding to industrial (IS1), biogenic (BL2) and volcanic (V) aerosol types, each having the same *AOT* of 0.5. Each of the above aerosols has a different vertical distribution, with the industrial aerosol concentration peaking very close to the ground, the biogenic aerosol peaking at 3 km and the volcanic aerosol having a peak height of 10 km. This should help understand the effect of the vertical distribution of aerosols on the reflectance profile of the atmosphere. Figures2.11-2.15 show the scattering behaviour of the atmosphere at different wavelengths in and around the $\mathsf{O_2}$ A and B-bands. In each figure, the upper left panel shows the vertical profiles of the optical thickness per unit layer height due to trace gas absorption and Rayleigh scattering respectively. The upper right panel shows the same vertical profiles for each of the afore mentioned aerosol scenarios. The bottom panel shows the corresponding reflectivities due to single and multiple-scattering per unit layer height for all the layers of the atmosphere.

It is seen that, at wavelengths of weak absorption, the single-scattering reflectance exhibits a single peak, nearly coincident with the peak of the vertical distribution of the aerosol, which can be readily explained by the greater number of aerosol particles intercepting the incident solar radiation at peak concentration. Multiple-scattering reflectance, on the other hand, exhibits multiple peaks, typically one above and one below the peak of single-scattering reflectance. The lower peak is caused by (mostly Rayleigh) scattering of light scattered in the forward direction by the overlying aerosol. Due to the strong forward peak of the aerosol phase function (see Section 2.6.1), this lower peak of multiple-scattering reflectance is very prominent inspite of the subsequent extinction caused by the overlying atmospheric layers. The upper peak is caused due to scattering by the (relatively fewer) air molecules and aerosol particles lying above the height of peak concentration of diffuse radiation produced mainly by back-scattering of incident solar radiation by the aerosol concentration peak. This relfectance peak is significantly smaller than the lower peak due to both, the diminished concentration of air molecules available to scatter radiation, and the weaker back-scattering phase function of the aerosol (see Section 2.6.1). Nonetheless, the peak remains discernible because the reflected light has to suffer far lesser extinction along the intermediate atmospheric layers. An extreme case of this situation is that of volcanic aerosols, which, inspite of a peak concentration at a height of 10 km, produces a strong reflectance peak at the surface. Figures2.11-2.15 suggest that this holds true even when trace gas absorption becomes fairly strong, causing all other multiple-scattering peaks to dissapear. Furthermore, it is apparent from Figures 2.12 and 2.14 that most of the light reaching the detector for each aerosol scenario is due to single-scattering by aerosol particles that may be present in the stratosphere (although their profile in reality is unlikely to match the idealized assumption made here). The volcanic peak, paradoxically, is smaller than the other two aerosol types inspite of the height of its peak concentration. This may be explained by the low effective single scattering albedo of its predominantly large particles.

2.7.2 Dependence of single and multiple-scattering reflectivity on aerosol loading

While the previous section considered the effect of different aerosol types on the reflectance profile of the atmosphere, this section focusses on the impact of changes in the loading of a given aerosol type. We consider an industrial aerosol (IS1), with AOT's varying from 0 through 0.25 and 0.5 to 1.0, again at all the wavelengths considered in the previous section. In Figures 2.16-2.20, the upper left panel represents the vertical profile of the optical thickness per unit layer height for trace gas absorption, while the right panel shows the corresponding profile for Rayleigh scattering. The following 4 rows in each figure represent the aerosol profile on the left and the corresponding reflectance profiles on the right, for successive values of AOT. In each case, single-scattered reflectance increases with aerosol loading, plateauing towards a constant value at higher AOT's [3]. As seen in the previous section, the peak of single-scattering reflectance seems to coincide with the peak of aerosol concentration. At 687 and 761 nm, though, the absorption due to trace gases is strong enough to reach saturation, so that the only reflected light at all values of AOT arrives from the upper troposphere and the stratosphere, where the concentration of the strongly absorbing species, viz. O_2 is not significant.

Since the bulk of atmospheric scatterers responsible for the creation of diffuse radiation coincides with increased O_2 concentration, the diffuse component is almost negligible at wavelengths of strong absorption as is evident from Figures 2.17 and 2.19. When trace gas absorption is not strong, the multiple-scattering component of reflectance increases sharply from being negligible in the absence of aerosol to exceeding the single-scattering component around $AOT \approx 1.0$. This is evident from Figures 2.16 and 2.18 representing scenarios at 682 and 757 nm, both ly-

---

[3] While this is true for the majority of aerosols encountered in the atmosphere, it does not imply a general rule, since a highly absorbing aerosol can have the opposite effect.

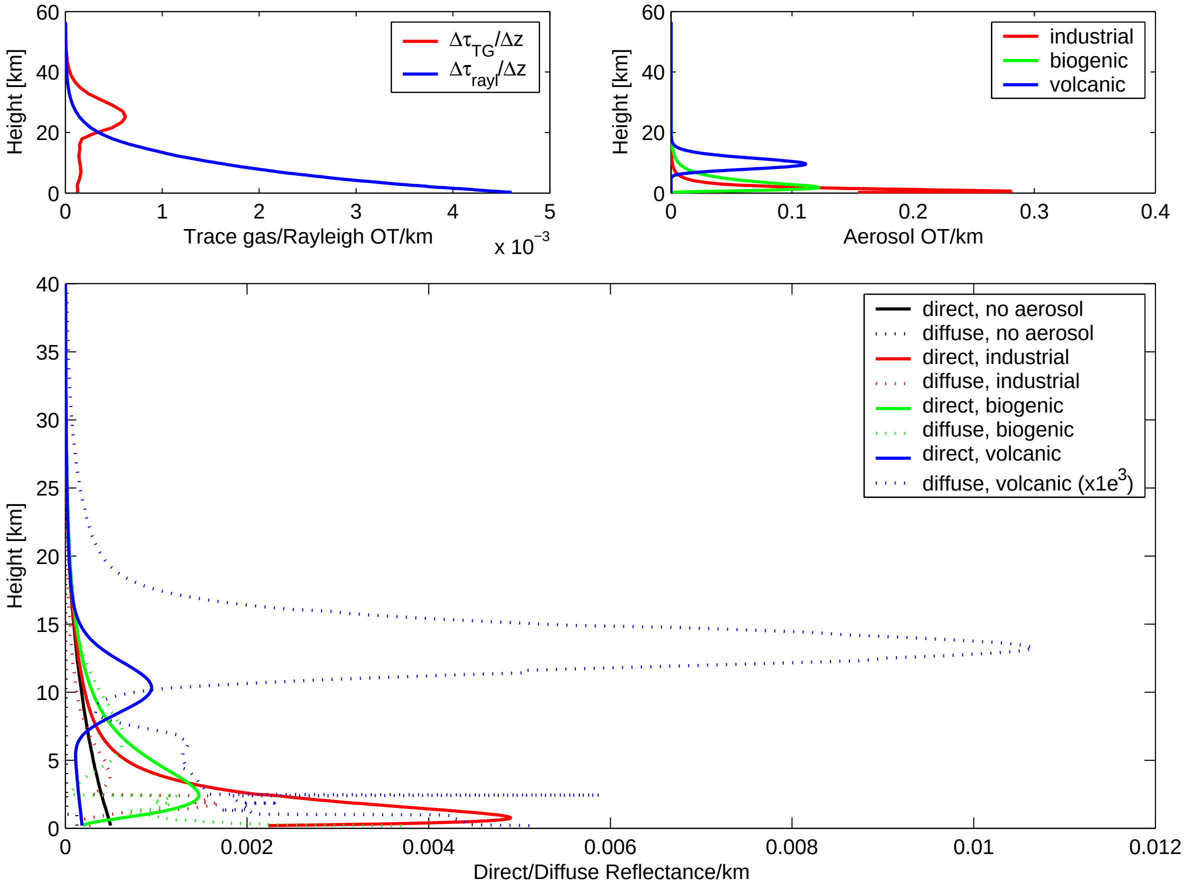

Figure 2.11: The top left panel shows vertical profiles for trace gas absorption and Rayleigh scattering per unit layer height. The top right panel shows vertical profiles of AOT/km for industrial, biogenic and volcanic aerosol, each of total $AOT = 0.5$. The bottom panel shows the corresponding reflectances/km, $\Delta_i^{ss}(I/I_0)$ and $\Delta_i^{ms}(I/I_0)$ at 682 nm for each of the aerosol types respectively.

ing outside of bands of strong absorption. The multiple-scattering reflectance subsides quickly with increasing absorption, as is evident from a comparison of Figures 2.16, 2.18 and 2.20. This is a direct result of the increased light path of diffuse radiation. The peaks of multiple-scattering reflectance occur at higher altitudes in response to increasing values of AOT. A peak occurs when both, the number of atmospheric scatterers and the amount of ambient diffuse radiation, reach a maximum, coupled with a minimum of extinction suffered along the intermediate atmospheric layers. As AOT increases, so does the number of scatterers and the amount of diffuse radiation. However, the extinction due to these scatterers increases as well, thereby forcing the reflectance peaks to higher altitudes. While most of the reflected light at low AOT originates from the single-scattering peak, it carries direct information on the vertical extent of the aerosol. As the AOT increases, however, two or more additional peaks of multiple-scattered reflectance emerge around the peak of single-scattered reflectance, thus increasingly blurring this information.

In Chapter 4, discussing senstitivity studies of our aerosol retrieval, we shall see how the aerosol

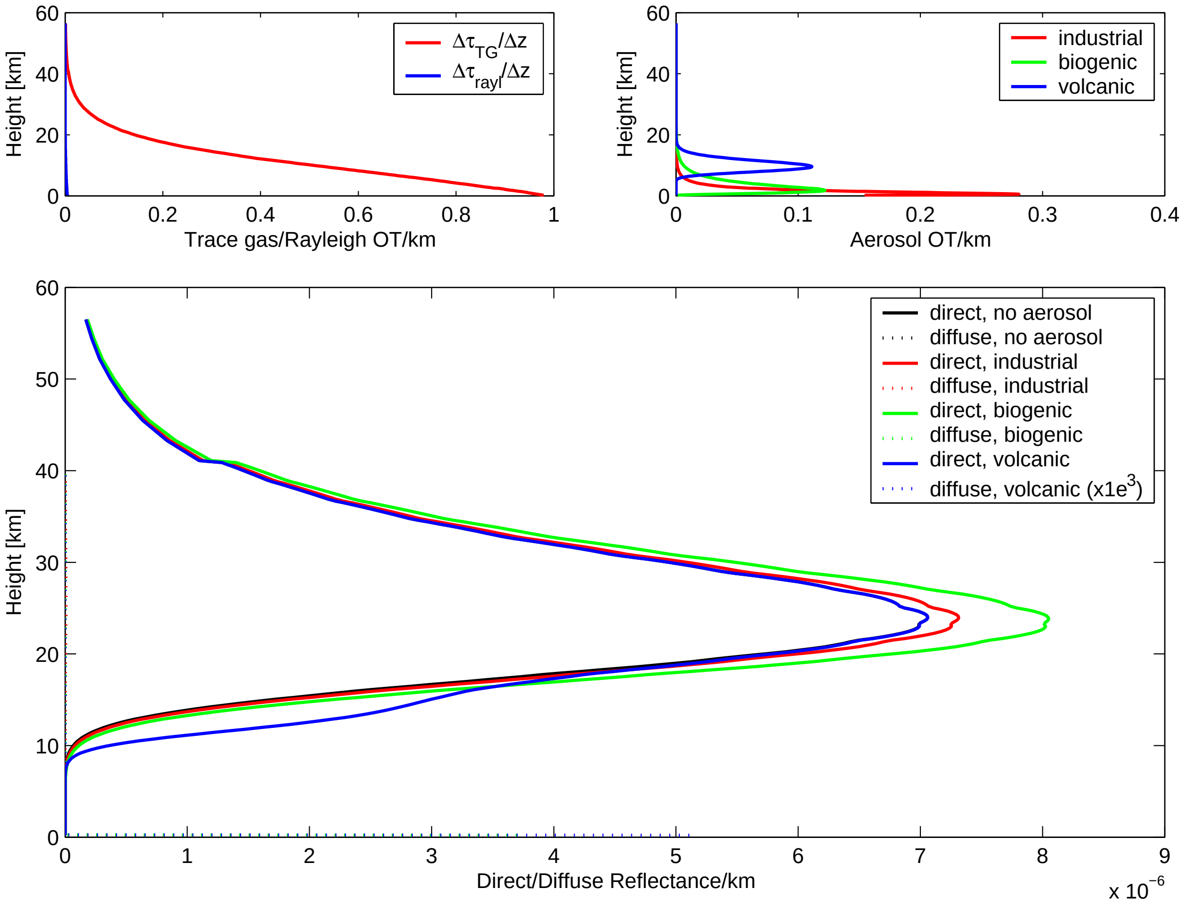

Figure 2.12: The top left panel shows vertical profiles for trace gas absorption and Rayleigh scattering per unit layer height. The top right panel shows vertical profiles of AOT/km for industrial, biogenic and volcanic aerosol, each of total $AOT = 0.5$. The bottom panel shows the corresponding reflectances/km, $\Delta_i^{ss}(I/I_0)$ and $\Delta_i^{ms}(I/I_0)$ at 687 nm for each of the aerosol types respectively.

loading and its vertical distribution influences the accuracy of the retrieval. In the following chapter, we first use our model to determine the surface albedo over a given ground pixel.

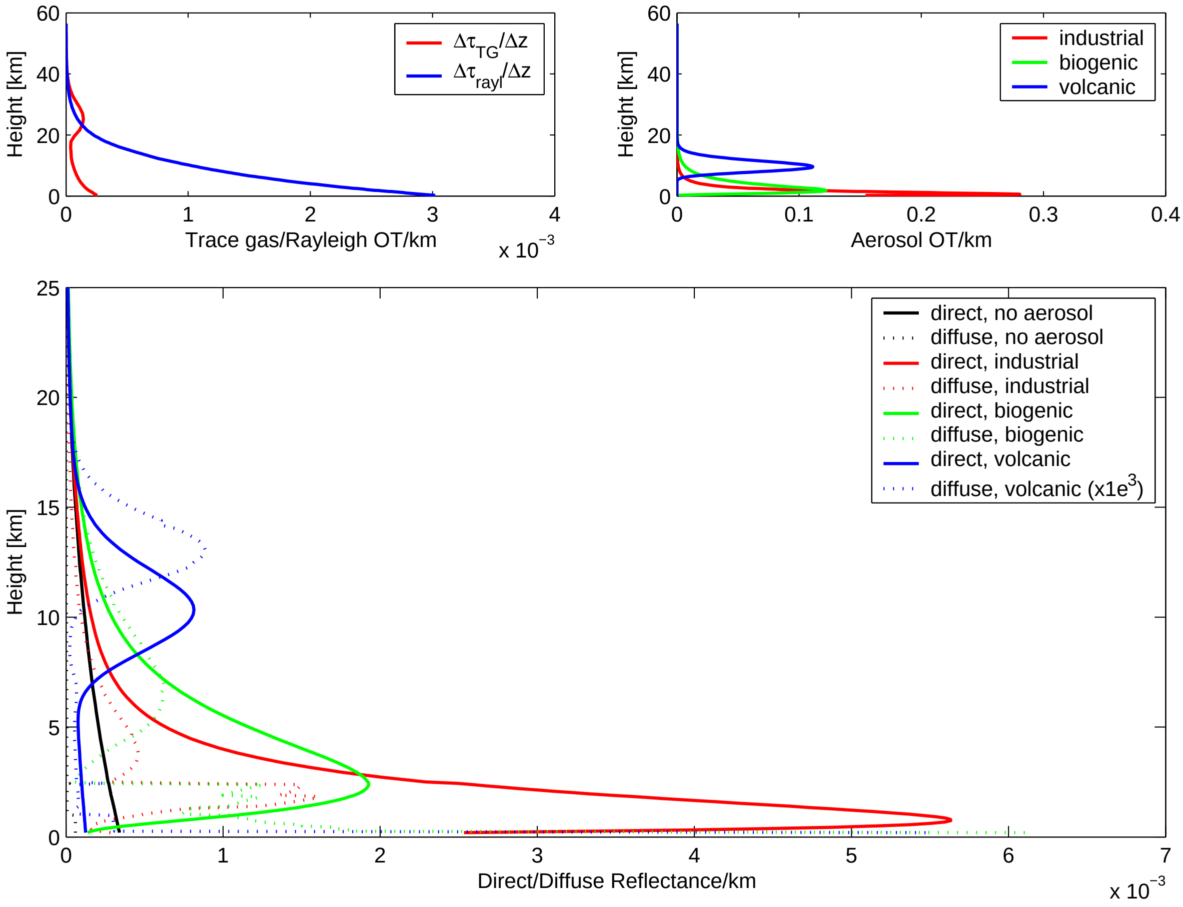

Figure 2.13: The top left panel shows vertical profiles for trace gas absorption and Rayleigh scattering per unit layer height. The top right panel shows vertical profiles of AOT/km for industrial, biogenic and volcanic aerosol, each of total $AOT = 0.5$. The bottom panel shows the corresponding reflectances/km, $\Delta_i^{ss}(I/I_0)$ and $\Delta_i^{ms}(I/I_0)$ at 757 nm for each of the aerosol types respectively.

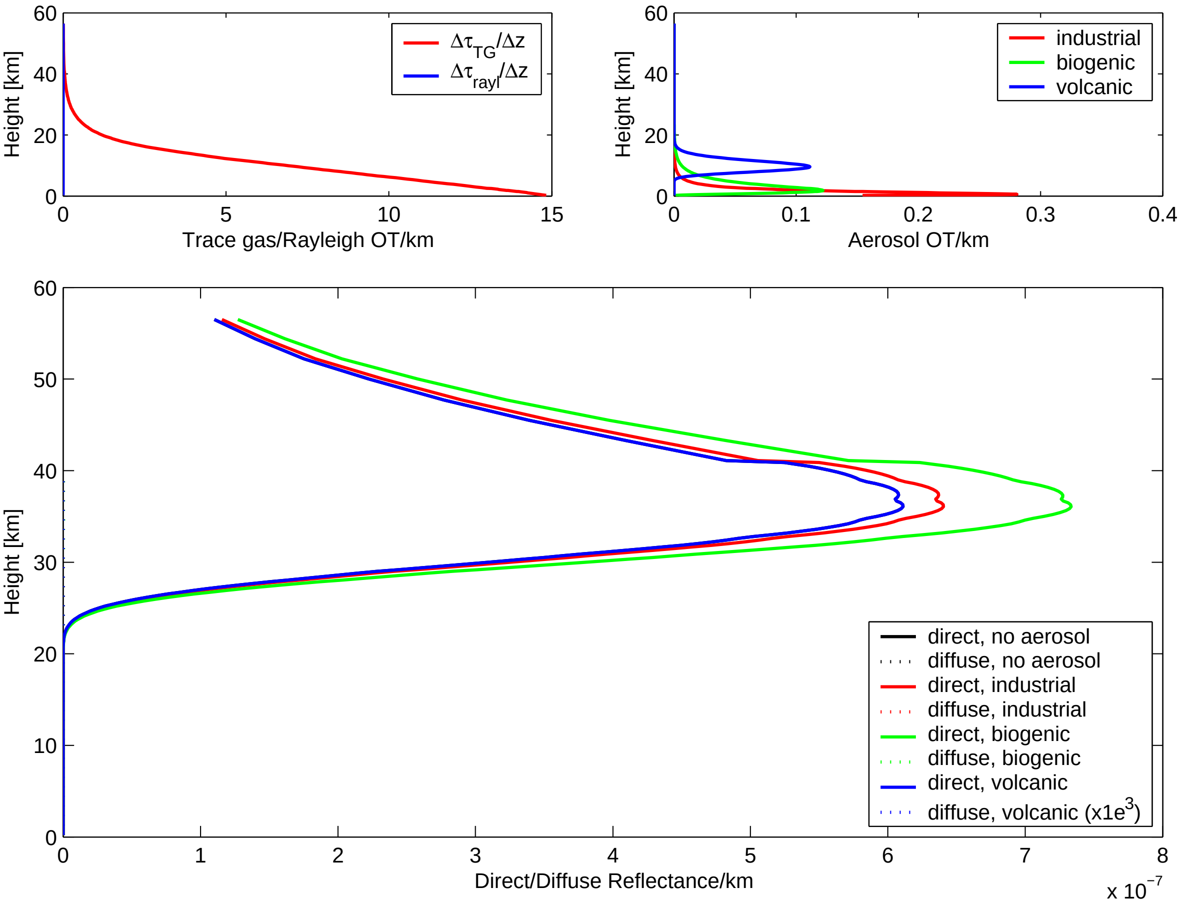

Figure 2.14: The top left panel shows vertical profiles for trace gas absorption and Rayleigh scattering per unit layer height. The top right panel shows vertical profiles of AOT/km for industrial, biogenic and volcanic aerosol, each of total $AOT = 0.5$. The bottom panel shows the corresponding reflectances/km, $\Delta_i^{ss}(I/I_0)$ and $\Delta_i^{ms}(I/I_0)$ at 761 nm for each of the aerosol types respectively.

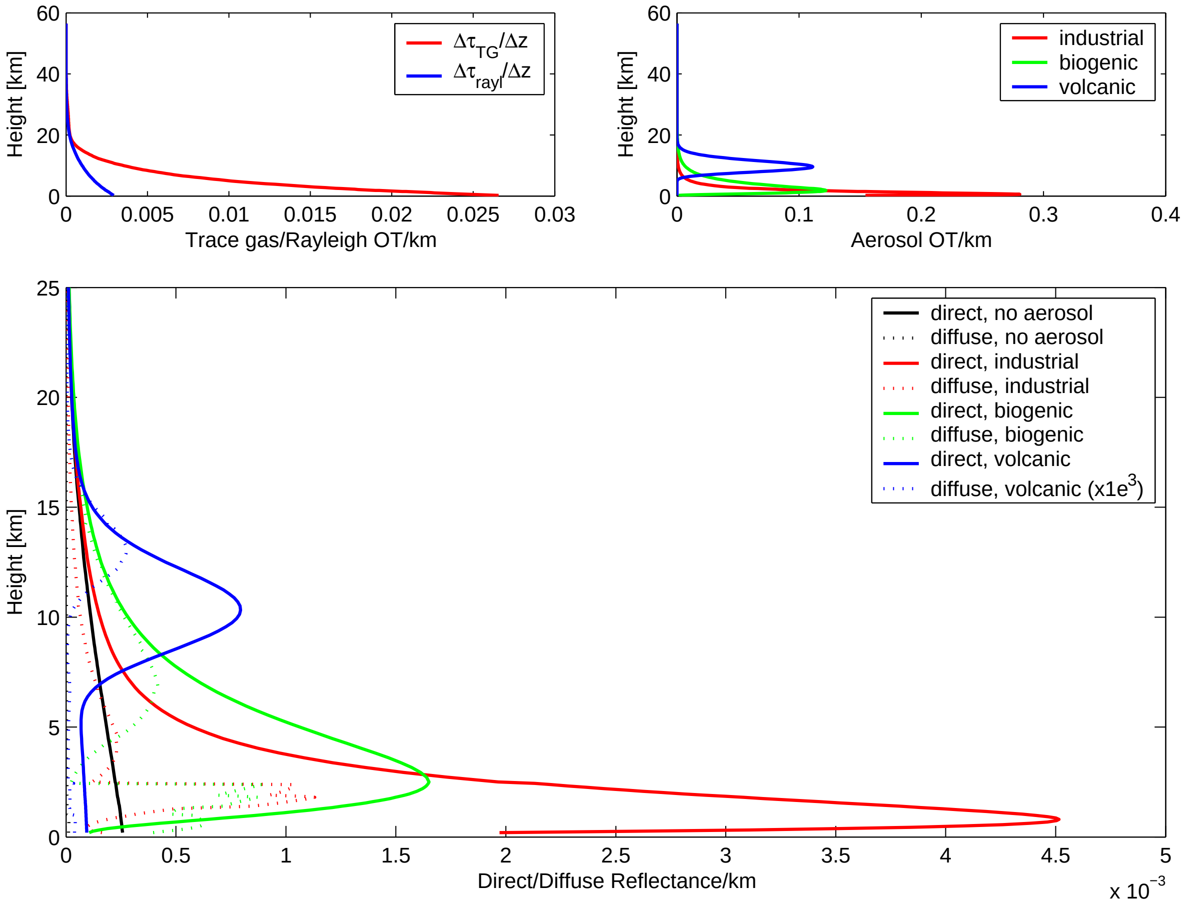

Figure 2.15: The top left panel shows vertical profiles for trace gas absorption and Rayleigh scattering per unit layer height. The top right panel shows vertical profiles of AOT/km for industrial, biogenic and volcanic aerosol, each of total $AOT = 0.5$. The bottom panel shows the corresponding reflectances/km, $\Delta_i^{ss}(I/I_0)$ and $\Delta_i^{ms}(I/I_0)$ at 763 nm for each of the aerosol types respectively.

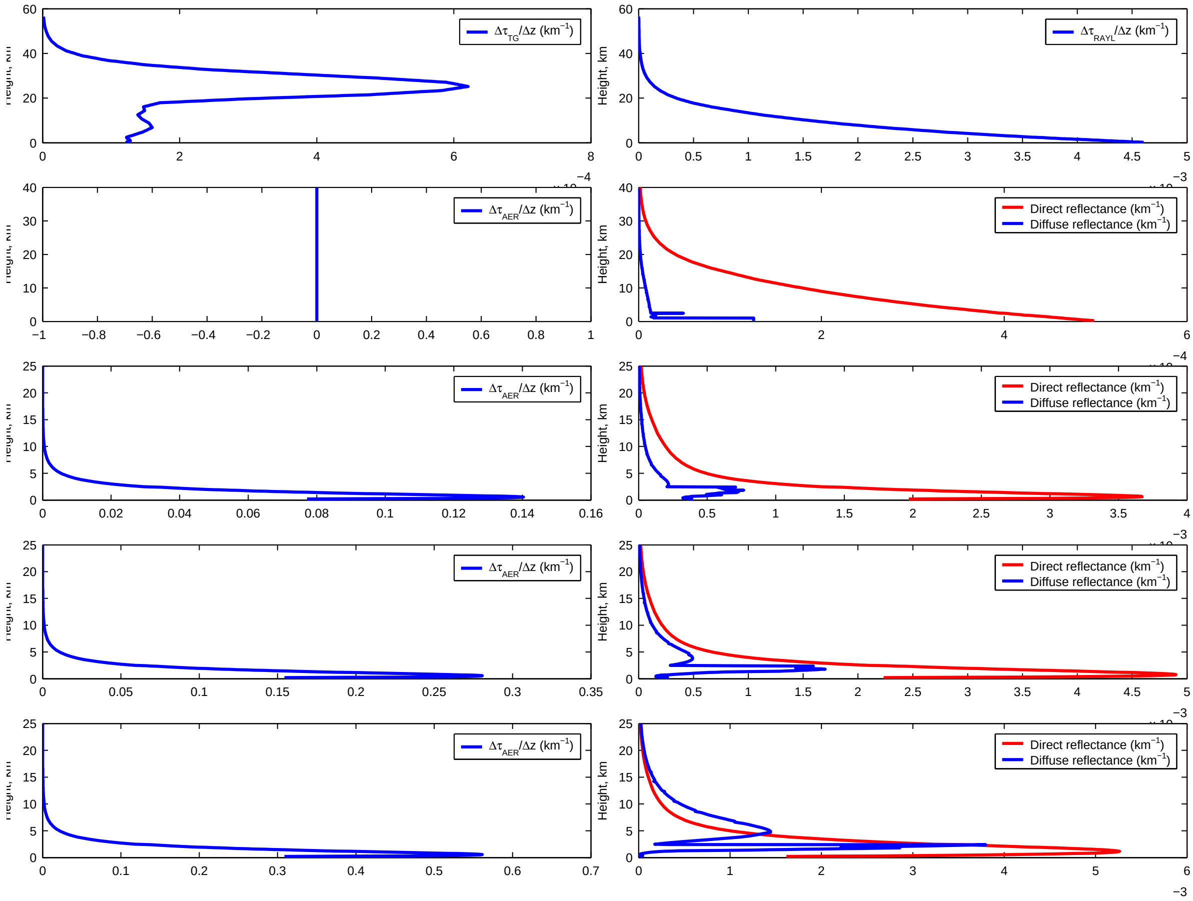

Figure 2.16: The top panels show vertical profiles for trace gas absorption and Rayleigh scattering per unit layer height. The following panels show vertical profiles of AOT/km on the left and the corresponding reflectances/km, $\Delta_i^{ss}(I/I_0)$ and $\Delta_i^{ms}(I/I_0)$ at 682 nm, on the right, for total AOT = 0, 0.25, 0.5 and 1.0 respectively.

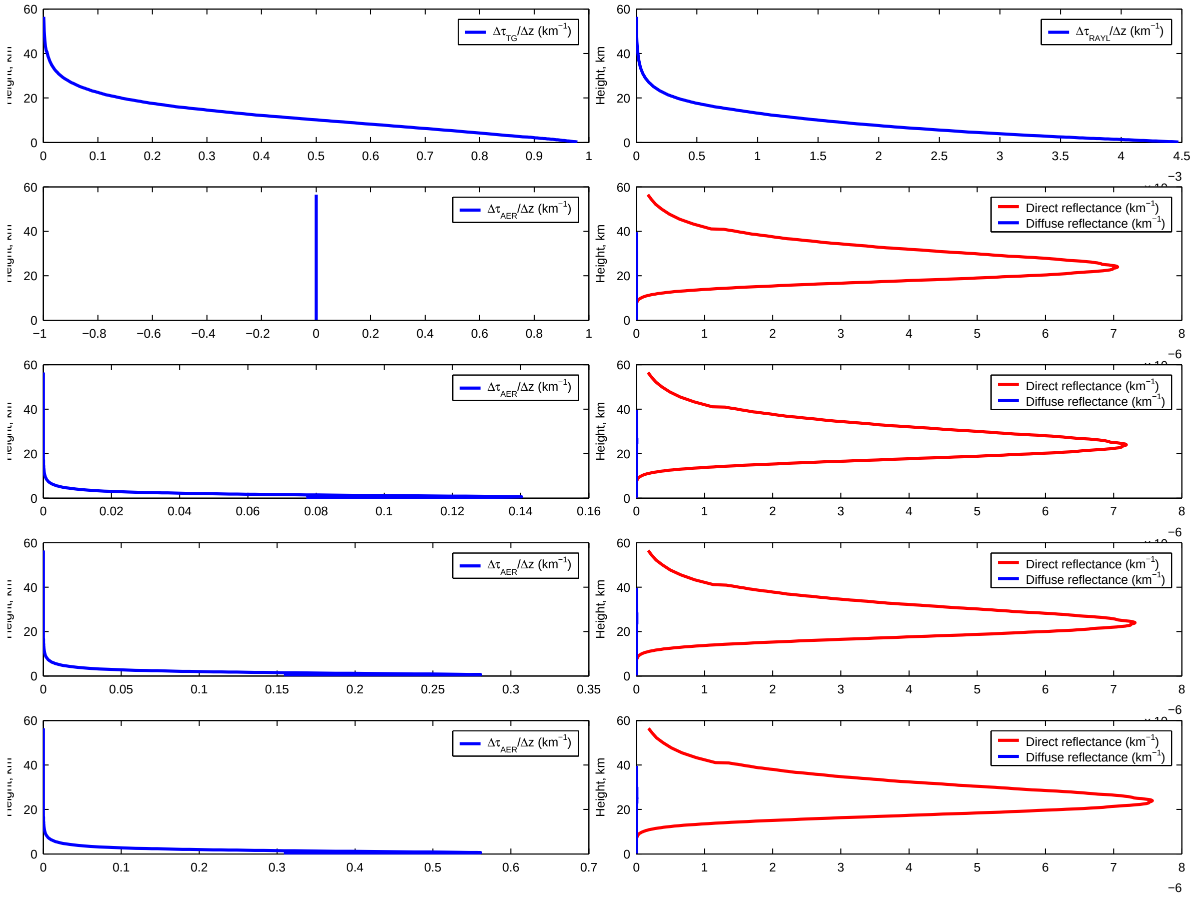

Figure 2.17: The top panels show vertical profiles for trace gas absorption and Rayleigh scattering per unit layer height. The following panels show vertical profiles of AOT/km on the left and the corresponding reflectances/km, $\Delta_i^{ss}(I/I_0)$ and $\Delta_i^{ms}(I/I_0)$ at 687 nm, on the right, for total AOT = 0, 0.25, 0.5 and 1.0 respectively.

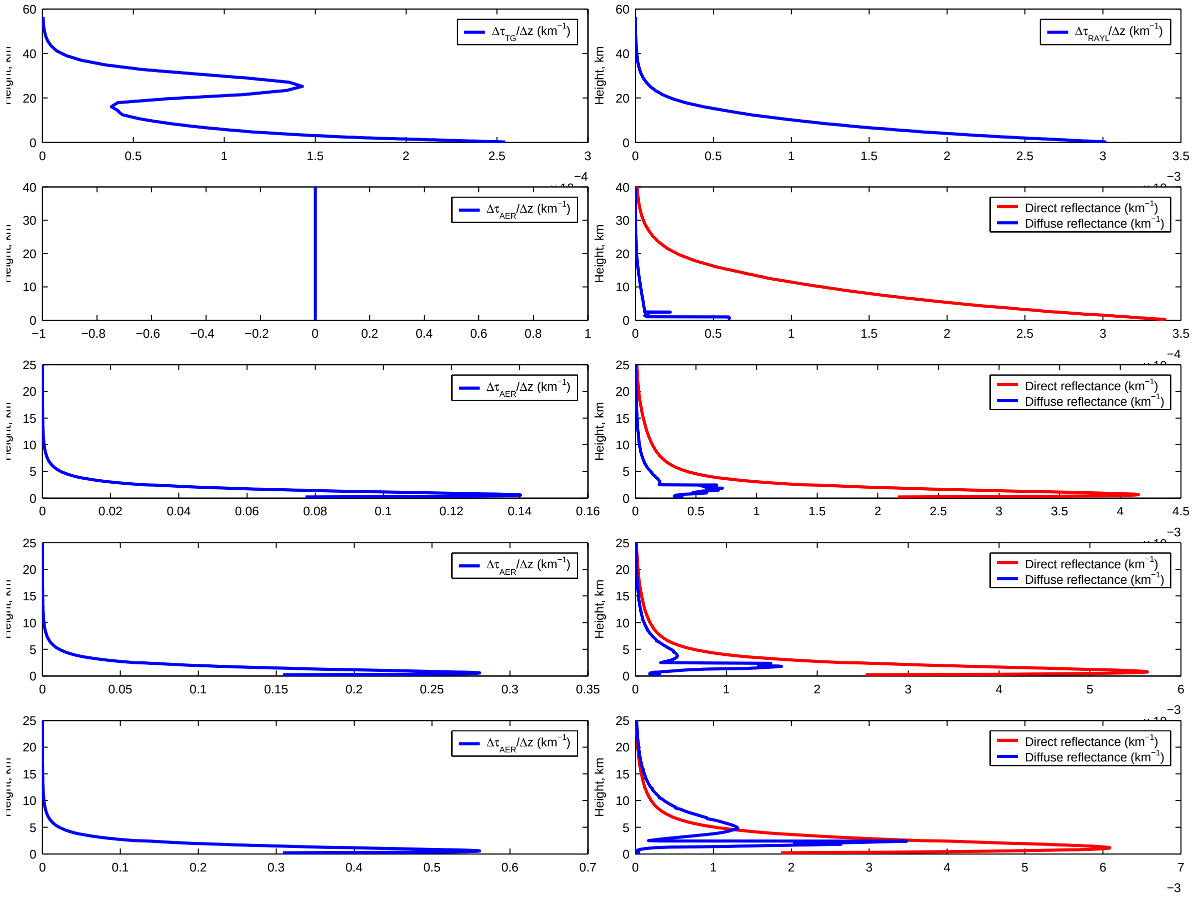

Figure 2.18: The top panels show vertical profiles for trace gas absorption and Rayleigh scattering per unit layer height. The following panels show vertical profiles of AOT/km on the left and the corresponding reflectances/km, $\Delta_i^{ss}(I/I_0)$ and $\Delta_i^{ms}(I/I_0)$ at 757 nm, on the right, for total AOT = 0, 0.25, 0.5 and 1.0 respectively.

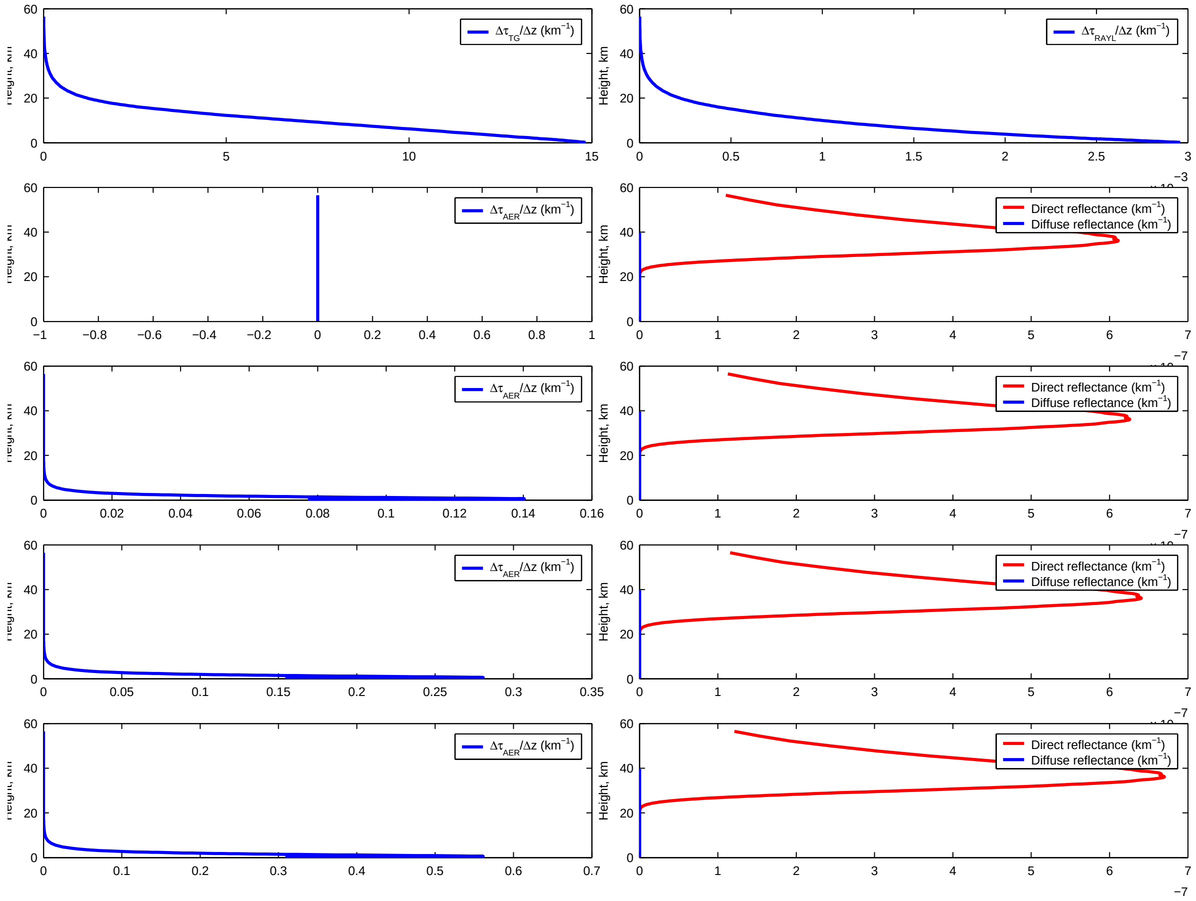

Figure 2.19: The top panels show vertical profiles for trace gas absorption and Rayleigh scattering per unit layer height. The following panels show vertical profiles of AOT/km on the left and the corresponding reflectances/km, $\Delta_i^{ss}(I/I_0)$ and $\Delta_i^{ms}(I/I_0)$ at 761 nm, on the right, for total AOT $= 0$, 0.25, 0.5 and 1.0 respectively.

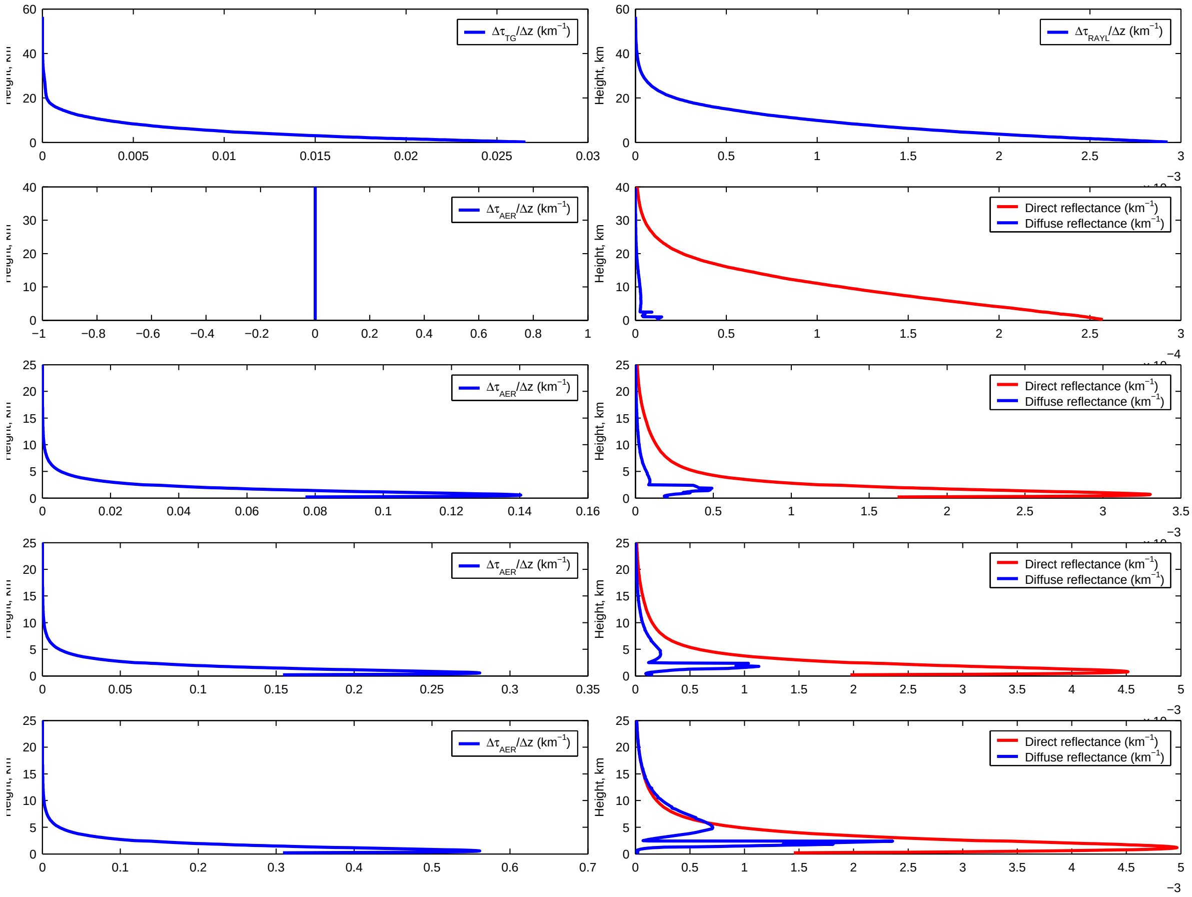

Figure 2.20: The top panels show vertical profiles for trace gas absorption and Rayleigh scattering per unit layer height. The following panels show vertical profiles of AOT/km on the left and the corresponding reflectances/km, $\Delta_i^{ss}(I/I_0)$ and $\Delta_i^{ms}(I/I_0)$ at 763 nm, on the right, for total AOT = 0, 0.25, 0.5 and 1.0 respectively.

Chapter 3

Determination of the lambertian albedo of a given ground pixel by time-series analysis

An accurate knowledge of surface reflectance is indispensable for the retrieval of aerosol properties over a given location. In this Chapter, we develop a method for the determination of the lambertian equivalent albedo given a clear sky scenario, followed by a criterion for the identification of a clear-sky using a two-wavelength approach. Work on the retrieval of surface properties has previously been done using GOME reflectances by *Koelemeijer et al.* (2003) using a minimum reflectance based method and using MERIS reflectances over Europe by *von Hoyningen-Huene et al.* (2003) using a Normalized Difference Vegetation Index (NDVI) based approach.

In a nadir viewing geometry, the reflectance measured by a satellite detector is made up of two single scattering components: an atmospheric component due to scattering by air molecules (Rayleigh scattering), aerosols and clouds, and a surface component, due to reflection at the Earth's surface, as well as an albedo-dependent multiple scattering component. In the absence of clouds and aerosols, the atmospheric single scattering component comprises only molecular (Rayleigh) scattering, which can be calculated to a high degree of accuracy in spectral windows where absorption due to trace gases is absent or accurately known. As a result, the surface component of the single scattering reflectance and the albedo dependent multiple scattering are the only unknowns given a clear-sky (as we shall henceforth refer to a scenario devoid of aerosol and clouds) measurement. If the bidirectional reflectance distribution function (BRDF) of the surface is not too irregular, we may approximate the surface to be lambertian, i.e. reflecting incident radiation with a uniform intensity in all directions. This assumption readily allows us to express the surface component in terms of the lambertian surface albedo, which is easily determinable using an iterative procedure described further in this chapter when the atmospheric variables are known.

Given the validity of the assumption of a lambertian surface, the main challenge is the determination of a clear-sky scenario. An average of nearly 75% of the earth is covered by clouds. In the absence of clouds, aerosols of varying optical thicknesses make up the more probable scenario. As a result, a large set of measurements may contain only few, if any, clear-sky measurements. Identifying a clear-sky measurement requires knowledge of the behavior of reflectance with respect to cloud-opacity and aerosol optical thickness. In the following, we examine the behaviour of reflectance with respect to different optical thicknesses of an absorbing and a scattering aerosol type at two different wavelengths for varying levels of surface albedo (brightness). It is found that a criterion for clear-sky determination is only possible in a few special cases, assuming complete knowledge of the aerosol and surface types involved. This prior knowledge is not available in practice. A general criterion cannot be developed due to non-uniform and frequently non-monotonic evolution of the reflectance with respect to aerosol loading for different aerosol and surface types for a given wavelength and viewing geometry.

We defer the development of a criterion for clear-sky identification, first developing a method for the determination of the lambertian equivalent albedo under the mere assumption of a clear sky scenario. We examine the effect of the presence of residual aerosol on the retrieved albedo, especially in terms of the differences in the expected (under a clear-sky assumption) and observed reflectances within lines of strong absorption such as the $\mathsf{O_2}$ A and B bands.

This discussion provides us with the background necessary to develop a two-wavelength (682 nm and 756 nm) criterion for clear-sky identification, which can be further validated by comparing the observed and expected reflectances around the $\mathsf{O_2}$ A and B bands. We apply this criterion to SCIAMACHY reflectances over three different locations in order to determine the surface albedo over the selected ground pixel. This surface albedo is used as an input parameter for the subsequent inversion of aerosol loadings over the given ground pixel.

3.1 Reflectances above a given ground pixel as measured by SCIAMACHY

SCIAMACHY measures backscattered radiation from the earth above a given pixel at a medium resolution of 0.2-1.5 nm over the spectral range of 240 nm to 1700 nm, and in selected regions between 2.0 µm and 2.4 µm, as can be seen in Fig. 3.1. While strong and weak absorbers produce absorption structures across much of this spectrum, there also exist spectral windows of weak or no absorption. These spectral windows are not significantly affected by variations in the concentrations of the absorbing trace gases. Moreover, incident solar radiation at these wavelengths is more likely to reach the surface without suffering strong extinction due to absorption. Hence, they are well-suited to reflectance measurements aimed at determining the ground albedo. Surface albedo, especially over land but also over water, varies slowly but non-linearly with wavelength, making it necessary to find spectral windows in the vicinity of the spectral region of interest. A typical reflectance spectrum between 200 and 1000 nm measured by SCIAMACHY is shown in Fig. 3.2. The different colours in the spectrum represent the so-called 'clusters' of detector pixels sharing a common instrumental slit function. Some of these clusters have a longer signal intergration time than the others, causing them to

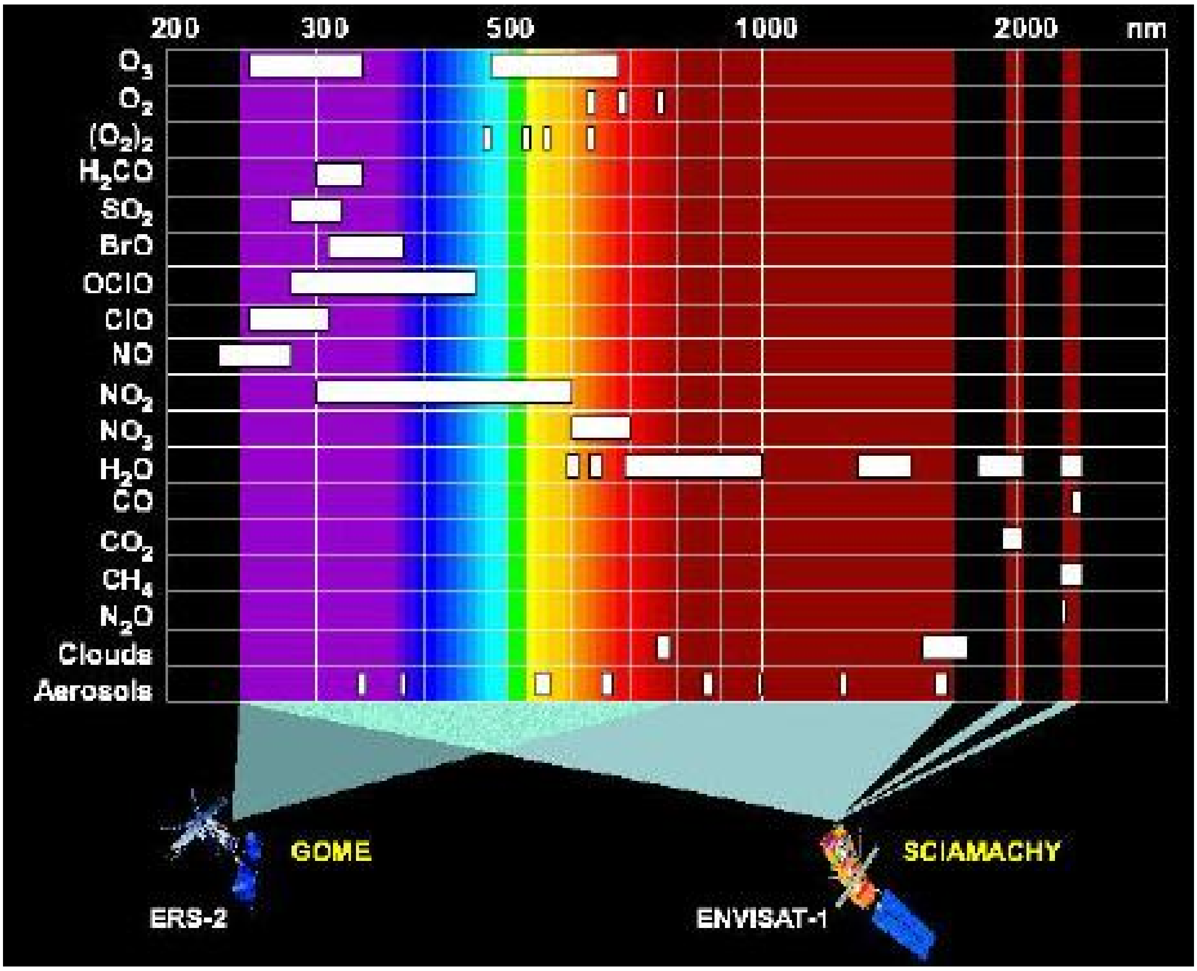

Figure 3.1: SCIAMACHY spectral range

cover more than the standard ground pixel during a scan. Since this does not exactly coincide with the ground pixel we wish to evaluate in a multispectral approach, we have to exclude measurements in such clusters.

The reflectance spectrum is marked by strong and weak absorption structures, notably the Herzberg continuum between 200 and 242 nm and the weak Herzberg bands in the range 242-260 nm, both associated with O_2 absorption, the three O_3 photo-dissociation continua, viz. the Hartley band, 200-310 nm, the Huggins band, 310-350 nm and the Chappuis band, 400-850 nm, the O_2 A- and B-bands around 690 and 760 nm respectively and a host of other weak absorption structures made by trace gases like NO_2, SO_2, OClO, ClO, BrO, HCHO, ClO, O_4, etc. Some parts of the spectrum, though, are devoid of any absorption structures and their forms are governed only by surface reflectance, molecular (Rayleigh) scattering and aerosol scattering, given a cloudfree atmosphere. 11 distinct spectral windows devoid of high frequency absorption structures can be easily identified, viz. 230-238 nm, 265-275 nm, 290-298 nm, 306-310 nm, 312-316 nm, 360-385 nm, 440-460 nm, 670-680 nm, 755-759 nm, 870-880 nm and 980-988 nm. Using the fact that only surface reflectance and molecular scattering contribute to these spectral windows under clear-sky conditions, the atmospheric component may be readily calculated,

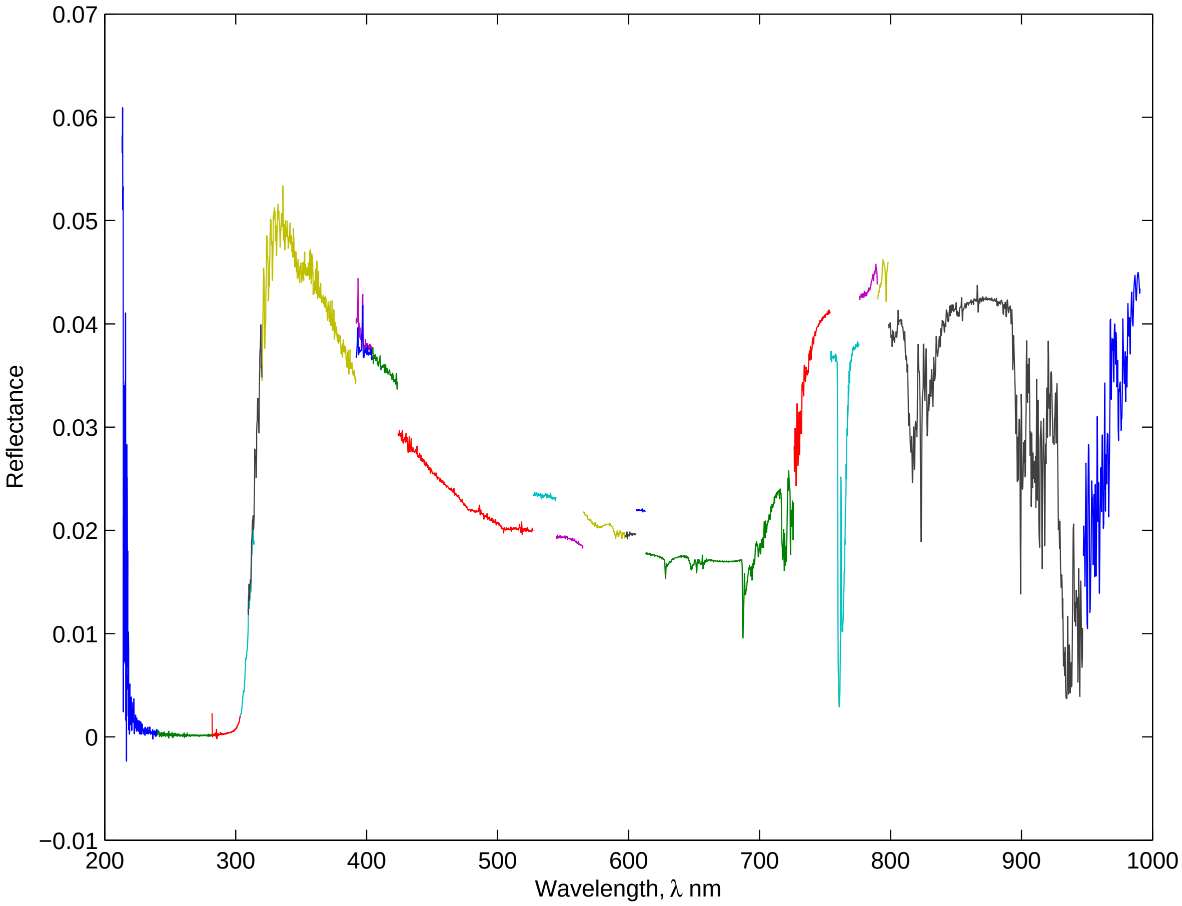

Figure 3.2: Reflectance between 200 and 1000 nm as measured by SCIAMACHY, different colours depict different 'clusters' of detector pixels, each having its own slit function. Some clusters show elevated reflectances due to higher integration times - they get longer exposure than the other clusters as the detector scans the ground, thus covering a larger ground pixel than the others. These clusters will be omitted in our studies, since they do not represent the same ground pixel measured by clusters having the standard integration time.

allowing us to deduce the lambertian equivalent albedo in the spectral neighbourhood of that window. We do not use all of those spectral ranges for the subsequent aerosol retrieval, hence, we shall focus on the determination of ground albedos in the spectral vicinity of the O_2 absorption bands, viz. 670-680 nm and 755-759 nm. Both these windows cover the standard ground pixel, i.e. they do not have the prolonged integration times that produce the discontinuous jumps in the reflectance spectrum. Nonetheless, the spectra still have to be corrected radiometrically, since SCIAMACHY systematically underestimates reflectances by about 20% (*Acarreta and Stammes*, 2005; *Noel*, 2005).

Figures 3.4, 3.5 and 3.6 respectively show a series of reflectances around the O_2 A- and B-bands measured by SCIAMACHY over Kanpur (26° N,80° E), La Parguera (17° N,67° W) and Mexico City (19° N,99° W) through the year 2003. Predominantly due to their tropical location, the surface albedos of these pixels do not display much seasonality, e.g. large-scale changes in vegetation or snow cover, as a result of which their reflectances are well suited for albedo

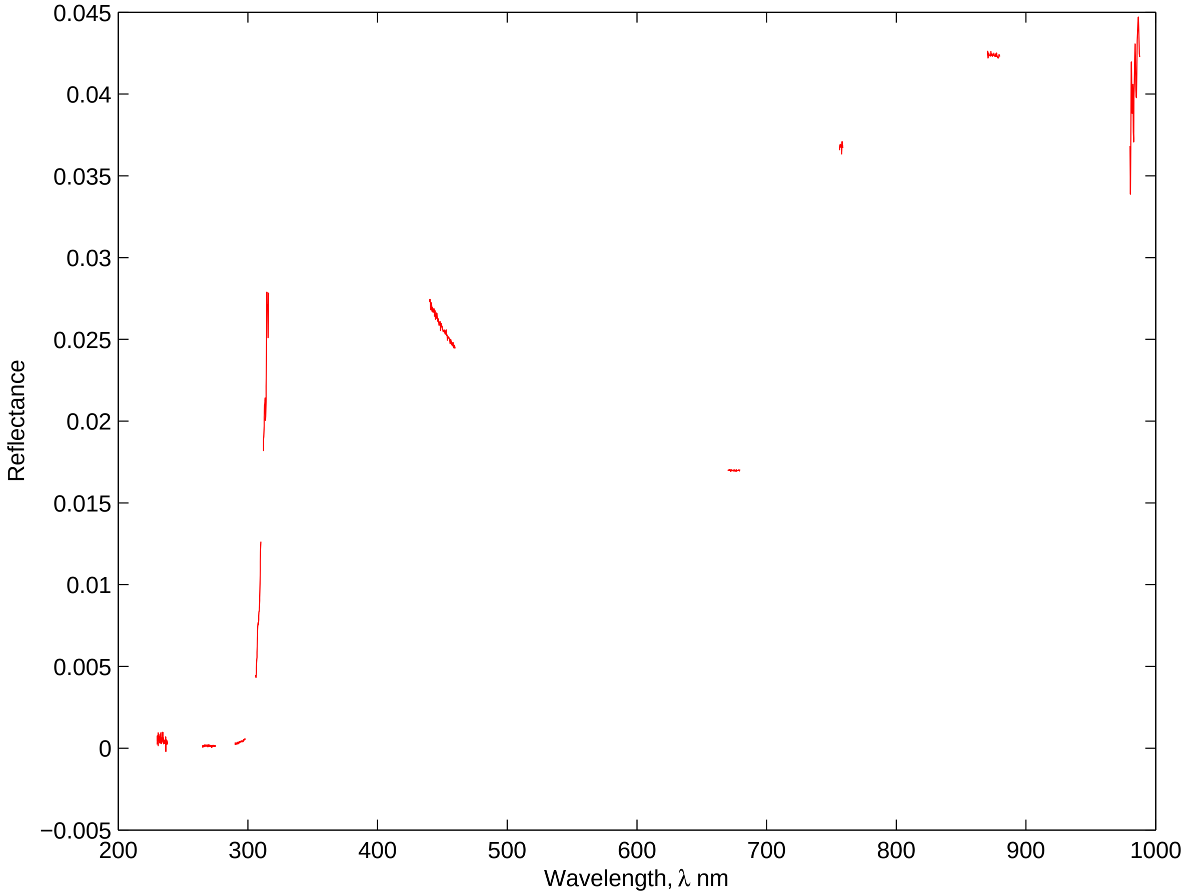

Figure 3.3: Reflectance as measured by SCIAMACHY within the spectral windows chosen to avoid high frequency absorption structures.

determination throughout the year. Furthermore, the tropical location of these pixels increases the probability of cloudless scenarios, providing a larger number of measurements that can potentially qualify as clear-sky scenarios. While Kanpur and Mexico City are expected to have urban industrial aerosol loadings, La Parguera is more likely to have maritime aerosol.

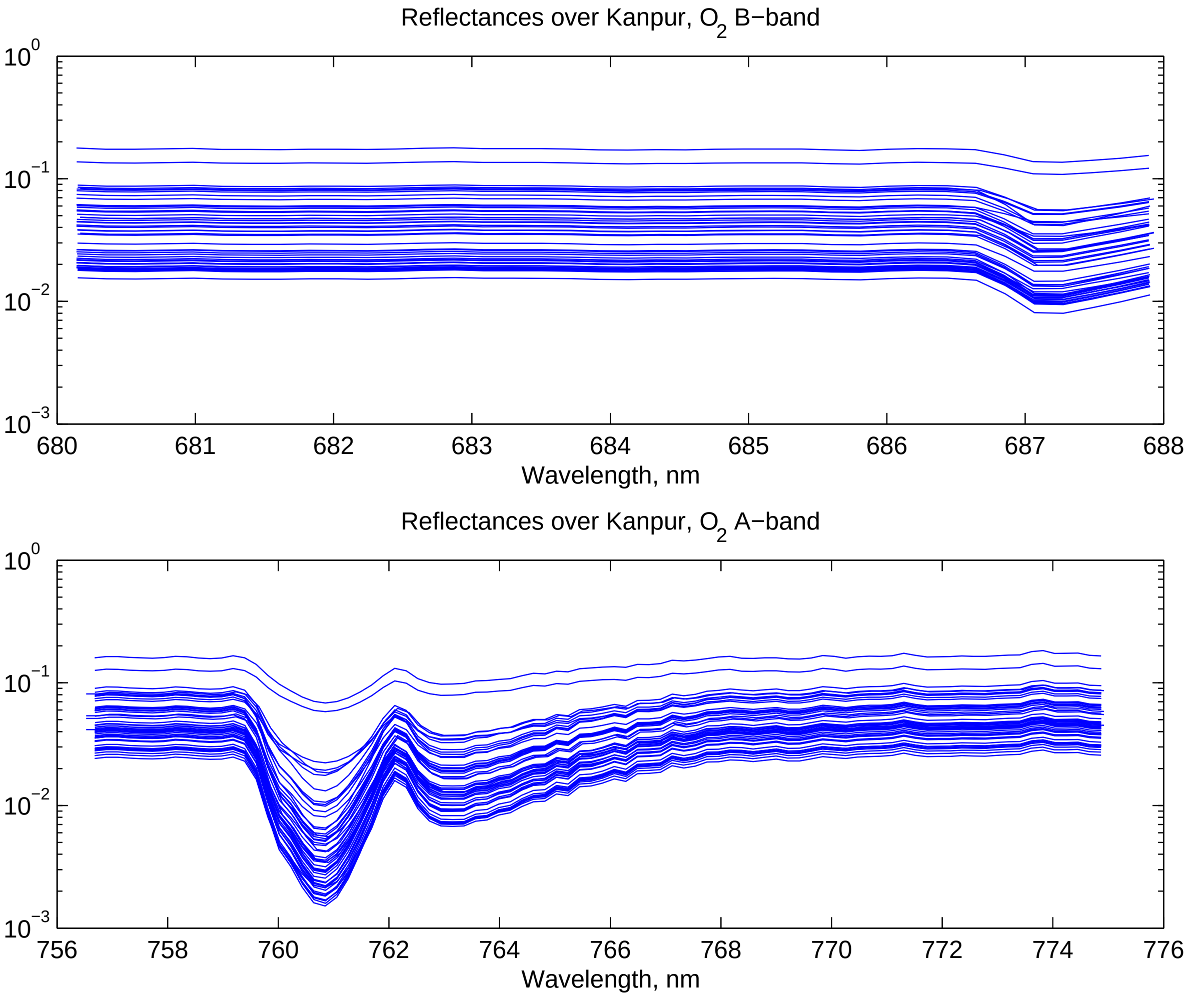

Figure 3.4: Reflectances measured by SCIAMACHY throughout 2003 over Kanpur, India (26° N, 80° E)

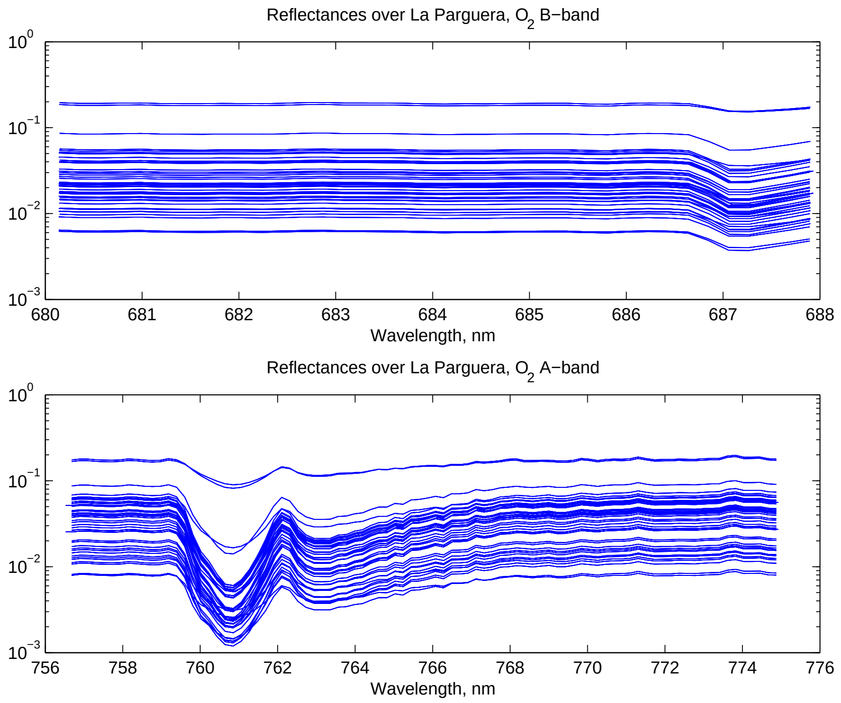

Figure 3.5: Reflectances measured by SCIAMACHY throughout 2003 over La Parguera, Puerto Rico, USA (17° N, 67° W)

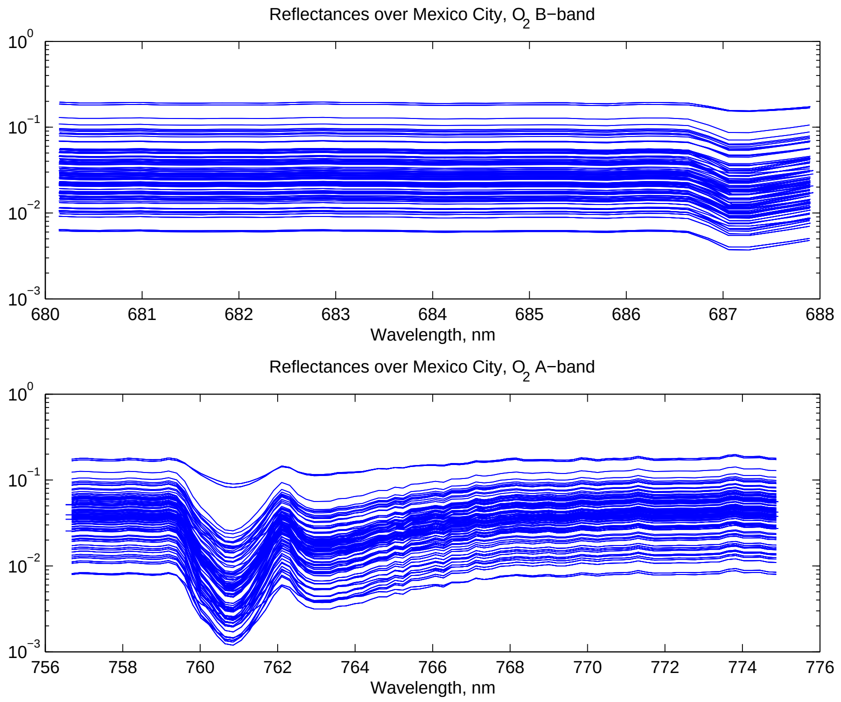

Figure 3.6: Reflectances measured by SCIAMACHY throughout 2003 over Mexico City, Mexico (19° N, 99° W)

3.2 Uncertainties associated with the identification of a clear-sky scenario

In order to identify a clear-sky day, we need to eliminate cloudy and hazy (due to aerosols) scenarios from the aforementioned measurement data sets. Clouds which cover most of the ground pixel possess three properties that make them easily recognizable:

1. They produce significantly higher reflectances as cloud ”plane” albedos approach unity (the corresponding lambertian albedo approaches its maximum value of $1/\pi$),
2. The reflectance spectrum loses its spectral gradient since clouds are white, i.e. they reflect uniformly at all wavelengths,
3. Thick clouds also effectively cut off lower layers of the atmosphere, leading to less absorption within the O_2 A and B-bands, making them conspicuously flatter.

While the above criteria may be used to screen out clouds, the effects of aerosols are less straightforward, producing either an increase or a decrease or both in reflectance with increasing optical thickness, depending on the aerosol type and more significantly, on the underlying surface albedo. This effect of aerosols varies with wavelength, and is made more complex due to the simultaneous variations in the surface albedo spectrum. Also, the information supplied by the depth of the absorption bands is ambiguous: aerosols may shorten the average light path by increased scattering above the ground, but also make it longer due to increased multiple scattering. In addition to the aerosol optical thickness, the average length of the light path is closely interlinked with the height of the aerosol and the underlying surface albedo, and knowledge of one factor alone generally does not suffice to predict the depth of the absorption band.

Fig. 3.7 and 3.10 show the change in single scattering, multiple scattering and total reflectances with increasing aerosol optical thickness at two different wavelengths for varying lambertian surface albedos, given a nadir-viewing geometry with the sun at zenith. The wavelengths 682nm and 756nm are chosen to be free of molecular absorption and to be in the vicinity of the O_2 B and A-bands respectively. The surface albedos increase in each case from 0 in the top panel through 0.03 in the second panel and 0.06 in the third panel to 0.09 in the bottom panel. Fig. 3.7 represents the clean industrial aerosol IS1, which is predominantly fine-grained and non-absorbing, typical of mainly SO_2 emissions and clean combustion processes. Due to its smaller size and high SO_2 content, it is a strongly scattering aerosol with a low positive asymmetry factor[1]. Due to its negligible soot content, this aerosol type has a single scattering albedo close to unity. Fig. 3.10 represents the polluted industrial aerosol IA2, having medium-sized particles and a soot content typical of incomplete combustion. While this aerosol also

---

[1] The asymmetry parameter, g, is a measure of the preferred scattering direction (forward or backward) for the light encountering the aerosol particles. The asymmetry factor approaches $+1$ for scattering strongly peaked in the forward direction and -1 for scattering strongly peaked in the backward direction. In general, $g = 0$ indicates scattering directions evenly distributed between forward and backward directions, i.e isotropic scattering (e.g scattering from air molecules.)

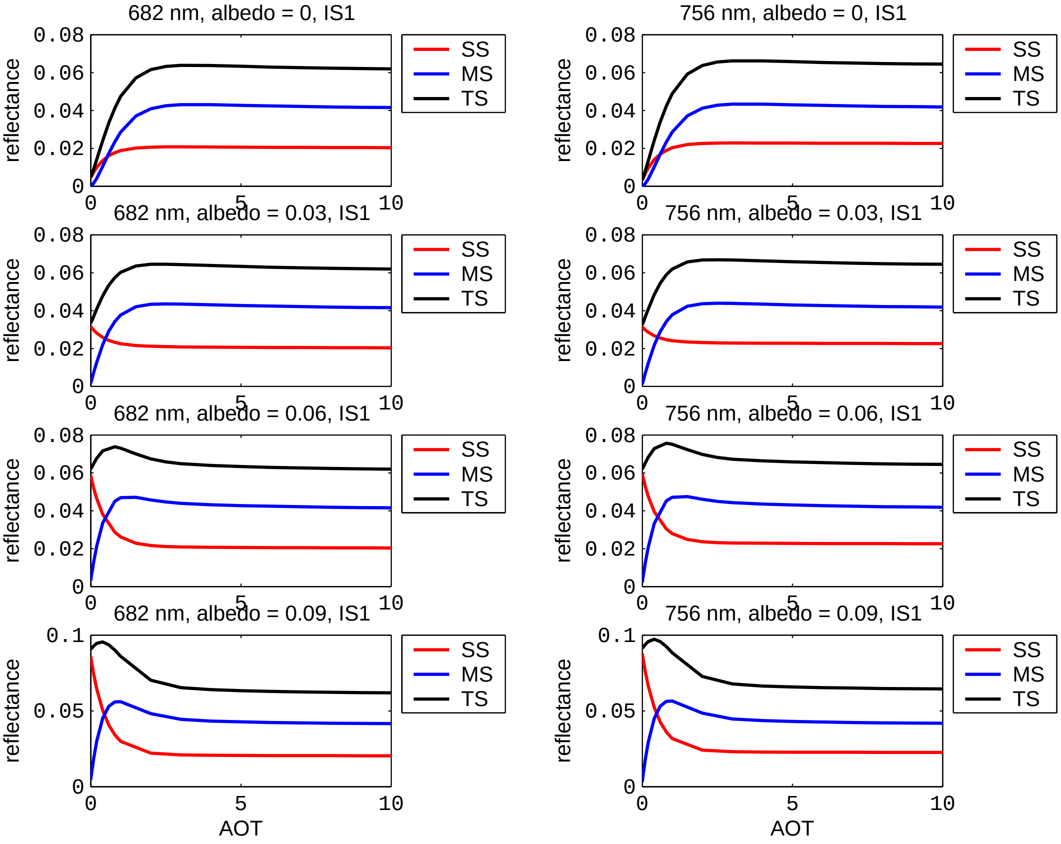

Figure 3.7: Modeled single scattering (SS), multiple scattering (MS) and total (TS) reflectances seen by a nadir-pointing satellite detector at $SZA = 0°$ over lambertian surfaces of different albedos for increasing aerosol optical thickness. The aerosol type used here is IS1 (fine sized scattering industrial). The left panels show reflectances at a non-absorbing wavelength (682nm) near the O_2 B-band and the right panels show reflectances at a non-absorbing wavelength (756nm) near the O_2 A-band

has a relatively high SO_2 content, it is contaminated with soot and other non-hygroscopic substances. A considerably high SO_2 content and the medium size of the particles cause it to have a greater positive asymmetry parameter than the IS1 type but not approaching unity. Due to its soot content, this aerosol type has a low single scattering albedo (≈ 0.7). Consequently, maximum reflectance is reached sooner by the IA2 aerosol type than by IS1 and maximum reflectance is consistently lower by about 30% for IA2 than for IS1 aerosol, as can be seen on comparison of Fig. 3.7 and 3.10.

From both Fig. 3.7 and 3.10, we can see that single scattering reflectance (shown by the red curve) exhibits a slight increase with respect to AOT in the case of a black surface (albedo=0) before reaching a plateau towards its asymptotic maximum. However, as the surface reflectance becomes stronger than scattering due to aerosol, this characteristic rapidly subsides with increasing albedo at both wavelengths. The single scattering reflectance curve eventually falls with increasing AOT, as can be seen for albedo=0.03. As the surface albedo increases, this fall becomes more pronounced, as seen in the case of albedo values of 0.06 and 0.09. In each of these cases, with increasing AOT the single scattering reflectance asymptotically approaches

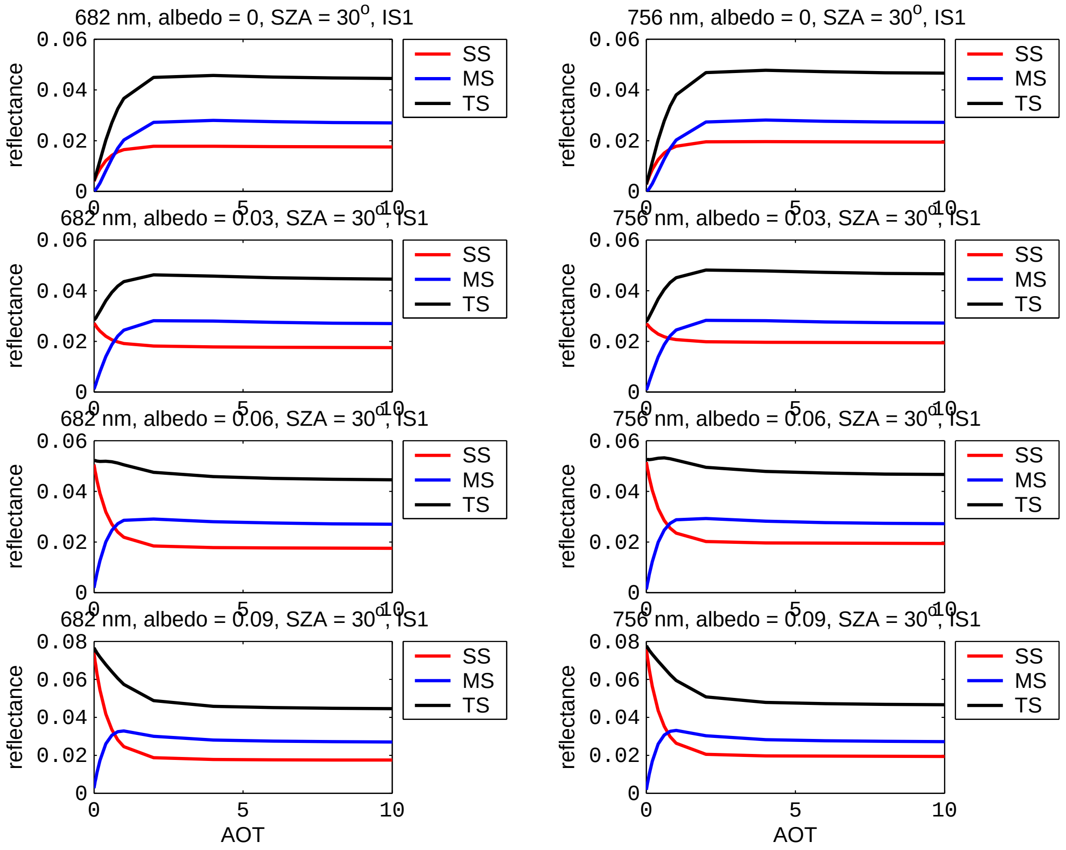

Figure 3.8: Modeled single scattering (SS), multiple scattering (MS) and total (TS) reflectances seen by a nadir-pointing satellite detector at $SZA = 30°$ over lambertian surfaces of different albedos for increasing aerosol optical thickness. The aerosol type used here is IS1 (fine sized scattering industrial). The left panels show reflectances at a non-absorbing wavelength (682nm) near the O_2 B-band and the right panels show reflectances at a non-absorbing wavelength (756nm) near the O_2 A-band

a minimum value.

Multiple scattering (represented by the blue curve), on the other hand, is always negligible at 682 and 756 nm in the absence of aerosol, rising rapidly with increasing AOT before reaching a peak around AOT=$1-3$. For dark surfaces, the multiple scattering reflectance attains a plateau near its peak value at high AOT. For brighter surfaces, however, the peak in reflectance becomes increasingly marked as the reflectance falls from its peak value before reaching a plateau at an intermediate level.

As a result, the total reflectance (shown by the black curve) varies in behavior for different surface albedos. For both aerosol types, we see a sharp initial increase in the total reflectance with increasing AOT at albedo=0 after which the reflectance becomes nearly constant. In the case of a surface albedo of 0.03 for both aerosol types and in case of a surface albedo of 0.06 for the scattering aerosol IS1, the initial jump in total reflectance is less sharp and the reflectance falls slightly from its peak value towards an intermediate plateau. For each instance, though, the minimum reflectance corresponds to the aerosol-free scenario, providing

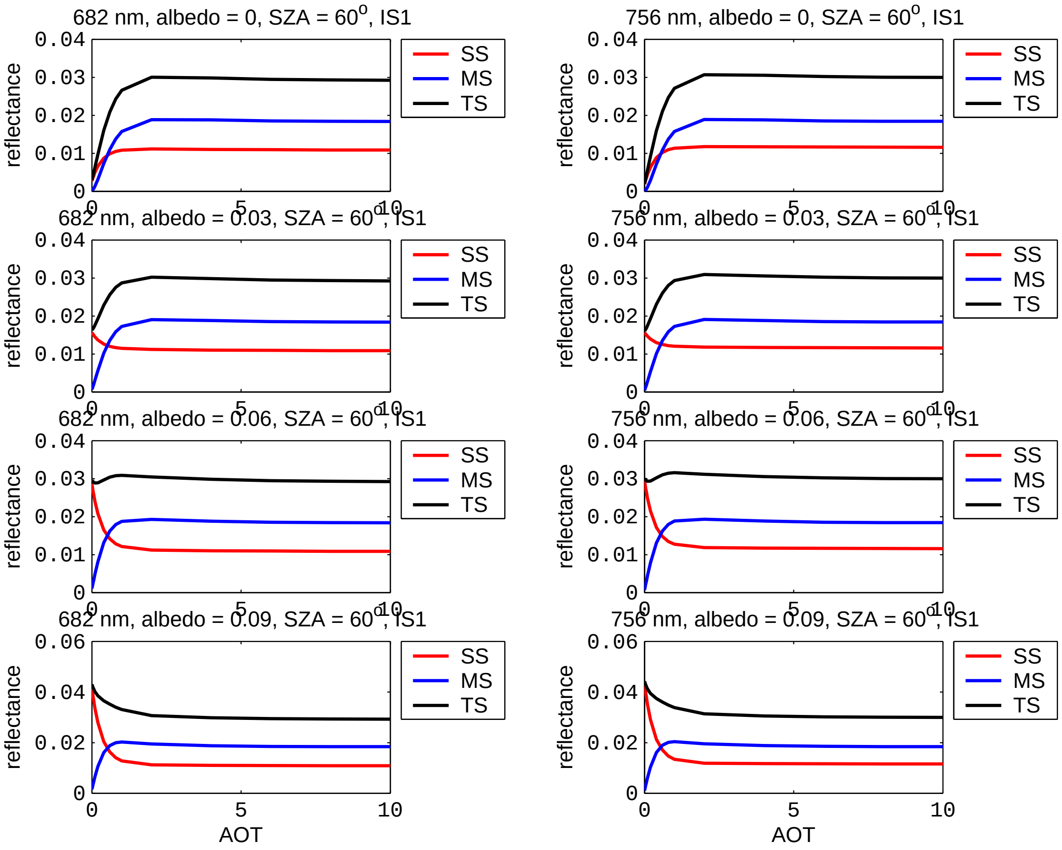

Figure 3.9: Modeled single scattering (SS), multiple scattering (MS) and total (TS) reflectances seen by a nadir-pointing satellite detector at $SZA = 60°$ over lambertian surfaces of different albedos for increasing aerosol optical thickness. The aerosol type used here is IS1 (fine sized scattering industrial). The left panels show reflectances at a non-absorbing wavelength (682nm) near the O_2 B-band and the right panels show reflectances at a non-absorbing wavelength (756nm) near the O_2 A-band

a clear-cut criterion for clear-sky determination.

For higher surface albedo, however, this criterion fails as the total reflectance falls with increasing AOT to a value lower than in the absence of aerosol. For the absorbing aerosol IA2 at albedo 0.06 and for the scattering aerosol IS1 at albedo 0.09, we observe that the total reflectance initially increases with AOT and eventually falls to a value lower than for the clear-sky scenario. This makes it impossible to map a given reflectance uniquely to AOT=0, even if the aerosol type were to be precisely known. This situation may be alleviated by use of other spectral windows where the albedo may be expected to be lower or, in principle, by analyzing the depth and structure of strong absorption bands.

The criterion for clear-sky determination is reversed in the case of high albedo and an absorbing aerosol as can be seen for aerosol type IA2 at albedo=0.09, where the total reflectance is maximum in the absence of aerosol, decreasing with increasing AOT until it plateaus at a minimum level.

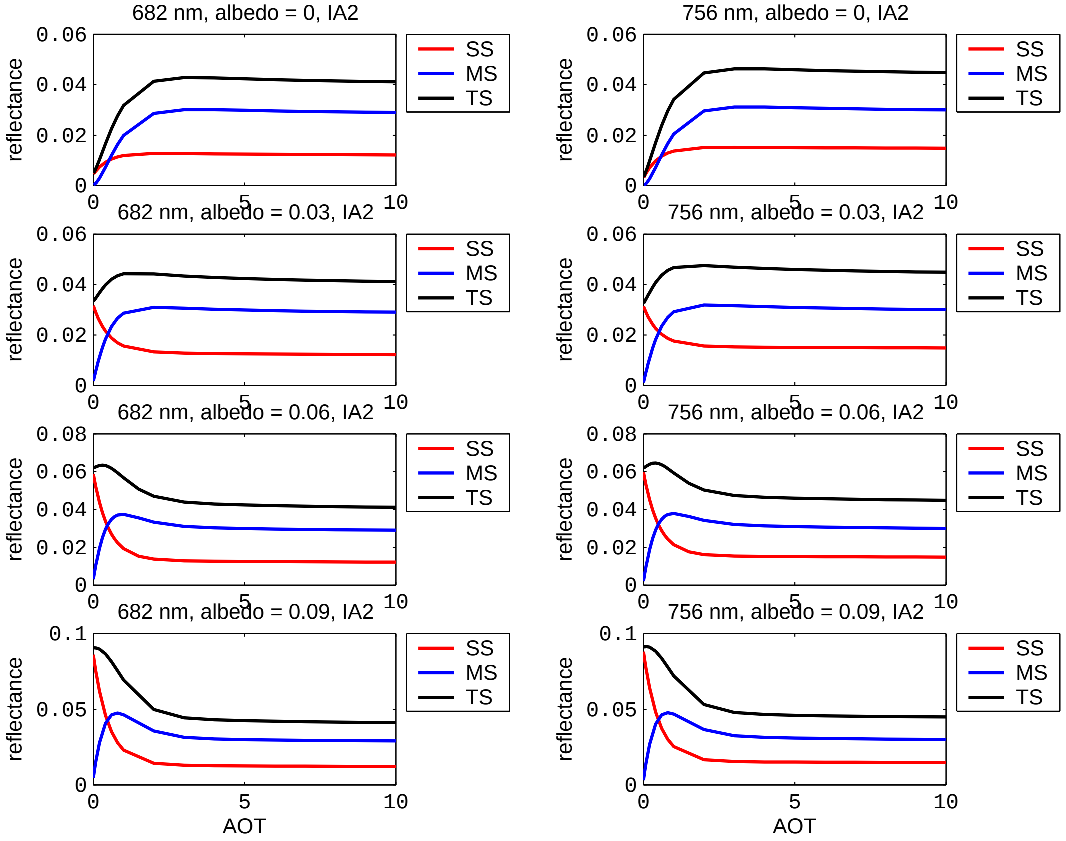

Figure 3.10: Modeled single scattering (SS), multiple scattering (MS) and total (TS) reflectances seen by a nadir-pointing satellite detector at $SZA = 0°$ over lambertian surfaces of different albedos for increasing aerosol optical thickness. The aerosol type used here is IA2 (medium sized absorbing industrial). The left panels show reflectances at a non-absorbing wavelength (682nm) near the O_2 B-band and the right panels show reflectances at a non-absorbing wavelength (756nm) near the O_2 A-band

A close examination of Fig. 3.7 and 3.10 also shows that for a given dark surface albedo, larger wavelengths offer more contrast to the clear-sky scenario with respect to aerosol-laden scenarios due to a sharper increase in reflectance with increasing aerosol optical thickness and higher asymptotic limits. At higher wavelengths, the relative size of the aerosol (also expressed as size parameter $x = 2\pi r/\lambda$) decreases, corresponding, in general, to an increase in single scattering albedo and a shift of the phase function towards more isotropic scattering.

Due to the strongly non-isotropic nature of scattering due to aerosol, the viewing geometry also plays an important role with regard to the reflectance registered by the detector. Assuming a nadir-pointing detector, we compare reflectances due to both aerosol types at different solar zenith angles (SZA). Figures 3.7, 3.8 and 3.9 show reflectances due to the IS1 type aerosol at SZA's of 0°, 30° and 60° respectively. Figures 3.10, 3.11 and 3.12 show the corresponding reflectances due to the IA2 type aerosol. Comparison of the different geometries reveal that reflectances drop and reflectance peaks become less marked or disappear as the SZA increases. This is a direct consequence of two factors: first, the strongly forward and backward-peaked nature of aerosol phase functions and second, the increase in light path for a slant incidence

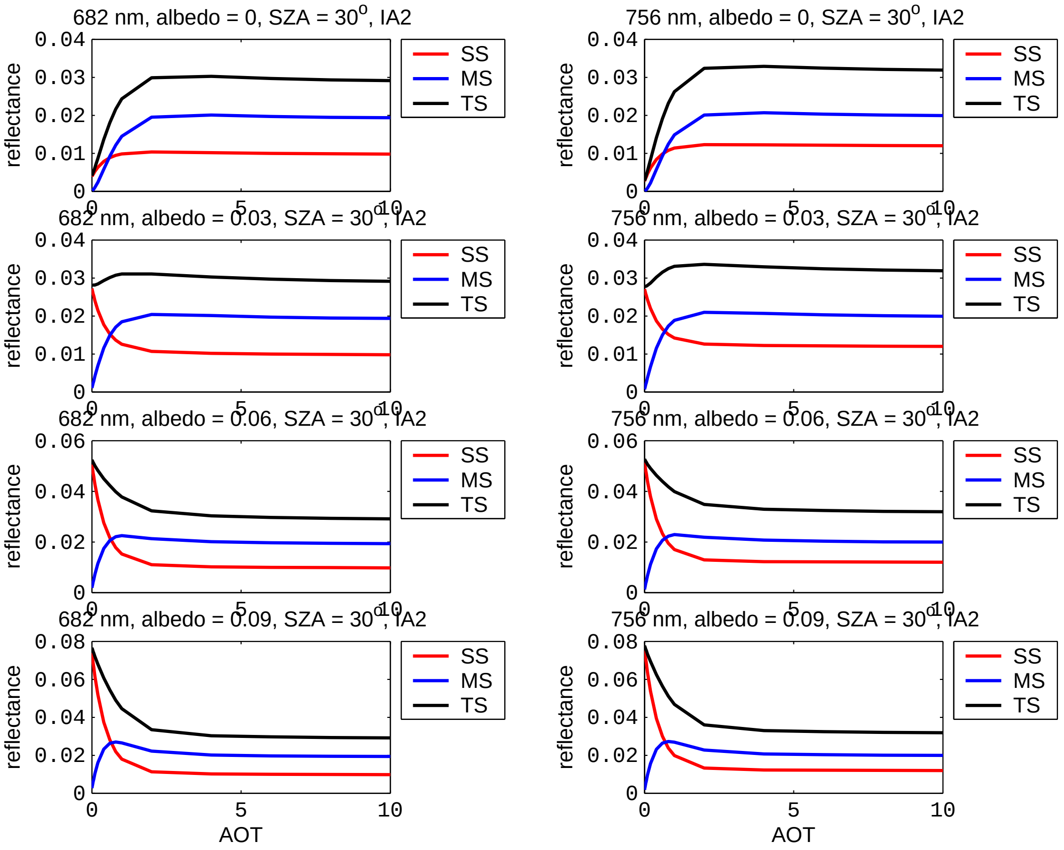

Figure 3.11: Modeled single scattering (SS), multiple scattering (MS) and total (TS) reflectances seen by a nadir-pointing satellite detector at $SZA = 30°$ over lambertian surfaces of different albedos for increasing aerosol optical thickness. The aerosol type used here is IA2 (medium sized absorbing industrial). The left panels show reflectances at a non-absorbing wavelength (682nm) near the O_2 B-band and the right panels show reflectances at a non-absorbing wavelength (756nm) near the O_2 A-band

of sunlight.

Common to all viewing geometries and aerosol types, however, is the relative asymptotic behavior of reflectances with respect to AOT for different albedos. It is seen that for all aerosol types in a given viewing geometry, the differences in reflectances at high AOT corresponding to different surface albedos decrease monotonically until they nearly vanish in the asymptotic limit as the aerosol begins to take on the character of a cloud. In the absence of marked reflectance peaks, this difference may be assumed to widen with decreasing AOT. This difference becomes maximum for a clear-sky scenario as the reflectances become directly proportional to the surface albedo. This fact may be utilized to effectively screen out aerosol-laden scenarios.

Having a rough idea of the aerosol type occurring at a given location and making use of multispectral data, it may be possible to identify clear-sky scenarios for albedo determination. After aerosols and clouds have been thus eliminated from the equation, uncertainties remain due to the generally non-lambertian character of the surface and the general non-uniformity of relief to be expected in a pixel of size 60km × 30km.

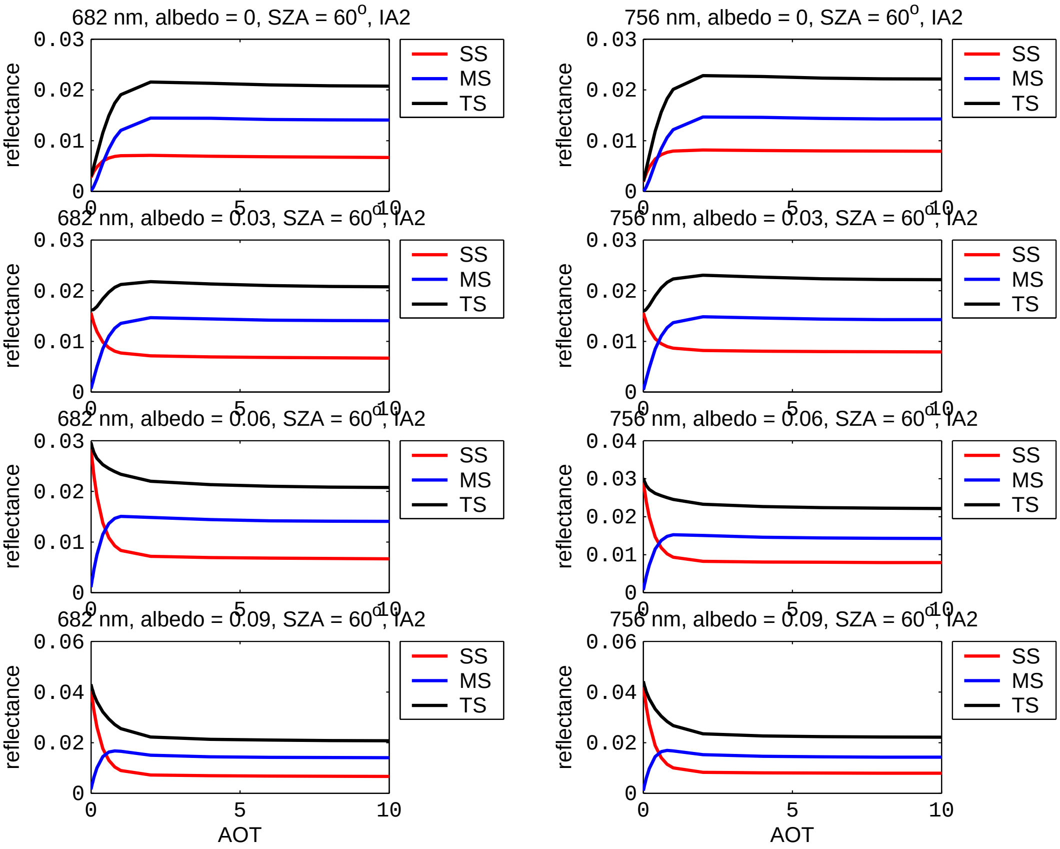

Figure 3.12: Modeled single scattering (SS), multiple scattering (MS) and total (TS) reflectances seen by a nadir-pointing satellite detector at $SZA = 60°$ over lambertian surfaces of different albedos for increasing aerosol optical thickness. The aerosol type used here is IA2 (medium sized absorbing industrial). The left panels show reflectances at a non-absorbing wavelength (682nm) near the O_2 B-band and the right panels show reflectances at a non-absorbing wavelength (756nm) near the O_2 A-band

3.3 Bidirectional reflectance and other uncertainties involved in albedo determination

Uncertainties persist with regard to ground albedo, even when a clear-sky day is identified. In most cases, the earth's surface does not reflect light in a lambertian fashion, as the intensity of reflected light varies with respect to measurement geometry, i.e. the angles of incidence and observation, eg. sun glint over ocean surfaces, differences in brightness of a surface viewed along and opposite incident sunlight, etc. This can best be described by a bidirectional reflectance distribution function specific to the ground pixel. The BRDF is not known locally for every pixel on the earth. BRDF exhibits at least as much temporal variation as the equivalent lambertian albedo and the amount of satellite data required to make a statistically sound estimation of the BRDF is immense. It is known that ground albedo changes with time as land usage changes. Besides such long-term changes, ground albedo also undergoes seasonal changes, which are especially marked in the mid-latitudes, owing to predominantly deciduous

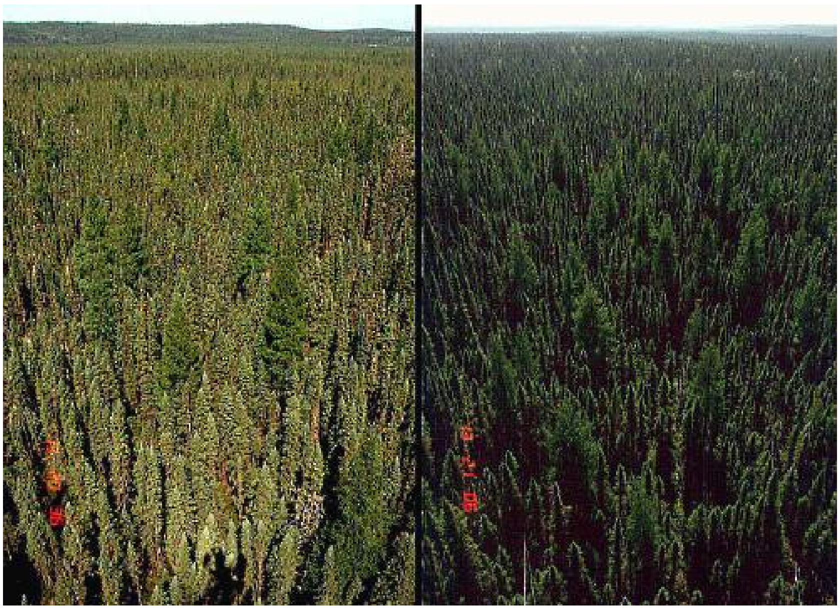

Figure 3.13: BRDF: This is a black spruce forest in the BOREAS experimental region in Canada. Left: backscattering (sun behind observer), note the bright region (hotspot) where all shadows are hidden. Right: forwardscattering (sun opposite observer), note the shadowed centers of trees and transmission of light through the edges of the canopies.

vegetation and snowfall in winter. Minor changes in vegetation (e.g. increased greenery during the wet seasons) throughout the globe can also produce large variations in the ground albedo, especially at wavelengths greater than 700 nm due to the so-called 'red edge' effect[2]. Rainfall also alters the ground albedo, since wet earth is significantly darker than dry earth. Also, in most cases, the ground albedo is not homogeneous throughout the ground pixel. This is especially true for the low spatial resolution of SCIAMACHY. This patchiness leads to an error, especially when the contrasts between the different patches is high. Furthermore, successive ground pixels containing a given location may not have an exact overlap during each satellite overpass. While analyzing the shape of the absorption bands, the surface elevation and contour of the ground pixel also introduce uncertainties, since a higher surface supports a smaller air column above it than a lower surface, leading to lesser absorption, and the strongly contoured surface produces a different line shape than a flat surface at the mean elevation of the contoured one.

In the following section, we overlook complications due to BRDF and describe the procedure used to determine the effective lambertian ground albedo.

---

[2] Red edge effect is the name given to the abrupt reflectance change in the $680 - 740$nm region of vegetation spectra that is caused by the combined effects of strong chlorophyll absorption and leaf internal scattering.

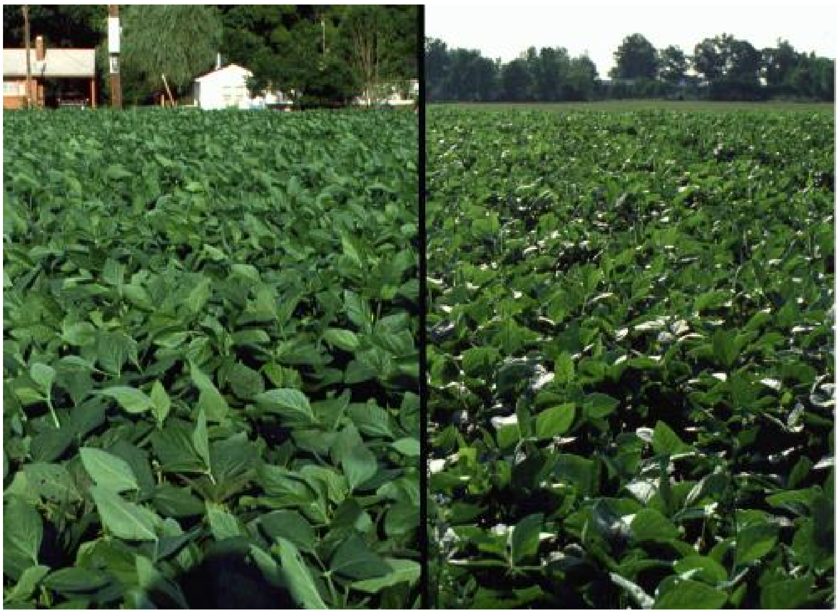

Figure 3.14: BRDF: A soybean field. Left: backscattering (sun behind observer). Right: forwardscattering (sun opposite observer), note the specular reflection of the leaves.

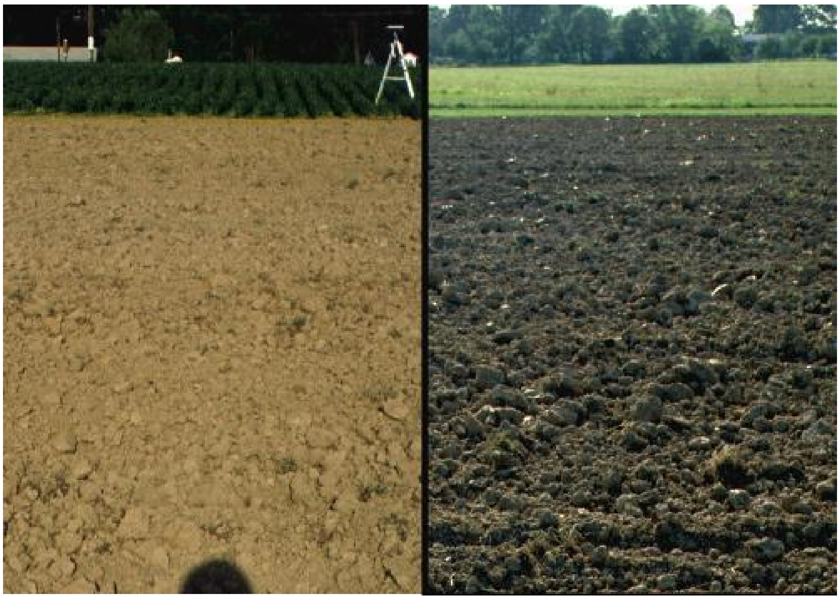

Figure 3.15: BRDF: A barren field with rough surface Left: backscattering (sun behind observer), note the bright region (hotspot) where all shadows are hidden. Right: forwardscattering (sun opposite observer), note the specular reflection.

3.4 Method for calculation of ground albedo from reflectance measurements given a clear-sky scenario

In view of the uncertainties involved and the lack of a general criterion for the identification of a clear-sky scenario using reflectances measured at a single wavelength, as seen in Section 3.2, we defer the development of such a criterion to Section 3.7.1, presently concentrating only on the determination of the equivalent lambertian ground albedo given reflectance measurements on an assumed clear-sky day.

The measurement set chosen for the identification of a clear sky scenario may vary from month-wise sets for high seasonality through year-long sets for negligible seasonality.

The total reflectance R measured by the satellite is made up of a ground component R_{grnd} arising from sole reflection of direct sunlight at the earth's surface, an atmospheric component R_{ss} due to single scattering (by molecules and aerosol particles) of direct solar radiation, and finally, the albedo-dependent diffuse component R_{ms} of light due to multiple scattering of incident sunlight entering the detector, so that

$$R(\lambda,\rho) = R_{grnd}(\lambda,\rho) + R_{ss}(\lambda) + R_{ms}(\lambda,\rho), \tag{3.1}$$

R_{ss} being the only quantity independent of ground albedo, ρ. The ground reflectance, assuming lambertian reflectance, can be written (see Section 2.3) as [3]

$$\begin{aligned} R_{grnd}(\lambda) &= \epsilon(\lambda)\,\epsilon'_i(\lambda)\,\rho_{Lamb}(\lambda)\cos\theta_{SZA} \\ &= \exp\left(-\tau(\lambda)\left\{\frac{1}{cos\theta_{LZA}} + \frac{1}{cos\theta_{SZA}}\right\}\right)\rho_{Lamb}(\lambda)\cdot\cos\theta_{SZA}, \end{aligned} \tag{3.2}$$

where $\rho_{Lamb}(\lambda)$ is the lambertian ground albedo, ϵ and ϵ' represent the extinction of light due to passage through the atmosphere along the incident and reflected paths respectively and τ denotes the total atmospheric optical depth. θ_{SZA} and θ_{LZA} are the solar and line-of-sight zenith angles at the time of the measurement. Thus,

$$\rho_{Lamb}(\lambda) = \frac{R(\lambda,\rho^*_{Lamb}(\lambda)) - (\,R_{ss}(\lambda) + R_{ms}(\lambda,\rho_{Lamb}))}{\exp\left(-\tau(\lambda)\left\{\frac{1}{cos\theta_{LZA}} + \frac{1}{cos\theta_{SZA}}\right\}\right)\cdot\cos\theta_{SZA}}, \tag{3.3}$$

where $R(\lambda,\rho^*_{Lamb}(\lambda))$ denotes the measured clear-sky reflectance corresponding to a true albedo ρ^*_{Lamb}.

Since there does not exist a linear analytical relationship between R_{ms} and ρ_{Lamb}, we set an initial value of $R^0_{ms} = 0$ and calculate R_{ss} as described in section 2.3 for a purely Rayleigh atmosphere (in accordance with our assumption of a clear sky), solving for the value ρ^1_{Lamb}. Substituting this value for ρ_{Lamb} in our model, we get the corresponding value for R^1_{ms} which in turn is used to determine ρ^2_{Lamb}. Thus we can iteratively solve for ρ^i_{Lamb} until it converges acceptably:

---

[3] The lambertian albedo is defined as the ratio of the reflected and incident *intensities* and may vary in the range $\{0, \frac{1}{\pi}\}$. The more commonly used definition is that of plane albedo which is the ratio of the reflected and incident *fluxes* and may take on a maximum value of unity.

$$\rho^{i}_{Lamb}(\lambda) = \frac{R(\lambda, \rho^{*}_{Lamb}(\lambda)) - \left(R_{ss}(\lambda) + R_{ms}(\lambda, \rho^{i-1}_{Lamb})\right)}{\exp\left(-\tau(\lambda)\left\{\frac{1}{cos\theta_{LZA}} + \frac{1}{cos\theta_{SZA}}\right\}\right) \cdot \cos\theta_{SZA}}, \tag{3.4}$$

Here, ρ^{i-1}_{Lamb} and ρ^{i}_{Lamb} denote the $(i-1)^{th}$ and i^{th} iterations of ρ_{Lamb}, and $\rho*_{Lamb}$ is the true value contained in the measurement.

Due to its slow variation with respect to wavelength, the albedo can be assumed to vary linearly in the vicinity of the spectral window in which it is calculated. For a window ranging in wavelength from λ_1 to λ_2, we calculate the corresponding albedos ρ_1 and ρ_2, and calculate the albedo gradient of the window as $d\rho/d\lambda = (\rho_1 - \rho_2)/(\lambda_1 - \lambda_2)$, so that the albedo at any wavelength near a given window can be determined as

$$\rho_{Lamb}(\lambda) = \rho_1 + \frac{d\rho}{d\lambda}\,(\lambda - \lambda_1)\,, \tag{3.5}$$

3.5 Accuracy of albedo determination in the absence of residual aerosol

To monitor the accuracy of our method for albedo determination given a correctly identified clear-sky scenario, we create synthetic clear-sky measurements for varying lambertian ground albedos around both the O_2 A and B-bands. Using AeroRad, we model measurements for for AOT=0 and lambertian ground albedos varying between 0 and 0.3 (corresponding to a plane albedo of nearly unity). Using these synthetic measurements as input, we determine the ground albedo of the scenario using the method described in the previous section. Fig. 3.16 shows the retrieved albedos plotted against their true values in both wavelength ranges in the top panel while the lower panels show the corresponding percentage error in the retrieval.

We observe an increase in the accuracy of the retrieval with increasing albedo. The percentage error of retrieval for 682nm initially decreases sharply from −0.25% at a true albedo of 0.02 until the accuracy gradually levels off around −0.05% for high albedos. The retrieval is more accurate at longer wavelengths, as is apparent from the percentage error of retrieval for 756nm, which shows a sharp initial decrease from 0.08% at a true albedo of 0.02 before gradually leveling off at less than −0.01% for high albedos.

This behaviour of the retrieval is easily explained by the source of error in the synthetic retrievals: the wavelength grid corresponding to the measured spectrum is distinct from the high resolution wavelength grid used in the forward model. The measured reflectance is sampled for albedo determination at a particular wavelength which is translated to the nearest wavelength on the high resolution forward model grid - this gives rise to a wavelength error of the order of 0.001nm, corresponding to the spectral resolution used in the forward model. The wavelength error translates into a reflectance sampling error which is proportional to the gradient $dR/d\lambda$ made by the observed reflectance with respect to the wavelength. Since we assume a wavelength independent albedo and a clear sky for the synthetic retrieval, the gradient $dR/d\lambda$ is solely governed by Rayleigh scattering. As the fractional contribution of Rayleigh scattering to the measured reflectance decreases with increasing albedo, the gradient becomes smaller and

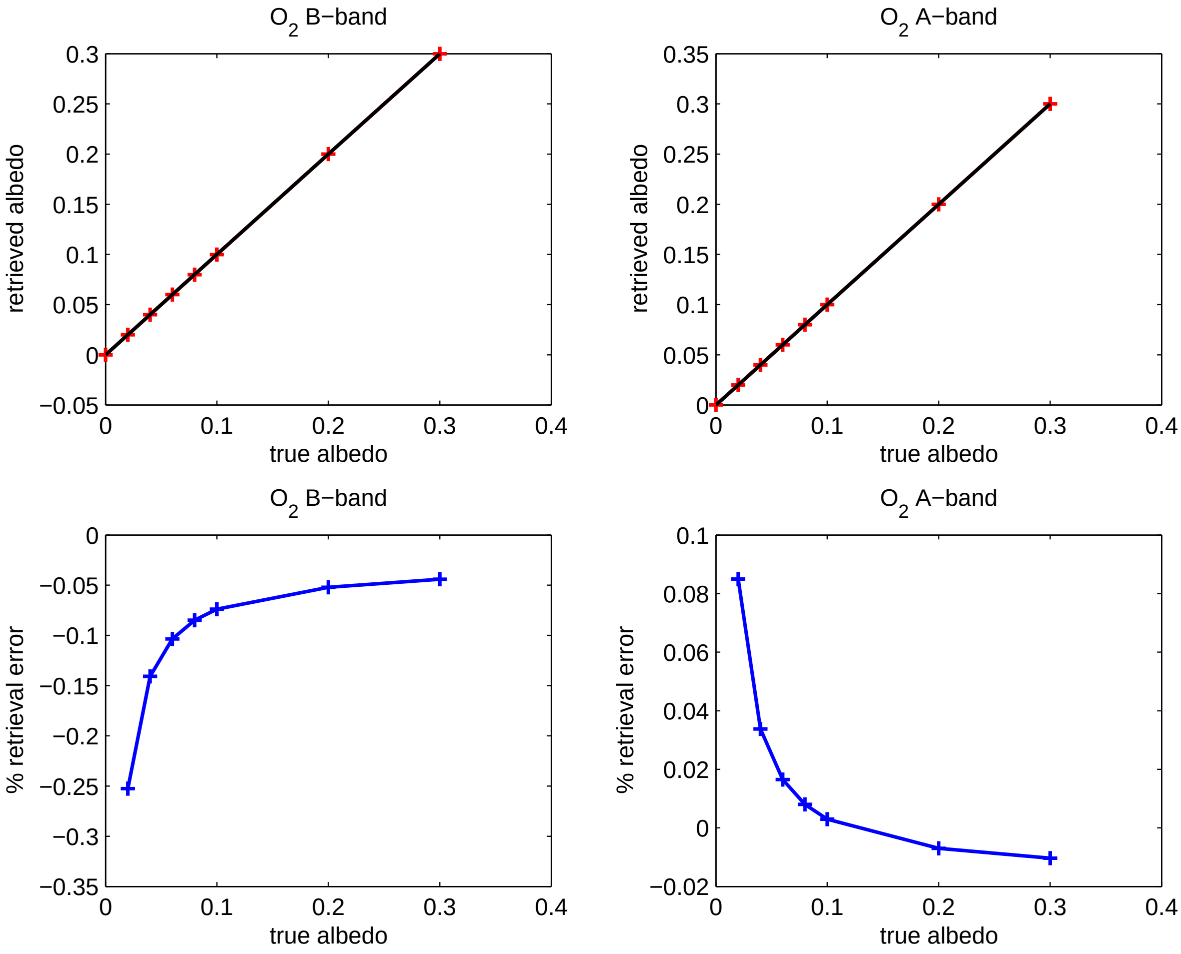

Figure 3.16: The upper left and right panels show the retrieved albedos near the O_2 B and A-bands plotted against their true values. The lower panels show the corresponding percentage error in the retrieval.

we see a corresponding improvement in the retrieval accuracy. The same is true for increasing wavelengths as Rayleigh scattering becomes progressively less dominant, also causing the reflectance gradient, and consequently, the retrieval error to taper off.

The retrieval error seen here is strongly amplified for real retrievals due to measurement noise and further sampling errors due to incorrect wavelength and/or radiometric calibration, and its absolute value is expected to lie between $0 - 1\%$.

3.6 Error in albedo determination due to the presence of residual aerosol and its potential use for verification of clear-sky scenarios: a sensitivity study

The possibility of residual aerosol contamination in an assumed clear-sky scenario is fairly substantial for any given data set. This residual aerosol leads to an error in the estimation of surface albedo, which in turn causes an error in the aerosol retrievals for which it is subsequently used. In this section, we examine the effect of residual aerosol of varying strengths on the albedo retrieval. While the observed reflectance R_{obs} is actually due to albedo $\rho = \rho_{true}$ and aerosol optical thickness $\tau = \tau^*$, the clear-sky assumption corresponds to $\tau = 0$ leading to the retrieval of an apparent albedo $\rho = \rho_{app}$, so that the expected reflectance would be $R_{exp} \neq R_{obs}$. An error in the retrieved albedo due to residual aerosol thus causes not only a general increase or decrease in reflectance at non-absorbing wavelengths but also a change in the shape of strong absorption bands such as the O_2 A and B-bands. While this discrepancy can sometimes severely hinder subsequent aerosol retrieval, especially for low aerosol loadings, it may also be used to test the veracity of our clear-sky assumption.

We consider 4 lambertian ground surfaces with albedos varying from $\rho_{true} = 0$ through 0.03 and 0.06 to a highest value of 0.09 (corresponding to a case where nearly 30% of incident light is reflected back by the surface). The low albedo values correspond to dark surfaces such as dense vegetation, calm oceans, etc. whereas arid soils, partial snow cover, rough seas, etc. form examples of bright surfaces having high albedos. The albedos are chosen to be identical at all wavelengths. For each surface, we simulate the reflectance R_{obs} in the spectral regions around both O_2 absorption bands registered by a nadir pointing detector for different residual aerosol loadings of type IA2, ranging from $\tau^* = 0$ to 0.3. Under a clear-sky assumption, each of these scenarios leads to the retrieval of an apparent surface albedo ρ_{app}, which in turn produces a reflectance R_{exp} for clear-sky conditions.

Figures 3.18 and 3.19 show the observed and expected reflectances and the difference thereof in the spectral regions around the O_2 B and A-bands respectively for a true albedo $\rho_{true} = 0$. As the residual AOT increases, so do the reflectances in both spectral regions, rising sharply from ≈ 0.0032 to ≈ 0.005 around the B-band and from ≈ 0.002 to ≈ 0.004 around the A-band as the AOT increases from 0 to 0.1. This leads to the retrieval of a higher albedo as can be seen in the upper left and right panels of Fig. 3.17. While the difference between the expected and observed reflectances should vanish at all wavelengths, we actually see a slight gradient caused by the error in albedo retrieval. This also gives rise to a small spurious structure in the absorption bands. The general effect of residual aerosol, however, is not distorted by these features. The lower panels of both figures show that while there is no marked difference in observed and expected reflectances in the absence of absorption, the presence of aerosols causes flattening of the absorption bands as more light gets scattered before it can reach the surface.

The discrepancy between the observed and the expected reflectances can be expressed as $\Delta R = \left(\Sigma_i[R_{exp}(\lambda_i) - R_{obs}(\lambda_i)]^2\right)^{1/2}$. Values of ΔR estimated for different residual aerosol loadings over a each true surface albedo $\rho_{true} = 0$ are tabulated in Table 3.6. It is seen that the discrepancy is smallest for a clear-sky (zero in the ideal retrieval) becoming larger with increasing AOT.

Figures 3.20 and 3.21 show the observed and expected reflectances and the difference thereof in the spectral regions around the O_2 B and A-bands respectively for a true albedo $\rho_{true} = 0.03$. At an albedo of 0.03 the surface becomes bright enough for the reflectances in both spectral regions to start falling with increasing albedo. The reflectances decline slowly from ≈ 0.0245 to ≈ 0.0225 around the B-band and from ≈ 0.0235 to ≈ 0.022 around the A-band as the

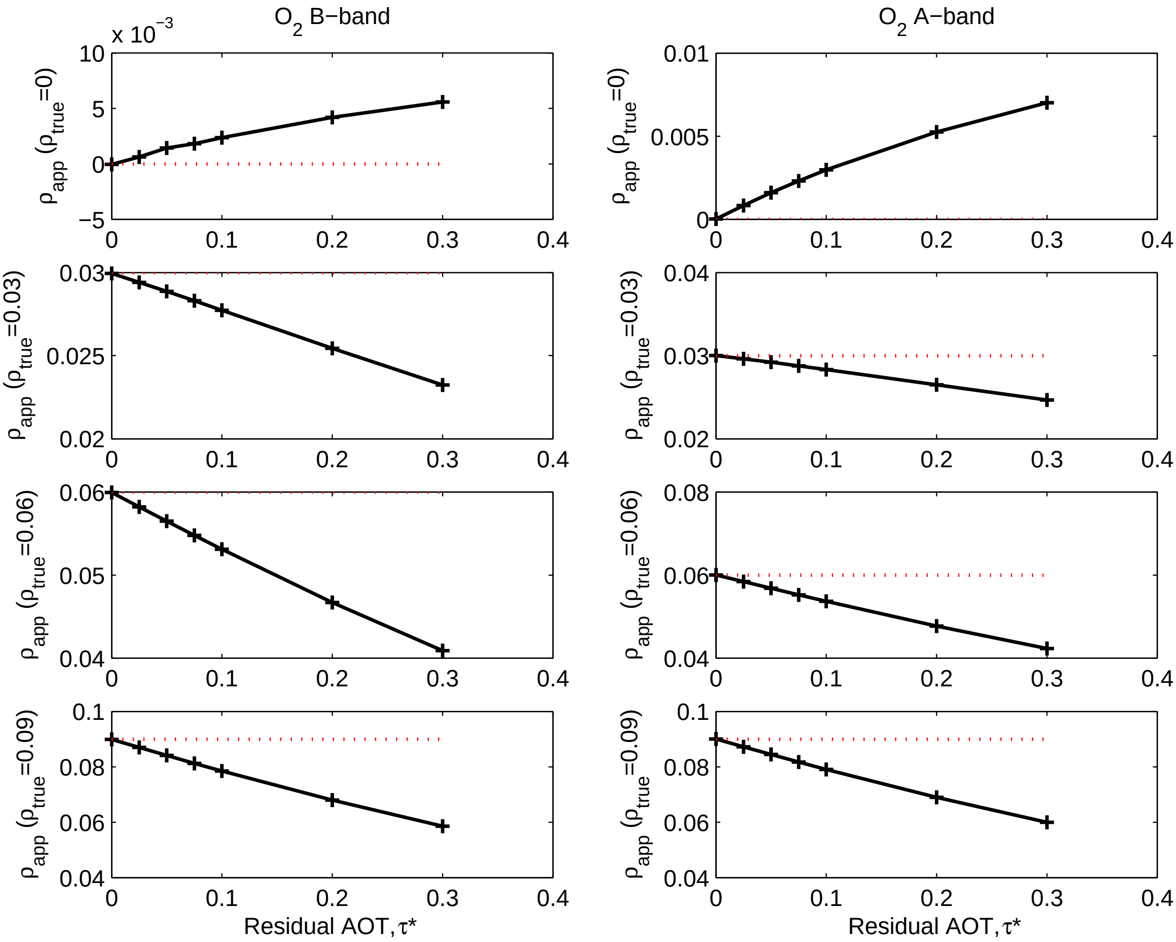

Figure 3.17: Case studies for albedo retrieval in the presence of residual aerosol are presented for true lambertian albedos, ρ^*, of $0, 0.03, 0.06$ and 0.09 (top-bottom) respectively. The left and right panels show the retrieved albedos near the O_2 B and A-bands, respectively, plotted against the optical thickness of the aerosol contaminating the assumed clear-sky scenario.

AOT increases from 0 to 0.1, leading to a small decrease in the retrieved albedo as can be seen in the second-from-top left and right panels of Fig. 3.17. While the difference between the expected and observed reflectances is seen to increase as the absolute error in albedo retrieval increases. The general effect of residual aerosol, however, still remains undistorted. Again, the lower panels show little difference in observed and expected reflectances in the absence of absorption, while the presence of aerosols causes flattening of the absorption bands as more light gets scattered before reaching the surface. The extent of the flattening remains more or less unchanged compared to that for $\rho_{true} = 0$.

Values of ΔR estimated for different residual aerosol loadings over a each true surface albedo $\rho_{true} = 0.03$ are tabulated in Table 3.6. Again, the discrepancy is smallest for a clear-sky becoming larger with increasing AOT.

This trend is reflected for higher albedos, as the decline in reflectances with increasing residual

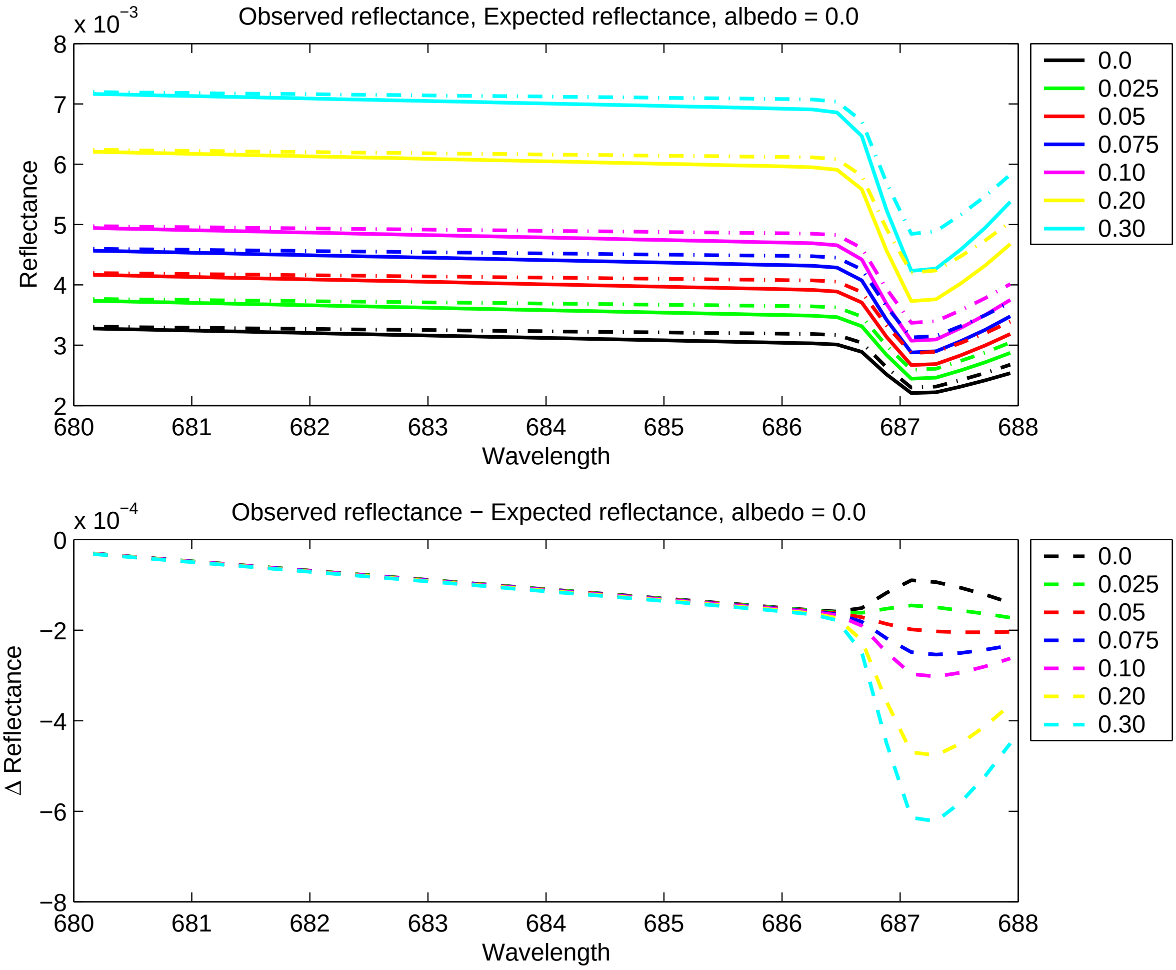

Figure 3.18: The top panel shows synthetic 'measured/observed' reflectances around the O$_2$ B-band (solid line) for different aerosol loadings at a 'true' albedo of $A_{true} = 0$. These reflectances are used for the determination of the corresponding ground albedo A_{retr} under a clear sky assumption. The expected reflectances for $AOT = 0$ and a ground albedo of A_{retr} are represented by dash-dotted lines. The bottom panel shows the deviation of the expected from the observed reflectances for different residual aerosol loadings. The aerosol here is assumed to be of type IA2.

aerosol loading becomes sharper. The extent of flattening of absorption lines decreases slightly with increasing albedo. This can be seen for $\rho_{true} = 0.06$ in Figures 3.22 and 3.23 and for $\rho_{true} = 0.09$ in Figures 3.24 and 3.25. Fig. 3.17 indicates that the decrease in retrieved albedo with residual AOT becomes sharper for higher albedos.

The values of ΔR tabulated in 3.6 and 3.6 again show increasing discrepancies for larger residual aerosol loadings. However, the discrepancies for different aerosol loadings are most distinct at low albedos, i.e. for dark surfaces.

Thus study emphasizes the capability of medium-high spectral resolution satellite instruments like SCIAMACHY for the verification of clear-sky scenarios by analyzing the discrepancy between expected and observed spectra. As absorption structures indicate the presence of aerosols

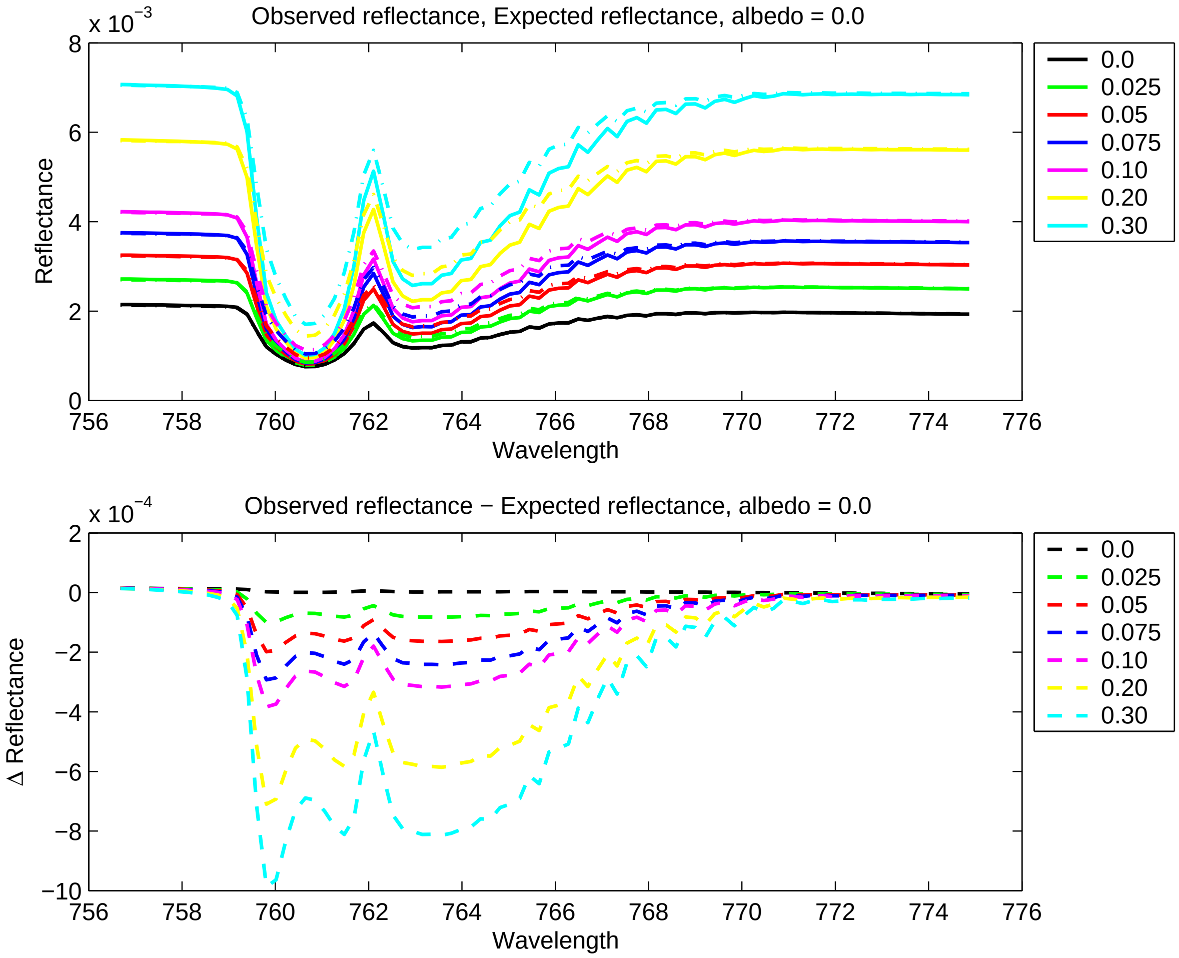

Figure 3.19: The top panel shows synthetic 'measured/observed' observed reflectances around the O_2 A-band (solid line) for different aerosol loadings at a 'true' albedo of $A_{true} = 0$. These reflectances are used for the determination of the corresponding ground albedo A_{retr} under a clear sky assumption. The expected reflectances for $AOT = 0$ and a ground albedo of A_{retr} are represented by dash-dotted lines. The bottom panel shows the deviation of the expected from the observed reflectances for different residual aerosol loadings. The aerosol here is assumed to be of type IA2.

much more clearly than mere reflectances, while reflectances measured with a high resolution allow for an accurate determination of apparent albedo at non absorbing wavelengths, such instruments have a clear edge over those with broadband measurements. However, due to the less optimal measurement noise and radiometric and wavelength calibration issues associated with SCIAMACHY, this method has only been explored in principle in this work.

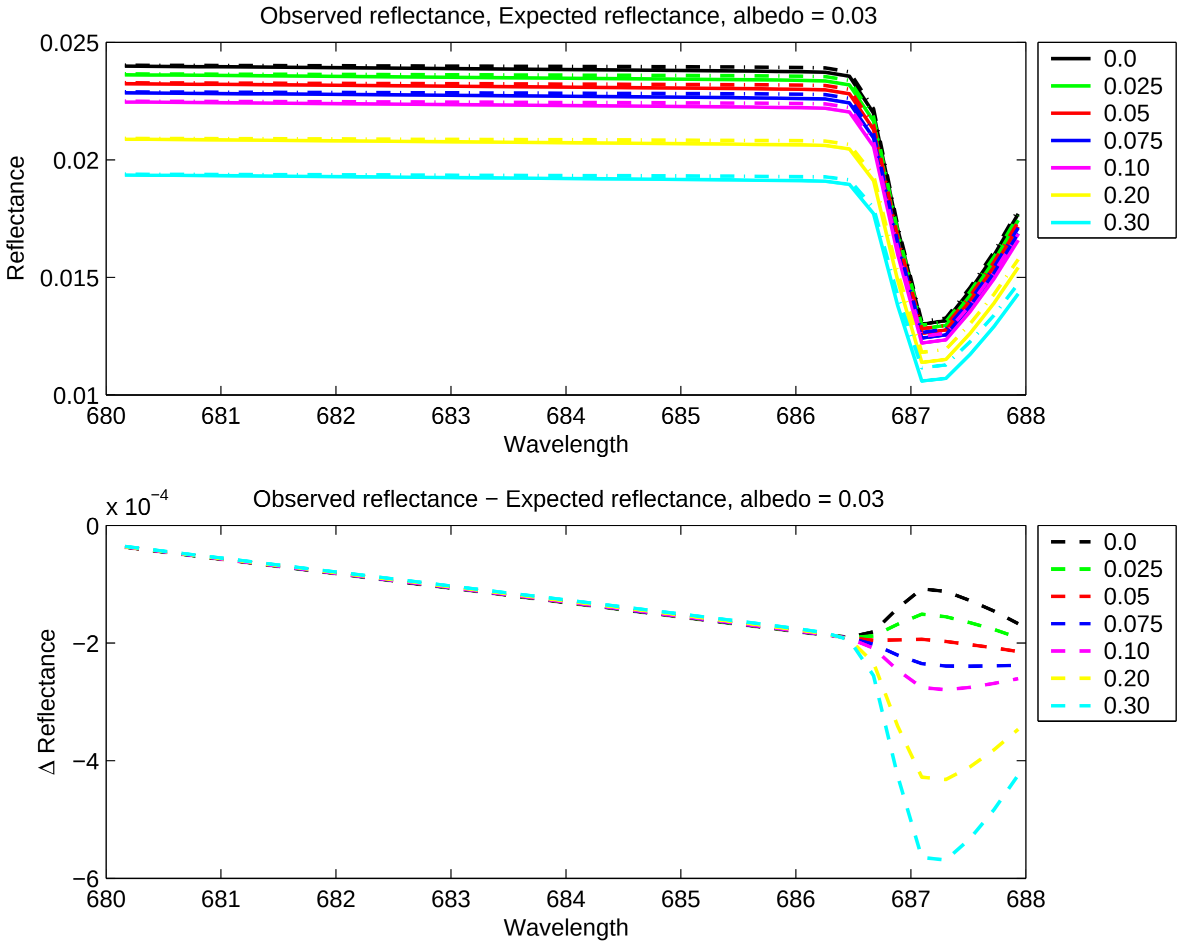

Figure 3.20: The top panel shows synthetic 'measured/observed' reflectances around the O_2 B-band (solid line) for different aerosol loadings at a 'true' albedo of $A_{true} = 0.03$. These reflectances are used for the determination of the corresponding ground albedo A_{retr} under a clear sky assumption. The expected reflectances for $AOT = 0$ and a ground albedo of A_{retr} are represented by dash-dotted lines. The bottom panel shows the deviation of the expected from the observed reflectances for different residual aerosol loadings. The aerosol here is assumed to be of type IA2.

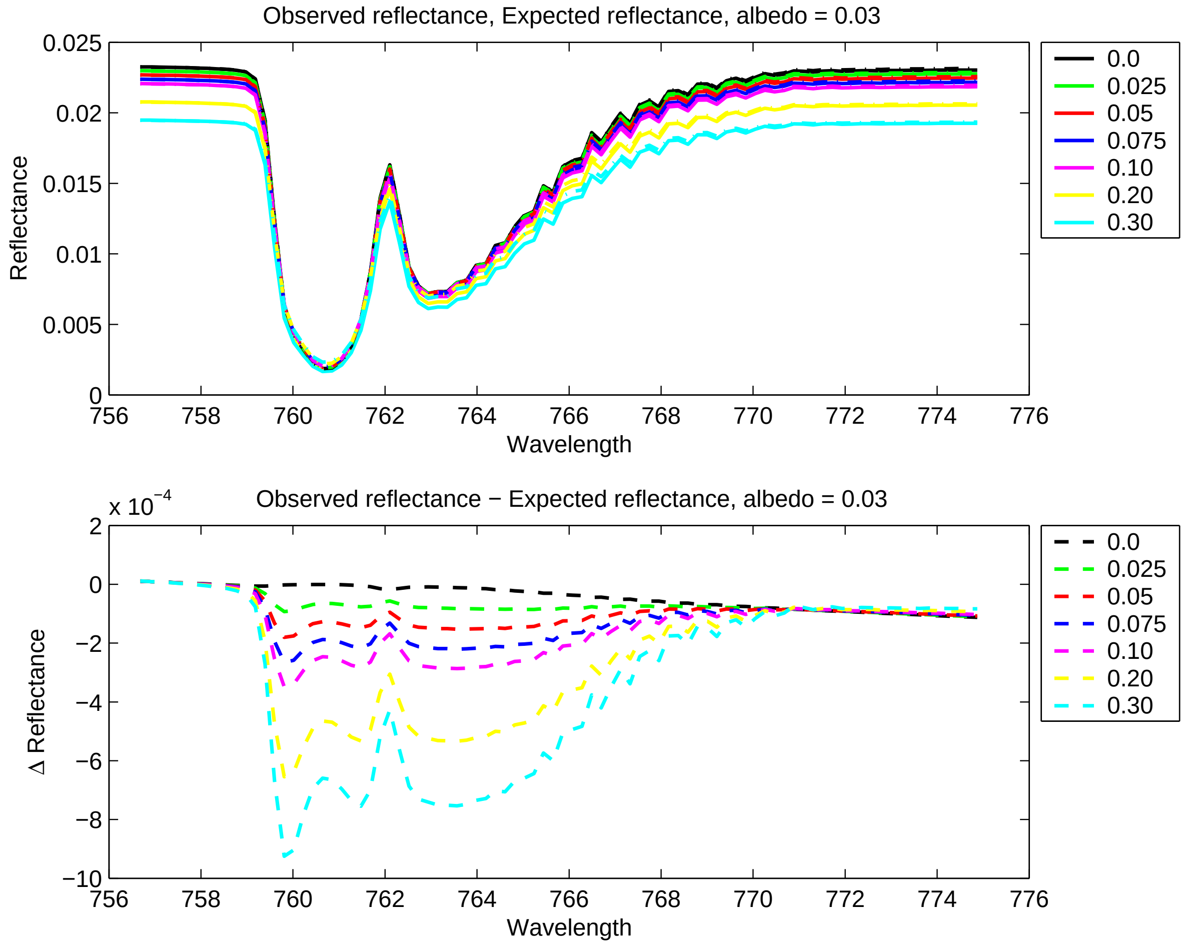

Figure 3.21: The top panel shows synthetic 'measured/observed' reflectances around the O_2 A-band (solid line) for different aerosol loadings at a 'true' albedo of $A_{true} = 0.03$. These reflectances are used for the determination of the corresponding ground albedo A_{retr} under a clear sky assumption. The expected reflectances for $AOT = 0$ and a ground albedo of A_{retr} are represented by dash-dotted lines. The bottom panel shows the deviation of the expected from the observed reflectances for different residual aerosol loadings. The aerosol here is assumed to be of type IA2.

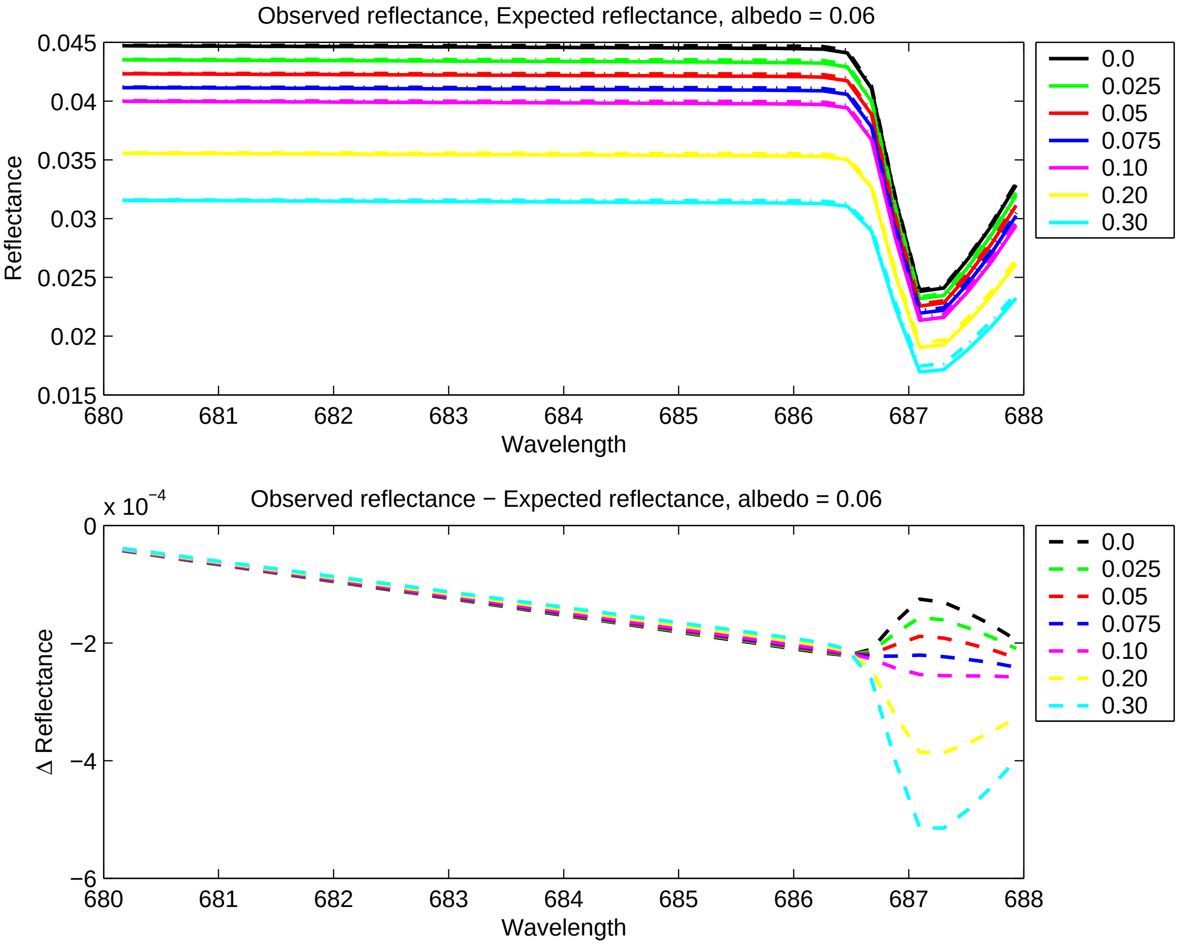

Figure 3.22: The top panel shows synthetic 'measured/observed' reflectances around the O_2 B-band (solid line) for different aerosol loadings at a 'true' albedo of $A_{true} = 0.06$. These reflectances are used for the determination of the corresponding ground albedo A_{retr} under a clear sky assumption. The expected reflectances for $AOT = 0$ and a ground albedo of A_{retr} are represented by dash-dotted lines. The bottom panel shows the deviation of the expected from the observed reflectances for different residual aerosol loadings. The aerosol here is assumed to be of type IA2.

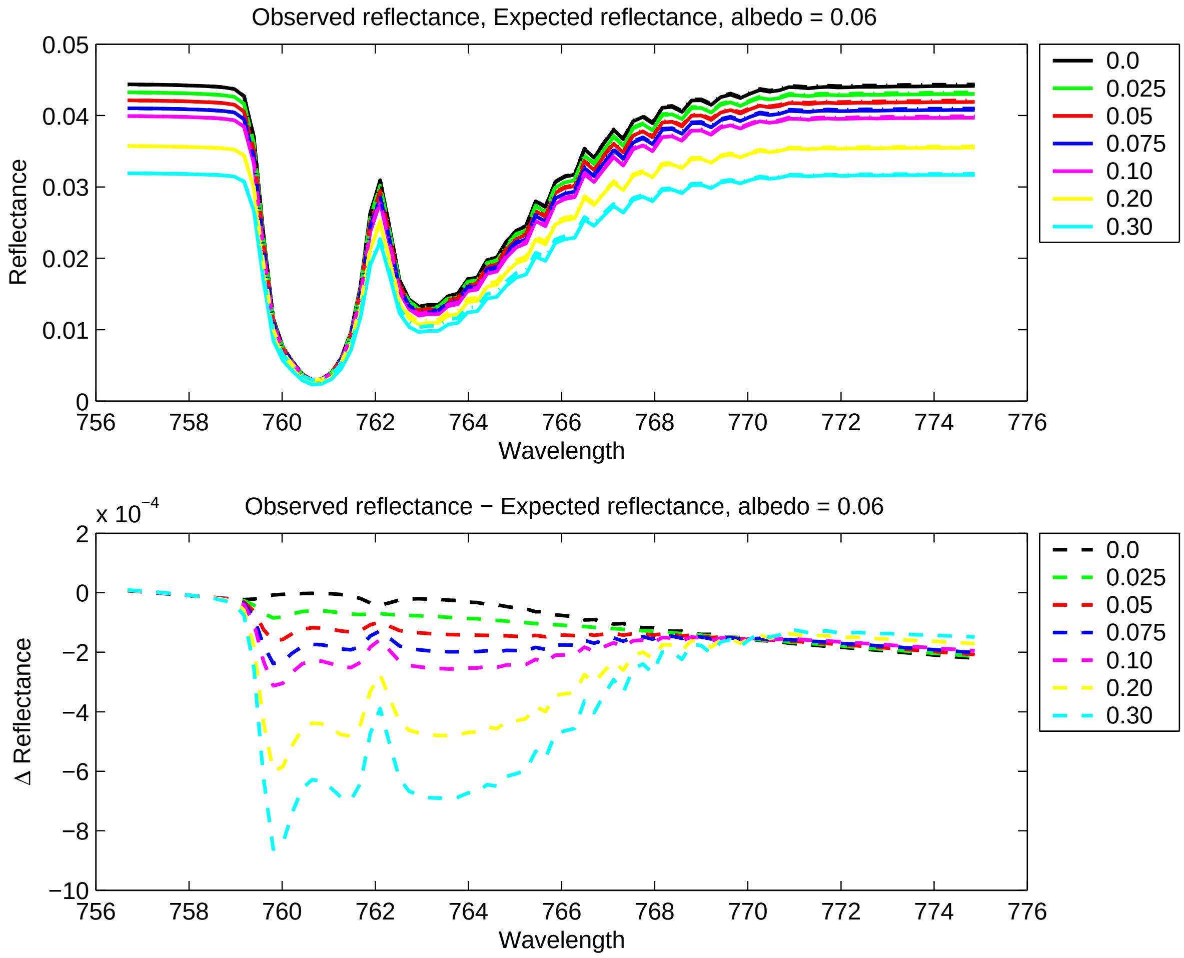

Figure 3.23: The top panel shows synthetic 'measured/observed' reflectances around the O_2 A-band (solid line) for different aerosol loadings at a 'true' albedo of $A_{true} = 0.06$. These reflectances are used for the determination of the corresponding ground albedo A_{retr} under a clear sky assumption. The expected reflectances for $AOT = 0$ and a ground albedo of A_{retr} are represented by dash-dotted lines. The bottom panel shows the deviation of the expected from the observed reflectances for different residual aerosol loadings. The aerosol here is assumed to be of type IA2.

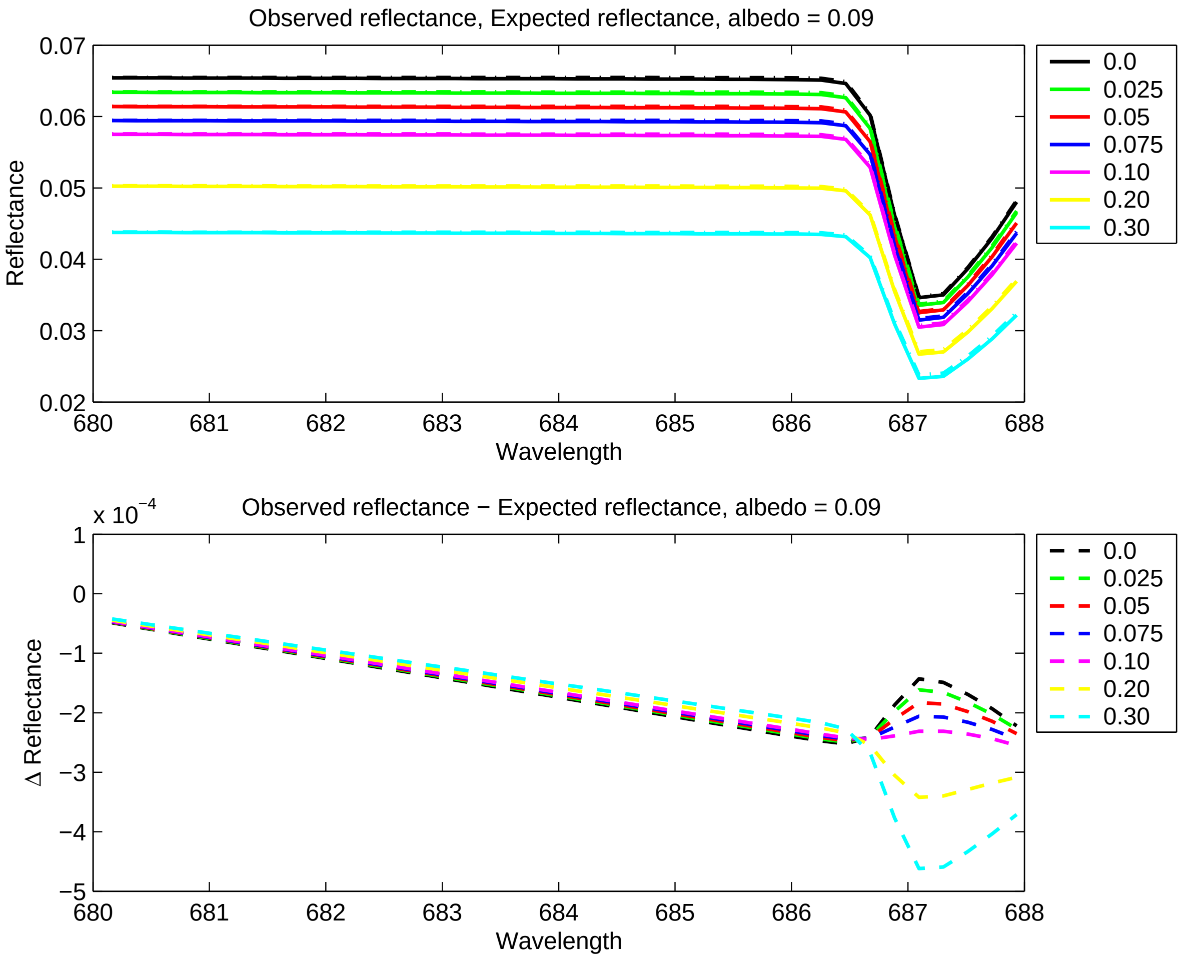

Figure 3.24: The top panel shows synthetic 'measured/observed' reflectances around the O_2 B-band (solid line) for different aerosol loadings at a 'true' albedo of $A_{true} = 0.09$. These reflectances are used for the determination of the corresponding ground albedo A_{retr} under a clear sky assumption. The expected reflectances for $AOT = 0$ and a ground albedo of A_{retr} are represented by dash-dotted lines. The bottom panel shows the deviation of the expected from the observed reflectances for different residual aerosol loadings. The aerosol here is assumed to be of type IA2.

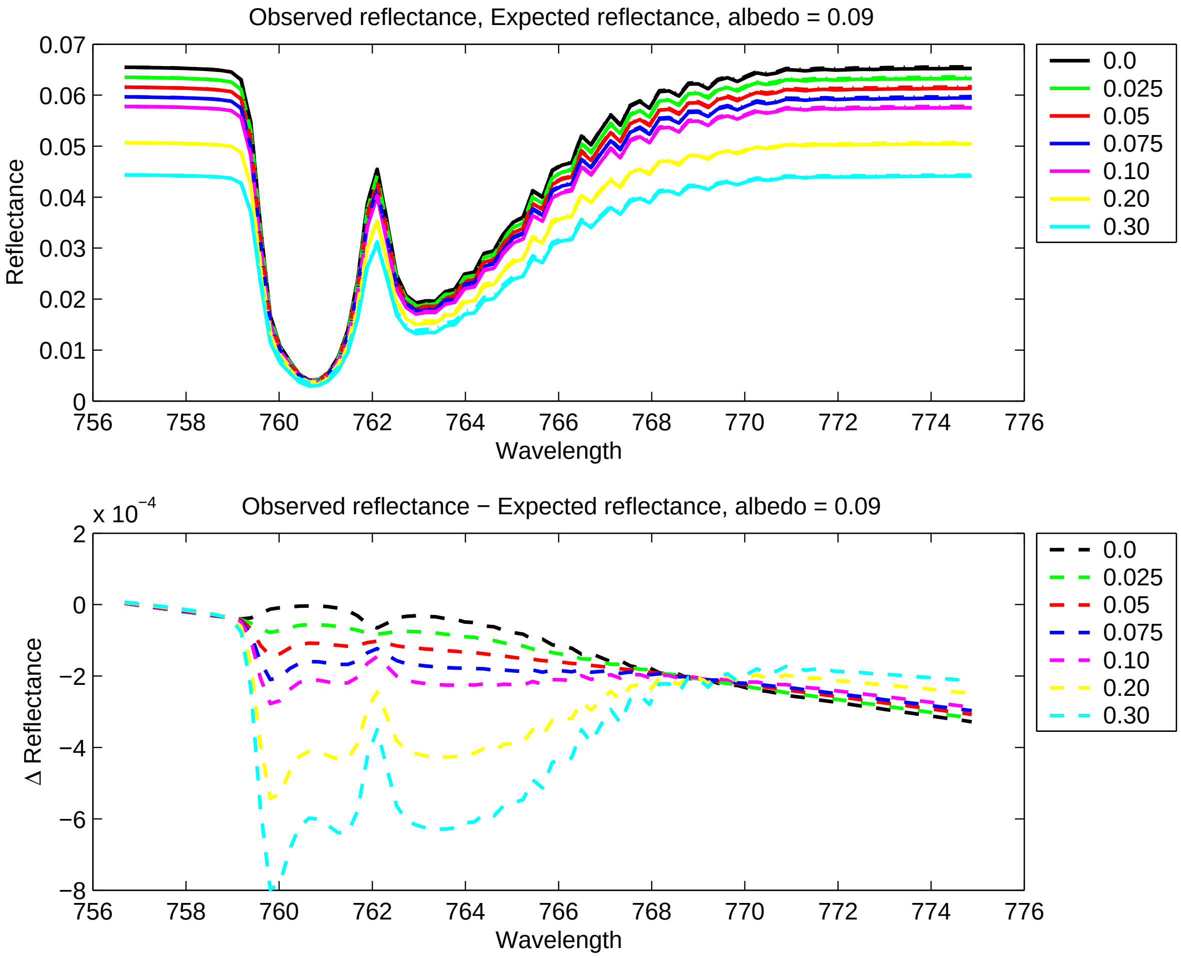

Figure 3.25: The top panel shows synthetic 'measured/observed' reflectances around the O$_2$ A-band (solid line) for different aerosol loadings at a 'true' albedo of $A_{true} = 0.09$. These reflectances are used for the determination of the corresponding ground albedo A_{retr} under a clear sky assumption. The expected reflectances for $AOT = 0$ and a ground albedo of A_{retr} are represented by dash-dotted lines. The bottom panel shows the deviation of the expected from the observed reflectances for different residual aerosol loadings. The aerosol here is assumed to be of type IA2.

Table 3.1: Discrepancy ΔR between the observed and the expected reflectances due to 'clear sky' assumption of different residual aerosol loadings at a true albedo, ρ_{true}, of 0.00.

ΔR,ρ_{true}: 0.00		
τ_i	B-band	A-band
0.0	$6.544\,10^{-4}$	$5.400\,10^{-5}$
0.025	$7.123\,10^{-4}$	$4.411\,10^{-4}$
0.05	$7.789\,10^{-4}$	$8.754\,10^{-4}$
0.075	$8.506\,10^{-4}$	0.0013
0.10	$9.248\,10^{-4}$	0.0017
0.20	0.0012	0.0031
0.30	0.0015	0.0044

Table 3.2: Discrepancy ΔR between the observed and the expected reflectances due to 'clear sky' assumption of different residual aerosol loadings at a true albedo, ρ_{true}, of 0.03.

ΔR, ρ_{true}: 0.03		
τ_i	B-band	A-band
0.0	$7.828\,10^{-4}$	$5.454\,10^{-4}$
0.025	$8.209\,10^{-4}$	$7.244\,10^{-4}$
0.05	$8.655\,10^{-4}$	0.0010
0.075	$9.154\,10^{-4}$	0.0013
0.10	$9.680\,10^{-4}$	0.0017
0.20	0.0012	0.0029
0.30	0.0014	0.0041

Table 3.3: Discrepancy ΔR between the observed and the expected reflectances due to 'clear sky' assumption of different residual aerosol loadings at a true albedo, ρ_{true}, of 0.06.

ΔR, ρ_{true}: 0.06		
τ_i	B-band	A-band
0.0	$9.107\,10^{-4}$	0.0011
0.025	$9.314\,10^{-4}$	0.0012
0.05	$9.570\,10^{-4}$	0.0013
0.075	$9.847\,10^{-4}$	0.0015
0.10	0.0010	0.0018
0.20	0.0012	0.0028
0.30	0.0014	0.0039

Table 3.4: Discrepancy ΔR between the observed and the expected reflectances due to 'clear sky' assumption of different residual aerosol loadings at a true albedo, ρ_{true}, of 0.09.

ΔR, ρ_{true}: 0.09		
τ_i	B-band	A-band
0.0	0.0010	0.0016
0.025	0.0010	0.0016
0.05	0.0010	0.0017
0.075	0.0011	0.0018
0.10	0.0011	0.0019
0.20	0.0012	0.0027
0.30	0.0013	0.0037

3.7 Albedo measurements from SCIAMACHY

In this section, we use the ideas developed using the above synthetic studies to devise a multispectral method for the identification of a clear-sky day using SCIAMACHY data. We conclude by determining the albedo at three different locations, viz. Kanpur, Mexico City and La Parguera using this method.

3.7.1 Multispectral method for the identification of a clear-sky scenario

The reflectance signal at a non-absorbing wavelength in a clear-sky scenario is made up of a surface component due to surface reflection attenuated by the Rayleigh particles of the atmosphere, and an atmospheric component consisting of single and multiple scattering due to Rayleigh particles. In an aerosol-laden scenario, the atmospheric attenuation of the surface component gets reinforced by extinction due to aerosols and Rayleigh single scattering may be slightly reduced due to shielding of incident light by intermediate aerosols, while there is new single scattering component due to aerosol and the multiple scattering component is greatly increased.

When an aerosol-laden scenario having a true albedo ρ_{true}, a total Rayleigh optical thickness τ_{Rayl} and a total aerosol optical thickness τ_{aer} is treated as a clear sky yielding an apparent albedo ρ_{app}, the implicit assumption is

$$\begin{aligned} & \rho_{app} \cdot \mu_S \cdot \exp\left(-\tau_{Rayl}/\bar{\mu}\right) + R^0_{Rayl} + R^0_{ms} \\ = \; & \rho_{true} \cdot \mu_S \cdot \exp\left(-(\tau_{Rayl} + \tau_{aer})/\bar{\mu}\right) + (R_{Rayl} + R_{aer}) + R_{ms}, \end{aligned} \tag{3.6}$$

where R^0_{Rayl} is the single scattering component of the reflectance due to Rayleigh scattering in the absence of aerosols, R^0_{ms} is the multiple scattering component of the reflectance in the absence of aerosols for surface albedo ρ_{app}, R_{Rayl} is the single scattering component of the reflectance due to Rayleigh scattering at the given AOT τ_{aer}, R_{aer} is the corresponding single scattering component of the reflectance due to scattering by aerosol, and R_{ms} is the multiple scattering component of the reflectance corresponding to τ_{aer} and surface albedo ρ_{true}. Here, $\mu_S = \cos(SZA)$ and $\bar{\mu}^{-1} = \mu_S^{-1} + \mu_L^{-1}$, where $\mu_L = \cos(LZA)$.

Rearranging the terms of Eq. 3.6, we can express ρ_{app} as

$$\rho_{app} \; = \; \rho_{true} \cdot \mu_S \cdot \exp\left(-\tau_{aer}/\bar{\mu}\right) + \frac{((R_{Rayl} - R^0_{Rayl}) + R_{aer}) + (R_{ms} - R^0_{ms})}{\mu_S \cdot \exp\left(-\tau_{Rayl}/\bar{\mu}\right)} \tag{3.7}$$

$$\tag{3.8}$$

Now, for a cloudy scenario, $\tau_{aer} \gg 0$, so that $\exp\left(-\tau_{aer}/\bar{\mu}\right) \rightarrow 0$ and $\|(R_{aer} + R_{ms})\| \gg \|R_{Rayl} - R^0_{Rayl} - R^0_{ms}\|$, yielding the limit of Eq.3.7 for cloudy skies

$$\rho_{app} \; = \; \frac{(R_{aer} + R_{ms})}{\mu_S \cdot \exp\left(-\tau_{Rayl}/\bar{\mu}\right)}. \tag{3.9}$$

For a medium aerosol loading, $\tau_{aer} > 0$, so that $R_{ms} \gg R^0_{ms}$ and $R_{Rayl} \approx R^0_{Rayl}$, yielding the limit of Eq.3.7 for hazy skies

$$\rho_{app} = \rho_{true} \cdot \mu_S \cdot \exp\left(-\tau_{aer}/\bar{\mu}\right) + \frac{(R_{aer} + R_{ms})}{\mu_S \cdot \exp\left(-\tau_{Rayl}/\bar{\mu}\right)}. \tag{3.10}$$

For a clear sky, of course, $\tau_{aer} = 0$, so that $R_{ms} = R^0_{ms}$ and $R_{Rayl} = R^0_{Rayl}$, so that

$$\rho_{app} = \rho_{true}. \tag{3.11}$$

Now, we consider two absorption-free wavelengths λ_B and λ_A near the O_2 B and A-bands, respectively, having true albedos ρ^B_{true} and ρ^A_{true}. It is known that $\tau^B_{Rayl} \geq \tau^A_{Rayl}$, while $\tau^B_{aer} \approx \tau^A_{aer} \approx \tau_{\bar{aer}}$. As a result, $R^B_{aer} + R^B_{ms} \approx R^A_{aer} + R^A_{ms} \approx R_{aer} \bar{+} R_{ms}$, where the subscripts A and B denote the chosen wavelengths near the O_2 A and B-bands respectively and $R_{aer} \bar{+} R_{ms}$ denotes the average of the values at λ_B and λ_A.

Thus, for a cloudy scenario,

$$\rho^A_{app} - \rho^B_{app} = \frac{(R_{aer} \bar{+} R_{ms})}{\mu_S} \cdot \left[\exp\left(\tau^A_{Rayl}/\bar{\mu}\right) - \exp\left(\tau^B_{Rayl}/\bar{\mu}\right)\right] \leq 0. \tag{3.12}$$

Thus, for cloudy skies, the apparent albedo at λ_A is always slightly lower than that at λ_B, irrespective of the true values.

For hazy skies,

$$\begin{aligned} \rho^A_{app} - \rho^B_{app} = {} & (\rho^A_{true} - \rho^B_{true}) \cdot \mu_S \cdot \exp\left(-\tau_{\bar{aer}}/\bar{\mu}\right) \\ & + \frac{(R_{aer} \bar{+} R_{ms})}{\mu_S} \cdot \left[\exp\left(\tau^A_{Rayl}/\bar{\mu}\right) - \exp\left(\tau^B_{Rayl}/\bar{\mu}\right)\right] \end{aligned} \tag{3.13}$$

If $\rho^A_{true} > \rho^B_{true}$, as is true for most terrestrial surfaces, Eq. 3.14 implies that

$$\rho^A_{app} - \rho^B_{app} < \rho^A_{true} - \rho^B_{true}, \tag{3.14}$$

becoming smaller with increasing aerosol loading and even becoming negative when τ_{aer} is large enough for the second (negative) term to outweigh the first.

For a clear sky, we have equality of the apparent and the true albedos, so that

$$\rho^A_{app} - \rho^B_{app} = \rho^A_{true} - \rho^B_{true}. \tag{3.15}$$

We can conclude that given $\rho^A_{true} > \rho^B_{true}$, the maximum value of $\rho^A_{app} - \rho^B_{app}$ corresponds to the scenario with the least aerosol loading, ideally, a clear sky scenario. In the following, we use this principle for albedo determination from a set of SCIAMACHY measurements over a given location.

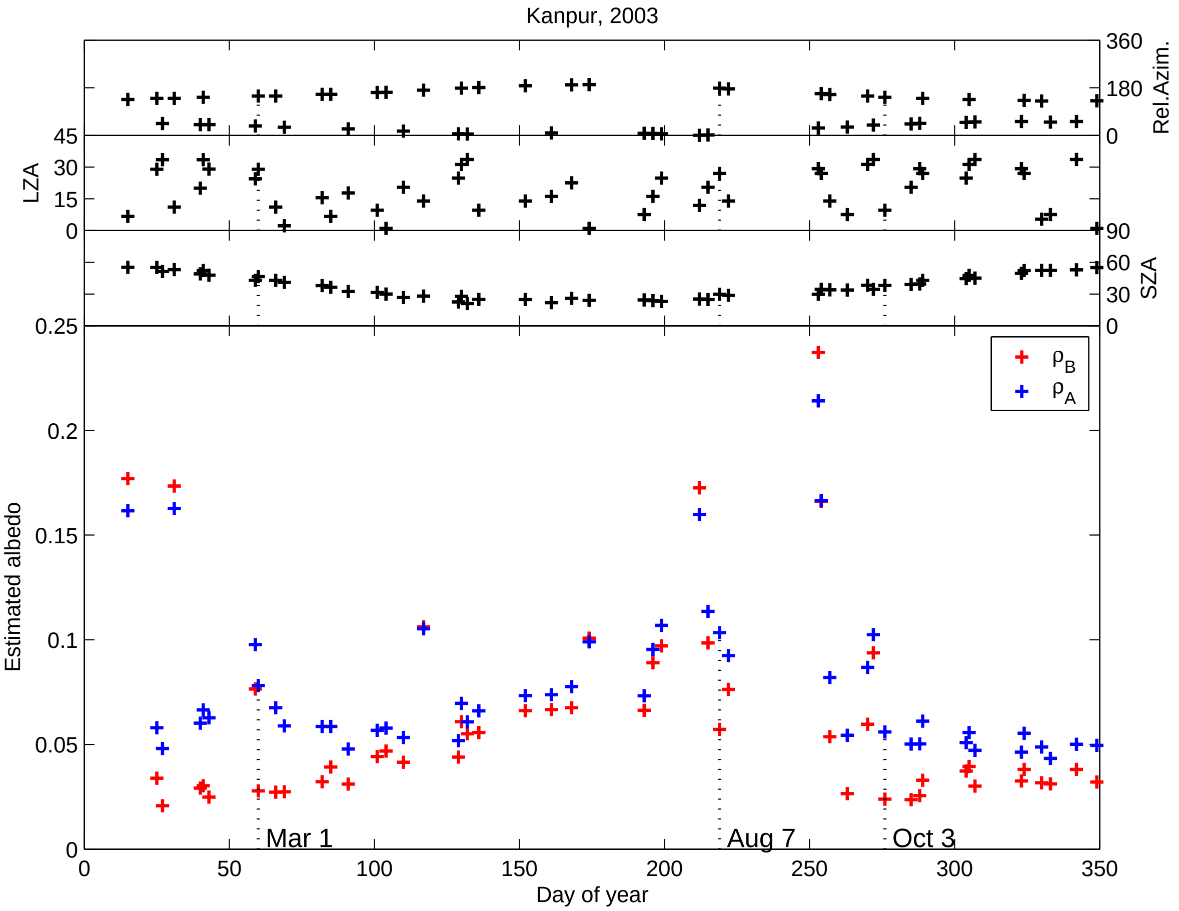

Figure 3.26: Apparent albedos ρ_A (blue crosses) and ρ_B (red crosses) around the O_2 A and B-bands respectively plotted against the day of the year 2003 on which the scenario was recorded by SCIAMACHY over Kanpur, India. Also shown in the first three panels are the solar zenith angle (SZA), the line-of-sight zenith angle (LZA) and the relative azimuthal angle (Rel. Azim.) between the direction of incident (direct) sunlight and the line-of-sight. Dotted lines map these angles and the apparent albedos ρ_A and ρ_B for days that may correspond to clear-sky scenarios.

3.7.2 Determination of surface albedo using SCIAMACHY measurements

To apply the above principle to SCIAMACHY measurements, we determine the apparent surface albedos of all measurements around the O_2 B and A-bands in a given data set as described in Section 3.4, irrespective of the scenario they may represent.

Figures 3.26, 3.28 and 3.30 show the estimated albedos, ρ_B and ρ_A, plotted against the day of the year for the three locations Kanpur, Mexico City and La Parguera introduced at the beginning of this chapter. It is evident that the viewing geometry, especially the SZA, also influences the observed reflectance, causing lower values with increasing SZA. We see that the SZA in each case is strongly correlated to the day of the year - while this could lead to a misinterpretation of seasonal effects, we have attempted to rule out this possibility by choosing locations that lie within/near the tropics featuring minimal seasonal variation.

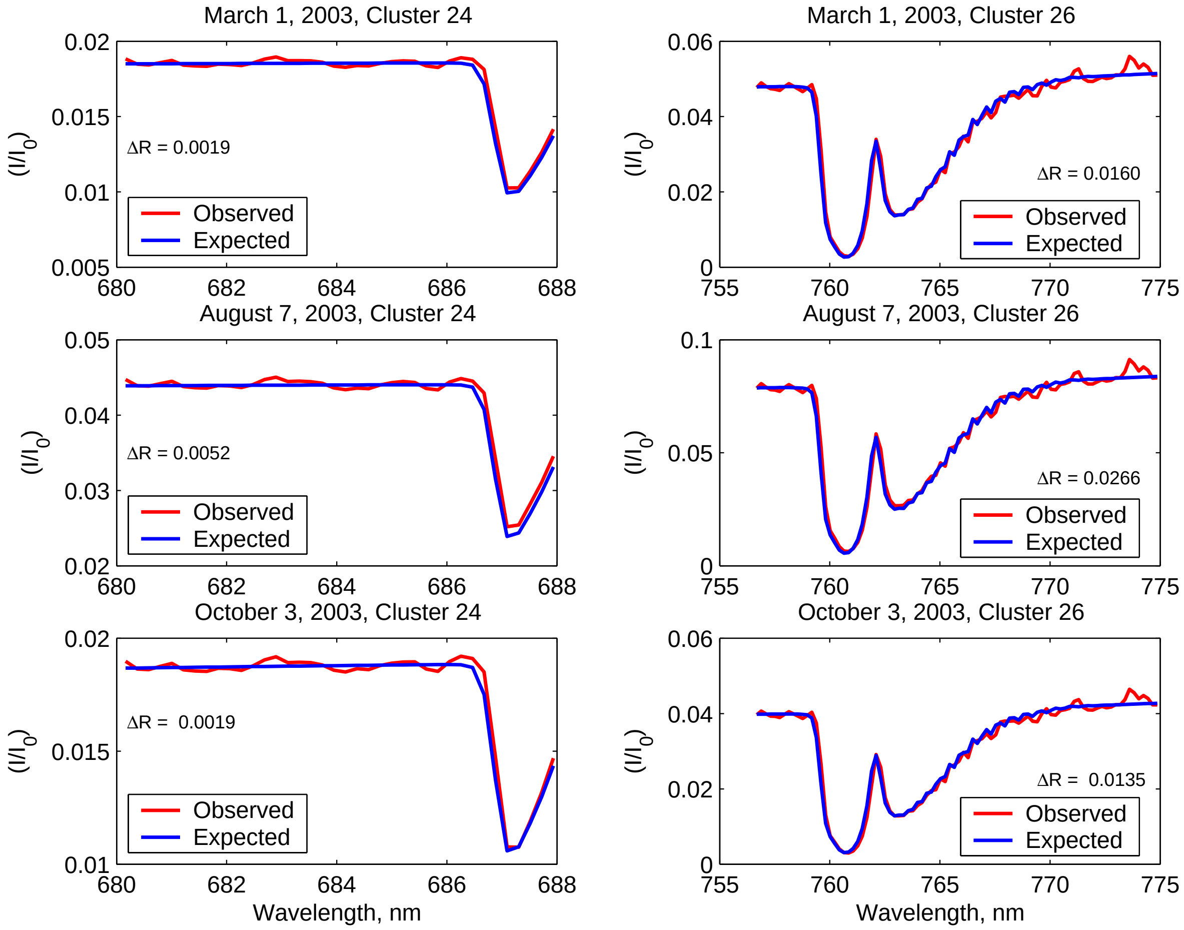

Figure 3.27: Observed (red curve) and expected (blue curve) reflectances under a clear-sky assumption for the selected spectral ranges around the O_2 B and A-bands on the left and right hand sides, respectively. The top panel shows the reflectance spectra for March 1, 2003 yielding discrepancies $\Delta R^B = 0.0019$ and $\Delta R^A = 0.0160$, the middle panel shows the reflectance spectra for August 7, 2003 yielding discrepancies $\Delta R^B = 0.0052$ and $\Delta R^A = 0.0266$ and the bottom panel shows the reflectance spectra for October 3, 2003 yielding discrepancies $\Delta R^B = 0.0019$ and $\Delta R^A = 0.0135$. Based on minimum discrepancy, we choose October 3, 2003 as a clear sky day.

Cloudy and very hazy scenarios become immediately apparent in each case due to highly elevated apparent albedos and negative values of $\rho_A - \rho_B$. Other scenarios having less elevated albedos show considerable variations in both the absolute values of ρ_A and ρ_B, as well as in $\rho_A - \rho_B$. It may be noted, however, that ρ_A consistently remains larger than ρ_B[4], confirming our conjecture that $\rho_A^* > \rho_B^*$ over most land surfaces, the asterisk denoting true values of the albedo.

Over Kanpur, we can observe an increased frequency of elevated albedos ρ_A and ρ_B during the months of June-September, coinciding with the rainy season. Scanning the entire data set, however, and allowing for variation in the absolute values of ρ_A and ρ_B with respect to SZA,

---

[4] except in the case of some measurements over La Parguera that happen to cover mostly ocean surface, where both $\rho_A^* = \rho_B^* \rightarrow 0$

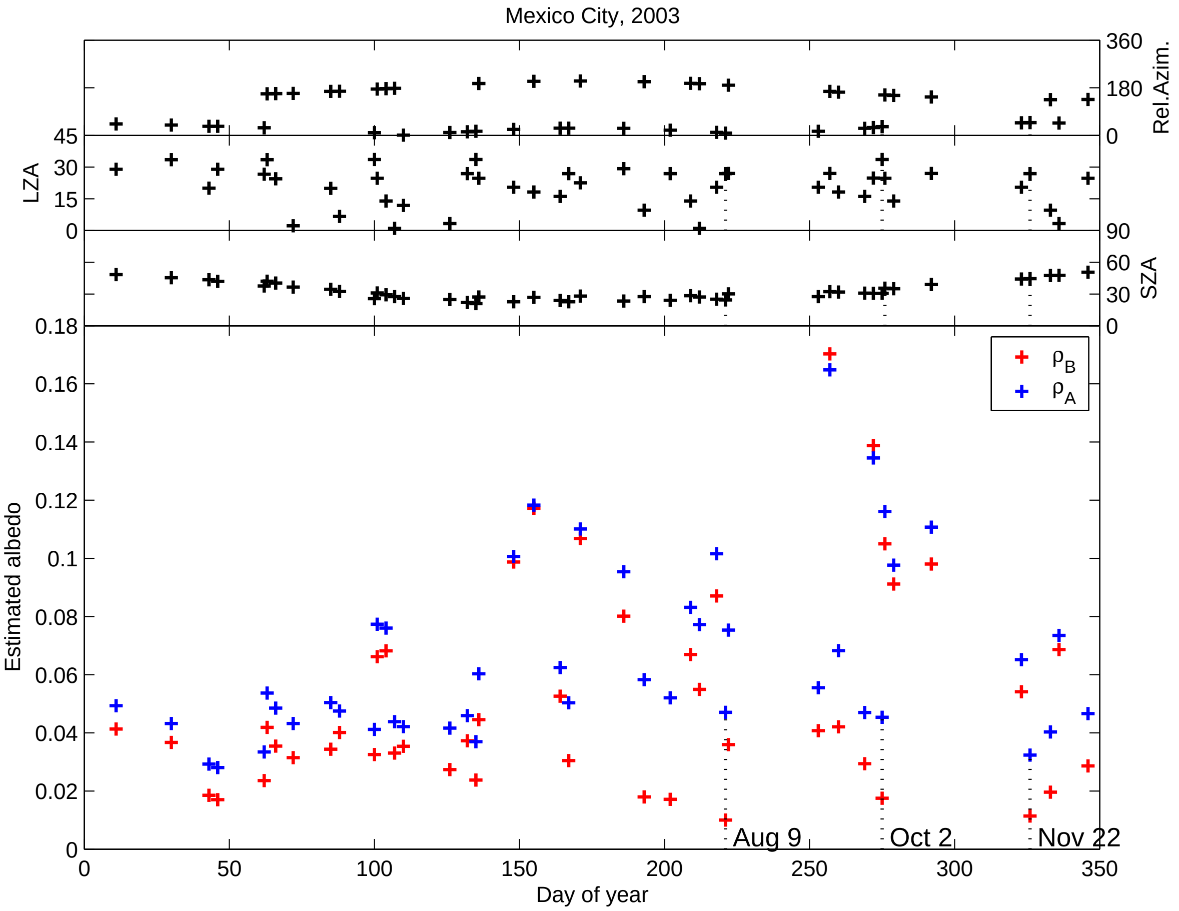

Figure 3.28: Apparent albedos ρ_A (blue crosses) and ρ_B (red crosses) around the O_2 A and B-bands respectively plotted against the day of the year 2003 on which the scenario was recorded by SCIAMACHY over Mexico City, Mexico. Also shown in the first three panels are the solar zenith angle (SZA), the line-of-sight zenith angle (LZA) and the relative azimuthal angle (Rel. Azim.) between the direction of incident (direct) sunlight and the line-of-sight. Dotted lines map these angles and the apparent albedos ρ_A and ρ_B for days that may correspond to clear-sky scenarios.

we are able to identify three scenarios viz. March 1, August 7 and October 3, 2003, exhibiting increased values of $\rho_A - \rho_B$, qualifying them for consideration as clear sky days.

Comparing the discrepancy ΔR between observed and expected reflectances produced by each as shown in Fig. 3.27, we choose Oct 3 as a clear sky day corresponding to a lambertian albedo of $\rho_B^* = 0.024$ around the B-band and $\rho_A^* = 0.056$ around the A-band.

Mexico City exhibits an increased frequency of elevated albedos ρ_A and ρ_B throughout the year except during the dry months of November-April. Again allowing for variation in the absolute values of ρ_A and ρ_B with respect to SZA, we can identify three scenarios viz. August 9, October 2 and November 22, 2003, exhibiting increased values of $\rho_A - \rho_B$, qualifying them for consideration as clear sky days.

From Fig. 3.29 we can see that none of the three scenarios produces a satisfactory fit. Mexico

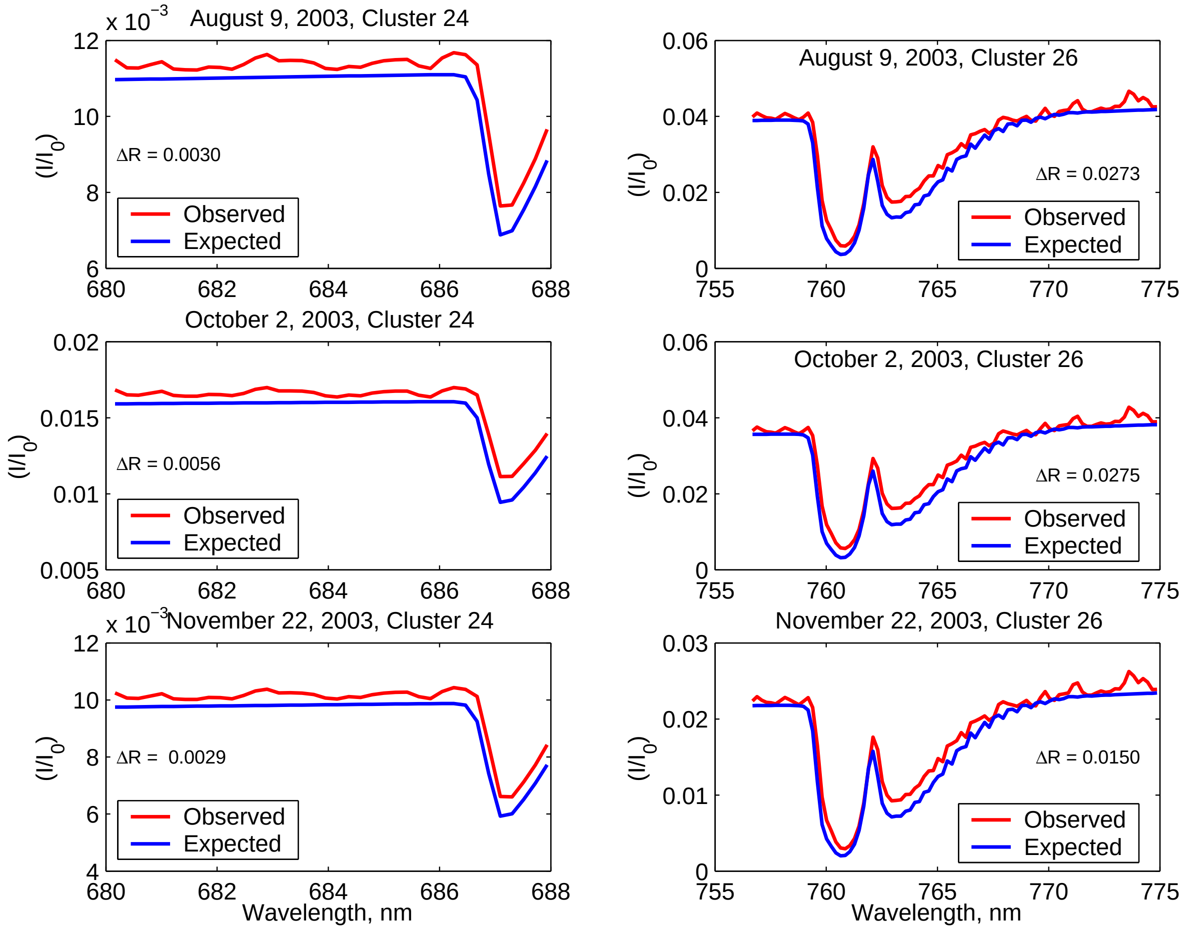

Figure 3.29: Observed (red curve) and expected (blue curve) reflectances under a clear-sky assumption for the selected spectral ranges around the O_2 B and A-bands on the left and right hand sides, respectively. The top panel shows the reflectance spectra for March 1, 2003 yielding discrepancies $\Delta R^B = 0.0019$ and $\Delta R^A = 0.0160$, the middle panel shows the reflectance spectra for August 7, 2003 yielding discrepancies $\Delta R^B = 0.0052$ and $\Delta R^A = 0.0266$ and the bottom panel shows the reflectance spectra for October 3, 2003 yielding discrepancies $\Delta R^B = 0.0019$ and $\Delta R^A = 0.0135$. Based on minimum discrepancy, we choose October 3, 2003 as a clear sky day.

City has a strong surface relief, which makes BRDF effects very probable. Furthermore, it may be improbable to observe a truly aerosol-free scenario in Mexico City, well-known for its photochemical smog. Thus, comparing the discrepancy ΔR between observed and expected reflectances produced by each, the closest choice for a clear sky day corresponds to November 22, 2003, and a lambertian albedo of $\rho_B^* = 0.0114$ around the B-band and $\rho_A^* = 0.0324$ around the A-band.

La Parguera shows relatively uniform reflectances throughout the year, with only two cloudy scenarios registered by SCIAMACHY in 2003. Again, for most scenarios $\rho_A > \rho_B$ to different extents depending on the aerosol loading. However, we also observe a few scenarios with both ρ_A and ρ_B approaching zero. These scenarios are typical of measurements over the ocean surface, caused in this case by the coastal location of La Parguera and the uneven overlap

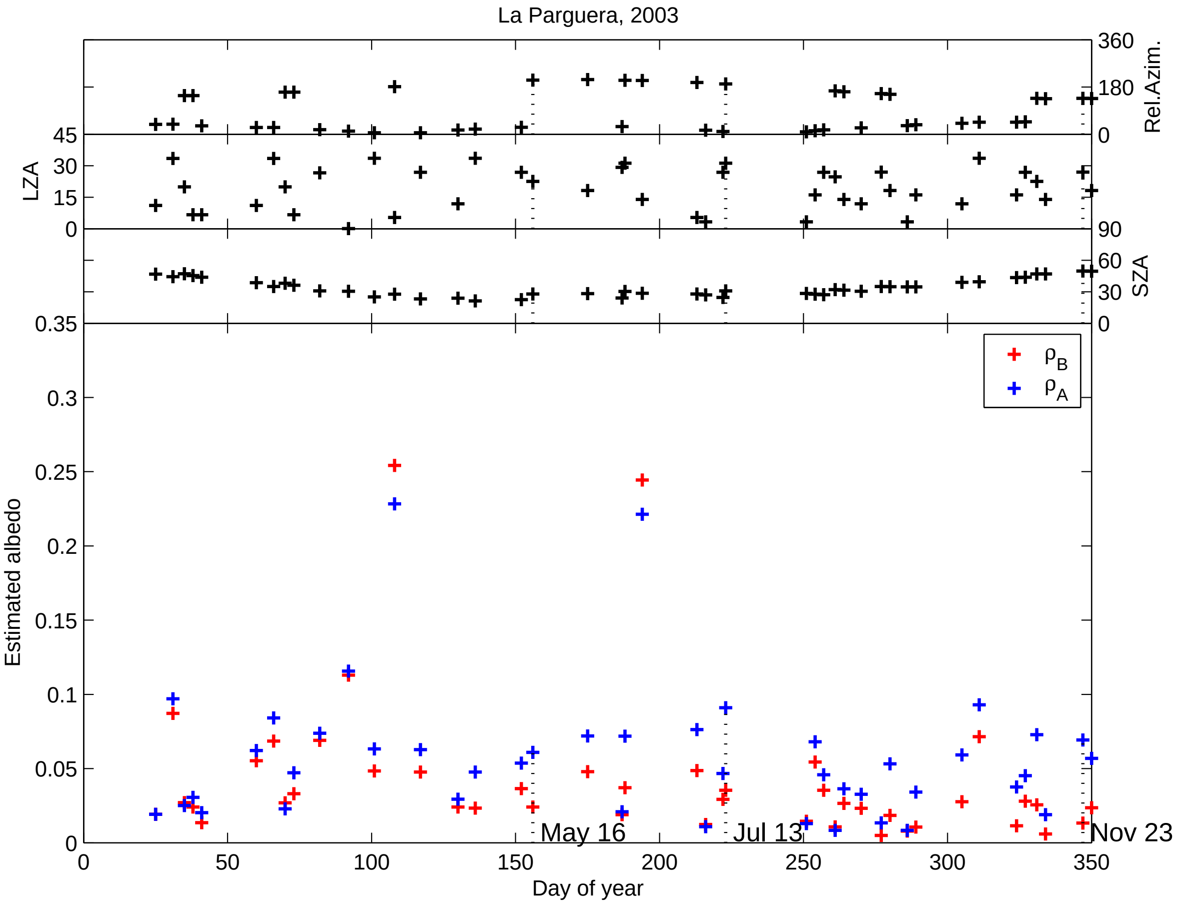

Figure 3.30: Apparent albedos ρ_A (blue crosses) and ρ_B (red crosses) around the O_2 A and B-bands respectively plotted against the day of the year 2003 on which the scenario was recorded by SCIAMACHY over La Parguera, Puerto Rico, USA. Also shown in the first three panels are the solar zenith angle (SZA), the line-of-sight zenith angle (LZA) and the relative azimuthal angle (Rel. Azim.) between the direction of incident (direct) sunlight and the line-of-sight. Dotted lines map these angles and the apparent albedos ρ_A and ρ_B for days that may correspond to clear-sky scenarios.

between the ground pixels covered by successive SCIAMACHY overpasses over a given location. We shall ignore these measurements as we wish to determine the albedo over land. Scanning the entire data set and allowing for variation in the absolute values of ρ_A and ρ_B with respect to SZA, we identify potentially clear-sky three scenarios viz. May 15, July 12 and November 22, 2003. Comparing the discrepancy ΔR between observed and expected reflectances produced by each, we choose November 23, 2003 as a clear sky day corresponding to a lambertian albedo of $\rho^*_B = 0.028$ around the B-band and $\rho^*_A = 0.0453$ around the A-band.

While the above procedure has limitations in the presence of strong BRDF effects and high seasonality, it provides a robust method for clear-sky identification and albedo determination over ground pixels where the surface reflectance may be safely approximated to be lambertian. The statistical accuracy and usability of the retrieved albedo for aerosol retrievals on other days of the year is dependent on the strength of seasonal changes and, over a longer term,

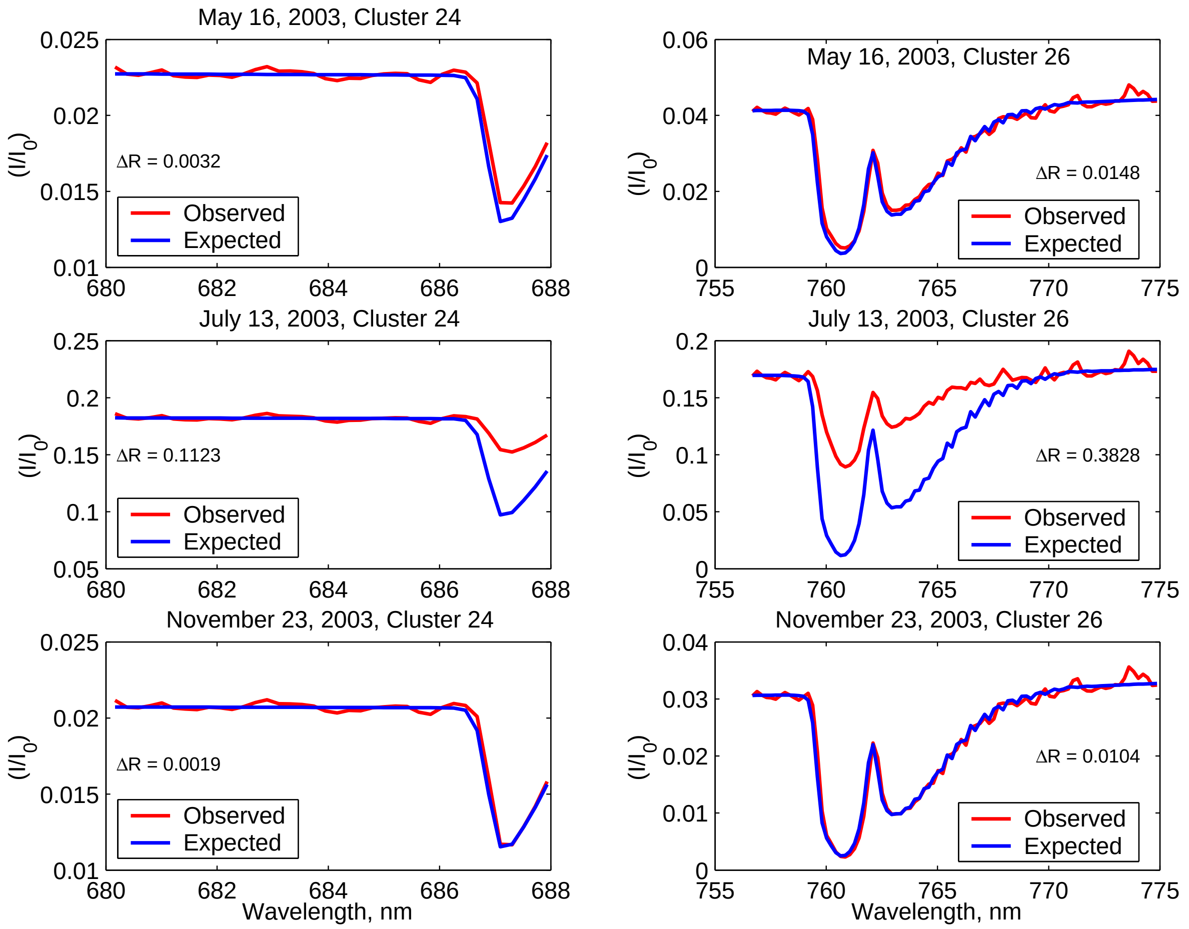

Figure 3.31: Observed (red curve) and expected (blue curve) reflectances under a clear-sky assumption for the selected spectral ranges around the O_2 B and A-bands on the left and right hand sides, respectively. The top panel shows the reflectance spectra for March 1, 2003 yielding discrepancies $\Delta R^B = 0.0019$ and $\Delta R^A = 0.0160$, the middle panel shows the reflectance spectra for August 7, 2003 yielding discrepancies $\Delta R^B = 0.0052$ and $\Delta R^A = 0.0266$ and the bottom panel shows the reflectance spectra for October 3, 2003 yielding discrepancies $\Delta R^B = 0.0019$ and $\Delta R^A = 0.0135$. Based on minimum discrepancy, we choose October 3, 2003 as a clear sky day.

on the rate of land use changes. In the following chapters we develop and use an algorithm for aerosol retrieval employing the albedos determined using our method as a primary input parameter. In Chapter 5, we test our retrieval algorithm for measurements over Kanpur in 2003, choosing it over Mexico City due to the difficulty in estimating a clear-sky day scenario and potential BRDF effects and over La Parguera due to the possibility of increased patchiness in the albedos contained within the ground pixel as a result of its coastal location.

Chapter 4

Method for retrieval of aerosol from satellite measurements around the O_2 A- and B-bands: synthetic studies

In this chapter, we lay out the theoretical basis for the retrieval of aerosols from SCIAMACHY data. The number of retrievable aerosol parameters depends on the information content of the measurement. We discuss the choice of our measurement vector, aimed at maximizing the information contained in it without introducing too much redundancy which costs valuable computing time. We compare the use of only O_2 A-band measurements with the use of both O_2 A- and B-bands for our retrieval with regard to information content. Having chosen our measurement vector and a state vector composed of the aerosol parameters to be retrieved from the measurement, we proceed to formulate our retrieval problem in terms of the radiative transfer involved. We solve this problem using the method of Optimal Estimation. To conclude, we present synthetic studies carried out with our retrieval algorithm as a test of its reliability.

4.1 Parametrization of aerosols: the state vector

The quantities describing the aerosol scenario, that are to be retrieved can be represented by a state vector, $\vec{x}$, with n elements, $x_1, x_2, x_3, \ldots x_n$.

As seen in Section 2.6, aerosols can be described by their microphysical (complex refractive index and size distribution) and macrophysical (vertical profile, AOT, Ångström exponent, single scattering albedo and phase function) parameters. The optical parameters AOT, the Ångström exponent, single scattering albedo and phase function, which are functions of all the microphysical parameters, play a direct role in radiative transfer, making them the least difficult to retrieve. The AOT and Ångström exponent are direct functions of the extinction coefficient of the aerosol, which is expected to produce stronger variation in the observed reflectance with respect to wavelength than the phase function and the single scattering albedo, which show little variation with respect to wavelength across wide spectral neighborhoods. Based on this, we choose the AOT and the Ångström exponent as variables to be included in our state vector, while fixing the values of the phase function and single scattering albedo of the aerosol according to an a priori assumption regarding the aerosol type over a given ground pixel, made on the basis of the geographical (continental, coastal, desert) and the socio-economic (urban, rural, clean, polluted) background of the location being observed.

Reflectances at a few wavelengths, preferably in spectral windows devoid of strong absorption as shown in Fig. 3.3, suffice for the calculation of the AOT and Ångström exponent. However, we also have at our disposal absorption spectra of species with well-known vertical profiles such as O_2, O_4 and CO_2, which also provide us with some information on the vertical extent of the aerosol. A similar approach was employed by *Koppers et al.* (1997) for retrieving aerosol optical thickness from GOME data.

An individual absorption structure, though, offers only partial information regarding the aerosol vertical profile, e.g. very strong lines of O_2 absorption like the R-branch of the A-band reach saturation long before reaching the ground, thus missing any information on aerosols in the lower troposphere. Absorption due to O_4, on the other hand, is weak enough not to reach saturation, potentially providing more information on aerosols present close to the ground where O_4 concentration is highest. We attempt to maximize the information available by combining the use of different absorption spectra. Taking advantage of the fact that the vertical profile of atmospheric aerosols can, in most cases, be approximated by a log-normal function defined only by a peak height and a peak width, we reduce the number of parameters required to describe the profile those two variables, making our vertical representation of aerosols responsive to higher vertical spatial resolution without introducing additional parameters into the state vector.

Thus, we describe the aerosol to be retrieved using four parameters in all: the aerosol optical thickness, τ_λ, the Ångström exponent α_λ, the peak height z_p and the peak width σ_p of the vertical distribution of the aerosol. The subscript λ denotes the reference wavelength at which the aerosol optical thickness and the Ångström exponent are measured. We shall see in the next section that the choice of the measurement vector will influence the reference wavelength denoted by λ.

4.2 Choice of measurement vector

The quantities actually measured in order to retrieve the state vector $\vec{x}$ can be represented by the measurement vector, $\vec{y}$, with m elements, $y_1, y_2, y_3, \ldots y_m$. This vector contains measured quantities that are functions of elements of the state vector.

Examining the reflectance spectrum of SCIAMACHY (see Fig. 3.2), we see several non-absorbing spectral windows and absorption structures.

In case of non-absorbing windows, the UV region would be most sensitive to high altitude aerosols such as those formed during a volcanic eruption, since the bulk of the incident sunlight at those wavelengths is already scattered before it penetrates the lower atmosphere. This part of the SCIAMACHY spectrum, however, is marred by severe radiometric fluctuations, making it difficult to use it for aerosol retrieval. Thankfully, high altitude aerosols do not have strongly interfering signals under normal circumstances. The optical depth to which radiation of a given wavelength is most sensitive increases from the blue end of the visible spectrum towards the red end, as Rayleigh scattering subsides ($\propto 1/\lambda^4$). The NIR, where a clear aerosol signal could be expected due to a negligible Rayleigh contribution to scattering and low multiple scattering, is also rendered useless by radiometric fluctuations and uncertainties regarding the instrumental slit function owing to the formation of ice layers on the detector.

The absorption structures of species with known vertical profiles include lines of O_4 absorption between 340nm and 660nm in the UV-VIS and between 1000nm and 1140nm in the NIR, the O_2 A (approx. $757-771$nm), B (approx. $687-700$nm) and other minor bands, eg. around 630nm, and the CO_2 absorption bands around 1500nm and 2000nm. All bands, excepting the O_2 bands and the O_4 bands between 500 and 660nm, lie in spectral regions where radiometric fluctuations are erratic. The O_2 band around 630nm and the O_4 bands between 500 and 660nm lie in cluster 18 of channel 4 of the detector, which, while being free of strong radiometric fluctuations, has a longer intergration time and thus a greater ground pixel size than the other clusters, making it impossible to combine its use with the O_2 A and B-bands. Furthermore, we have to discard the portion of the B-band lying beyond 690nm as it coincides with absorption due to water vapour, whose abundance and vertical distribution is highly variable in the atmosphere.

Hence, we choose our measurement vector to be a composite of the reflectances measured in and around the O_2 A-band $756.5-775$nm, the part of the B-band free of water-vapor absorption $680-688$nm. These spectral ranges include neighbouring spectral windows devoid of absorption. As 700nm lies between both these wavelength ranges, we shall use it as the reference wavelength at which the aerosol parameters τ and α are retrieved, resulting in the state vector $\{\tau_{700}, \alpha_{700}, z_p, \sigma_p\}$.

4.3 Basic principle: Optimal estimation

Having defined the state and measurement vectors of the retrieval, the main elements of the method of optimal estimation (*Rodgers*, 2000) are outlined in the following, using an example (synthetic) retrieval for illustration whenever applicable.

4.3.1 The forward model, $\mathbf{F}(\vec{x})$

Each state vector maps to an ideal measurement vector $\vec{y_I}$ governed by the physics of the measurement. Denoting the physics of the measurement by a forward function $\mathbf{f}(\vec{x})$, we can write

$$\vec{y_I} = \mathbf{f}(\vec{x}). \tag{4.1}$$

In practice, though, we have a measurement error, ϵ, associated with the measurement vector, and the physics of the measurement can only be approximated by a forward model $\mathbf{F}(\vec{x})$, which in our case is AeroRad (see Chapter 2). Thus, the relationship between the state and the measurement vectors is given by

$$\vec{y} = \mathbf{F}(\vec{x}) + \vec{\epsilon}. \tag{4.2}$$

The construction of the forward model entails a knowledge of how the measuring device works and an understanding of how the quantity measured, viz. the reflectance at a chosen wavelength, is related to the one that is really wanted, viz. the aerosol parameters represented by the state vector elements. Since the physics of the measurement is generally too complicated, approximations (such as replacing continuous functions with discrete approximations) have to be made in order to construct the model, thereby introducing modeling errors.

4.3.2 The Jacobi matrix, K

The jacobian or the weighting function matrix, $\mathbf{K}$, is an $m \times n$ matrix in which each element is the partial derivative of a forward model element with respect to a state vector element, i.e. $K_{ij} = \partial F_i(\vec{x})/\partial x_j$.

If $\mathbf{F}(\vec{x})$ is linear within the error bounds of the retrieval, the forward model can be linearized about some reference state $\vec{x_0}$ as

$$\vec{y} - \mathbf{F}(\vec{x_0}) = \frac{\partial \mathbf{F}(\vec{x})}{\partial \vec{x}}(\vec{x} - \vec{x_0}) + \epsilon = \mathbf{K}(\vec{x} - \vec{x_0}) + \epsilon \tag{4.3}$$

If $m < n$, the problem represented by Eq.4.3 is said to be underconstrained since there are fewer measurements than unknowns, whereas if $m > n$, the problem is described as overconstrained. This, however, is an oversimplification, as the m rows of the jacobian matrix, $\vec{k_j}$, span a subspace of state space of dimension not greater than m (less than m in the case where the vectors are not linearly independent). The dimension of this subspace is known as the rank p of the matrix $\mathbf{K}$, and is equal to the number of linearly independent rows or columns of $\mathbf{K}$.

The rank p cannot be greater than n, even if $m > n$, and may even be less than n. Thus, only p components of the state vector contribute to the measurement vector. The remaining $n - p$ components do not contribute to the measurement, i.e. they are unmeasureable. This undetermined part of the state space is referred to as the null space. If a retrieved state has components that lie in the null space, their values cannot have been obtained from the measurements. The null space can be identified by singular value decomposition of the Jacobian matrix $\mathbf{K}$.

4.3.3 Bayes' Theorem

The Optimal Estimation method is based on Bayesian theory, which provides a formalism with which to express uncertainly in measurements and the resulting uncertainly in retrievals. The retrieval method ensures that the latter is as small as possible.

Bayes' theory states that

$$P(\vec{x}|\vec{y}) = \frac{P(\vec{y}|\vec{x})P(\vec{x})}{P(\vec{y})}, \tag{4.4}$$

where $P(\vec{x}|\vec{y})$ is the posterior probability density function (*pdf*) of the state vector $\vec{x}$ when the measurement $\vec{y}$ is given. This is the quantity of interest for solving the inverse problem. $P(\vec{x})$ is the prior knowledge of the state that is to be updated using the measurement. $P(\vec{y}|\vec{x})$ describes the knowledge of $\vec{y}$ that would be obtained given state $\vec{x}$. $P(\vec{y})$ is the *pdf* of the measurement before it is made (this is only a normalizing factor that is generally not needed).

This lays down the following conceptual approach to the inverse problem:

- Before making a measurement, prior knowledge of the state (and the measurement) are expressed as a prior *pdf*,
- The measurement process is expressed as a forward model mapping the state space into measurement space,
- Bayes' theorem provides a formalism to invert this mapping and calculate a posterior *pdf* by updating the prior *pdf* with a measurement *pdf*.

4.3.4 Uncertainties associated with the measurement and the a priori state vector: the covariance matrices $\mathbf{S}_\epsilon$ and $\mathbf{S}_\mathbf{a}$

Assuming a Gaussian distribution, the *pdf*'s of the measurement and the a priori state can each be described in terms of a value of maximum probability (expected value) and the covariance of the distribution about the expected value. In the case of the measurement, this expected value is represented by the actual measurement denoted here as $\bar{\vec{y}}$, and the covariance matrix associated with the measurement is given by $\mathbf{S}_\epsilon$ where

$$S_{\epsilon\ ij} = E\left\{(y_i - \bar{y_i})(y_j - \bar{y_j})\right\}, \tag{4.5}$$

where E is the expected value operator.

SCIAMACHY reflectance measurements around the $\mathsf{O_2}$ A and B bands have a standard deviation of about 2% about the measured value due to instrumental noise. This corresponds to an absolute standard deviation of 0.02 for the logarithm of the reflectances. The errors associated with different parts of the measurement spectrum may be assumed to be uncorrelated, so that only the diagonal elements of S_ϵ have the non-zero value of 0.0004.

For the a priori state, the expected value is represented by the an a priori assumption (obtained generally from climatology or as a first guess) denoted here as $\vec{x_a}$, and the covariance matrix associated with the a priori state is given by $\mathbf{S_a}$ where

$$S_{a\,ij} = E\left\{(x_i - x_{a\,i})(x_j - x_{a\,j})\right\}. \tag{4.6}$$

The a priori assumption for the state vector used in our retrieval includes a fixed first guess of 0.5 for the AOT τ_{700} and of 0.0 for the Ångström exponent α_{700}.

The a priori parameters describing the vertical distribution are obtained from the climatology listed in Table 2.6 for the chosen aerosol type. As mentioned before, the a priori choice of the aerosol type, made in accordance with the location being observed, also fixes the single scattering characteristics of the aerosol.

4.3.5 Degrees of freedom

While there are p independent pieces of information that can, in principle, be determined from the measurement in the absence of experimental error, these p values become uncertain to some extent in the presence of error, which may be large enough to reduce the number of useful independent pieces of information, also called the 'effective' rank of the problem, to less than p. The effective rank, p', is determined by a transformation called 'prewhitening', which transforms noise into white noise (*Rodgers*, 2000). Consequently, the effective rank of the problem, p', or the number of independent measurements made to better than measurement error, is the number of singular values of $\mathbf{S}_\epsilon{}^{-\frac{1}{2}}\mathbf{K}\mathbf{S_a}{}^{\frac{1}{2}}$ greater than about unity.

It should be noted that the uncertainty in the retrieved state arises from two sources: in the simple case of one degree of freedom, it would be due to prior variance σ_a and that due to measurement error σ_ϵ. If $\sigma_a \gg \sigma_\epsilon$, then the measurement will be providing more information about the state, but if $\sigma_a \ll \sigma_\epsilon$, then it will be providing information about the measurement noise ϵ. In the first case, the measurement can be seen as providing a 'degree of freedom for signal', d_s, and in the second case a 'degree of freedom for noise', d_n. The 'degree of freedom for signal', d_s, can be expressed as

$$\begin{aligned} d_s &= E\left\{(\hat{x} - x_a)^T \mathbf{S}_a^{-1} (\hat{x} - x_a)\right\} \\ &= E\left\{\mathsf{tr}\left[(\hat{x} - x_a)^T (\hat{x} - x_a)\mathbf{S}_a^{-1}\right]\right\} \\ &= \mathsf{tr}(\mathbf{S}_{\hat{x}}\mathbf{S_a^{-1}}), \end{aligned} \tag{4.7}$$

where $\mathbf{S}_{\hat{x}}$ can be shown to have the form

$$\mathbf{S}_{\hat{x}} = \mathbf{S}_a\mathbf{K}^T\left(\mathbf{K}\mathbf{S}_a\mathbf{K}^T + \mathbf{S}_\epsilon\right)^{-1}\mathbf{K}\mathbf{S}_a, \tag{4.8}$$

resulting in

$$d_s = \mathsf{tr}\left(\left[\mathbf{K}^T\mathbf{S}_\epsilon^{-1}\mathbf{K} + \mathbf{S}_a^{-1}\right]^{-1}\mathbf{K}^T\mathbf{S}_\epsilon^{-1}\mathbf{K}\right). \tag{4.9}$$

The matrix

$$\mathbf{A} = \left[\mathbf{K}^T\mathbf{S}_\epsilon^{-1}\mathbf{K} + \mathbf{S}_a^{-1}\right]^{-1}\mathbf{K}^T\mathbf{S}_\epsilon^{-1}\mathbf{K} \tag{4.10}$$

is known as the averaging kernel matrix, representing the sensitivity of the estimated state vector to the true state. The matrix

$$\mathbf{G} = \left[\mathbf{K}^T\mathbf{S}_\epsilon^{-1}\mathbf{K} + \mathbf{S}_a^{-1}\right]^{-1}\mathbf{K}^T\mathbf{S}_\epsilon^{-1} \tag{4.11}$$

is known as the gain matrix, which represents the sensitivity of the estimated state vector to the measurement, yielding the relation $\mathbf{A} = \mathbf{GK}$.

Thus,

$$d_s = \mathsf{tr}\left(\mathbf{A}\right). \tag{4.12}$$

4.3.6 Information content of a measurement

The information content according to Shannon can be defined qualitatively as the factor by which knowledge of a quantity is improved by making a measurement. In information theory, the logarithm of this factor to the base of 2 is used in order to express it in units of ’bits’. Thus, if $P_1(x)$ and $P_2(x)$ describe the knowledge of state x before and after a measurement, the information content of the measurement is the reduction in entropy

$$H = S(P_1) - S(P_2), \tag{4.13}$$

where, using the *pdf* $P(x)$ of the state x as a measure of knowledge of the system and analogous to the thermodynamic definition, the entropy $S(P)$ is defined as

$$S(P) = -k\Sigma_i \, p_i \log p_i, \tag{4.14}$$

where p_i is the probability of the system being in state i, $k = 1$ and the logarithm is (usually) taken to base two. Thus, for the linear gaussian case, the information content may be expressed as

$$\begin{aligned} H &= S\left[P(\vec{x})\right] - S\left[P(\vec{x}|\vec{y})\right] \text{ (in state space)} \\ &= S\left[P(\vec{y})\right] - S\left[P(\vec{y}|\vec{x})\right] \text{ (in measurement space)} \\ &= -\frac{1}{2}\ln|\mathbf{I} - \mathbf{A}|, \end{aligned} \tag{4.15}$$

where the expression for $\mathbf{A}$ is given in 4.12.

4.3.7 The retrieval method

The retrieval $\mathbf{R}$ is a function that operates on the measurement resulting in the retrieval of the state vector $\hat{\vec{x}}$, so that

$$\hat{\vec{x}} = \mathbf{R}(\vec{y}, \hat{\vec{b}}, \vec{x_a}, \vec{c}), \tag{4.16}$$

where, as in Eq.4.2, $\vec{y}$ denotes the measurement vector. The vector $\hat{\vec{b}}$ represents the best estimate of the set of forward function parameters not included in the state vector. In case of our aerosol retrieval, these parameters include the vertical pressure and temperature profiles, concentration profiles of various atmospheric trace gases (obtained from climatology) and the ground albedo determined as described in Chapter 3. The vectors $\vec{x_a}$, denoting the a priori state vector, and $\vec{c}$ comprising retrieval method parameters such as convergence criteria, do not appear in the forward function but still affect the retrieval and may be subject to uncertainty.

Linearization of the above equation results in the following relationship

$$\begin{aligned} \hat{\vec{x}} - \vec{x_a} &= \mathbf{R}(\mathbf{F}(\vec{x_a}, \hat{\vec{b}}), \hat{\vec{b}}, \vec{x_a}, \vec{c}) \;\ldots\text{bias} \\ &+ \mathbf{A}(\vec{x} - \vec{x_a}) \;\ldots\text{smoothing} \\ &+ \mathbf{G}_y \vec{\epsilon_y} \;\ldots\text{retrieval error}, \end{aligned} \tag{4.17}$$

where $\mathbf{A}$ and $\mathbf{G}_y$ are the averaging kernel and gain matrix respectively and

$$\vec{\epsilon_y} = \mathbf{K}_b(\vec{b} - \hat{\vec{b}}) + \Delta f(\vec{x}, \vec{b}, \vec{b'}) + \vec{\epsilon} \tag{4.18}$$

is the total measurement error relative to the forward model. Since $\mathbf{R}(\mathbf{F}(\vec{x_a}, \hat{\vec{b}}), \hat{\vec{b}}, \vec{x_a}, \vec{c}) = \vec{x}_a$, the bias in Eq.4.17 is expected (and found) to be zero, resulting in

$$\hat{\vec{x}} = \vec{x}_a + (\mathbf{I}_n - \mathbf{A})\vec{x}_a + \mathbf{A}\vec{x} + \mathbf{G}_y \epsilon_y, \tag{4.19}$$

so that, in an ideal inverse method, $\mathbf{A}$ would be a unit matrix. In practice though, the rows of $\mathbf{A}$ are peaked functions, peaking at the approriate level. The vector of areas of the averaging kernel, defined as $\mathbf{A}\vec{u}$, where $\vec{u}$ is a vector with unit elements, is found to be approximately unity at levels where the retrieval is accurate (see Fig. 4.2), and can in general be thought of as the fraction of the retrieval that comes from the data rather than the a priori.

For error analysis, the remaining terms of Eq. 4.17 can be rearranged using Eq.4.18, so that

$$\begin{aligned} \hat{\vec{x}} - \vec{x} &= (\mathbf{A} - \mathbf{I}_n)(\vec{x} - \vec{x_a}) \;\ldots\text{smoothing error} \\ &+ \mathbf{G}_y \mathbf{K}_b(\vec{b} - \hat{\vec{b}}) \;\ldots\text{model parameter error} \\ &+ \mathbf{G}_y \Delta\mathbf{f}(\vec{x}, \vec{b}, \vec{b'}) \;\ldots\text{forward model error} \\ &+ \mathbf{G}_y \vec{\epsilon} \;\ldots\text{retrieval noise}, \end{aligned} \tag{4.20}$$

To developing an optimal inverse method, one approach is to use the posteriori *pdf* of the state vector, representing the solution as the expected value of the state, together with the second moment (covariance) matrix as a measure of the uncertainty of the solution. The maximum a posteriori solution to a linear gaussian problem can be written as follows:

$$\hat{\vec{x}} = \vec{x_a} + (\mathbf{K}^T \mathbf{S}_\epsilon^{-1} \mathbf{K} + \mathbf{S}_a^{-1})^{-1} \mathbf{K}^T \mathbf{S}_\epsilon^{-1} (\vec{y} - \mathbf{K}\vec{x_a}). \tag{4.21}$$

Its covariance is given by

$$\hat{\mathbf{S}} = \left(\mathbf{K}^T \mathbf{S}_\epsilon^{-1} \mathbf{K} + \mathbf{S}_a^{-1}\right)^{-1}. \tag{4.22}$$

The above solution is adapted to our non-linear problem using Gauss-Newton iteration, which results in

$$\vec{x}_{i+1} = \vec{x}_a + (\mathbf{K}_i^T \mathbf{S}_\epsilon^{-1} \mathbf{K}_i + \mathbf{S}_a^{-1})^{-1} \left[\mathbf{K}_i^T \mathbf{S}_\epsilon^{-1} (\vec{y} - \mathbf{F}(\vec{x}_i)) + \mathbf{K}_i(\vec{x}_i - \vec{x}_a)\right]. \tag{4.23}$$

For convenience, the iteration is started with $\vec{x}_0 = \vec{x}_a$. The iterations are assumed to have converged when the difference in the solutions obtained during consecutive iterations is an order of magnitude smaller than the estimated error. Thus our test of convergence is

$$d_i^2 = (\vec{x}_i - \vec{x}_{i+1})^T \hat{\mathbf{S}}^{-1} (\vec{x}_i - \vec{x}_{i+1}) \ll n, \tag{4.24}$$

where

$$\hat{\mathbf{S}} = \left(\mathbf{K}_i^T \mathbf{S}_\epsilon^{-1} \mathbf{K}_i + \mathbf{S}_a^{-1}\right)^{-1}. \tag{4.25}$$

4.4 Sensitivity studies

To determine the sensitivity of our retrieval, we construct synthetic measurements of different scenarios using our model. These measurements are inverted using our method with a uniform a priori, $\vec{x}_a = \{\tau_{700}\colon 0.5, \alpha_{700}\colon 0, z_p\colon 3\mathsf{km}, \sigma_p\colon 0.693\}$. The use of synthetic measurements eliminates forward model error, since the forward function is identical to the forward model. We also eliminate model parameter error by choosing $\hat{\vec{b}} = \vec{b}$. Thus the only sources of error involved are due to smoothing and measurement noise ϵ. While we assume a measurement noise of 2% for the construction of $\mathbf{S}_\epsilon$, we analyze each scenario for an actual measurement noise of 1% and 3% (see Fig. 4.1) respectively. The red circles in Fig. 4.1 represent a measurement noise, $\epsilon = 1\%$, while the blue circles represent $\epsilon = 3\%$. Crossed circles indicate that the iterations failed to achieve the desired convergence.

4.4.1 Sensitivity to aerosol optical thickness, τ_{700}

For determining the behaviour of the retrieval with respect to AOT, we create synthetic scenarios where all other state vector elements are kept constant, varying only the AOT, τ_{700}. From Fig. 4.1, we can see that in the presence of increased measurement noise, the retrieval consistently fails to meet the required convergence conditions (crossed blue circles). Furthermore, the accuracy of the retrieval deteriorates at high AOT. This leads to the conclusion that smoothing error increases with respect to AOT. The overall accuracy of the retrieval, however, improves with increase in AOT. This is as expected from the increase in averaging kernel areas with increasing AOT (see the top left panel of Fig. 4.2) and is also observed in the retrieved data.

The averaging kernel area corresponding to all the retrieved parameters is nearly one at $\tau_{700} = 1$, suggesting a high information content of the measurement data at high AOT, making the retrieval independent of the a priori. For $\tau_{700} = 0.1$ and $\tau_{700} = 0.5$, there occurs a slight dip in the averaging kernel area associated with τ_{700} and a strong dip with respect to σ_p, other values remaining largely unaltered, indicating in the case of σ_p a loss in the information content of the measurement with respect to vertical peak height at low values of aerosol optical thickness. An aerosol-free scenario obviously does not contain any information about its vertical profile, as is reflected by the negligible averaging kernel areas corresponding to z_p and σ_p at $\tau_{700} = 0$.

Since $\mathbf{S}_a$ and $\mathbf{S}_\epsilon$ are independent of the state vector, $\mathbf{A}$ depends on $\vec{x}$ through the jacobian $\mathbf{K}$. Fig. 4.3 shows the four columns of the jacobian matrix representing the partial derivatives of

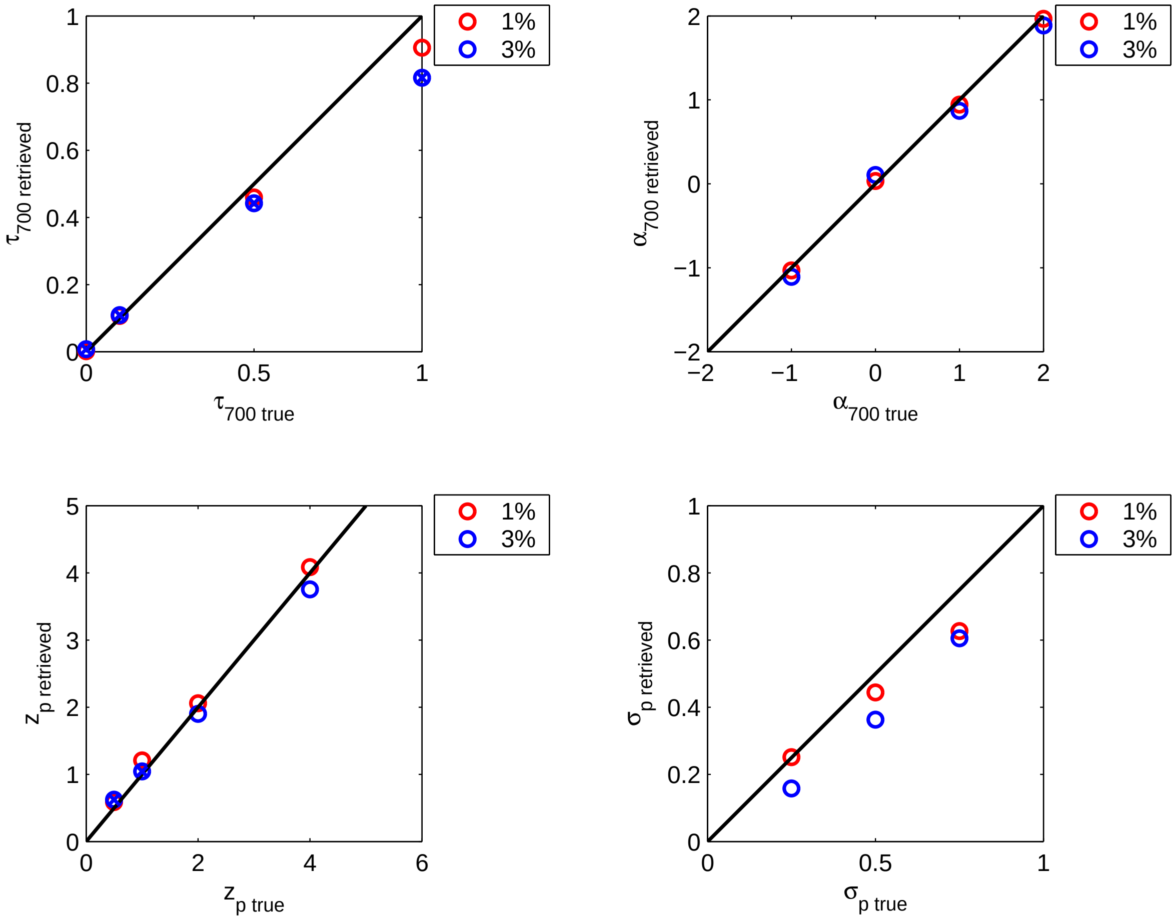

Figure 4.1: The top left panel shows plots of retrieved aerosol optical thickness against the true value for which the synthetic measurement is made. The other components of the true state vector are $\{\alpha_{700}\colon 0, z_p\colon 0.5\mathsf{km}, \alpha_{700}\colon 0.25\}$. The top right panel shows plots of retrieved Ångström exponent against its true value. The other components of the true state vector are $\{\tau_{700}\colon 0.5, z_p\colon 2.0\mathsf{km}, \alpha_{700}\colon 0.75\}$. The lower left panel shows plots of the retrieved peak height of the aerosol vertical distribution against the true value for which the synthetic measurement is made. The other components of the true state vector are $\{\tau_{700}\colon 0.5, \alpha_{700}\colon 0, \sigma_p\colon 0.25\}$. The lower right panel shows plots of the retrieved peak width of the aerosol vertical distribution against the true value for which the synthetic measurement is made. The other components of the true state vector are $\{\tau_{700}\colon 0.5, \alpha_{700}\colon 0, z_p\colon 2.0\}$. The red circles represent a measurement noise, $\epsilon = 1\%$, while the blue circles represent $\epsilon = 3\%$. Crossed circles indicate that the iterations failed to achieve the desired convergence.

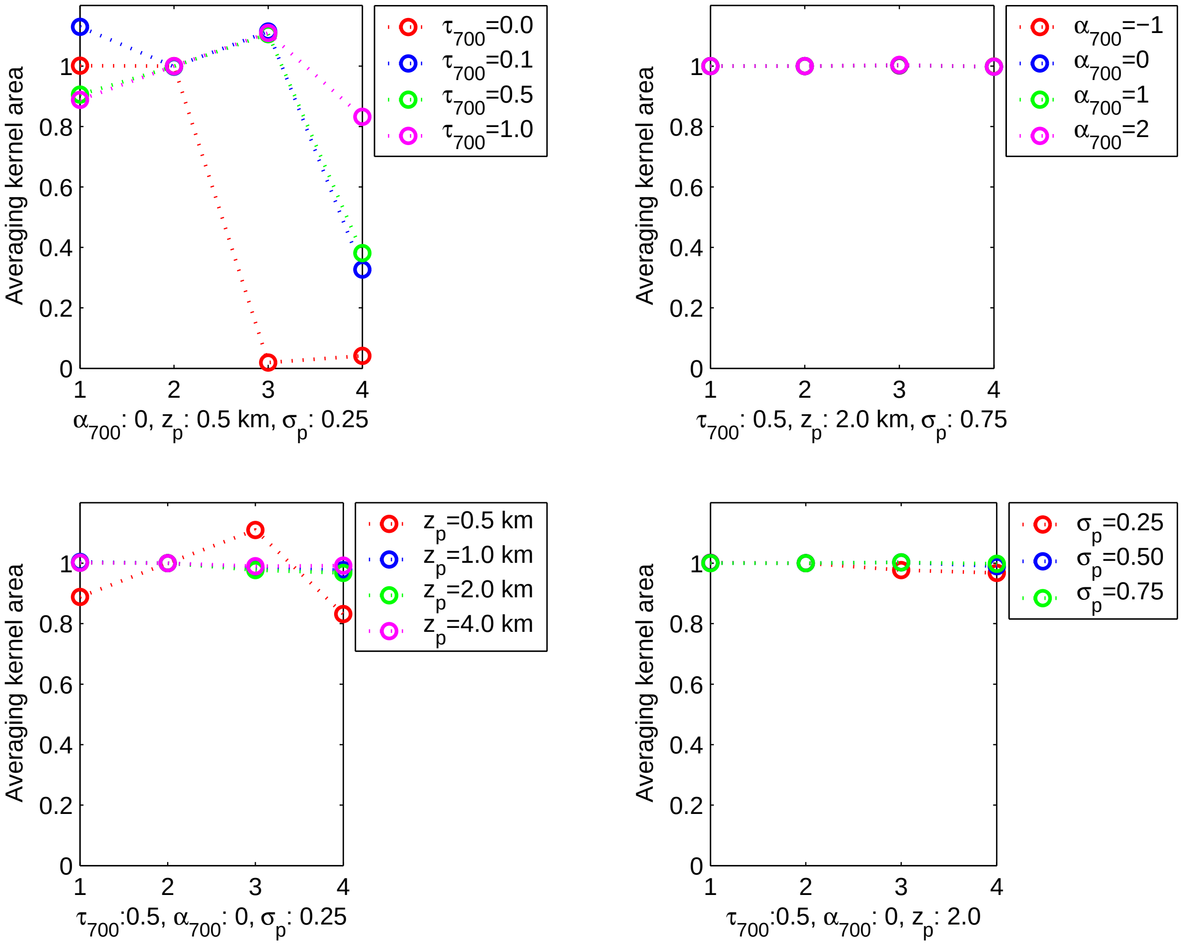

Figure 4.2: Top left: Averaging kernel areas for varying τ_{700}. The other components of the true state vector are $\{\alpha_{700}: 0, z_p: 0.5\text{km}, \alpha_{700}: 0.25\}$. Top right: Averaging kernel areas for varying α_{700}. The other components of the true state vector are $\{\tau_{700}: 0.5, z_p: 2.0\text{km}, \alpha_{700}: 0.75\}$. Bottom left: Averaging kernel areas for varying z_p. The other components of the true state vector are $\{\tau_{700}: 0.5, \alpha_{700}: 0, \sigma_p: 0.25\}$. Bottom right: Averaging kernel areas for varying σ_p. The other components of the true state vector are $\{\tau_{700}: 0.5, \alpha_{700}: 0, z_p: 2.0\}$. The x-axis represents the index number of the corresponding state vector element: $1: \tau_{700}, 2: \alpha_{700}, 3: z_p, 4: \sigma_P$.

the measured quantity with respect to τ_{700}, α_{700}, z_p and σ_p in the left and right panels of the first row and the left and right panels of the second row respectively. The measurement noise here is 1%.

It can be seen from the left panel in the first row that the sensitivity of the reflectance with respect to the AOT of the atmosphere steadily increases with AOT until it plateaus between an aerosol optical thickness of 0.5 and 1.0, where extinction due to increased multiple scattering causes a slower increase in reflectance with respect to AOT. It can also be seen that the shapes of the absorption bands change rapidly with τ_{700} at low values, whereas at higher AOT they remain nearly unchanged. This is because a thick aerosol layer can make lower atmospheric layers virtually opaque by blocking off all light emerging from the layers of the atmosphere below its peak height, the proportion of which is responsible for the changes in depth of the absorption bands.

The jacobian columns representing partial derivation with respect to α_{700}, shown in the upper right panel, are easily recognizable due to their distinctive gradients. For a given value of τ_{700}, α_{700} is directly proportional to $d\tau_{700}/d\lambda$, giving rise to a nearly linear change in $\ln(I/I_0)$ with respect to λ.

The dependence of $\ln(I/I_0)$ on the peak height z_p of the aerosol vertical distribution is shown in the left panel of the second row of Fig. 4.3. As the AOT increases, we can see that the dependence of the measured quantity with respect to the peak height, z_p, increases. This is again attributable to the effective blocking off of light emerging from lower atmospheric layers by an optically thick aerosol layer. As a result, most of the light arriving at at the detector is scattered close to the peak of the aerosol vertical distribution, making the height of scattering less ambiguous.

The right panel of the second row shows the dependence of the jacobian on the width of the aerosol vertical distribution, which suggests here a decrease in reflectance with increasing σ_p. The σ_p of a lognormal distribution involves the square root of the second moment of logarithm of height with respect to the peak, taking on values from 0 to ∞. Smaller values of σ_p correspond to sharply pointed peaks whereas breader peaks have larger σ_p. Although the determination of σ_p is poor, it seems to be facilitated at higher AOT.

The third and fourth rows of Fig. 4.3 show the $\ln(I/I_0)$ fit on the left and the fit residual on the right, corresponding to the measurement around O_2 B and A-band respectively. The fit shows a uniform peak to peak error of less than 1%, which is acceptable given a measurement noise of 1%.

4.4.2 Sensitivity to Ångström exponent, α_{700}

The Ångström exponent of aerosol distributions found in nature usually varies from values around $\alpha \approx -1$ to $\alpha \approx 2$, the exponent increasing with decreasing particle size. Hence, we have examined synthetic scenarios of constant τ_{700}, z_p and σ_p with only α_p varying between -1 and 2.

The upper right panel of Fig. 4.1 shows that α_{700} is retrieved with high accuracy at all values.

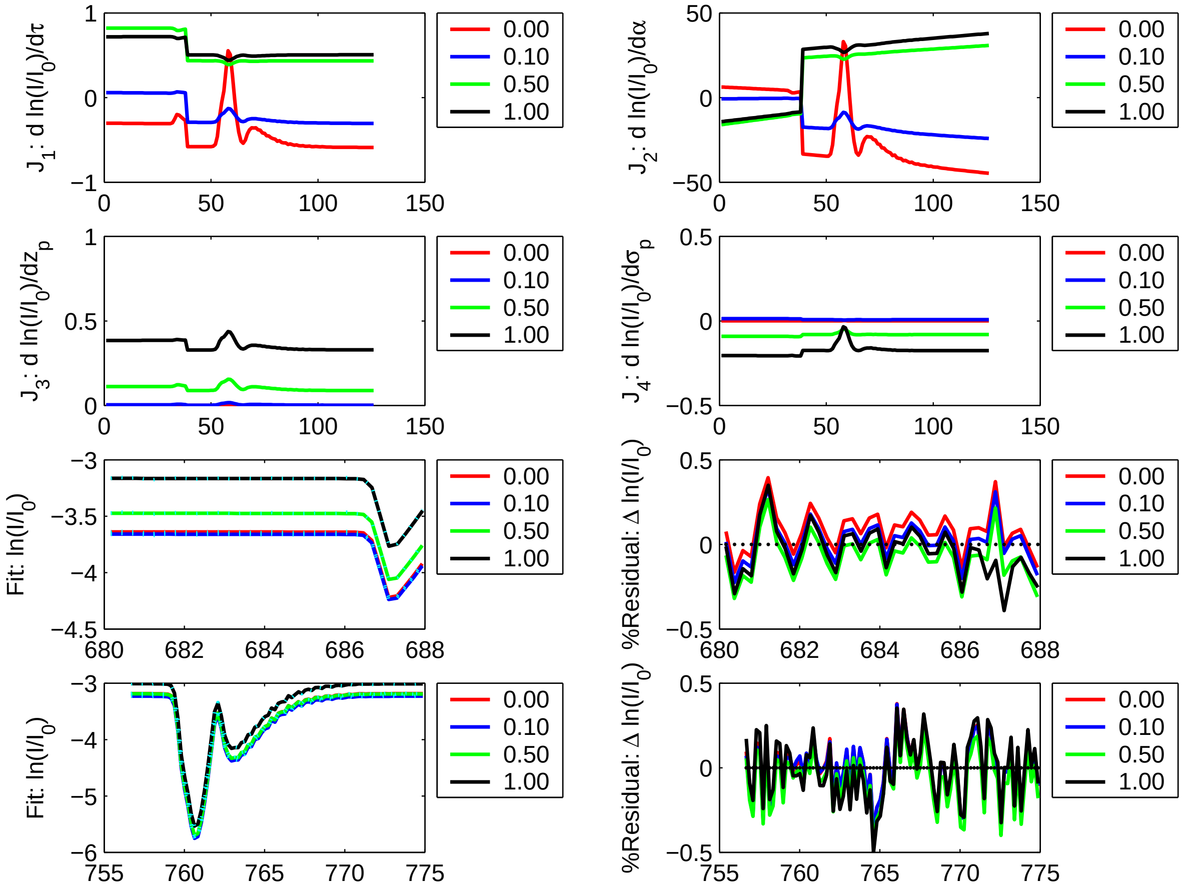

Figure 4.3: The top four panels show the four columns of the Jacobian matrix, each corresponding to the partial derivative of the logarithm of the reflectances around the $\mathsf{O_2}$ A and B bands with respect to aerosol optical thickness τ_{700}, Ångström parameter α_{700}, peak height z_p and peak width σ_p respectively. The lower two panels show the fit on the left and the percentage residual of the fit on the right hand side of the logarithm of the reflectances around the B and A bands respectively. The abscissa represents the wavelength in nm. In each panel, the red, blue, green and black curves represent synthetic ”true” values of $\tau_{700} = 0.0, 0.1, 0.5$ and 1.0 respectively, the synthetic ”true” values for the other state vector elements remaining the same, viz. $\alpha_{700} = 0.0, z_p = 0.5\mathsf{km}, \sigma_p = 0.25$. The a priori assumption is the same in each case, viz. $x_a = \{0.5, 0.0, 3.0, 0.693\}$. The aerosol is assumed to be biogenic of type BL2.

The averaging kernel areas in Fig. 4.2 show consistently high accuracy retrievals for all α_{700} considered. z_p is retrieved with a good accuracy, although values slightly greater than unity suggest an artificial gain attributable to smoothing error. Given the medium aerosol optical thickness $\tau_{700} = 0.5$, we obtain slightly lower averaging kernel areas for σ_p.

The first four panels of Fig. 4.4 represent the columns of the jacobian due to derivation with respect to each element of the state vector. For each of the chosen scenarios in this case, we notice that each of the columns has a distinct form, thereby reducing the probability of a null space.

The two lower rows show the fit of the modeled spectrum with the measured spectrum around the B and A-bands respectively. At all values of α_{700}, we obtain an acceptable residual of less than 1%.

4.4.3 Sensitivity to the peak height of the vertical distribution of aerosol, z_p

To study the sensitivity of our retrieval to the height of the aerosol, we choose scenarios with constant τ_{700}, α_{700} and σ_p, varying the peak height z_p between 0.5-4km to represent most tropospheric aerosols.

The bottom left panel of Fig. 4.1 shows that the retrieval of z_p is fairly accurate at a measurement noise of 1%, deteriorating slightly at 3% and failing to achieve satisfactory convergence at low z_p. The bottom left panel of Fig. 4.2 suggests a consistently high accuracy of measurements for high aerosol peaks, decreasing slightly at lower vertical distribution peak heights.

Fig. 4.5 shows the jacobian columns for each scenario in the first two rows. The dependence of the reflectance on the AOT is stronger at heigher z_p. A likely explanation is that at greater aerosol peak heights, the reflectance peaks due to aerosol and due to Rayleigh scattering do not coincide with each other to an extent that all information carried by light scattered at lower atmospheric layers gets smudged. Furthermore, longer path lengths due to multiple scattering at higher altitudes are less susceptible to extinction due to lower concentration of strong absorbers. This allows the atmospheric to remain more transparent. This behaviour with respect to τ_{700} is repeated in case of jacobian columns representing derivation with respect to α_{700}, the main difference being an amplification factor proportional to $(\lambda - 700)$. An observation of the left and right panels of the second panel of Fig. 4.5 seems to suggest a highly non-linear relationship between the reflectance and the vertical distribution of the aerosol. This can be confirmed by the results of the model study of the vertical behaviour of atmospheric reflectance in the presence of aerosol (see Sec. 2.7 of Chapter 2). This may also be responsible for the relatively poor sensitivity of the retrieval with respect to vertical distribution.

The fits shown in the lower two panels show an error within the range of measurement noise.

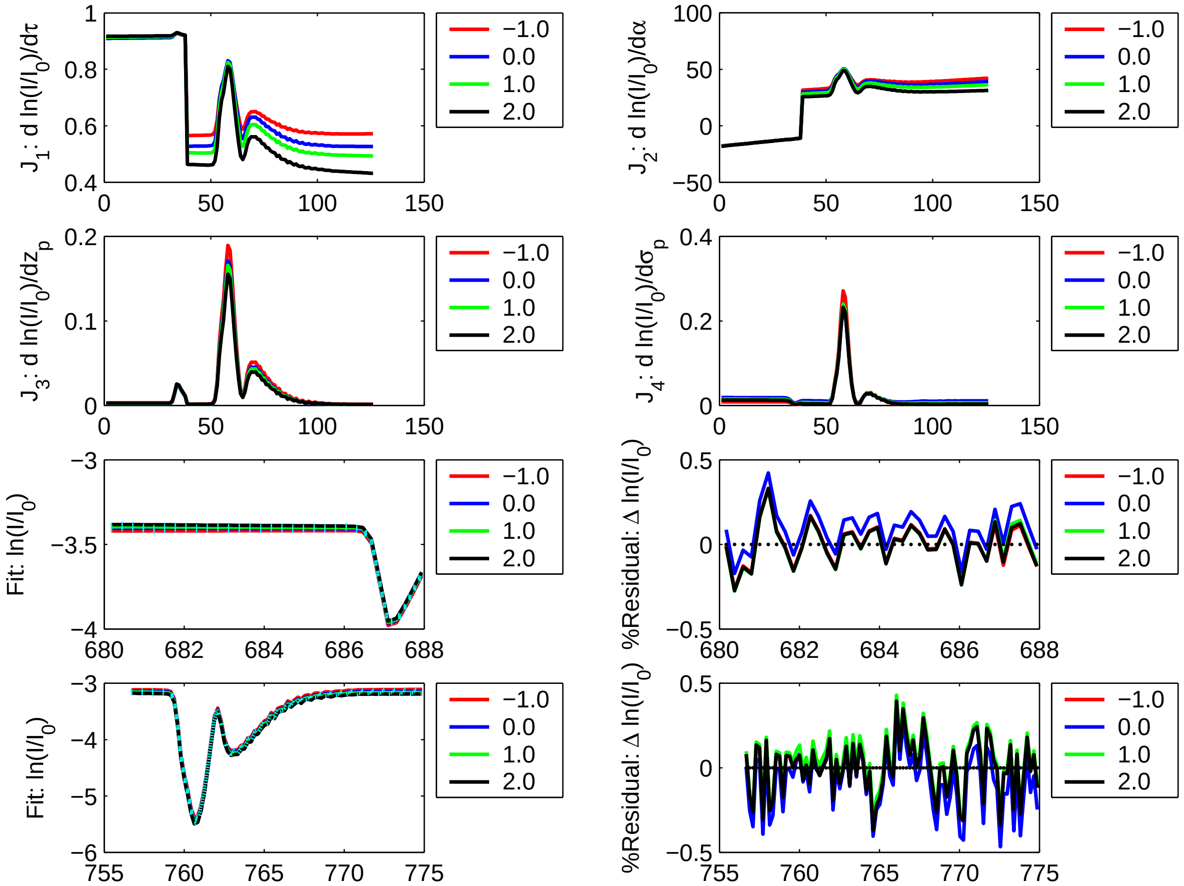

Figure 4.4: The top four panels show the four columns of the Jacobian matrix, each corresponding to the partial derivative of the logarithm of the reflectances around the O_2 A and B bands with respect to the aerosol optical thickness τ_{700}, Ångström exponent α_{700}, peak height z_p and peak width σ_p respectively. The lower two panels show the fit on the left and the percentage residual of the fit on the right hand side of the logarithm of the reflectances around the B and A bands respectively. The abscissa represents the wavelength in nm. In each panel, the red, blue, green and black curves represent synthetic "true" values of $\alpha_{700} = -1.0, 0.0, 1.0$ and 2.0 respectively, the synthetic "true" values for the other state vector elements remaining the same, viz. $\tau_{700} = 0.5, z_p = 2.0\text{km}, \sigma_p = 0.75$. The a priori assumption is the same in each case, viz. $x_a = \{0.5, 0.0, 3.0, 0.693\}$. The aerosol is assumed to be biogenic of type BL2.

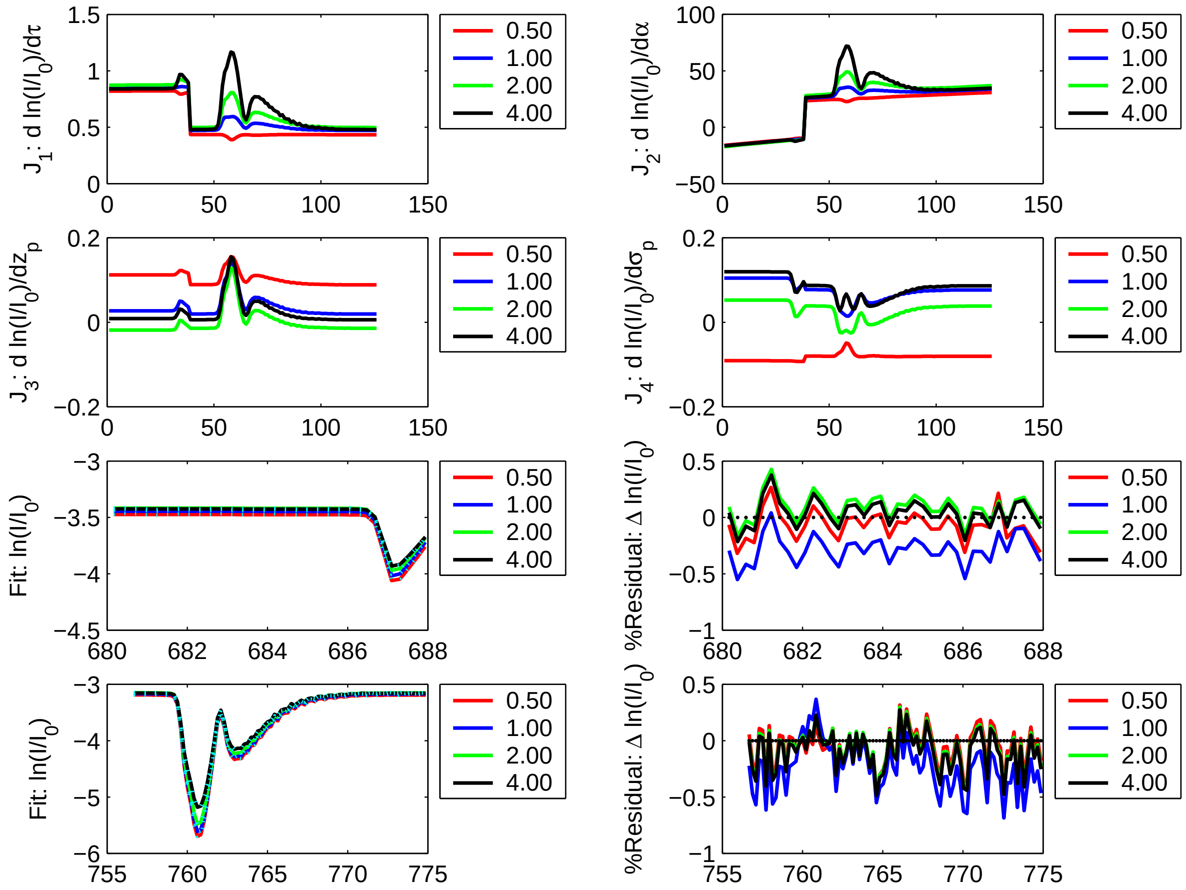

Figure 4.5: The top four panels show the four columns of the Jacobian matrix, each corresponding to the partial derivative of the logarithm of the reflectances around the O_2 A and B bands with respect to aerosol optical thickness τ_{700}, Ångström parameter α_{700}, peak height z_p and peak width σ_p respectively. The lower two panels show the fit on the left and the percentage residual of the fit on the right hand side of the logarithm of the reflectances around the B and A bands respectively. The abscissa represents the wavelength in nm. In each panel, the red, blue, green and black curves represent synthetic ”true” values of $z_p = 0.5, 1.0, 2.0$ and 4.0km respectively, the synthetic ”true” values for the other state vector elements remaining the same, viz. $\tau_{700} = 0.5, \alpha_{700} = 0.0, \sigma_p = 0.25$. The a priori assumption is the same in each case, viz. $x_a = \{0.5, 0.0, 3.0, 0.693\}$. The aerosol is assumed to be biogenic of type BL2.

4.4.4 Sensitivity to peak width of the vertical distribution of aerosol, σ_p

The bottom right panel of Fig. 4.1 shows the retrieval of σ_p, which allows for good convergence in case of both 1% and 3% measurement noise. However, its retrieval is the least accurate of all state vector parameters. The averaging kernel areas plotted in the bottom right panel of Fig. 4.2 suggest that the overall retrieval improves with increasing σ_p, implying that vertical distributions of a wider extent are more accurately retrieved than sharply peaked profiles.

The jacobians with respect to changes in τ_{700}, α_{700} and z_p shown in Fig. 4.6 show little variation at different σ_p. The right panel of the second row shows, however, distinct variations in the absorption structures corresponding to different values of σ_p. This is reflected in negligible changes in the reflectance spectra shown in the left panels of the third and fourth rows of Fig. 4.6. The main variation that can be discerned is a change in the depth of the absorption bands.

The fits shown in the lower two panels show an error within the range of measurement noise, albeit with a slight offset.

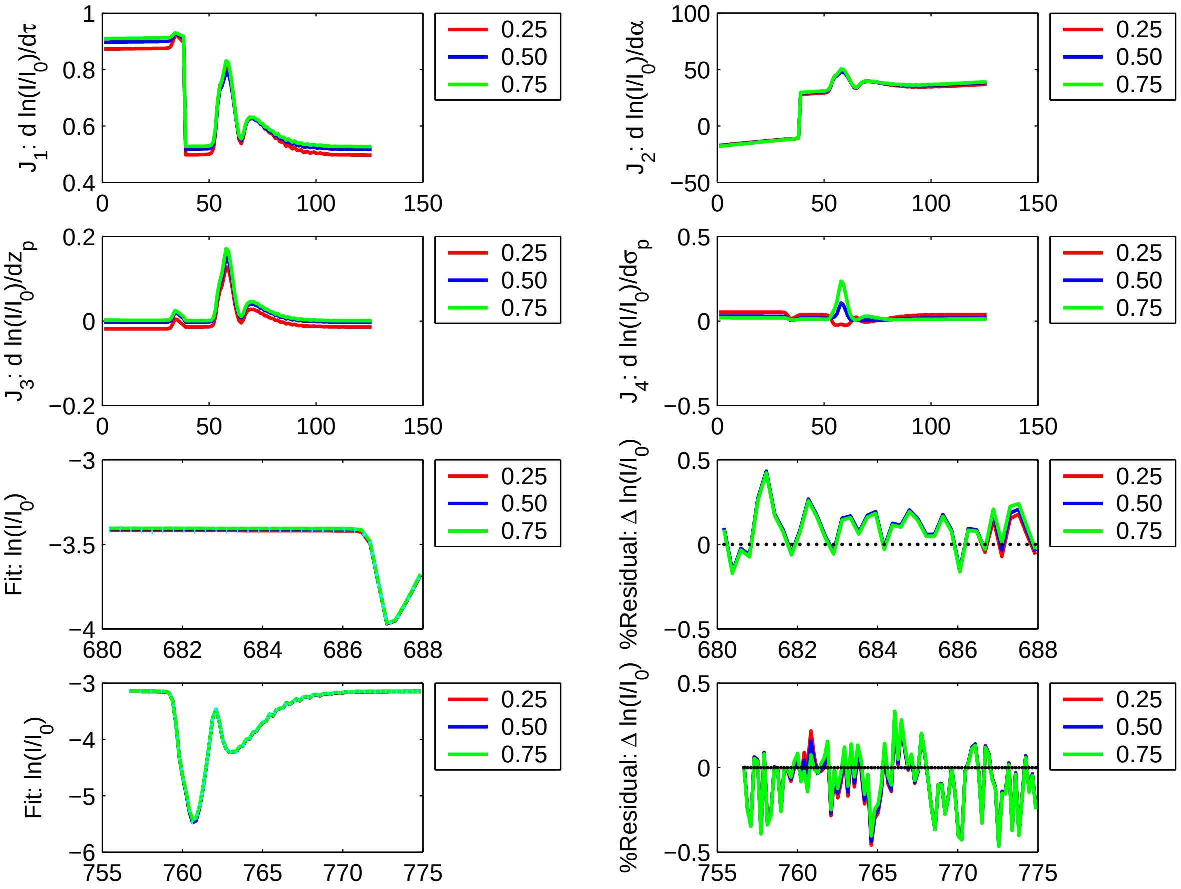

Figure 4.6: The top four panels show the four columns of the Jacobian matrix, each corresponding to the partial derivative of the logarithm of the reflectances around the O_2 A and B bands with respect to aerosol optical thickness τ_{700}, Ångström parameter α_{700}, peak height z_p and peak width σ_p respectively. The lower two panels show the fit on the left and the percentage residual of the fit on the right hand side of the logarithm of the reflectances around the B and A bands respectively. The abscissa represents the wavelength in nm. In each panel, the red, blue, green and black curves represent synthetic "true" values of $\sigma_p = 0.25, 0.50$ and 0.75 respectively, the synthetic "true" values for the other state vector elements remaining the same, viz. $\tau_{700} = 0.5, \alpha_{700} = 0.0, z_p = 2.0$km. The a priori assumption is the same in each case, viz. $x_a = \{0.5, 0.0, 3.0, 0.693\}$. The aerosol is assumed to be biogenic of type BL2.

4.5 Summary

The synthetic studies carried out in this chapter allow us to appraise the sensitivity of our retrieval to each element of the state vector. Thus we know that the retrieval is most accurate with regard to the Ångström exponent α_{700}, followed by the aerosol optical thickness (τ_{700}) and the peak height of the vertical distribution of the aerosol z_p, which appear to be more subject to smoothing error. However, the retrieval of all three parameters τ_{700}, α_{700} and z_p demonstrates a high degree of independence from a priori assumptions for all scenarios. The width of the vertical distribution of the aerosol σ_p is generally less independent of the a priori, especially for low true values of τ_{700}, z_p and σ_p.

The good agreement between modeled and (synthetically) measured spectra ascertain the proper working of the retrieval method and the forward model. Using the synthetic studies, we could also demonstrate the tolerance (and the limits thereof) of the retrieval method to measurement noise. The degrees of freedom associated with the measured signal were found to vary consistently in the range of $3.73 - 3.97$, while the information content of the retrieval was found in the range of $11.24 - 17.90$ (barring the case where no aerosols are present), proving robustness of the inversion algorithm in principle.

Real measurements are expected to add forward model error and model parameter error to the problem represented by synthetic measurements. In the following, we deal with adapting our retrieval method to real measurements and analyzing the accuracy of the resulting retrieval.

Chapter 5

Application of the method for aerosol retrieval to measurements around the O_2 A and B bands from the satellite instrument SCIAMACHY onboard ENVISAT

While the previous chapter dealt with synthetic retrievals devoid of forward model error and model parameter error, we now consider retrieval from real measurements made by the instrument SCIAMACHY onboard Envisat. The peculiarities of the instrument, e.g. displacement of the solar irradiance spectrum with respect to the earth's backscatter spectrum, wavelength shift and squeeze and the uncertainty in the radiometric calibration of the instrument, entail a few modifications to the original retrieval method and the forward model, as will be elucidated in the first part of this chapter.

In order to minimize model parameter error, we choose a climatology dependent on latitude and month of the year for the vertical profiles of meteorological parameters like temperature and pressure and concentrations of various trace gases, updating the data available on the surface elevation and ground temperature and pressure at the location being observed during the time of observation from fine-grid ECMWF data. We also aim to serve this end by determining the ground albedo of the given ground pixel using the time series method developed in Chapter 3. These measures, however, cannot compensate for the immense variability in the type, size and vertical distribution of aerosols, which we attempt to cover using merely 24 aerosol models. Furthermore, there is no long-term guarantee that the aerosol model deemed to fit a given location is always valid. The error due to the assumption of a false aerosol model will be analyzed in the latter part of this chapter.

Finally, we present the aerosol retrievals made over a fixed location (Kanpur, India) over the year 2003.

5.1 Adaptation of the forward model and/or retrieval method to the SCIAMACHY instrument

SCIAMACHY has various observation modes designed to obtain spectra from the earth's atmosphere, the sun and the moon. Two scanner modules, the so-called Elevation Scanner Module (ESM) and Azimuth Scanner Module (ASM) can be used to direct light into the instrument. Both scanner modules can be rotated a full 360° and have identical flat, uncoated mirrors mounted on one side and a diffuser mounted on the other side. The scanners enable SCIAMACHY to perform observations in the following modes (*Noël et al.*, 2002; *Skupin et al.*, 2003a): nadir, limb, solar occultation, solar irradiance, lunar occultation, monitoring and calibration. Of interest in this work are the nadir, solar irradiance and calibration modes.

In the nadir mode, the instrument looks directly down to the earth and uses only the ESM mirror. The Instantaneous Field of View (IFoV) is approximately 25km × 0.6km (along×across track), the typical ground pixel size is 32km × 60km at a full swath width of 960km (scanning east-west). Higher spatial resolution is possible in special operation modes.

In the solar irradiance mode, a solar spectrum is measured with a mirror diffuser combination (either ASM mirror + ESM diffuser + NDF lter or ASM diffuser + ESM mirror) to obtain a solar reference spectrum.

For calibration, SCIAMACHY has a dedicated calibration unit with a 5Watt Tungsten halogen white light source (WLS) for instrument monitoring and a PtCrNe spectral line source (SLS) to perform in-ßight spectral calibration. Both lamps can be observed only with the ESM (mirror or diffuser).

A simplified optical train for all possible observation modes is shown in Fig. 5.1. After passing the scanners a 31 mm diameter telescope mirror produces a focus on the entrance slit of the spectrometer. The entrance slit is 180µm wide and 8 mm high, resulting in an Instantaneous Field of View (IFoV) of 0.045° in the dispersion direction and 1.88° in the cross-dispersion direction. After the slit the beam is collimated and is directed into the Optical Bench Module (OBM).

The OBM design is based on the principle of a double dispersing spectrometer. The light is first dispersed by a predisperser prism creating an intermediate spectrum. Small pick-off prisms and subsequent dichroic mirrors then direct the light into the 8 so-called science channels. Each of these channels contains a grating for the final dispersion of the light to moderate spectral resolution. The science channels of SCIAMACHY employ two types of detectors. For the UV/VIS range (channels 1-5) standard silicon detectors with 1024 pixels are used. The pixels are sequentially read out in approximately 30 ms for the complete array. The near IR channels 6-8 employ Indium Gallium Arsenide (InGaAs) detectors.

The following instrumental issues call for modifications to the the forward model/inverse

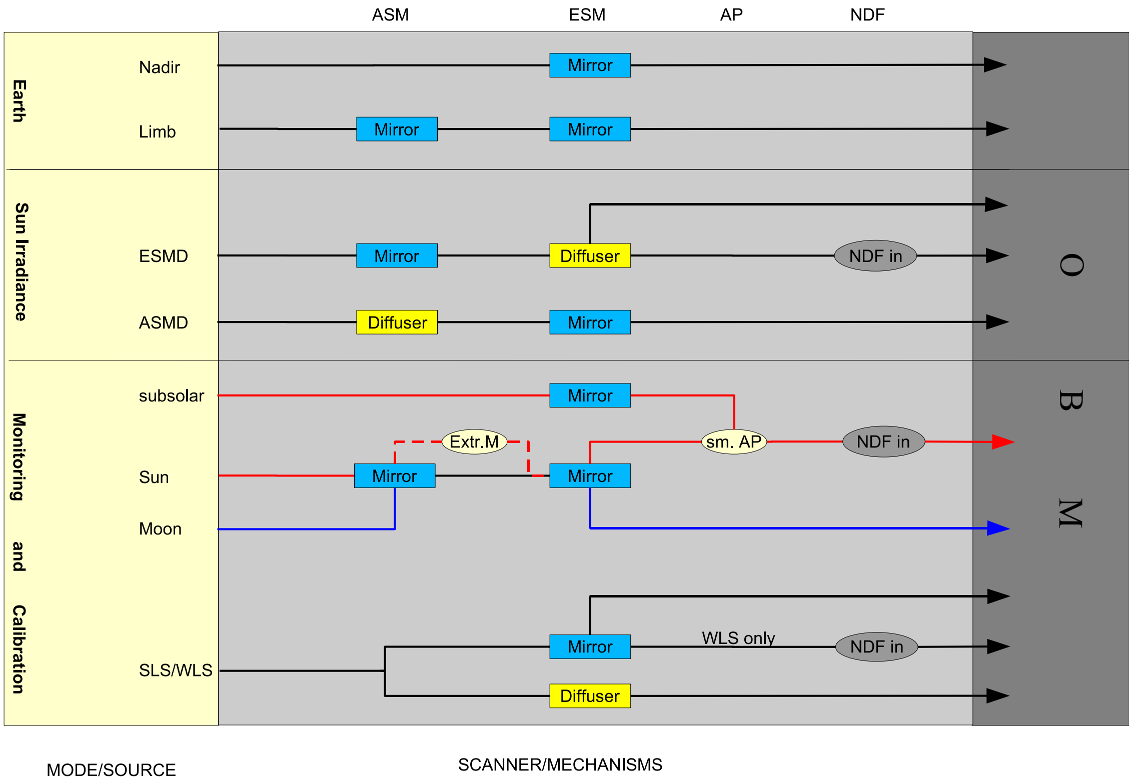
ASM
ESM
AP
NDF
Earth
Nadir
Limb
Sun Irradiance
ESMD
ASMD
Monitoring and Calibration
subsolar
Sun
Moon
SLS/WLS
Mirror
Diffuser
Extr.M
sm. AP
NDF in
WLS only
O B M
MODE/SOURCE
SCANNER/MECHANISMS

Figure 5.1: Simplied optical train of SCIAMACHY for the different observation modes. Only elements not common to all paths are shown. Note that the NDF is only in the light path of channels 36. Mirrors are marked blue, diffusers yellow. The optical path in the monitoring mode for the sun is marked red, the path for the moon is marked blue, *sm. AP denotes the small aperture,* Extr. M the extra mirror that can be put into the light path optionally.(*Skupin et al.*, 2003a)

method for the retrieval of aerosol from SCIAMACHY data:

5.1.1 Shifting of the measured solar irradiance spectrum with respect to the measured earthshine spectrum

The reflectance over a given ground pixel is calculated by division of the nadir 'earthshine' spectrum by a sun spectrum. However, due to the movement of the satellite relative to the sun, the solar spectrum is slightly Doppler shifted. This small shift can suppress actual spectral structures while giving rise to spurious noise. Also, there exist parts of the spectrum for which the data output for both the solar and earthshine measurements apparently occurs in units different from the rest of the spectrum, which can give rise to abrupt jumps or dips due to a relative shifting of the wavelength grids.

Hence, we consider the solar and the earthshine spectra seperately before calculating the reflectance, shifting the solar spectrum by grid very small wavelength intervals of the order of $0.001\,\mathrm{nm}$ from a shift of $-0.2\,\mathrm{nm}$ through $+0.2\,\mathrm{nm}$, resampling the solar spectrum at each interval onto the shifted grid. The solar spectrum shift is chosen as the shift between the two

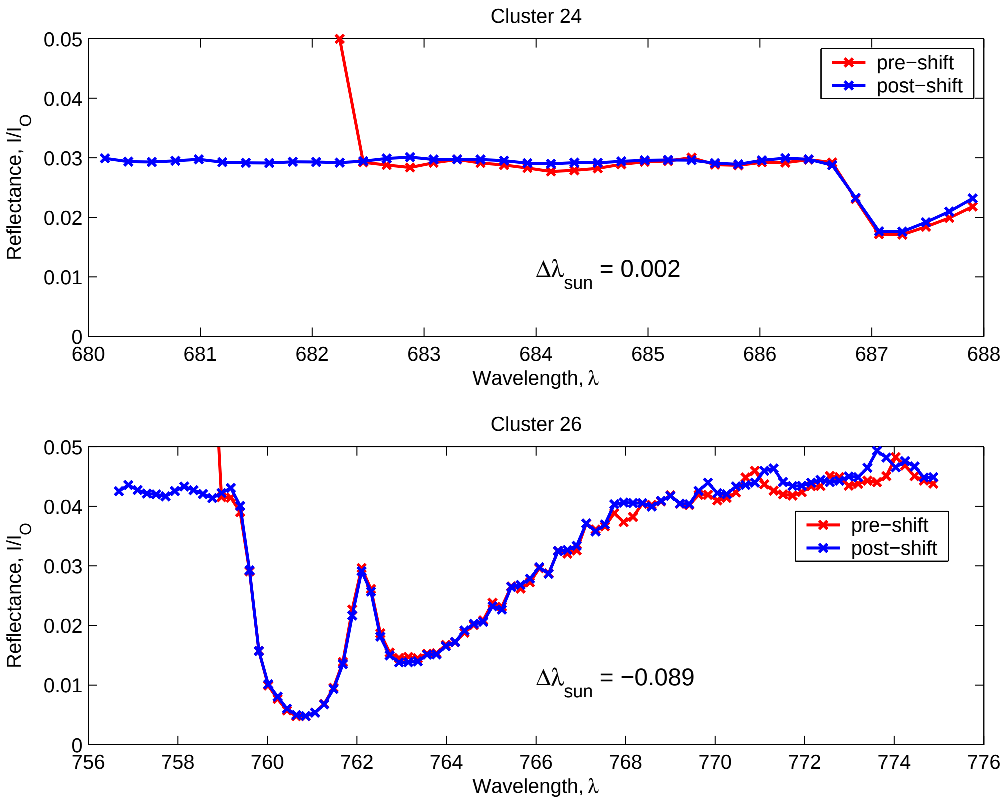

Figure 5.2: The upper and lower panels show the reflectances given by the ratio of the earthshine and the solar spectra around the O_2 B and A-bands respectively. The respective spectral measurements are made in clusters 24 and 26 of channel 4 of the SCIAMACHY instrument. The red curves show the reflectances in each case before shifting the solar spectrum by $\Delta\lambda_{sun}$ relative to the earthshine spectrum, while the blue curves show the post-shift reflectances.

spectra which minimizes the noise in the reflectance spectrum.

Fig.5.2 demonstrates the impact of a solar spectrum shift on a typical spectrum, around the O_2 A and B bands each. We see in both cases, the disappearance of the jump at the beginning of the spectrum. In the case of the spectrum around the B-band (measured in cluster 24), there is also a reduction in the noise contained in the signal. In the case of the A-band (measured in cluster 26), however, we have to partly forfeit a good signal-to-noise ratio in the rest of the spectrum in order to remove the spectral jump.

5.1.2 Spectral shift and squeeze

The spectral calibration of SCIAMACHY data is regularly updated using in-flight data with the exception of channels 7 and 8 (which we do not employ in our retrieval and hence will not discuss here). In order to determine the exact wavelength corresponding to each detector pixel, a combination of a basis wavelength calibration and an in-flight wavelength calibration is used. The basis wavelength calibration is determined from on-ground data. The in-flight calibration calculates only the shift in wavelength with respect to the basis wavelength calibration. This has the advantage that only a small correction has to be applied, because it is expected that the wavelength calibration of SCIAMACHY is relatively stable over the mission lifetime. As a result, the small correction can be modeled with a lower order polynomial function, averting the problem of oscillations typical of higher order polynomial fits, especially at the channel edges.

We assume a polynomial of maximum order 2, which is expected to suffice for the correction of the wavelength calibration of channel 4 covering the spectral ranges containing the $\mathsf{O_2}$ A and B bands. Expressing the wavelength grid of the measured spectrum as the polynomial $\lambda_i = a_0 + a_1 i + a_2 i^2$, where $i = 0, 1, 2, \ldots, L$ are the indices of the grid and a_0, a_1 and a_2 are the coefficients defining the basis wavelength calibration, we add Δa_0, Δa_1 and Δa_2 to our set of state vector parameters, thus effectively retrieving the adjusted polynomial for wavelength calibration, $\lambda'_i = (a_0 + \Delta a_0) + (a_1 + \Delta a_1)i + (a_2 + \Delta a_2)i^2$, where $i = 0, 1, 2, \ldots, L$. The jacobian column vectors corresponding to Δa_0, Δa_1 and Δa_2 are simply $j^i_{a_0} = 1$, $j^i_{a_1} = i$ and $j^i_{a_2} = i^2$, respectively.

This is done seperately for the parts of the wavelength grid around the B band ($680 - 688\,\mathsf{nm}$ belonging to cluster 24 of channel 4) and the A band ($756.5 - 775\,\mathsf{nm}$ belonging to cluster 26 of channel 4), so that a total of 6 parameters are added to the state vector, viz. Δa^A_0, Δa^A_1 and Δa^A_2, and Δa^B_0, Δa^B_1 and Δa^B_2.

5.1.3 Uncertainties in the radiometric calibration of the instrument

Shortly after launch, comparisons of modeled sun spectra from *Kurucz* (1995) and measured sun spectra showed that the solar irradiance measured by SCIAMACHY was around 10% too high for all wavelengths (*Skupin et al.*, 2003b; *Gurlit et al.*, 2003). The reflectance, on the other hand, was around 10-20% too low as comparisons with GOME (*Tilstra et al.*, 2003; *Latter et al.*, 2003), MERIS (*Acarreta and Stammes*, 2005) and radiative transfer models (*van Soest et al.*, 2005) revealed. The deviations could be traced back to two causes: 1. a wrong absolute value of the reflectivity and 2. an insufficient scan angle correction derived from ambient measurements.

To work around this problem, correction factors have been developed using different methods (*Noel*, 2005). Figures 5.3 and 5.4 show correction factors for channel 4 obtained by two different methods. It is evident that the two results are not identical, suggesting that the correction factors may themselves be subject to uncertainty. Furthermore, the correction factors are not constant but fluctuate over the spectral range of the cluster. They are thus subject to both temporal and spectral variation.

Since our retrieval employs separate (ranging over several days, weeks or months) measurements for albedo determination, which again is wavelength dependent, the correction factor applicable in the spectral region around the $\mathsf{O_2}$ A-band may differ slighly (by a few percent) from that applicable to the B-band. Assuming the same radiometric correction factor for both spectral regions results in a highly erratic retrieval of the Ångström exponent, severe cases rendering a physically sound retrieval impossible.

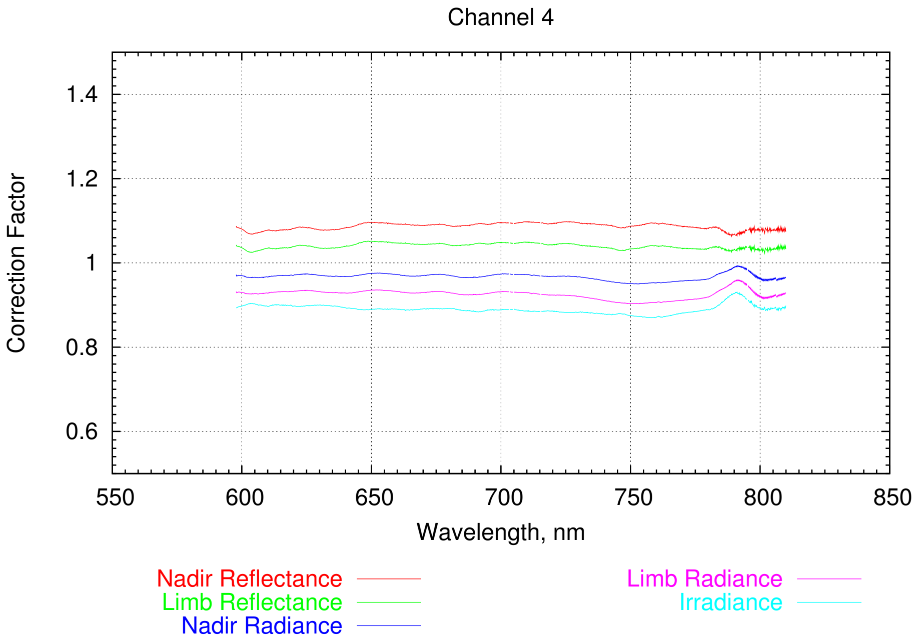

Figure 5.3: Correction factors for SCIAMACHY radiances, irradiance and reflectances derived from NASA measurements.

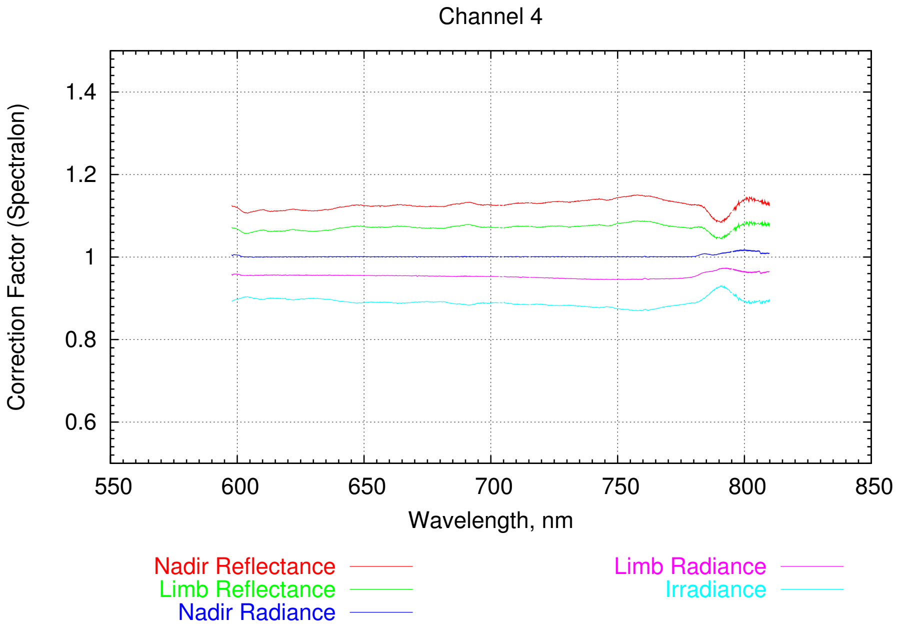

Figure 5.4: Correction factors for SCIAMACHY radiances, irradiance and reflectances derived from spectralon measurements.

To reduce the severity of this problem, we leave the measured reflectances uncorrected and again resort to incorporating into our state vector the so-called 'adjustment factors' f_B and f_A, assumed to be distinct for the two wavelength ranges around the B band ($680 - 688\,\mathrm{nm}$ belonging to cluster 24 of channel 4) and the A band ($756.5 - 775\,\mathrm{nm}$ belonging to cluster 26 of channel 4), respectively. If the correction factors for reflectance are denoted by f'_B and f'_A, we can write

$$R^A_{meas} = \frac{1}{f'_A} R^A_{true} + c_A \quad \text{and} \quad R^B_{meas} = \frac{1}{f'_B} R^B_{true} + c_B, \tag{5.1}$$

where R represents reflectance and c represents a potential constant offset. The subscripts/supercripts A and B denote measurements made around the A and B-band respectively. Equivalently, we can write

$$\ln{(R^A_{meas})} = f_A + \ln{(R^A_{true})} \quad \text{and} \quad \ln{(R^B_{meas})} = f_B + \ln{(R^B_{true})}, \tag{5.2}$$

where for small c, both c and f' can be encapsulated into f. For good measure, we add a coefficient g to account for any first order wavelength dependence of the radiometric calibration factor, yielding

$$\ln{(R^A_{meas})} = f_A + g_A \cdot i_A + \ln{(R^A_{true})} \quad \text{and} \quad \ln{(R^B_{meas})} = f_B + g_B \cdot i_B + \ln{(R^B_{true})}, \tag{5.3}$$

where $i_A = 1, 2, \ldots, L_A$ and $i_B = 1, 2, \ldots, L_B$, are wavelength grid indices with L_A and L_B denoting the lengths of the wavelength grids chosen around the A and B-bands respectively.

The parameters g_A and g_B are reserved in practice for extreme cases and are generally strictly constrained to 0. In case of f_A and f_B, we expect both values to be $\approx 1/f'_A$ and $1/f'_B$ respectively. Since the relative correction is more critical to our retrieval than the absolute value, we constrain the adjustment factor f_B tightly to $1/f'_B$ while retrieving f_A under more relaxed constraints. This choice is made in order to reduce the smoothing error introduced by every new state-vector element.

Consequently, we have for our retrieval with real SCIAMACHY measurements a state vector comprising 14 components in all, i.e. 10 more components than in Chapter 4, even though only three are actually retrieved from measurement, all others being strongly constrained.

5.2 Synthetic examples to test the simultaneous retrieval of the wavelength and radiometric calibration parameters

In this section, we create synthetic scenarios having a wavelength shift $\Delta a^A_0 = \Delta a^B_0 = 0.01$ (assumed representative since most wavelength shifts are of this order of magnitude) and values of the radiometric degradation factor f_A ranging from $0.8 - 1.2$, given $f_B = 0.8929 (1/f_B = 1.12)$. We analyze the resulting retrieval for accuracy, plotting the retrieved quantities against their true values. We do not delve into the retrieval of $\Delta a^A_2, \Delta a^B_2$ and g_A and g_B as these quantities are reserved for highly anomalous measurements, and are generally tightly constrained to 0, as they play too minor a role in most retrievals.

The determination of the wavelength shift by the naked eye is easiest when the shift produces an overlap between the measured and modeled spectrum. An incomplete or excessive shift are

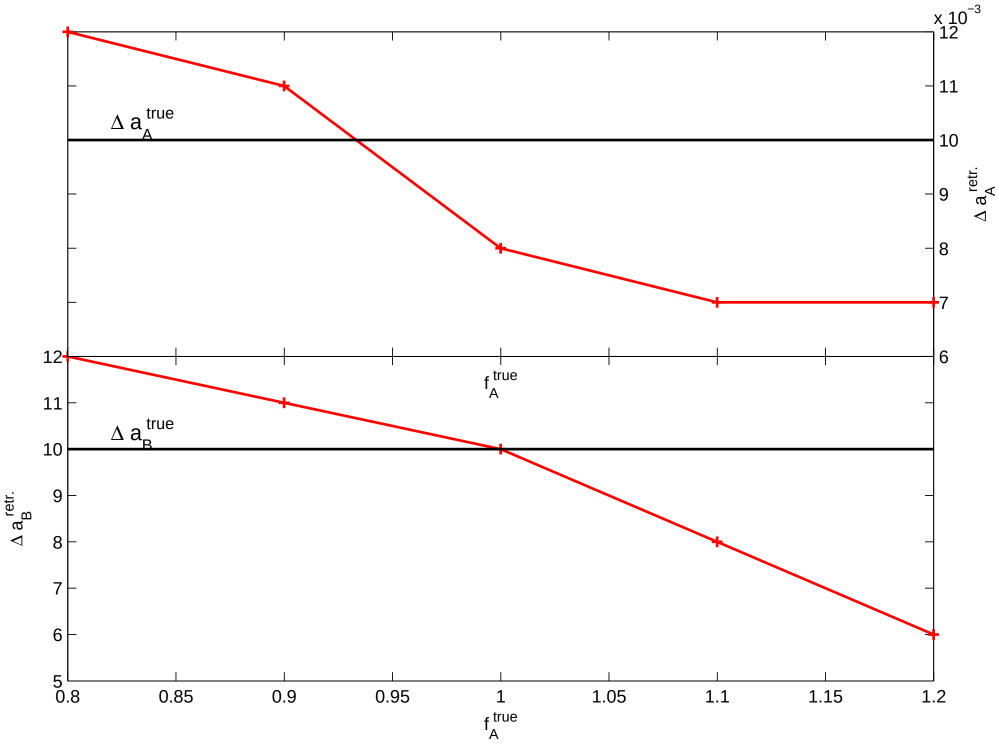

Figure 5.5: Wavelength shifts Δa_0^A and Δa_0^B retrieved for different values of the radiometric degradation factor f_A and f_B respectively. The true shift in each case is 0.01nm.

difficult to discern if there is little or no overlap between the two spectra. This principle also holds true for the inversion procedure, as can be seen from Fig.5.5 where the accuracy of the retrieval improves when the retrieval of f_A is most accurate (see Fig.5.6), producing a better overlap between the modeled and the measured spectra.

From Fig.5.6, we observe an overestimation of $f_A < 0.9$, a nearly accurate retrieval of $f_A = 0.9$ and underestimation of $f_A > 0.9$, which seems to suggest a tendency of the retrieval method to maintain $f_A \approx f_B$. The retrieved aerosol optical thickness has higher values for underestimated f_A and vice-versa, in order to compensate for the change in reflectance caused by a faulty f_A. The retrieved Ångström exponent shows the opposite behaviour as can be seen from Fig.5.6 in order to maintain the gradient of the spectrum. As a result, the Ångström exponent assumes more of a balancing role between the retrieved values of f_A and τ, thereby losing its physical meaning.

The retrieved values of z_p and σ_p both fluctuate around their true values for different f_A but do not exhibit any clear-cut trend with respect to the radiometric degradation factor.

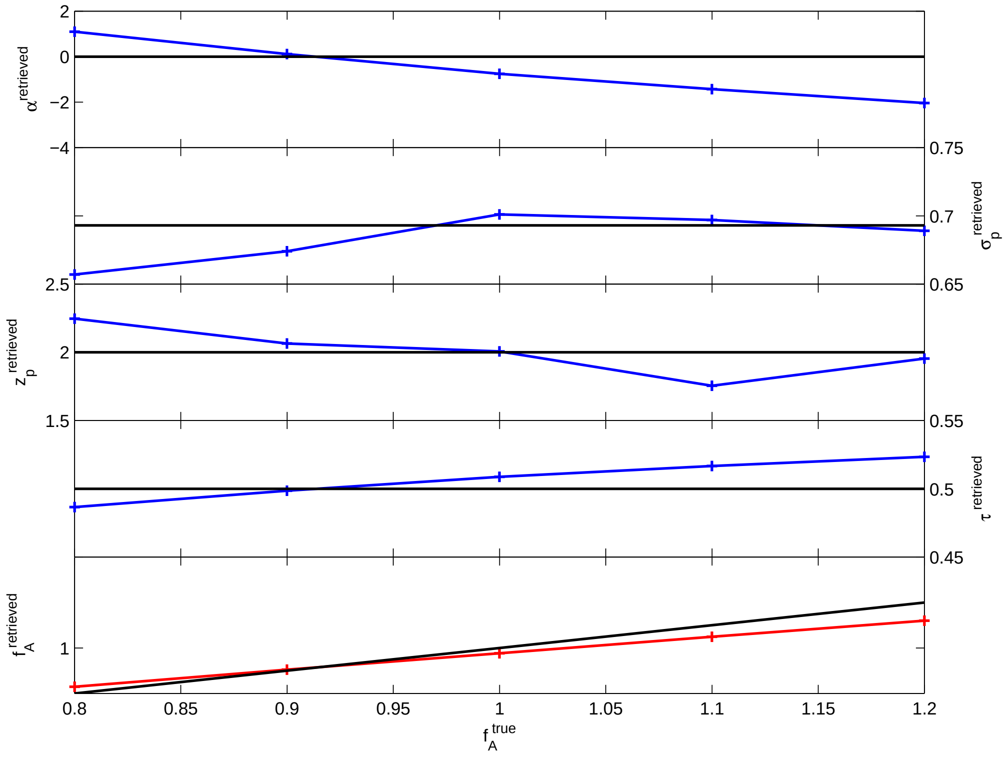

Figure 5.6: Retrieval of the radiometric degradation factor f_A (red line, bottom panel). The corresponding retrievals (blue curves) of the Ångström exponent α, the peak height z_p, the peak width σ_p and the optical thickness τ of the aerosol scenario having true values (black lines) $\alpha_{true} = 0$, $z_{ptrue} = 2.0\mathrm{km}$, $\sigma_{ptrue} = 0.693$ and $\tau_{true} = 0.5$ are plotted in the first four panels.

5.3 Sensitivity of the retrieval to model parameter error

The sensitivity studies carried out in Sec. 4.4 dealt exclusively with measurement error and smoothing error. The model parameters used in the forward model were assumed to be known accurately. This is, however, hardly valid in case of real measurements as the true value of each model parameter, e.g. concentration of O_2, temperature and pressure profiles, etc. may vary with a given uncertainty from the one assumed in the model, resulting in a 'model parameter error'. This is especially true of parameters like surface albedo and the a priori aerosol type, which directly impact the retrieval. In the following, we examine our retrieval for its sensitivity to errors in surface albedo and aerosol type by applying our retrieval method to actual SCIAMACHY measurements under different assumptions of the respective model parameters.

5.3.1 Surface albedo

The method described in Chap.3 for the determination of the surface albedo over a given location always carries a degree of uncertainty regarding whether the day chosen as a clear sky day really is aerosol free. Also, several days over a given location that can qualify as clear sky days - in this section, we test the assumption of 4 different days, viz. Jan 27, Mar 1, Oct 3 and Dec 15, 2003 as clear sky days over Kanpur. We use the surface albedos obtained in each case for the retrieval of aerosol properties on April 11, 2003. It is found that only Dec 15 assumed as a clear sky day allows for a good convergence of our retrieval method, yielding the retrieved state vector elements $\tau_{700} = 0.51$, $z_p = 1.7\,\mathsf{km}$ and $\sigma_{700} = 0.94$. For lack of detailed studies, e.g. involving aerosol retrievals on other days, we are unable provide a general explanation for this behaviour.

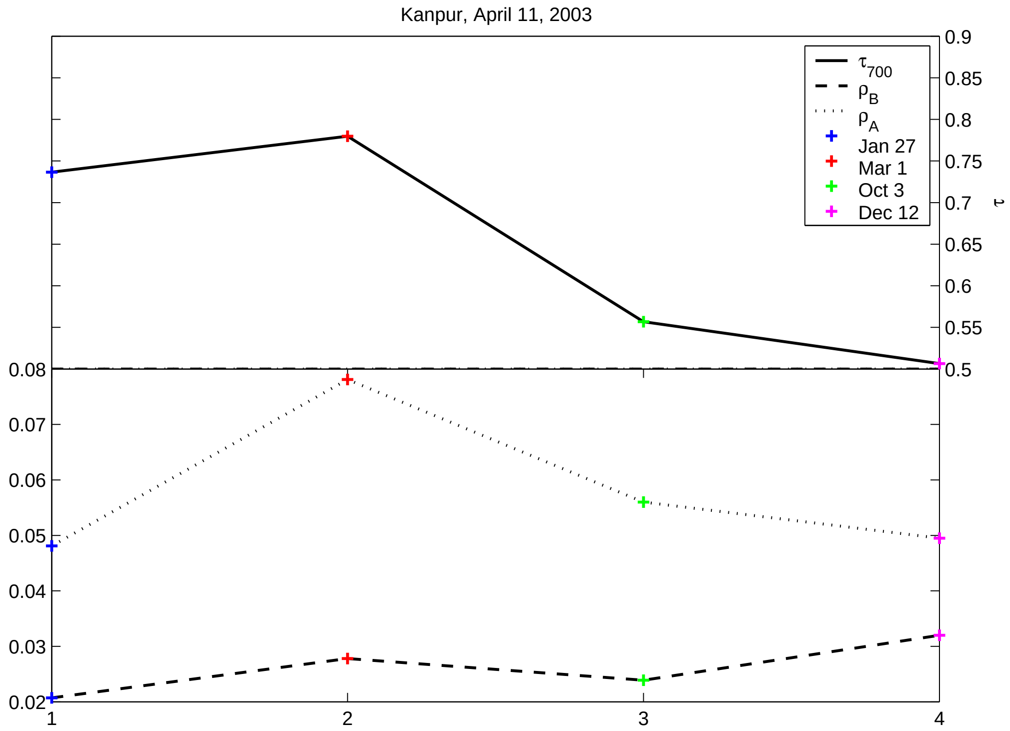

Figure 5.7: SCIAMACHY retrieval of aerosol optical thickness over Kanpur on April 11, 2003 for different assumptions of clear sky day.

Fig. 5.7 shows the variations in the retrieved aerosol optical thickness for a given scenario (Kanpur, April 11, 2003) for corresponding to different pairs of the albedo around the O_2 B and A bands, respectively, $\{\rho_B, \rho_A\}$, implied by different clear sky day assumptions.

5.3.2 A priori aerosol type

Our a priori assumption of the aerosol type representing the observed aerosol scenario fixes the values of the scattering phase function and the single scattering albedo of the aerosol as described in Section 4.1. In this respect, we expect the a priori assumption to influence our retrieval. As in the previous section, we examine the behavior of the retrieval over Kanpur on April 11, 2003 for a priori aerosol types IS2, IS3, IA1, IA2, IA3 and BL2 (see Table 2.6). Assuming Dec 15, 2003 as a clear sky day, we obtain a good convergence of the retrieval method for only aerosol types IA2 ($\tau_{700} = 0.51, z_p = 1.70\mathsf{km}, \sigma_p = 0.94$) and IA3 ($\tau_{700} = 0.61, z_p =$

$1.15\mathsf{km}, \sigma_p = 0.67)$.

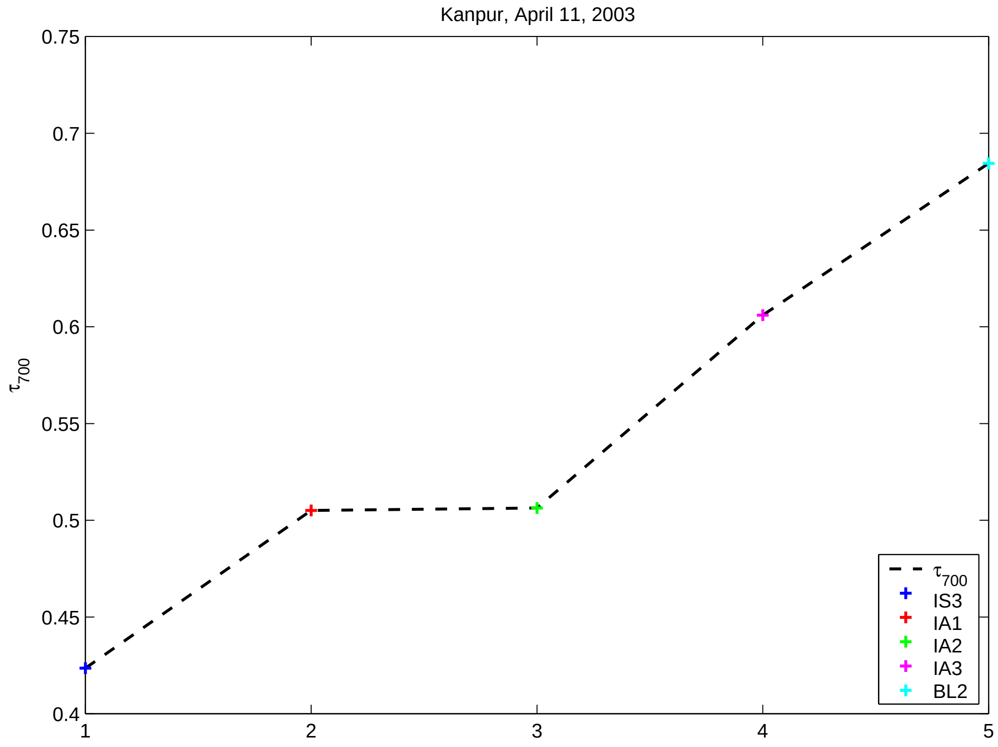

Figure 5.8: SCIAMACHY retrieval of aerosol optical thickness over Kanpur on April 11, 2003 for different a priori assumptions of aerosol type.

Fig. 5.8 shows the variations in the retrieved aerosol optical thickness corresponding to different a priori assumptions of the aerosol type. It is clearly seen in this case that the retrieved optical thickness increases as the scattering ability of the aerosol (due to sulphate content, particle size or both) declines. Exhaustive studies are needed, however, for a generalization in this respect.

5.4 Aerosol retrievals from SCIAMACHY measurements over Kanpur in 2003

Out of the 52 measurements made over Kanpur in 2003, we have been able to successfully retrieve aerosol properties for a total of 9 scenarios, under the assumption of a clear sky on December 15, 2003 and an IA2 aerosol type. While it is relatively easy to retrieve an approximate aerosol optical thickness by fitting the reflectance in a single spectral region outside the absorption bands, the simultaneous use of two disjoint spectral regions and the fitting of the O_2 A and B-bands enables us to retrieve the vertical profile in addition to the aerosol optical thickness, posing at the same time more stringent conditions for a successful retrieval. The retrieved Ångström exponent has to be discarded due to the limitations discussed in Section 5.2.

The full retrieval calls for an absence of partly cloudy scenarios, and and rules out viewing geometries that produce strong BRDF effects relative to the clear sky scenario. Relaxing the convergence conditions of iterative inversion procedure results in the stable retrieval of the aerosol optical thickness for scenarios that may oscillate between different values of z_p and σ_p.

Fig. 5.9 shows the retrieved aerosol optical thickness τ (red crosses) and the peak height z_p (blue crosses) and peak width σ_p (green crosses) of the vertical distribution of the aerosol under stringent convergence conditions. Also shown in the bottom panel are the AOT retrievals allowed by relaxing the convergence conditions of the full retrieval. Scenarios inferred as cloudy on the basis of high reflectances and increased flattening of the absorption bands are shown circled in light blue.

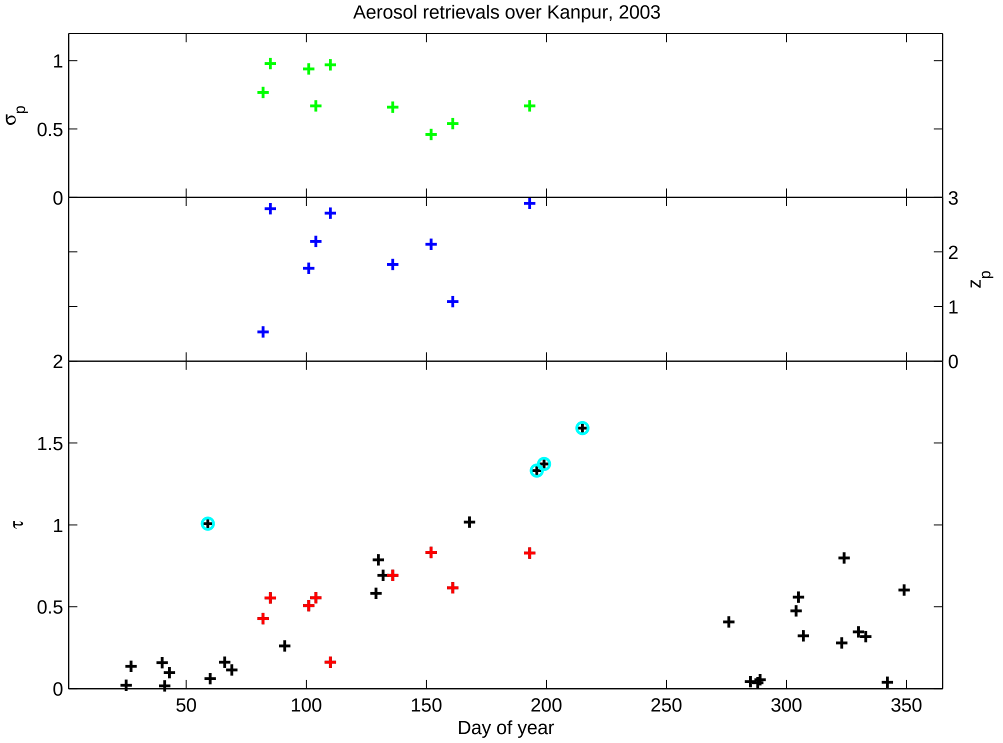

Figure 5.9: SCIAMACHY retrieval of aerosol properties over Kanpur in 2003. The aerosol optical thickness τ, peak height z_p and peak width σ_p retrieved under stringent convergence conditions are shown in the bottom panel (red crosses), the second panel (blue crosses) and the top panel (green crosses). The bottom panel also shows AOT retrievals made under relaxed convergence conditions, represented by black crosses. Cloudy scenarios are shown circled in light blue.

From Fig. 5.9, we see a steady increase in AOT from the beginning of the year till the start of the rainy season in early July. We present comparisons of our AOT retrievals with those obtained from Aeronet data in the following section. The peak height of the aerosol concentration is found to lie between 0-3km with a mean height of 1.98km, which is in agreement with a boundary layer height of about 2km. The width of the aerosol concentration is found to lie between 0.5-1.0 with a mean width of 0.74, corresponding to aerosol loading, on average, between 1-4km.

5.4.1 Comparison of SCIAMACHY aerosol retrievals with AERONET

A direct comparison of SCIAMACHY retrievals with AERONET data is not possible because the majority of SCIAMACHY measurements with successful aerosol retrievals do not have coincident AERONET measurements. Even when measurements at the AERONET site take place on the same day as a successful SCIAMACHY retrieval, there is often a time lag between the SCIAMACHY overpass (around local noon) and the AERONET measurement, causing difficulty in comparison due to the high temporal variability of aerosol loading.

To circumvent this limitation, we compare the monthly mean AOT data for both measurement sets. Fig. 5.10 shows mean monthly AOT's obtained from AERONET and SCIAMACHY measurements, plotted against the month of the year. We see a general agreement until the month of June, after which there occurs a stark divergence as AERONET values fall while SCIAMACHY retrievals show a rise in the mean monthly AOT. Figure5.9 shows a strong weighting (100% for August) of cloudy scenarios in the data constituting the monthly means for July and August. The remaining data points are well-correlated with each other, with SCIAMACHY retrievals exhibiting a nearly systematic underestimation of the AOT. This may be caused by the overestimation of reflectance at a given optical thickness by our forward model AeroRad, but might also reflect the fact that the AERONET station is located within Kanpur City registering peak urban pollution, whereas the SCIAMACHY ground pixel extends over an area of $60\,\mathrm{km} \times 30\,\mathrm{km}$ around Kanpur, diluting the pollution signal. Further, the retrieval calls for the assumption of a clear sky day, which in fact, must contain at least background aerosol. This is also expected to introduce a small negative bias in our retrieval of aerosol optical thickness.

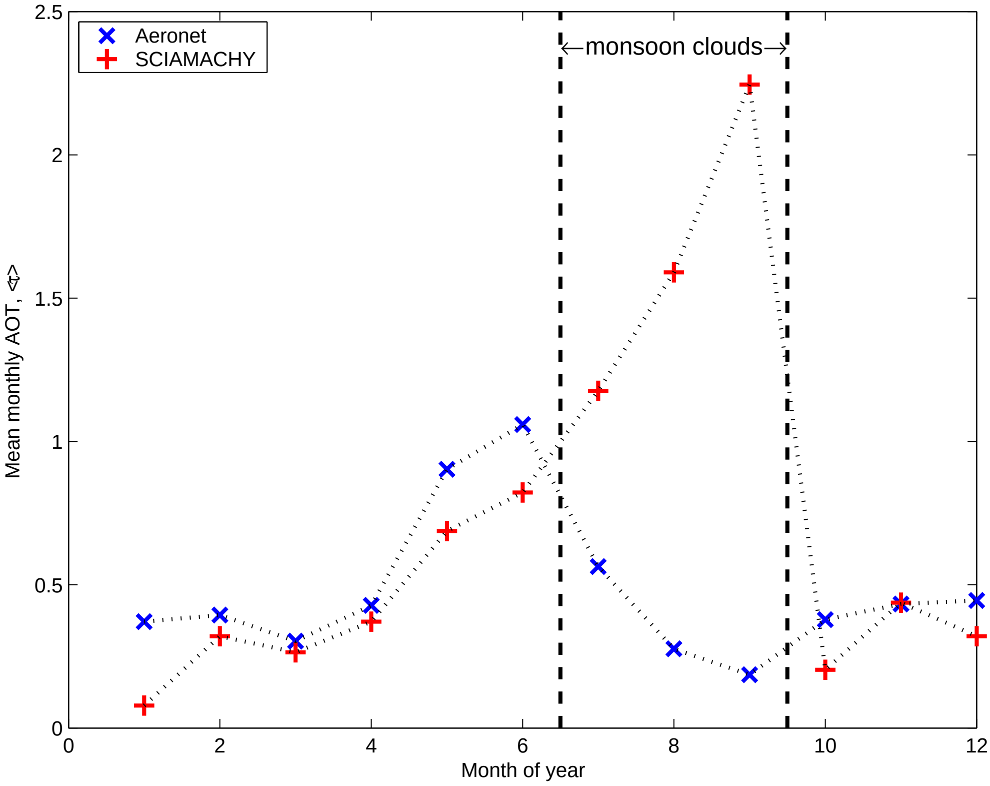

Figure 5.10: Averaged monthly aerosol optical thicknesses obtained from AERONET data (blue) and from SCIAMACHY retrievals (red).

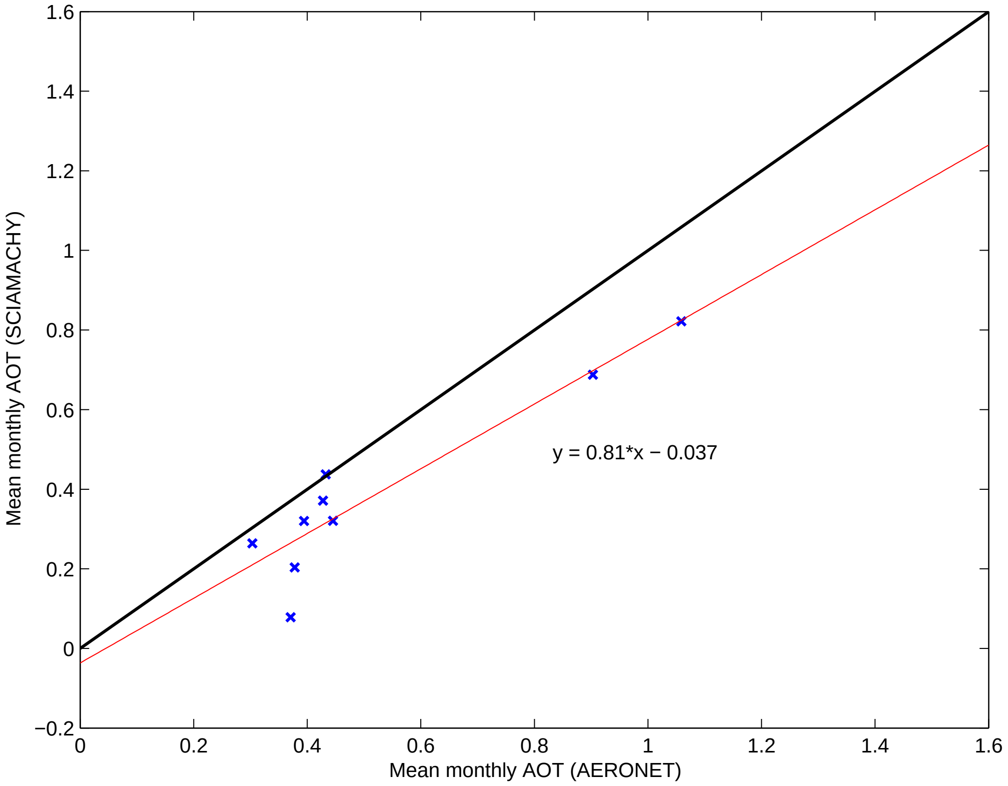

Figure 5.11: Scatter plot of mean monthly aerosol optical thicknesses obtained from AERONET data (blue) and from SCIAMACHY retrievals (red).

5.5 A brief analysis of aerosol retrievals from SCIAMACHY measurements over Kanpur in 2003

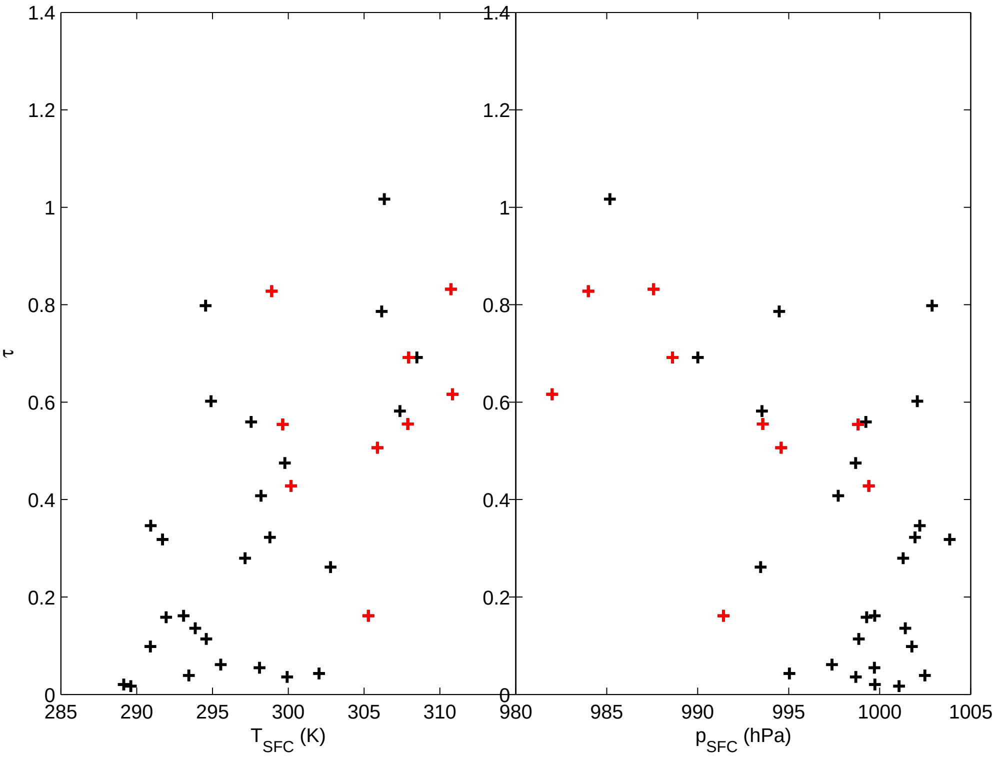

Figure 5.12: Trends of the retrieved aerosol optical thickness with respect to surface temperature T (left) and surface pressure p (right).

Ignoring the cloudy-sky measurements during monsoon, Fig. 5.9 suggests a seasonal variation in the aerosol optical thickness that may reflect a correlation of the aerosol loading with the meteorological conditions prevailing during the measurement. Plotting our measurements against the forecast surface temperature and pressure over Kanpur (obtained from ECMWF data), we detect a positive trend of the AOT retrievals with respect to surface temperature and a negative trend with respect to surface pressure as can be seen in Fig. 5.12. We can combine these two trends by plotting the retrieved parameters against T/p^{κ}[1] as shown in Fig. 5.13. The choice of the parameter T/p^{κ} is made to reflect the thermodynamic constant associated with a parcel of air rising adiabatically from the surface of the earth in a convective cycle. We observe a positive trend of the retrieved AOT with respect to T/p^{κ}, while the retrieved values of z_p and σ_p demonstrate negative trends with respect to T/p^{κ}.

These trends may be explained by the source of the observed aerosol loading, which may be either of primary or secondary origin or both. A primary aerosol would imply a seasonally varying emission pattern or a seasonal transport of mineral dust/sea-salt to Kanpur.

---

[1] $\kappa = \frac{R}{c_p}$, where R is the specific gas constant and c_p is the specific heat capacity at constant pressure. For air, which can be treated as a largely diatomic gas, $\kappa \approx \frac{2}{7}$.

Dust storms are known to be meteorological phenomena common in the western part of India during the months of April-June, leading to a seasonal transport of dust over Delhi, Kanpur, Varanasi (Benaras) and the surrounding Indo-Gangetic plains (*Bhattacharjee et al.*, 2007). This may explain the retrieval of increasing aerosol optical thicknesses from April through June as seen in Fig. 5.10.

However, the strong correlation of AOT with the surface pressure and temperature also suggests a role played by the adiabatic uplifting of air parcels warmed by the surface before noon, possibly leading to the formation of secondary aerosols (see Sec.1.5) due to the condensation of volatile vapors, a process that would be accelerated by the presence of dust particles.

The formation of secondary aerosols requires the onset of nucleation (homogeneous/heterogeneous), which is expected to take place approximately when the partial vapor pressure of the aerosol forming species exceeds the corresponding saturation vapor pressure. To illustrate this, we consider the example of water vapor (see red curve in Fig. 5.14), whose saturation vapor pressure is obtained from the Clausius-Clayperon equation as a function of temperature by

$$e_s(T) = e_1 \exp\left(-\frac{L}{R_v T}\right), \tag{5.4}$$

where $e_1 = 3.5894e^8\,\mathsf{hPa}$ is a constant derived from the vapor pressure of water at the triple point, $L = 2257\mathsf{J/g}$ and R_v is the specific gas constant for the vapor ($\approx R$ for most atmospheric values of temperature and pressure).

Diurnal heating of the earth's surface causes an increased lapse rate close to the ground and a subsequent adiabatic rise of the parcel of air directly above the earth's surface. This is especially true of the atmosphere before local noon, which coincides with the SCIAMACHY overpass time. The rising parcel, if having sufficient momentum, continues to rise to the Maximum Parcel Level (MPL) where negative buoyancy decelerates it to a stop. As a parcel having temperature T_{SFC} and pressure p_{SFC} at the surface rises through the atmosphere, volatile gases get cooled and may become sufficiently supersaturated to form aerosol (see Sec. 1.2.2). Again, taking water vapor (with an assumed volume mixing ratio of $\rho(\mathsf{H_2O})$=3%) as an example, we plot isentropes of the partial pressure e_p of water vapor against the parcel temperature T for different values of surface temperature T_{SFC} and pressure p_{SFC} found to prevail over Kanpur at 12:00 noon (Fig. 5.14).

$$e_p(T) = \rho(\mathsf{H_2O})\, p_{SFC} \left(\frac{T}{T_{SFC}}\right)^{\frac{1}{\kappa}}, \tag{5.5}$$

As the warm air rises through the atmosphere (moving along the isentrope from left to right), it gets cooled as it moves higher, eventually becoming supersaturated. The points of intersection of the isentropes with the saturation vapor pressure curve (red) denote the temperature and pressure at which the vapor becomes saturated. The green curve represents a saturation ratio of 2 (RH = 200%).

In order to estimate the height at which saturation sets in, we create equivalent plots of the altitude z against temperature T as shown in Fig. 5.15, assuming a pressure scale height of 8 km. The solid black (surface pressure p_{SFC} = 1013.25hPa) and blue (surface pressure

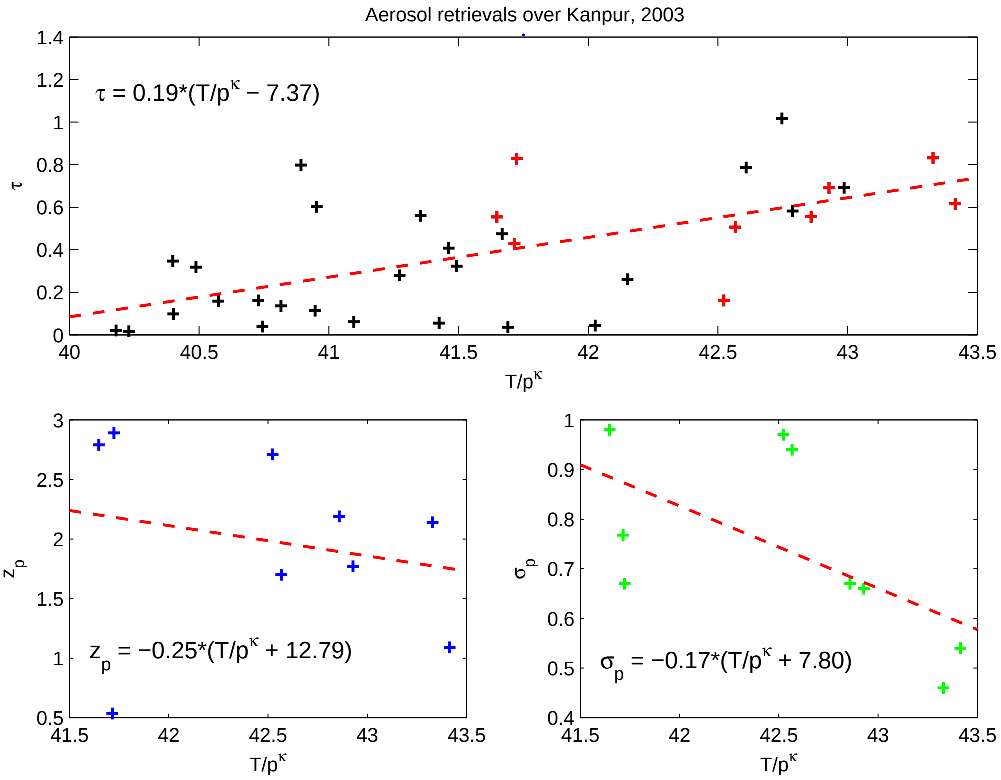

Figure 5.13: Trends of the retrieved aerosol optical thickness (top panel) and of the peak height (bottom left) and peak width (bottom right) of the aerosol vertical distribution with respect to T/p^{κ}.

p_{SFC} = 980hPa) lines indicate a saturation ratio $S = 1$ and the broken black/blue lines indicate supersaturation at $S = 2$. It is evident that saturation sets in at lower altitudes for lower surface temperatures and (marginally) for higher surface pressures. In Fig. 5.15, the red lines represent adiabatically expanding air parcels of surface temperature $T_{SFC} = 280$ K (solid), $T_{SFC} = 290$ K (dashed), $T_{SFC} = 300$ K (dash-dotted) and $T_{SFC} = 310$ K (dotted). It is seen that at low temperatures ($280 - 290$K in Fig. 5.15), saturation already occurs at the ground level and no volatile vapors are available for secondary aerosol formation. For higher temperatures ($300 - 310$K in Fig. 5.15), saturation sets in after the air parcel has risen to a specific height z_s above the ground, z_s increasing with increasing T_{SFC}/p^{κ}_{SFC}.

An increase in T_{SFC}/p^{κ}_{SFC} can thus be expected to increase the availability of volatile gases at the surface, while also providing sufficient momentum to propel the air parcel containing these vapors to an altitude suitable for condensation of secondary aerosol nuclei. Due to the presence of wind-blown dust at higher altitudes, the formation of aerosols is further accelerated. This explains the positive trend observed in the aerosol optical thickness with respect to T_{SFC}/p^{κ}_{SFC}.

It is interesting to note that altitudes of peak aerosol concentration $1 - 3$ km retrieved from SCIAMACHY data saturation correlate well to the higher temperature saturation altitudes expected from Fig.5.15. The data samples available for retrieved values of z_p and σ_p are to small to reach a reliable statistical conclusion to account for the trends exhibited by them with respect to T_{SFC}/p^{κ}_{SFC}. It may be possible, however, that higher temperatures propel more volatile gases to higher altitudes, where rapid condensation on the ambient dust particles leads to a more effective gravimetric settling of the secondary particles toward lower altitudes, causing both reduced z_p and σ_p at higher aerosol optical thicknesses.

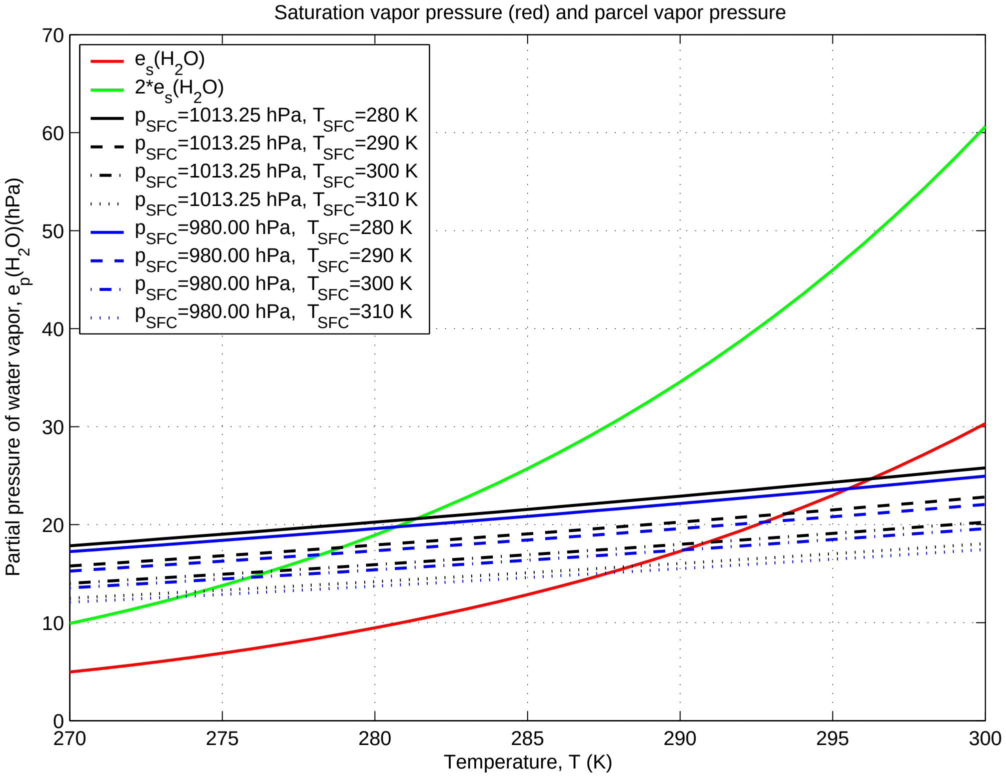

Figure 5.14: The red curve shows the saturation vapor pressure of water as a function of ambient temperature. The green curve represents a saturation ratio $S = 2$ for water vapor, i.e. a relative humidity of 200%. Isentropes representing the partial pressure of water vapor against the temperature in adiabatically expanding air masses of different surface temperatures and pressures expected over Kanpur are shown. The points of intersection of the isentropes with the red and green curves represent the partial vapor pressure and temperature at which the water vapor becomes saturated and 200% supersaturated, respectively.

The above discussion suggests that high aerosol loadings observed during the period April-June over Kanpur are caused by the accelerated condensation of volatile gases on dust particles suspended at higher atmospheric altitudes due to wind-transport. Their vertical distributions peak at an altitude of $\approx 2\,\mathsf{km}$. Aerosol formation over Kanpur is found to be closely correlated to temperature and pressure conditions prevailing at the surface and hence may be regarded as a consequence of the adiabatic transport of volatile gases to higher altitudes. On the other hand, colder temperatures increases subsidence of clean free tropospheric air causing higher surface pressure, effectively diluting the aerosol loading near the surface and blocking any large scale formation of secondary aerosol at higher altitudes.

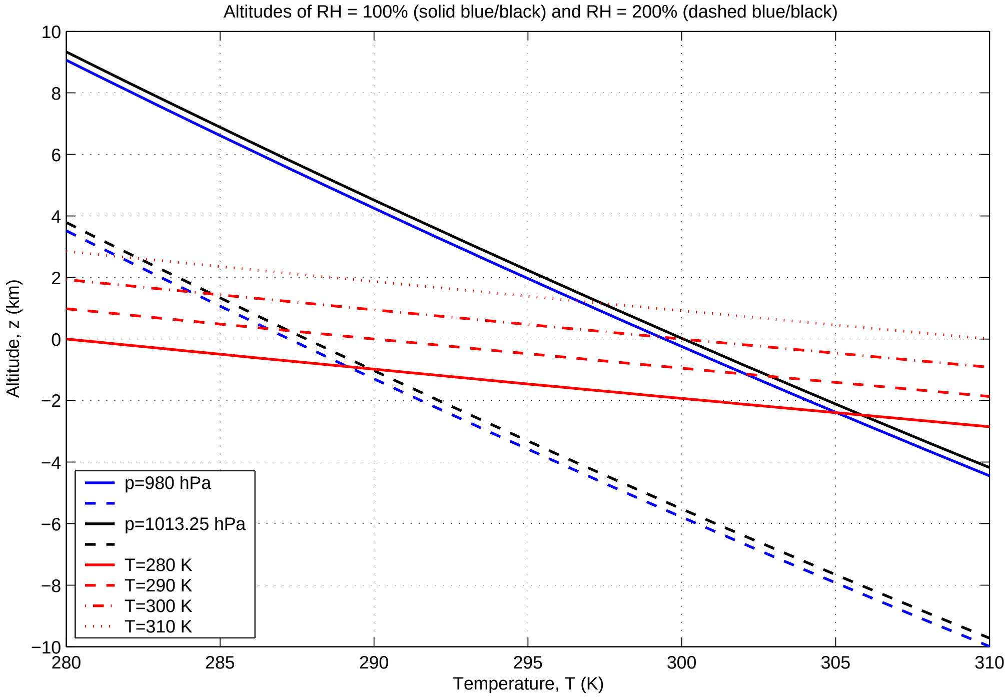

Figure 5.15: The blue and black solid curves show the altitude plotted against the temperature at which water vapor reaches saturation, given a surface pressure of 980 hPa and 1013.25 hPa, respectively. The dashed blue and black curves show a similar plot for a saturation ratio of 2. The red curves show the altitude of adiabatically expanding air parcels of various surface temperatures against the temperature of the parcel. The points of intersection represent the altitude and temperature at which the water vapor becomes saturated and 200% supersaturated, respectively.

5.6 Conclusion

The work carried out in this dissertation leads to the conclusion that simultaneous retrievals of aerosol optical thickness τ, Ångström exponent α, and the vertical distribution of the aerosol given by a peak height z_p and a peak width σ_p are possible, given a good knowledge of ground albedo, a homogeneous ground pixel devoid of strong surface relief and a cloud-free atmosphere.

These conditions, however, are fulfilled only by a small subset of SCIAMACHY measurements. Further complications are created by irregularities in the radiometric calibration of the instrument, as a result of which physical information carried by the Ångström exponent is compromised.

The determination of the vertical profile parameters z_p and σ_p is made difficult, presumably by the presence of residual aerosol or BRDF effects in the scenario assumed to be a clear sky for the determination of the surface albedo. Partly cloudy scenarios are also expected to hinder proper convergence of the iterative inversion procedure.

The aerosol optical thickness τ, while being easiest to retrieve, is sensitive to the a priori assumption made of the aerosol type representing a hazy scenario. Thus, the accuracy, and in extreme cases, the stability of the retrieval depends on how closely the a priori aerosol type describes the true loading.

While the main purpose of aerosol retrieval from satellite-based measurements is to obtain global coverage, SCIAMACHY poses major instrumental impediments to the full retrieval of aerosol properties on a global basis. By choosing a smaller ground pixel, a higher overpass frequency and by ensuring radiometry stability, future generations of medium-resolution, nadir-viewing satellite instruments may achieve their full potential with regard to aerosol retrieval. Stable radiometric calibration would also help reduce the length of the state vector by eliminating the need for the simultaneous retrieval of correction factors. The smaller the state vector, the lesser is the smoothing error due to different state vector elements, leading to a more stable retrieval.

The forward model AeroRad could be improved by refining the averaging within the streams in order to produce simulate reflectances more accurately. Time constraints notwithstanding, a higher resolution may be used for data-sampling and forward modeling in order to minimize forward model error.

The most important requirement for global retrievals is the availability of a global fine-grid BRDF map. Such a map may be created and regularly updated using ground based, air-borne or satellite-based measurements or a combination of all. Satellite measurements have the advantage of providing global coverage and reflecting BRDF effects characteristic of satellite observation geometries, whereas cloud and residual aerosol contamination are less obstructive to ground-based albedo determination.

Chapter 6

Conclusion and Outlook

We conclude this thesis with a summary of the work done within the framework of this dissertation:

- Aerosols are very diverse atmospheric species. This diversity makes it difficult to characterize them without involving a large number (of the order of 10 or more) of variable parameters. This difficulty of characterization is partly responsible for the lag in the knowledge available about atmospheric aerosols in comparison to other atmospheric species. We have devised a characterization for aerosols that reduces the number of parameters to four (aerosol optical thickness, Ångström exponent, and the peak height and width describing the vertical distribution of the aerosol) without greatly diminishing the flexibility of our representation.

- Hitherto available SCIAMACHY products quantify observed aerosol scenarios in terms of a pseudo-inversion of the aerosol optical thickness or in terms of the empirically defined aerosol absorbing index (AAI). Our approach is based on the extraction of the maximum information contained in the medium-resolution multispectral data provided by SCIAMACHY, resulting in the development of

    1. AeroRad, a radiative transfer model specifically designed for the simulation of atmospheric aerosols in a satellite observation geometry,
    2. A method (using AeroRad) for the identification of a clear sky scenario from a series of SCIAMACHY measurements over a given location and the subsequent determination of the equivalent lambertian surface albedo over that location,
    3. The development and sensitivity analysis of a robust algorithm based on optimal estimation for the retrieval of all four aforementioned aerosol parameters from SCIAMACHY nadir-mode measurements in and around the O_2 A and B-bands, and
    4. The adaptation of the retrieval algorithm to instrumental shortcomings for application to real SCIAMACHY measurements.

- AeroRad is a 1-D plane parallel 10-stream radiative transfer model using a Gauss-Seidel iterative scheme for the simulation of multiple scattering. The novel alignment of the streams around the direction of incident direct sunlight in AeroRad allows for a more accurate simulation of highly peaked scattering common to aerosols while also saving valuable computational time. AeroRad has been compared with the established analytical models LINTRAN and SCIATRAN and the Monte Carlo model McArtim, with good results in each case.

- Given a clear sky scenario, the reflectance over a given ground pixel contains an atmospheric and a surface component, which, at a wavelength devoid of molecular absorption, allows for an easy calculation of the (assumed) lambertian surface albedo ρ_{retr}. We analyze a series of SCIAMACHY measurements over a given ground pixel in order to identify the clear sky scenario. The reflectance at a given wavelength over a given homogeneous lambertian ground pixel observed under a given viewing geometry is, however, a non-monotonous function of the aerosol loading, so that a direct identification of the aerosol-free scenario is not always possible. This is further complicated by different behaviour of the reflectance for different surface albedos and different aerosol types. Different viewing geometries also register different reflectances.

  A solution is to this problem is the use of reflectances R_1 and R_2 at two different wavelengths λ_1 and λ_2 devoid of strong atmospheric absorption such that $\rho_{true}(\lambda_1) \neq \rho_{true}(\lambda_2)$ to determine $\rho_{retr}(\lambda_1)$ and $\rho_{retr}(\lambda_2)$ for all scenarios, irrespective of whether they are aerosol free or not. It is found that the difference between the retrieved ground albedos $\|\rho_{retr}(\lambda_1) - \rho_{retr}(\lambda_2)\|$ is maximum for the clear sky scenario. Using this criterion, we identify a scenario of least aerosol loading (some residual aerosol cannot be ruled out) allowing the determination of the surface albedo of the ground pixel to be examined.

- The method of optimal estimation is used to develop an inversion algorithm for the retrieval of the aforementioned parameters, viz. aerosol optical thickness, Ångström exponent, and the peak height and width characterizing the vertical distribution of the aerosol. Our measurement vector consists of the reflectances detected by SCIAMACHY in spectral ranges $680 - 690\,\mathsf{nm}$ around the $\mathsf{O_2}$ B-band and $755 - 775\,\mathsf{nm}$ around the $\mathsf{O_2}$ A-band. Lambertian surface albedos obtained by the method described above are used as an input parameter. An aerosol model considered most probable for the location being observed is chosen as a priori, which in our case also fixes the phase function and the single scattering albedo of the aerosol to be retrieved. A circumvention of this limitation would entail a simultaneous retrieval of the aerosol size distribution and the complex refractive index of the aerosol, which falls out of the scope of the instrument. AeroRad is the forward model used, also providing the elements of the Jacobian matrix.

- An attempt to retrieve all four aerosol paramters using only $\mathsf{O_2}$ A-band measurements fails consistently for varying synthetic aerosol scenarios, proving that both A and B band measurements are needed to provide the information required to retrieve all four aerosol parameters.

- Sensitivity studies show a very high retrieval accuracy for the aerosol optical thickness, the Ångström exponent and the vertical peak height. The accuracy of retrieval for the vertical peak width is generally lower, decreasing with increasing AOT and decreasing width of the true aerosol vertical distribution. The degrees of freedom associated with the measured synthetic signal were found to vary consistently in the range of $3.72 - 3.97$, while the information content of the retrieval was found to lie in the range of $11.24 - 17.90$, proving the robustness of the inversion method in principle.

- The application of our retrieval method to actual SCIAMACHY measurements entails the addition of wavelength and radiometric correction factors to the state vector. This is found to compromise the retrieval of the Ångström exponent α of the aerosol observed. However, simultaneous retrievals of aerosol optical thickness τ, and the vertical distribution of the aerosol given by a peak height z_p and a peak width σ_p are still possible as found for 9 out of the 52 scenarios observed (without application of a cloud filter). Relaxing the convergence conditions allows for a reliable retrieval of the aerosol optical thickness for more scenarios, as is shown by a good correlation with AERONET sunphotometer data.

- Our retrievals are able to capture a seasonal dust storm event over Kanpur during the hot, dry months of April-June. Furthermore, the retrieved aerosol optical thicknesses over Kanpur show a strongly correlation with T/p^{κ}, where T and p represent the absolute surface temperature and pressure, suggesting a role of convective circulation in the formation of aerosols over Kanpur.

6.1 Outlook

This work establishes that moderate spectral resolution, nadir viewing instruments like SCIAMACHY are capable not only of reliably retrieving aerosol optical thicknesses, but also the vertical distribution of the aerosol. Further development in this area could lead to a method on par with currently used LIDAR measurements. The greatest barriers to operational implementation of our method are the large ground pixel size and the unstable radiometric calibration of the instrument. Frequently updated and accurate BRDF maps would also greatly facilitate the global monitoring of aerosols using an instrument like SCIAMACHY.

The complexity of aerosols gives rise to a large number of uncertainties in the retrieval of aerosols, e.g. due to surface effects, aerosol type and distribution etc. These uncertainties are compounded by instrumental issues like instrumental noise, radiometric calibration and the heterogeneity within the observed ground pixel. Exhaustive theoretical investigations of the effects of each source of uncertainty on the retrieval method may be expected to help not only better identify the cause of errors in the retrieval, but also to make the retrieval more efficient, e.g. by a more informed choice of a priori and measurement covariances.

Model studies of aerosols and their radiative transfer effects may be invaluable with regard to the identification of clear skies and for the distinction of hazy from partly cloudy and clouded scenarios, insufficient knowledge of which is a major cause for incorrect or unstable aerosol retrievals. An important step forward would be improving the computational speed of radiative transfer simulations.

Ultimately, an instrumental design that incorporates the results of rigorous theoretical studies should make possible the global monitoring of aerosols using a compact, long-lived and cost-efficient instrument such as SCIAMACHY.

List of Figures

1.1 Aerosol pollution over Northern India and Bangladesh (http://visibleearth.nasa.gov/). 3

1.2 Sea spray droplet formation due to the bursting of entrained bubbles. 5

1.3 Typical number and volume distributions of atmospheric particles with the different modes (*Seinfeld and Pandis*, 2006). 8

1.4 Idealized schematic of the distribution of particle surface area of an atmospheric aerosol (*Whitby and Cantrell*, 1976). Principal modes, sources, and particle formation and removal mechanisms are indicated. (Adapted from *Seinfeld and Pandis* (2006)) 9

1.5 Annual average source strength in $\mathsf{kg km^{-2} hr^{-1}}$ for each of the aerosol types considered here (a to g) with total aerosol optical depth (h). Shown are (a) the column average H_2SO_4 production rate from anthropogenic sources, (b) the column average H_2SO_4 production rate from natural sources (DMS and SO_2 from volcanoes), (c) anthropogenic sources of organic matter, (d) natural sources of organic matter, (e) anthropogenic sources of black carbon, (f) dust sources for dust with diameters less than 2 µm, (g) sea salt sources for sea salt with diameters less than 2 µm, and (h) total optical depth simulated by the CHAM/GRANTOUR model. Source: IPCC 2001, Ch. 5, Fig. 5.2 18

1.6 As volcanoes erupt, they blast huge clouds into the atmosphere. These clouds are made up of particles and gases, including sulfur dioxide SO_2. Several megatons of sulfur dioxide gas from a major volcanic eruption can reach the stratosphere. There, the sulfur dioxide is converted to tiny persistent sulfuric acid (H_2SO_4) aerosols by reaction with the ambient water vapor H_2O. These aerosols reflect energy coming from the sun, thereby preventing the sun's rays from heating Earth's surface. Volcanic eruptions are thought to be responsible for the global cooling that has been observed for a few years after a major eruption. The amount and global extent of the cooling depend on the force of the eruption and, possibly, on its location relative to prevailing wind patterns. (Graphic by Robert Simmon, Goddard DAAC) 19

1.7 Retrieval of global AOT over ocean surfaces from GOME data (http://www.temis.nl/airpollution/aerosol.html) 24

1.8 Mean AOT at 500 nm for September, October and November 2004 as retrieved by ASP from SCIAMACHY nadir measurements. 25

1.9 Latest Absorbing Aerosol Index (AAI) results obtained by SCIAMACHY . . . 25

2.1 Vertical structure of the model atmosphere. S represents the sun as the source of incoming radiation and D represents the detector pointing at a point on the earths surface whose zenith is is directed along $\vec{z}$. 30

2.2 Division of space into streams in the 10-stream version of AeroRad. The z-axis is aligned with the direction of incident solar radiation. The cone (outlined in blue) around the direction of propagation of the incident solar beam is made narrow in order to be able to better account for strongly forward and backward peaked scattering, common in case of aerosols. The green line outlines on of the the four forward azimuthal streams. 35

2.3 The left panels show the optical thickness $\Delta\tau_i$ of layer i with respect to the optical thickness of the atmosphere at the layer ($\tau_i = 0$ at TOA). The panels on the right hand side show the effective single scattering albedo $\Delta\omega_i$ of layer i with respect to the optical thickness of the atmosphere at the layer. The red curves represent 682 nm and the blue curve represents 756 nm. On each side, the panels represent a Rayleigh scaling factor of 1x in the top row, 5x in the middle and 20x at the bottom. 42

2.4 Variation in reflectance with respect to solar zenith angle. Line-of-sight is assumed to be aligned with nadir and the earth's surface is assumed to be completely black. The left panels show reflectances at 682 nm for a Rayleigh scaling factor of 1x at the top, 5x in the middle and 20x at the bottom panel. The right hand side panels represent reflectances at 756 nm in the same order of scaling factors. In each case, the red curve indicates single scattering reflectance and the blue curve shows total (single+multiple scattering) reflectance as simulated by AeroRad. The green line indicates the total reflectance simulated by SCIATRAN. 44

2.5 Variation in reflectance with respect to line-of-sight zenith angle. The sun is assumed to be at zenith and the earth's surface is assumed to be completely black. The left panels show reflectances at 682 nm for a Rayleigh scaling factor of 1x at the top, 5x in the middle and 20x at the bottom panel. The right hand side panels represent reflectances at 756 nm in the same order of scaling factors. In each case, the red curve indicates single scattering reflectance and the blue curve shows total (single+multiple scattering) reflectance as simulated by AeroRad. The green line indicates the total reflectance simulated by SCIATRAN. 45

2.6 Variation in reflectance with respect to albedo. The sun is assumed to be at zenith and the line-of-sight is assumed to be aligned with nadir. The reflection at the earth's surface is assumed to be lambertian. The left panels show reflectances at 682 nm for a Rayleigh scaling factor of 1x at the top, 5x in the middle and 20x at the bottom panel. The right hand side panels represent reflectances at 756 nm in the same order of scaling factors. In each case, the red curve indicates single scattering reflectance and the blue curve shows total (single+multiple scattering) reflectance as simulated by AeroRad. The green line indicates the total reflectance simulated by SCIATRAN. 46

2.7 Reflectance spectra simulated in the O_2 A- and B-bands. The sun is assumed to be at zenith and the line-of-sight is assumed to be aligned with nadir. The earth's surface is assumed to be completely black. The left panels show reflectances in the B-band for a Rayleigh scaling factor of 1x at the top, 5x in the middle and 20x at the bottom panel. The right hand side panels represent reflectances in the A-band in the same order of scaling factors. In each case, the red curve indicates single scattering reflectance and the blue curve shows total (single+multiple scattering) reflectance as simulated by AeroRad. The green line indicates the total reflectance simulated by SCIATRAN. 47

2.8 Reflectance spectra simulated in the O_2 A- and B-bands. The sun is assumed to be at zenith and the line-of-sight is assumed to be aligned with nadir. The earth's surface is assumed to be completely black. The left panels show reflectances in the B-band for a Rayleigh scaling factor of 1x at the top, 5x in the middle and 20x at the bottom panel. The right hand side panels represent reflectances in the A-band in the same order of scaling factors. In each case, the red curve indicates single scattering reflectance and the blue curve shows total (single+multiple scattering) reflectance as simulated by AeroRad. The green line indicates the total reflectance simulated by SCIATRAN. 48

2.9 Phase functions of all spherical model aerosol types plotted against angle of scattering at 685 nm. 51

2.10 Phase functions of all spherical model aerosol types plotted against angle of scattering at 760 nm. 52

2.11 The top left panel shows vertical profiles for trace gas absorption and Rayleigh scattering per unit layer height. The top right panel shows vertical profiles of AOT/km for industrial, biogenic and volcanic aerosol, each of total $AOT = 0.5$. The bottom panel shows the corresponding reflectances/km, $\Delta_i^{ss}(I/I_0)$ and $\Delta_i^{ms}(I/I_0)$ at 682 nm for each of the aerosol types respectively. 57

2.12 The top left panel shows vertical profiles for trace gas absorption and Rayleigh scattering per unit layer height. The top right panel shows vertical profiles of AOT/km for industrial, biogenic and volcanic aerosol, each of total $AOT = 0.5$. The bottom panel shows the corresponding reflectances/km, $\Delta_i^{ss}(I/I_0)$ and $\Delta_i^{ms}(I/I_0)$ at 687 nm for each of the aerosol types respectively. 58

2.13 The top left panel shows vertical profiles for trace gas absorption and Rayleigh scattering per unit layer height. The top right panel shows vertical profiles of AOT/km for industrial, biogenic and volcanic aerosol, each of total $AOT = 0.5$. The bottom panel shows the corresponding reflectances/km, $\Delta_i^{ss}(I/I_0)$ and $\Delta_i^{ms}(I/I_0)$ at 757 nm for each of the aerosol types respectively. 59

2.14 The top left panel shows vertical profiles for trace gas absorption and Rayleigh scattering per unit layer height. The top right panel shows vertical profiles of AOT/km for industrial, biogenic and volcanic aerosol, each of total $AOT = 0.5$. The bottom panel shows the corresponding reflectances/km, $\Delta_i^{ss}(I/I_0)$ and $\Delta_i^{ms}(I/I_0)$ at 761 nm for each of the aerosol types respectively. 60

2.15 The top left panel shows vertical profiles for trace gas absorption and Rayleigh scattering per unit layer height. The top right panel shows vertical profiles of AOT/km for industrial, biogenic and volcanic aerosol, each of total $AOT = 0.5$. The bottom panel shows the corresponding reflectances/km, $\Delta_i^{ss}(I/I_0)$ and $\Delta_i^{ms}(I/I_0)$ at 763 nm for each of the aerosol types respectively. 61

2.16 The top panels show vertical profiles for trace gas absorption and Rayleigh scattering per unit layer height. The following panels show vertical profiles of AOT/km on the left and the corresponding reflectances/km, $\Delta_i^{ss}(I/I_0)$ and $\Delta_i^{ms}(I/I_0)$ at 682 nm, on the right, for total AOT = 0, 0.25, 0.5 and 1.0 respectively. 62

2.17 The top panels show vertical profiles for trace gas absorption and Rayleigh scattering per unit layer height. The following panels show vertical profiles of AOT/km on the left and the corresponding reflectances/km, $\Delta_i^{ss}(I/I_0)$ and $\Delta_i^{ms}(I/I_0)$ at 687 nm, on the right, for total AOT = 0, 0.25, 0.5 and 1.0 respectively. 63

2.18 The top panels show vertical profiles for trace gas absorption and Rayleigh scattering per unit layer height. The following panels show vertical profiles of AOT/km on the left and the corresponding reflectances/km, $\Delta_i^{ss}(I/I_0)$ and $\Delta_i^{ms}(I/I_0)$ at 757 nm, on the right, for total AOT = 0, 0.25, 0.5 and 1.0 respectively. 64

2.19 The top panels show vertical profiles for trace gas absorption and Rayleigh scattering per unit layer height. The following panels show vertical profiles of AOT/km on the left and the corresponding reflectances/km, $\Delta_i^{ss}(I/I_0)$ and $\Delta_i^{ms}(I/I_0)$ at 761 nm, on the right, for total AOT = 0, 0.25, 0.5 and 1.0 respectively. 65

2.20 The top panels show vertical profiles for trace gas absorption and Rayleigh scattering per unit layer height. The following panels show vertical profiles of AOT/km on the left and the corresponding reflectances/km, $\Delta_i^{ss}(I/I_0)$ and $\Delta_i^{ms}(I/I_0)$ at 763 nm, on the right, for total AOT = 0, 0.25, 0.5 and 1.0 respectively. 66

3.1 SCIAMACHY spectral range 69

3.2 Reflectance between 200 and 1000 nm as measured by SCIAMACHY, different colours depict different 'clusters' of detector pixels, each having its own slit function. Some clusters show elevated reflectances due to higher integration times - they get longer exposure than the other clusters as the detector scans the ground, thus covering a larger ground pixel than the others. These clusters will be omitted in our studies, since they do not represent the same ground pixel measured by clusters having the standard integration time. 70

3.3 Reflectance as measured by SCIAMACHY within the spectral windows chosen to avoid high frequency absorption structures. 71

3.4 Reflectances measured by SCIAMACHY throughout 2003 over Kanpur, India (26° N, 80° E) 72

3.5 Reflectances measured by SCIAMACHY throughout 2003 over La Parguera, Puerto Rico, USA (17° N, 67° W) 73

3.6 Reflectances measured by SCIAMACHY throughout 2003 over Mexico City, Mexico (19° N, 99° W) 73

3.7 Modeled single scattering (SS), multiple scattering (MS) and total (TS) reflectances seen by a nadir-pointing satellite detector at $SZA = 0°$ over lambertian surfaces of different albedos for increasing aerosol optical thickness. The aerosol type used here is IS1 (fine sized scattering industrial). The left panels show reflectances at a non-absorbing wavelength (682nm) near the O_2 B-band and the right panels show reflectances at a non-absorbing wavelength (756nm) near the O_2 A-band 75

3.8 Modeled single scattering (SS), multiple scattering (MS) and total (TS) reflectances seen by a nadir-pointing satellite detector at $SZA = 30°$ over lambertian surfaces of different albedos for increasing aerosol optical thickness. The aerosol type used here is IS1 (fine sized scattering industrial). The left panels show reflectances at a non-absorbing wavelength (682nm) near the O_2 B-band and the right panels show reflectances at a non-absorbing wavelength (756nm) near the O_2 A-band 76

3.9 Modeled single scattering (SS), multiple scattering (MS) and total (TS) reflectances seen by a nadir-pointing satellite detector at $SZA = 60°$ over lambertian surfaces of different albedos for increasing aerosol optical thickness. The aerosol type used here is IS1 (fine sized scattering industrial). The left panels show reflectances at a non-absorbing wavelength (682nm) near the O_2 B-band and the right panels show reflectances at a non-absorbing wavelength (756nm) near the O_2 A-band 77

3.10 Modeled single scattering (SS), multiple scattering (MS) and total (TS) reflectances seen by a nadir-pointing satellite detector at $SZA = 0°$ over lambertian surfaces of different albedos for increasing aerosol optical thickness. The aerosol type used here is IA2 (medium sized absorbing industrial). The left panels show reflectances at a non-absorbing wavelength (682nm) near the O_2 B-band and the right panels show reflectances at a non-absorbing wavelength (756nm) near the O_2 A-band 78

3.11 Modeled single scattering (SS), multiple scattering (MS) and total (TS) reflectances seen by a nadir-pointing satellite detector at $SZA = 30°$ over lambertian surfaces of different albedos for increasing aerosol optical thickness. The aerosol type used here is IA2 (medium sized absorbing industrial). The left panels show reflectances at a non-absorbing wavelength (682nm) near the O_2 B-band and the right panels show reflectances at a non-absorbing wavelength (756nm) near the O_2 A-band 79

3.12 Modeled single scattering (SS), multiple scattering (MS) and total (TS) reflectances seen by a nadir-pointing satellite detector at $SZA = 60°$ over lambertian surfaces of different albedos for increasing aerosol optical thickness. The aerosol type used here is IA2 (medium sized absorbing industrial). The left panels show reflectances at a non-absorbing wavelength (682nm) near the O_2 B-band and the right panels show reflectances at a non-absorbing wavelength (756nm) near the O_2 A-band 80

3.13 BRDF: This is a black spruce forest in the BOREAS experimental region in Canada. Left: backscattering (sun behind observer), note the bright region (hotspot) where all shadows are hidden. Right: forwardscattering (sun opposite observer), note the shadowed centers of trees and transmission of light through the edges of the canopies. 81

3.14 BRDF: A soybean field. Left: backscattering (sun behind observer). Right: forwardscattering (sun opposite observer), note the specular reflection of the leaves. 82

3.15 BRDF: A barren field with rough surface Left: backscattering (sun behind observer), note the bright region (hotspot) where all shadows are hidden. Right: forwardscattering (sun opposite observer), note the specular reflection. 82

3.16 The upper left and right panels show the retrieved albedos near the O_2 B and A-bands plotted against their true values. The lower panels show the corresponding percentage error in the retrieval. 85

3.17 Case studies for albedo retrieval in the presence of residual aerosol are presented for true lambertian albedos, ρ^*, of $0, 0.03, 0.06$ and 0.09 (top-bottom) respectively. The left and right panels show the retrieved albedos near the O_2 B and A-bands, respectively, plotted against the optical thickness of the aerosol contaminating the assumed clear-sky scenario. 87

3.18 The top panel shows synthetic 'measured/observed' reflectances around the O_2 B-band (solid line) for different aerosol loadings at a 'true' albedo of $A_{true} = 0$. These reflectances are used for the determination of the corresponding ground albedo A_{retr} under a clear sky assumption. The expected reflectances for $AOT = 0$ and a ground albedo of A_{retr} are represented by dash-dotted lines. The bottom panel shows the deviation of the expected from the observed reflectances for different residual aerosol loadings. The aerosol here is assumed to be of type IA2. 88

3.19 The top panel shows synthetic 'measured/observed' observed reflectances around the O_2 A-band (solid line) for different aerosol loadings at a 'true' albedo of $A_{true} = 0$. These reflectances are used for the determination of the corresponding ground albedo A_{retr} under a clear sky assumption. The expected reflectances for $AOT = 0$ and a ground albedo of A_{retr} are represented by dash-dotted lines. The bottom panel shows the deviation of the expected from the observed reflectances for different residual aerosol loadings. The aerosol here is assumed to be of type IA2. 89

3.20 The top panel shows synthetic 'measured/observed' reflectances around the O_2 B-band (solid line) for different aerosol loadings at a 'true' albedo of $A_{true} = 0.03$. These reflectances are used for the determination of the corresponding ground albedo A_{retr} under a clear sky assumption. The expected reflectances for $AOT = 0$ and a ground albedo of A_{retr} are represented by dash-dotted lines. The bottom panel shows the deviation of the expected from the observed reflectances for different residual aerosol loadings. The aerosol here is assumed to be of type IA2. 90

3.21 The top panel shows synthetic 'measured/observed' reflectances around the O_2 A-band (solid line) for different aerosol loadings at a 'true' albedo of $A_{true} = 0.03$. These reflectances are used for the determination of the corresponding ground albedo A_{retr} under a clear sky assumption. The expected reflectances for $AOT = 0$ and a ground albedo of A_{retr} are represented by dash-dotted lines. The bottom panel shows the deviation of the expected from the observed reflectances for different residual aerosol loadings. The aerosol here is assumed to be of type IA2. 91

3.22 The top panel shows synthetic 'measured/observed' reflectances around the O_2 B-band (solid line) for different aerosol loadings at a 'true' albedo of $A_{true} = 0.06$. These reflectances are used for the determination of the corresponding ground albedo A_{retr} under a clear sky assumption. The expected reflectances for $AOT = 0$ and a ground albedo of A_{retr} are represented by dash-dotted lines. The bottom panel shows the deviation of the expected from the observed reflectances for different residual aerosol loadings. The aerosol here is assumed to be of type IA2. 92

3.23 The top panel shows synthetic 'measured/observed' reflectances around the O_2 A-band (solid line) for different aerosol loadings at a 'true' albedo of $A_{true} = 0.06$. These reflectances are used for the determination of the corresponding ground albedo A_{retr} under a clear sky assumption. The expected reflectances for $AOT = 0$ and a ground albedo of A_{retr} are represented by dash-dotted lines. The bottom panel shows the deviation of the expected from the observed reflectances for different residual aerosol loadings. The aerosol here is assumed to be of type IA2. 93

3.24 The top panel shows synthetic 'measured/observed' reflectances around the O_2 B-band (solid line) for different aerosol loadings at a 'true' albedo of $A_{true} = 0.09$. These reflectances are used for the determination of the corresponding ground albedo A_{retr} under a clear sky assumption. The expected reflectances for $AOT = 0$ and a ground albedo of A_{retr} are represented by dash-dotted lines. The bottom panel shows the deviation of the expected from the observed reflectances for different residual aerosol loadings. The aerosol here is assumed to be of type IA2. 94

3.25 The top panel shows synthetic 'measured/observed' reflectances around the O_2 A-band (solid line) for different aerosol loadings at a 'true' albedo of $A_{true} = 0.09$. These reflectances are used for the determination of the corresponding ground albedo A_{retr} under a clear sky assumption. The expected reflectances for $AOT = 0$ and a ground albedo of A_{retr} are represented by dash-dotted lines. The bottom panel shows the deviation of the expected from the observed reflectances for different residual aerosol loadings. The aerosol here is assumed to be of type IA2. 95

3.26 Apparent albedos ρ_A (blue crosses) and ρ_B (red crosses) around the O_2 A and B-bands respectively plotted against the day of the year 2003 on which the scenario was recorded by SCIAMACHY over Kanpur, India. Also shown in the first three panels are the solar zenith angle (SZA), the line-of-sight zenith angle (LZA) and the relative azimuthal angle (Rel. Azim.) between the direction of incident (direct) sunlight and the line-of-sight. Dotted lines map these angles and the apparent albedos ρ_A and ρ_B for days that may correspond to clear-sky scenarios. 100

3.27 Observed (red curve) and expected (blue curve) reflectances under a clear-sky assumption for the selected spectral ranges around the O_2 B and A-bands on the left and right hand sides, respectively. The top panel shows the reflectance spectra for March 1, 2003 yielding discrepancies $\Delta R^B = 0.0019$ and $\Delta R^A = 0.0160$, the middle panel shows the reflectance spectra for August 7, 2003 yielding discrepancies $\Delta R^B = 0.0052$ and $\Delta R^A = 0.0266$ and the bottom panel shows the reflectance spectra for October 3, 2003 yielding discrepancies $\Delta R^B = 0.0019$ and $\Delta R^A = 0.0135$. Based on minimum discrepancy, we choose October 3, 2003 as a clear sky day. 101

3.28 Apparent albedos ρ_A (blue crosses) and ρ_B (red crosses) around the O_2 A and B-bands respectively plotted against the day of the year 2003 on which the scenario was recorded by SCIAMACHY over Mexico City, Mexico. Also shown in the first three panels are the solar zenith angle (SZA), the line-of-sight zenith angle (LZA) and the relative azimuthal angle (Rel. Azim.) between the direction of incident (direct) sunlight and the line-of-sight. Dotted lines map these angles and the apparent albedos ρ_A and ρ_B for days that may correspond to clear-sky scenarios. 102

3.29 Observed (red curve) and expected (blue curve) reflectances under a clear-sky assumption for the selected spectral ranges around the O_2 B and A-bands on the left and right hand sides, respectively. The top panel shows the reflectance spectra for March 1, 2003 yielding discrepancies $\Delta R^B = 0.0019$ and $\Delta R^A = 0.0160$, the middle panel shows the reflectance spectra for August 7, 2003 yielding discrepancies $\Delta R^B = 0.0052$ and $\Delta R^A = 0.0266$ and the bottom panel shows the reflectance spectra for October 3, 2003 yielding discrepancies $\Delta R^B = 0.0019$ and $\Delta R^A = 0.0135$. Based on minimum discrepancy, we choose October 3, 2003 as a clear sky day. 103

3.30 Apparent albedos ρ_A (blue crosses) and ρ_B (red crosses) around the O_2 A and B-bands respectively plotted against the day of the year 2003 on which the scenario was recorded by SCIAMACHY over La Parguera, Puerto Rico, USA. Also shown in the first three panels are the solar zenith angle (SZA), the line-of-sight zenith angle (LZA) and the relative azimuthal angle (Rel. Azim.) between the direction of incident (direct) sunlight and the line-of-sight. Dotted lines map these angles and the apparent albedos ρ_A and ρ_B for days that may correspond to clear-sky scenarios. 104

3.31 Observed (red curve) and expected (blue curve) reflectances under a clear-sky assumption for the selected spectral ranges around the O_2 B and A-bands on the left and right hand sides, respectively. The top panel shows the reflectance spectra for March 1, 2003 yielding discrepancies $\Delta R^B = 0.0019$ and $\Delta R^A = 0.0160$, the middle panel shows the reflectance spectra for August 7, 2003 yielding discrepancies $\Delta R^B = 0.0052$ and $\Delta R^A = 0.0266$ and the bottom panel shows the reflectance spectra for October 3, 2003 yielding discrepancies $\Delta R^B = 0.0019$ and $\Delta R^A = 0.0135$. Based on minimum discrepancy, we choose October 3, 2003 as a clear sky day. 105

4.1 The top left panel shows plots of retrieved aerosol optical thickness against the true value for which the synthetic measurement is made. The other components of the true state vector are $\{\alpha_{700}\colon 0, z_p\colon 0.5\mathsf{km}, \alpha_{700}\colon 0.25\}$. The top right panel shows plots of retrieved Ångström exponent against its true value. The other components of the true state vector are $\{\tau_{700}\colon 0.5, z_p\colon 2.0\mathsf{km}, \alpha_{700}\colon 0.75\}$. The lower left panel shows plots of the retrieved peak height of the aerosol vertical distribution against the true value for which the synthetic measurement is made. The other components of the true state vector are $\{\tau_{700}\colon 0.5, \alpha_{700}\colon 0, \sigma_p\colon 0.25\}$. The lower right panel shows plots of the retrieved peak width of the aerosol vertical distribution against the true value for which the synthetic measurement is made. The other components of the true state vector are $\{\tau_{700}\colon 0.5, \alpha_{700}\colon 0, z_p\colon 2.0\}$. The red circles represent a measurement noise, $\epsilon = 1\%$, while the blue circles represent $\epsilon = 3\%$. Crossed circles indicate that the iterations failed to achieve the desired convergence. 115

4.2 Top left: Averaging kernel areas for varying τ_{700}. The other components of the true state vector are $\{\alpha_{700}\colon 0, z_p\colon 0.5\mathsf{km}, \alpha_{700}\colon 0.25\}$. Top right: Averaging kernel areas for varying α_{700}. The other components of the true state vector are $\{\tau_{700}\colon 0.5, z_p\colon 2.0\mathsf{km}, \alpha_{700}\colon 0.75\}$. Bottom left: Averaging kernel areas for varying z_p. The other components of the true state vector are $\{\tau_{700}\colon 0.5, \alpha_{700}\colon 0, \sigma_p\colon 0.25\}$. Bottom right: Averaging kernel areas for varying σ_p. The other components of the true state vector are $\{\tau_{700}\colon 0.5, \alpha_{700}\colon 0, z_p\colon 2.0\}$. The x-axis represents the index number of the corresponding state vector element: $1\colon \tau_{700}, 2\colon \alpha_{700}, 3\colon z_p, 4\colon \sigma_P$. 116

4.3 The top four panels show the four columns of the Jacobian matrix, each corresponding to the partial derivative of the logarithm of the reflectances around the $\mathsf{O_2}$ A and B bands with respect to aerosol optical thickness τ_{700}, Ångström parameter α_{700}, peak height z_p and peak width σ_p respectively. The lower two panels show the fit on the left and the percentage residual of the fit on the right hand side of the logarithm of the reflectances around the B and A bands respectively. The abscissa represents the wavelength in nm. In each panel, the red, blue, green and black curves represent synthetic "true" values of $\tau_{700} = 0.0, 0.1, 0.5$ and 1.0 respectively, the synthetic "true" values for the other state vector elements remaining the same, viz. $\alpha_{700} = 0.0, z_p = 0.5\mathsf{km}, \sigma_p = 0.25$. The a priori assumption is the same in each case, viz. $x_a = \{0.5, 0.0, 3.0, 0.693\}$. The aerosol is assumed to be biogenic of type BL2. 118

4.4 The top four panels show the four columns of the Jacobian matrix, each corresponding to the partial derivative of the logarithm of the reflectances around the O_2 A and B bands with respect to the aerosol optical thickness τ_{700}, Ångström exponent α_{700}, peak height z_p and peak width σ_p respectively. The lower two panels show the fit on the left and the percentage residual of the fit on the right hand side of the logarithm of the reflectances around the B and A bands respectively. The abscissa represents the wavelength in nm. In each panel, the red, blue, green and black curves represent synthetic "true" values of $\alpha_{700} = -1.0, 0.0, 1.0$ and 2.0 respectively, the synthetic "true" values for the other state vector elements remaining the same, viz. $\tau_{700} = 0.5, z_p = 2.0\mathsf{km}, \sigma_p = 0.75$. The a priori assumption is the same in each case, viz. $x_a = \{0.5, 0.0, 3.0, 0.693\}$. The aerosol is assumed to be biogenic of type BL2. 120

4.5 The top four panels show the four columns of the Jacobian matrix, each corresponding to the partial derivative of the logarithm of the reflectances around the O_2 A and B bands with respect to aerosol optical thickness τ_{700}, Ångström parameter α_{700}, peak height z_p and peak width σ_p respectively. The lower two panels show the fit on the left and the percentage residual of the fit on the right hand side of the logarithm of the reflectances around the B and A bands respectively. The abscissa represents the wavelength in nm. In each panel, the red, blue, green and black curves represent synthetic "true" values of $z_p = 0.5, 1.0, 2.0$ and 4.0km respectively, the synthetic "true" values for the other state vector elements remaining the same, viz. $\tau_{700} = 0.5, \alpha_{700} = 0.0, \sigma_p = 0.25$. The a priori assumption is the same in each case, viz. $x_a = \{0.5, 0.0, 3.0, 0.693\}$. The aerosol is assumed to be biogenic of type BL2. 121

4.6 The top four panels show the four columns of the Jacobian matrix, each corresponding to the partial derivative of the logarithm of the reflectances around the O_2 A and B bands with respect to aerosol optical thickness τ_{700}, Ångström parameter α_{700}, peak height z_p and peak width σ_p respectively. The lower two panels show the fit on the left and the percentage residual of the fit on the right hand side of the logarithm of the reflectances around the B and A bands respectively. The abscissa represents the wavelength in nm. In each panel, the red, blue, green and black curves represent synthetic "true" values of $\sigma_p = 0.25, 0.50$ and 0.75 respectively, the synthetic "true" values for the other state vector elements remaining the same, viz. $\tau_{700} = 0.5, \alpha_{700} = 0.0, z_p = 2.0\mathsf{km}$. The a priori assumption is the same in each case, viz. $x_a = \{0.5, 0.0, 3.0, 0.693\}$. The aerosol is assumed to be biogenic of type BL2. 123

5.1 Simplied optical train of SCIAMACHY for the different observation modes. Only elements not common to all paths are shown. Note that the NDF is only in the light path of channels 36. Mirrors are marked blue, diffusers yellow. The optical path in the monitoring mode for the sun is marked red, the path for the moon is marked blue, *sm. AP denotes the small aperture,* Extr. M the extra mirror that can be put into the light path optionally.(*Skupin et al.*, 2003a) . . . 127

5.2 The upper and lower panels show the reflectances given by the ratio of the earthshine and the solar spectra around the O_2 B and A-bands respectively. The respective spectral measurements are made in clusters 24 and 26 of channel 4 of the SCIAMACHY instrument. The red curves show the reflectances in each case before shifting the solar spectrum by $\Delta\lambda_{sun}$ relative to the earthshine spectrum, while the blue curves show the post-shift reflectances. 128

5.3 Correction factors for SCIAMACHY radiances, irradiance and reflectances derived from NASA measurements. 130

5.4 Correction factors for SCIAMACHY radiances, irradiance and reflectances derived from spectralon measurements. 130

5.5 Wavelength shifts Δa_0^A and Δa_0^B retrieved for different values of the radiometric degradation factor f_A and f_B respectively. The true shift in each case is 0.01nm. 132

5.6 Retrieval of the radiometric degradation factor f_A (red line, bottom panel). The corresponding retrievals (blue curves) of the Ångström exponent α, the peak height z_p, the peak width σ_p and the optical thickness τ of the aerosol scenario having true values (black lines) $\alpha_{true} = 0$, $z_{ptrue} = 2.0\mathsf{km}$, $\sigma_{ptrue} = 0.693$ and $\tau_{true} = 0.5$ are plotted in the first four panels. 133

5.7 SCIAMACHY retrieval of aerosol optical thickness over Kanpur on April 11, 2003 for different assumptions of clear sky day. 134

5.8 SCIAMACHY retrieval of aerosol optical thickness over Kanpur on April 11, 2003 for different a priori assumptions of aerosol type. 135

5.9 SCIAMACHY retrieval of aerosol properties over Kanpur in 2003. The aerosol optical thickness τ, peak height z_p and peak width σ_p retrieved under stringent convergence conditions are shown in the bottom panel (red crosses), the second panel (blue crosses) and the top panel (green crosses). The bottom panel also shows AOT retrievals made under relaxed convergence conditions, represented by black crosses. Cloudy scenarios are shown circled in light blue. 136

5.10 Averaged monthly aerosol optical thicknesses obtained from AERONET data (blue) and from SCIAMACHY retrievals (red). 138

5.11 Scatter plot of mean monthly aerosol optical thicknesses obtained from AERONET data (blue) and from SCIAMACHY retrievals (red). 139

5.12 Trends of the retrieved aerosol optical thickness with respect to surface temperature T (left) and surface pressure p (right). 140

5.13 Trends of the retrieved aerosol optical thickness (top panel) and of the peak height (bottom left) and peak width (bottom right) of the aerosol vertical distribution with respect to T/p^{κ}. 142

5.14 The red curve shows the saturation vapor pressure of water as a function of ambient temperature. The green curve represents a saturation ratio $S = 2$ for water vapor, i.e. a relative humidity of 200%. Isentropes representing the partial pressure of water vapor against the temperature in adiabatically expanding air masses of different surface temperatures and pressures expected over Kanpur are shown. The points of intersection of the isentropes with the red and green curves represent the partial vapor pressure and temperature at which the water vapor becomes saturated and 200% supersaturated, respectively. 143

5.15 The blue and black solid curves show the altitude plotted against the temperature at which water vapor reaches saturation, given a surface pressure of 980 hPa and 1013.25 hPa, respectively. The dashed blue and black curves show a similar plot for a saturation ratio of 2. The red curves show the altitude of adiabatically expanding air parcels of various surface temperatures against the temperature of the parcel. The points of intersection represent the altitude and temperature at which the water vapor becomes saturated and 200% supersaturated, respectively. 144

List of Tables

1.1 Overview of the different aerosol indirect effects and range of the radiative budget perturbation [$\mathsf{W\,m^{-2}}$] at the top-of-the atmosphere (F_{TOA}), at the surface (F_{SFC}) and the likely sign of the change in global mean surface precipitation (P) (*Lohmann and Feichter*, 2001) 12

1.2 Annual source strength for present day emissions of aerosol precursors (Tg N, S or C /year) 20

2.1 Aerosol size distribution and refractive index for the selected aerosol models . . 53

2.2 Aerosol size distribution and refractive index for the selected aerosol models . . 54

3.1 Discrepancy ΔR between the observed and the expected reflectances due to 'clear sky' assumption of different residual aerosol loadings at a true albedo, ρ_{true}, of 0.00. 96

3.2 Discrepancy ΔR between the observed and the expected reflectances due to 'clear sky' assumption of different residual aerosol loadings at a true albedo, ρ_{true}, of 0.03. 96

3.3 Discrepancy ΔR between the observed and the expected reflectances due to 'clear sky' assumption of different residual aerosol loadings at a true albedo, ρ_{true}, of 0.06. 96

3.4 Discrepancy ΔR between the observed and the expected reflectances due to 'clear sky' assumption of different residual aerosol loadings at a true albedo, ρ_{true}, of 0.09. 97

References

Acarreta, J. R., and P. Stammes (2005), Calibration Comparison Between SCIAMACHY and MERIS Onboard ENVISAT, *IEEE Geoscience and Remote Sensing Letters, vol. 2, issue 1, pp. 31-35*, *2*, 31–35, doi:10.1109/LGRS.2004.838348.

Adams, P., J. Seinfeld, D. Koch, L. Mickley, and D. Jacob (2001), General circulation model assessment of direct radiative forcing by the sulfate-nitrate-ammonium-water inorganic aerosol system, *J. Geophys. Res.*, *106*(D1).

Albrecht, B. A. (1989), Aerosols, Cloud Microphysics, and Fractional Cloudiness, *Science*, *245*(4923), 1227–1230.

Andreae, M., and A. Henderson-Sellers (1995), Climatic effects of changing atmospheric aerosol levels, *World Survey of Climatology*, *16*, 341–392.

Andreae, M. O. (1995), Climatic effects of changing atmospheric aerosol levels, *World Survey of Climatology*, *16*, 341–392.

Andres, R. J., and A. D. Kasgnoc (1998), A time-averaged inventory of subaerial volcanic sulfur emissions, *J. Geophys. Res.*, *103*(D19), 25,251–25,262.

Bassett, M. E., and J. H. Seinfeld (1984), Atmospheric Equilibrium-Model of Sulfate and Nitrate Aerosols, 2. Particle-Size Analysis, *Atmos. Environ*, *18*(6), 1163–1170.

Bhattacharjee, P. S., A. K. Prasad, M. Kafatos, and R. P. Singh (2007), Influence of a dust storm on carbon monoxide and water vapor over the Indo-Gangetic Plains, *Journal of geophysical research, 112.*

Claquin, T., M. Schulz, Y. Balkanski, and O. Boucher (1998), Uncertainties in assessing radiative forcing by mineral dust, *Tellus B*, *50*(5), 491–505.

Claquin, T., M. Schulz, and Y. Balkanski (1999), Modeling the mineralogy of atmospheric dust sources, *J. Geophys. Res.*, *104*, 22,243–22,256.

Clarke, A. D. (1992), Atmospheric nuclei in the remote free-troposphere, *Journal of Atmospheric Chemistry*, *14*, 479–488.

Clarke, A. D. (1993), Atmospheric nuclei in the Pacific midtroposphere: Their nature, concentration, and evolution, *Journal of Geophysical Research*, *98*, 20,633–20,647.

Cooke, W., and J. Wilson (1996), A global black carbon aerosol model, *J. Geophys. Res.*, *101*(D 14), 19,395–19,409.

Cooke, W., C. Liousse, H. Cachier, and J. Feichter (1999), Construction of a 1 degrees× 1 degrees fossil fuel emission data set for carbonaceous aerosol and implementation and radiative impact in the ECHAM4 model, *J. Geophys. Res*, *104*(22), 137–22.

Deutschmann, T. (2009), Atmospheric radiative transfer modelling with monte carlo methods, Master's thesis, Institute of Environmental Physics, Heidelberg.

Di Nicolantonio, W., A. Cacciari, S. Scarpanti, G. Ballista, E. Morisi, and R. Guzzi (2006), SCIAMACHY TOA REFLECTANCE CORRECTION EFFECTS ON AEROSOL OPTICAL DEPTH RETRIEVAL , in *Proceedings of the 1st Atmospheric Science Conference, ESRIN, Frascati.*

Erickson, D. J., and R. A. Duce (1988), On the global flux of atmospheric sea salt, *J. Geophys. Res.*, *93*, 14,079–14,088.

Forster, P., V. Ramaswamy, P. Artaxo, T. Berntsen, R. Betts, D. W. Fahey, J. Haywood, J. Lean, D. C. Lowe, G. Myhre, J. Nganga, R. Prinn, G. Raga, M. Schulz, and R. V. Dorland (2007), Changes in Atmospheric Constituents and in Radiative Forcing. In: Climate Change 2007: The Physical Science Basis., *Contribution of Working Group I to the Fourth Assessment Report of the Intergovernmental Panel on Climate Change [Solomon, S., D. Qin, M. Manning, Z. Chen, M. Marquis, K.B. Averyt, M.Tignor and H.L. Miller (eds.)].*

Gard, E. E., M. J. Kleeman, D. S. Gross, L. S. Hughes, J. O. Allen, B. D. Morrical, D. P. Fergenson, T. Dienes, et al. (1998), Direct Observation of Heterogeneous Chemistry in the Atmosphere, *Science*, *279*(5354), 1184.

Graf, H. F., J. Feichter, and B. Langmann (1997), Volcanic degassing: Contribution to global sulphate burden and climate, *J. Geophys. Res*, *102*, 10–727.

Gras, J. L. (1991), Southern hemisphere tropospheric aerosol microphysics, *Journal of Geophysical Research*, *96*, 5345–5356.

Griffin, R. J., D. R. Cocker, R. C. Flagan, and J. H. Seinfeld (1999a), Organic aerosol formation from the oxidation of biogenic hydrocarbons, *J. Geophys. Res.*, *104*(D3), 3555–3567.

Griffin, R. J., D. R. Cocker, J. H. Seinfeld, and D. Dabdub (1999b), Estimate of global atmospheric organic aerosol from oxidation of biogenic hydrocarbons, *Geophys. Res. Lett.,*, *26*(17), 2721–2724.

Gurlit, W., K. Gerilowski, H. Krause, and J. P. Burrows (2003), SCIAMACHY solar irradiance validation using radiometric calibration of balloonborne spectrometers, in *European Rocket and Balloon Programmes and Related Research*, *ESA Special Publication*, vol. 530, edited by B. Warmbein, pp. 433–437.

Guzzi, R. (2001), Aerosol maps from GOME data, *Atmospheric Environment*, *35*, 5079–5091.

Hasekamp, O., and J. Landgraf (2002), A linearized vector radiative transfer model for atmospheric trace gas retrieval, *Journal of Quantitative Spectroscopy and Radiative Transfer*, *75*, 221–238.

Havers, N., P. Burba, J. Lambert, and D. Klockow (1998), Spectroscopic Characterization of Humic-Like Substances in Airborne Particulate Matter, *Journal of Atmospheric Chemistry*, *29*(1), 45–54.

Hegerl, G. C., K. Hasselmann, U. Cubasch, J. F. B. Mitchell, E. Roeckner, R. Voss, and J. Waszkewitz (1997), Multi-fingerprint detection and attribution analysis of greenhouse gas, greenhouse gas-plus-aerosol and solar forced climate change, *Climate Dynamics*, *13*(9), 613–634.

Herman, B. M., W. Asous, and S. R. Browning (1980), A semi-analytic technique to integrate the radiative transfer equation over optical depth, *Journal of the atmospheric sciences*, *37*, 1828–1838.

Hoffmann, T., J. R. Odum, F. Bowman, D. Collins, D. Klockow, R. C. Flagan, and J. H. Seinfeld (1997a), Formation of organic aerosols from the oxidation of biogenic hydrocarbons, *Journal of Atmospheric Chemistry*, *26*(2), 189–222.

Hoffmann, T., J. R. ODUM, F. BOWMAN, D. COLLINS, D. KLOCKOW, R. C. FLAGAN, and J. H. SEINFELD (1997b), Formation of Organic Aerosols from the Oxidation of Biogenic Hydrocarbons, *The Journal of Atmospheric Chemistry*, *26*(2), 189–222, doi: 10.1023/A:1005734301837.

Jaenicke, R. (1993), Tropospheric aerosols, *INTERNATIONAL GEOPHYSICS SERIES*, *54*.

John, W., S. Wall, J. Ondo, and W. Winklmayr (1990), Modes in the size distributions of atmospheric inorganic aerosol, *Atmospheric Environment*, *24-A*, 2349–2359.

Jones, A., D. L. Roberts, and A. Slingo (1994), A climate model study of indirect radiative forcing by anthropogenic sulphate aerosols, *Nature*, *370*(6489), 450–453.

Kent, G. S., and M. P. McCormick (1984), SAGE and SAM II measurements of global stratospheric aerosol optical depth and mass loading, *J. Geophys. Res.*, *89*.

Kettle, A. J., and M. O. Andreae (2000), Flux of dimethylsulfide from the oceans: A comparison of updated data sets and flux models, *J. Geophys. Res.*, *105*(D22).

Kiehl, J. T., and B. P. Briegleb (1993), The Relative Roles of Sulfate Aerosols and Greenhouse Gases in Climate Forcing, *Science*, *260*(5106), 311–314.

Koelemeijer, R. B. A., J. F. de Haan, and P. Stammes (2003), A database of spectral surface reflectivity in the range $335 - 772\,\mathrm{nm}$ derived from 5.5 years of GOME observations , *Journal of geophysical research*, *108*.

Koppers, G. A. A., J. Jansson, and D. P. Murtagh (1997), Aerosol optical thickness retrieval from GOME data in the oxygen A-band, in *Scientific proceedings of the* 3^{rd} *ERS symposium on space at the service of our environment, Florence , Italy*, pp. 693–696.

Kulmala, M., and A. Laaksonen (1990), Binary nucleation of water–sulfuric acid system: Comparison of classical theories with different HSO saturation vapor pressures, *The Journal of Chemical Physics*, *93*, 696.

Kulmala, M., P. Korhonen, Y. Viisanen, and A. Laaksonen (2000), The homogeneous heteromolecular nucleation of sulphuric acid, water and ammonia in the coastal environment, *The Journal of Aerosol Science*, *31*, 652–653.

Kurucz, H. L. (1995), The Solar Spectrum: Atlases and Line Identifications, in *Laboratory and Astronomical High Resolution Spectra*, *Astronomical Society of the Pacific Conference Series*, vol. 81, edited by A. J. Sauval, R. Blomme, and N. Grevesse, pp. 17–+.

Kusmierczyk-Michulec, J., and G. de Leeuw (2005), Aerosol optical thickness retrieval over land and water using Global Ozone Monitoring Experiment (GOME) data, *Journal of Geophysical Research*, *110*.

Latter, B. G., R. Siddans, and B. J. Kerridge (2003), Intercomparison of Reflectances Observed by SCIAMACHY, GOME, AATSR and ATSR-2, *EGS - AGU - EUG Joint Assembly, Abstracts from the meeting held in Nice, France, 6 - 11 April 2003, abstract #11451*, pp. 11,451–+.

Lelieveld, J., G. J. Roelofs, L. Ganzeveld, J. Feichter, and H. Rodhe (1997), Terrestrial sources and distribution of atmospheric sulphur, *Philosophical Transactions of the Royal Society B: Biological Sciences*, *352*(1350), 149.

Lenoble, J. (1985), *Radiative transfer in scattering and absorbing atmospheres: standard computational procedures*, A. Deepak Publishing.

Lenoble, J., M. Herman, J. L. Deuzé, B. Lafrance, R. Santer, and D. Tanré (2007), A successive order of scattering code for solving the vector equation of transfer in the earth's atmosphere with aerosols, *Journal of Quantitative Spectroscopy and Radiative Transfer*, *107*, 479–507.

Li-Jones, X., and J. M. Prospero (1998), Variations in the size distribution of non-sea-salt sulfate aerosol in the marine boundary layer at Barbados: Impact of African dust, *J. Geophys. Res.*, *103*(D13).

Liou, K. N. (1992), *Radiation and Cloud Processes in the Atmosphere*, Oxford University Press, New York Oxford.

Lohmann, U., and J. Feichter (2001), Can the direct and semi-direct aerosol effect compete with the indirect effect on a global scale?, *Geophys. Res. Lett.,*, *28*(1), 159–161.

Matthias-Maser, S., and R. Jaenicke (1995), The size distribution of primary biological aerosol particles with radii $> 0.2\,\mu$m in an urban/rural influenced region, *Atmospheric Research*, *39*(4), 279–286.

Murphy, D. M., and D. S. Thomson (1997), Chemical composition of single aerosol particles at Idaho Hill: Negative ion measurements, *J. Geophys. Res*, *102*(6,353), 6–368.

Murphy, D. M., J. R. Anderson, P. K. Quinn, L. M. McInnes, F. J. Brechtel, S. M. Kreidenweiss, A. M. Middlebrook, M. Posfai, D. S. Thomson, and P. R. Buseck (1998), Influence of sea-salt on aerosol radiative properties in the southern ocean marine boundary layer, *Nature*, *392*, 62–65.

Noel, S. (2005), Determination of correction factors for SCIAMACHY radiances and irradiances, *Univ. Bremen, Bremen, Germany, Tech. Rep. IFE-SCIA-SN-20050203_IrrRadCorrection.[Online]. Available: http://www. iup. physik. uni-bremen. de/sciamachy/SCIA_CAL/irrad_corr. pdf.*

Noël, S., H. Bovensmann, M. W. Wuttke, J. P. Burrows, M. Gottwald, E. Krieg, A. P. H. Goede, and C. Muller (2002), Nadir, limb, and occultation measurements with SCIAMACHY, *Advances in Space Research*, *29*, 1819–1824.

O'Dowd, C. D., M. H. Smith, I. E. Consterdine, and J. A. Lowe (1997), Marine aerosol, sea-salt, and the marine sulphur cycle: a short review, *Atmospheric Environment*, *31*, 73–80.

Odum, J. R., T. Hoffmann, F. Bowman, D. Collins, R. C. Flagan, and J. H. Seinfeld (1996), Gas/particle partitioning and secondary organic aerosol yields, *Environmental Science & Technology*, *30*(8), 2580–2585.

Penner, J., C. Chuang, and C. Liousse (1996), The contribution of carbonaceous aerosols to climate change, in *14. international conference on nucleation and atmospheric aerosols, Helsinki (Finland), 26-30 Aug 1996.*

Penner, J., C. Chuang, and K. Grant (1998), Climate forcing by carbonaceous and sulfate aerosols, *Climate Dynamics*, *14*(12), 839–851.

Penner, J. E., H. Eddleman, and T. Novakov (1991), Towards the development of a global inventory for black carbon emissions, in *4. international conference on carbonaceous particles in the atmosphere*, 5.

Picott, S. D., J. J. Watson, and J. W. Jones (1992), A Global inventory of volatile organic compound emissions from anthropogenic sources, *J. Geophys. Res.*, *97*(D9).

Quinn, P., D. Coffman, V. Kapustin, T. Bates, and D. Covert (1998), Aerosol optical properties in the marine boundary layer during the first aerosol characterization experiment (ace 1) and the underlying chemical and physical aerosol properties, *J. Geophys. Res.*, *103*, 16,547–16,564.

Reader, M., and G. Boer (1998), The modification of greenhouse gas warming by the direct effect of sulphate aerosols, *Climate Dynamics*, *14*(7), 593–607.

Robertson, A., J. Overpeck, D. Rind, E. Mosley-Thompson, G. Zielinski, J. Lean, D. Koch, J. Penner, I. Tegen, and R. Healy (2001), Hypothesized climate forcing time series for the last 500 years, *J. Geophys. Res.*, *106*(D14), 14,783–14,803.

Rodgers, C. D. (2000), *Inverse methods for atmospheric sounding - Theory and Practice*, World Scientific.

Roedel, W. (2000), *Physik unserer Umwelt - die Atmosphäre*, Springer.

Rozanov, A., V. Rozanov, M. Buchwitz, A. Kokhanovsky, and J. P. Burrows (2005), Sciatran 2.0 - a new radiative transfer model for geophysical applications in the $175-2400\,\mathsf{nm}$ spectral region, *Advances in Space Research*, *36*, 1015–1019.

Sanghavi, S. (2003), An efficient mie theory implementation to investigate the influence of aerosols on radiative transfer, Master's thesis, Institute of Environmental Physics, Heidelberg.

Schnell, R. C., and G. Vali (1976), Biogenic Ice Nuclei: Part I. Terrestrial and Marine Sources, *Journal of the Atmospheric Sciences*, *33*(8), 1554–1564.

Scholes, R. J., D. E. Ward, and C. O. Justice (1996), Emissions of trace gases and aerosol particles due to vegetation burning in southern hemisphere Africa, *J. Geophys. Res*, *101*(23), 677–23.

Seinfeld, J. H., and S. N. Pandis (2006), *Atmospheric chemistry and physics - from air pollution to climate change*, Wiley.

Skupin, J., S. Noel, M. W. Wuttke, H. Bovensmann, J. P. Burrows, R. Hoogeveen, Q. Kleipool, and G. Lich tenberg (2003a), In-flight calibration of the SCIAMACHY solar irradiance spectrum, *Advances in Space Research*, *32*, 2129–2134, doi:10.1016/S0273-1177(03)90533-3.

Skupin, J., S. Noel, M. W. Wuttke, H. Bovensmann, J. P. Burrows, R. Hoogeveen, Q. Kleipool, and G. Lichtenberg (2003b), In-flight calibration of the SCIAMACHY solar irradiance spectrum, *Advances in Space Research*, *32*, 2129–2134, doi:10.1016/S0273-1177(03)90533-3.

Sokolik, I. N., and O. B. Toon (1996), Direct radiative forcing by anthropogenic airborne mineral aerosols, *Nature*, *381*, 681–683.

Spiro, P. A., D. J. Jacob, and J. A. Logan (1992), Global inventory of sulfur emissions with $1\times\ 1$ resolution, *J. Geophys. Res*, *97*, 6023–6036.

Stoiber, R. E., S. N. Williams, and B. Huebert (1987), Annual contribution of sulfur dioxide to the atmosphere by volcanoes, *J. Volcanol. Geotherm. Res*, *33*, 1–8.

Tegen, I., and A. A. Lacis (1996), Modeling of particle size distribution and its influence on the radiative properties of mineral dust aerosol, *J. Geophys. Res.*, *101*, 19,237–19,244.

Tegen, I., A. A. Lacis, and I. Fung (1996), The influence on climate forcing of mineral aerosols from disturbed soils, *Nature*, *380*, 419–422.

Tegen, I., P. Hollrig, M. Chin, I. Fung, D. Jacob, and J. Penner (1997), Contribution of different aerosol species to the global aerosol extinction optical thickness: Estimates from model results, *J. Geophys. Res.*, *102*, 23,895–23,916.

Tilstra, L., J. Acarreta, J. Krijger, and P. Stammes (2003), VERIFICATION OF SCIAMACHYÕS POLARISATION CORRECTION OVER THE SAHARA DESERT, *ESA Special Publication, 531.*

Twomey, S. (1991), Aerosols, clouds and radiation, *Atmospheric environment*, *25*(11), 2435–2442.

van Soest, G., L. G. Tilstra, and P. Stammes (2005), Large-scale validation of SCIAMACHY reflectance in the ultraviolet, *Atmospheric Chemistry & Physics*, *5*, 2171–2180.

von Hoyningen-Huene, W., M. Freitag, and J. P. Burrows (2003), Retrieval of aerosol optical thickness over land surfaces from top-of-atmosphere radiance, *Journal of geophysical research*, *108*.

Weisenstein, D. K., G. K. Yue, M. K. W. Ko, N. D. Sze, J. M. Rodriguez, and C. J. Scott (1997), A two-dimensional model of sulfur species and aerosols, *J. Geophys. Res.*, *102*(D11), 13,019–13,036.

Whitby, K., and B. Cantrell (1976), Atmospheric aerosols - characteristics and measurements, in *ICESA Conference Proceedings.*

Wolf, M., and G. Hidy (1997), Aerosols and climate: anthropogenic emissions and trends for 50 years, *Fuel and Energy Abstracts*, *38*(5), 348–348.

Acknowlegements

Foremost, I wish to express my gratitude toward the following people for their vital contributions to the progress of this dissertation:

- Prof. Dr. Platt, who provided me with the opportunity to work on this challenging but exciting subject and his enduring support through the ups and downs of it.
- Dr. Jochen Landgraf for his indispensable guidance on the subject of radiative transfer modeling. I'm also indebted to him for his painstaking and exhaustive corrections of the raw drafts of this thesis. Jochen's feedback turned the process of correction from a mundane necessity into a much appreciated learning experience!
- Dr. Otto Hasekamp for his guidance on the subject of radiative transfer modeling.
- André Butz for running LINTRAN simulations that I used as a reference while fine-tuning AeroRad during its final development phase.
- Jochen Landgraf, Christian Frankenberg and Tim Deutschmann for making model simulations (LINTRAN, SCIATRAN and McArtim, respectively) available for comparison with AeroRad.
- Christian Frankenberg for valuable inputs with regard to Optimal Estimation.

This dissertation has demanded considerable background knowledge of meteorological and atmospheric chemistry concepts and a great amount of programming expertise - both areas I was an utter novice to as I started this work. I would like to thank Roland von Glasow and Christian Frankenberg for making subjects pertaining to meteorology and atmospheric chemistry more easily accessible. Many thanks are also due to Tim Deutschmann who brought alive to me the myriad possibilities and tremendous freedom offered by Linux, turning me quickly from a nervous beginner to an ardent enthusiast. In this regard, I wish to thank both Tim Deutschmann and Christian Frankenberg for introducing me to shell script programming and the large number of nifty applications that have put computing freedom at my fingertips!

The birth of my son Neal in June, 2006, and our subsequent move to Utrecht has made this dissertation more of a family endeavour than I would ever have thought possible! As the teething problems of the dissertation were compounded by Neal's persistent early illnesses, and the little free time available for me to work was eaten into by compulsory intensive Dutch language classes, my commitment to continue this dissertation was only reinforced by every

member of my immediate family. At this point, I would also like to extend my sincere thanks to Mr. Platt for his kindness and flexibility during that critical period.

Special heartfelt thanks are due to my parents-in-law, Marianne and Klaus, who actively helped us simplify our (high entropy) lives. It would have been much more difficult to jump start this dissertation without the combined nanny and B&B services that Marianne provided unflinchingly during Neal's illnesses.

I thank Neal, today an increasingly self-sufficient, co-operative and enthusiastic 2 year old, who has filled our lives with unparalleled joy - a joy that always miraculously took the burden off the most testing situations!

Finally, I thank my parents, Bharati and Vinod, who took great pains to give me wings to fly on, and kept their faith when those wings took me to unfathomable places. Last and most, I thank Christian, my wise uncomplaining rock, giving much and demanding little in return - thank you for being in my life!